Lecture Notes in Chemistry 110

Samantha Jenkins
Steven Robert Kirk

# Next Generation Quantum Theory of Atoms in Molecules

## From Stereochemistry to Photochemistry and Molecular Devices

Springer

# Lecture Notes in Chemistry

Volume 110

**Series Editors**
Barry Carpenter, Cardiff, UK
Paola Ceroni, Bologna, Italy
Katharina Landfester, Mainz, Germany
Jerzy Leszczynski, Jackson, USA
Tien-Yau Luh, Taipei, Taiwan
Eva Perlt, Bonn, Germany
Nicolas C. Polfer, Gainesville, USA
Reiner Salzer, Dresden, Germany
Kazuya Saito, Department of Chemistry, University of Tsukuba, Tsukuba, Japan

The series Lecture Notes in Chemistry (LNC), reports new developments in chemistry and molecular science - quickly and informally, but with a high quality and the explicit aim to summarize and communicate current knowledge for teaching and training purposes. Books published in this series are conceived as bridging material between advanced graduate textbooks and the forefront of research. They will serve the following purposes:

- provide an accessible introduction to the field to postgraduate students and nonspecialist researchers from related areas,
- provide a source of advanced teaching material for specialized seminars, courses and schools, and
- be readily accessible in print and online.

The series covers all established fields of chemistry such as analytical chemistry, organic chemistry, inorganic chemistry, physical chemistry including electrochemistry, theoretical and computational chemistry, industrial chemistry, and catalysis. It is also a particularly suitable forum for volumes addressing the interfaces of chemistry with other disciplines, such as biology, medicine, physics, engineering, materials science including polymer and nanoscience, or earth and environmental science.

Both authored and edited volumes will be considered for publication. Edited volumes should however consist of a very limited number of contributions only. Proceedings will not be considered for LNC.

The year 2010 marked the relaunch of LNC.

Samantha Jenkins · Steven Robert Kirk

# Next Generation Quantum Theory of Atoms in Molecules

## From Stereochemistry to Photochemistry and Molecular Devices

Springer

Samantha Jenkins
College of Chemistry and Chemical Engineering
Hunan Normal University
Changsha, Hunan, China

Steven Robert Kirk
College of Chemistry and Chemical Engineering
Hunan Normal University
Changsha, Hunan, China

ISSN 0342-4901 ISSN 2192-6603 (electronic)
Lecture Notes in Chemistry
ISBN 978-981-99-0328-3 ISBN 978-981-99-0329-0 (eBook)
https://doi.org/10.1007/978-981-99-0329-0

© The Editor(s) (if applicable) and The Author(s), under exclusive license to Springer Nature Singapore Pte Ltd. 2023
This work is subject to copyright. All rights are solely and exclusively licensed by the Publisher, whether the whole or part of the material is concerned, specifically the rights of translation, reprinting, reuse of illustrations, recitation, broadcasting, reproduction on microfilms or in any other physical way, and transmission or information storage and retrieval, electronic adaptation, computer software, or by similar or dissimilar methodology now known or hereafter developed.
The use of general descriptive names, registered names, trademarks, service marks, etc. in this publication does not imply, even in the absence of a specific statement, that such names are exempt from the relevant protective laws and regulations and therefore free for general use.
The publisher, the authors, and the editors are safe to assume that the advice and information in this book are believed to be true and accurate at the date of publication. Neither the publisher nor the authors or the editors give a warranty, expressed or implied, with respect to the material contained herein or for any errors or omissions that may have been made. The publisher remains neutral with regard to jurisdictional claims in published maps and institutional affiliations.

This Springer imprint is published by the registered company Springer Nature Singapore Pte Ltd.
The registered company address is: 152 Beach Road, #21-01/04 Gateway East, Singapore 189721, Singapore

# Preface

Chemistry is a science that is as broad as it is fundamental that defines molecules, nanostructures, extended solids, their properties, reactions and photochemistry, in addition to the chemical compositions of geological and astronomical objects including stars, planets and galaxies. A background in chemistry is essential for careers in all these disciplines. In addition, chemistry is central to technology, the inter- and multi-disciplinary areas of molecular biology, molecular genetics, nanotechnology, medicinal chemistry, drug design and the development of environmentally friendly chemical industry.

Richard F. W. Bader, the originator of the Quantum Theory of Atoms in Molecules (QTAIM), elegantly defined an atom in a molecule in real space without the need for arbitrary molecular orbitals or crude charge density differences. We refer to original QTAIM as scalar QTAIM, and this forms the foundation upon which we build. We do not, however, limit ourselves to the use of scalars but also use the vectors, in the form of eigenvectors that previously have been overlooked as useful predictive chemical tools.

This book is aimed at undergraduate and graduate students and persons in the chemical industries, but is also accessible to students in secondary schools. We provide familiar, water, benzene, lactic acid as well as molecules of contemporary interest to illustrate and explain the development of vector-based QTAIM that we refer to as Next-Generation QTAIM (NG-QTAIM). The required background is knowledge of mathematics, quantum chemistry and physics at the level of secondary schools or the first year of university. From mathematics, basic concepts in the following: linear algebra, differential geometry and calculus.

The origins of NG-QTAIM started by accident: during my Ph.D. on the phonons of various phases of water ($H_2O$) ice. I noticed when I considered the bottom of the rotational band where correlated motion indicated that interactions were present between the sub-lattices in ice VI, ice VII and ice VIII. I further investigated this with a simple investigation of a crude scratch-built QTAIM code I made in partnership with Steven R. Kirk and discovered that bond critical points (*BCP*s) were associated with these sub-lattice interactions. I also notice for cubic ice Ic that the bottom of the rotational band, where structures most easily deform, strongly corresponded to

the directions that the easy deformation directions of the QTAIM eigenvectors of the hydrogen bonding. The development of NG-QTAIM was prompted by a simple static QTAIM investigation of the *cis*-effect that was shortly afterward explored further to better understand the unusual structure and bonding of biphenyl. This further exploration took the form of a pair of $\pm 80.0°$ torsions about the central C-C bond that tracked how the QTAIM properties varied.

All our NG-QTAIM publications are available as pre-prints in the form of .pdf files along with the corresponding supplementary materials at our BEACON website www.beaconresearch.org.

Free-to-use electronic structure software [1] can be used to obtain the wave functions that are the input of NG-QTAIM. QuantVec is our free-to-use NG-QTAIM software [2].

Chapter 1 provides a simplified version of the computational quantum chemistry sufficient to calculate the wave functions that are the basic input of NG-QTAIM. Chapter 2 presents sufficient scalar QTAIM to understand the later chapters in addition to presenting our developments of scalar QTAIM. Chapter 3 presents the bridge between scalar QTAIM and NG-QTAIM. Chapter 4 presents the NG-QTAIM interpretation of the chemical bond, and Chap. 5 presents applications to the stress tensor $\boldsymbol{\sigma}(\mathbf{r})$ and Ehrenfest Force $\mathbf{F}(\mathbf{r})$. Chapters 6–8 concern the NG-QTAIM stress tensor $\boldsymbol{\sigma}(\mathbf{r})$, Hessian $\rho(\mathbf{r})$ and Ehrenfest Force $\mathbf{F}(\mathbf{r})$ trajectories. A detailed overview of the content is given in Sect. 1.3.

Changsha, China

Samantha Jenkins
Steven Robert Kirk

**Acknowledgements** We would like to thank all current and past BEACON group members, faculty at our College of Chemistry and Engineering, Hunan Normal University, and research collaborators whose efforts ensured the completion of this book. In particular, we give special thanks to the BEACON group members Yu Wenjing for compiling the references, Xiao Peng Mi, Hui Lu and Yu Wenjing for organizing journal publisher permissions and Tianlv Xu for collecting the lists of thesis repositories. In addition, we give special thanks for the continuous support and funding of Hunan Province in addition to the National Natural Science Foundation of China (NSFC).

We would also like to thank the staff at Springer for their help and support.

## References

1. Lehtola S, Karttunen AJ, Free and open source software for computational chemistry education. WIREs Comput Mol Sci e1610. https://doi.org/10.1002/wcms.1610
2. Kirk SR, Jenkins S (2021) QuantVec. https://doi.org/10.5281/Zenodo.5553686

# Contents


**1 Introduction to Computational Quantum Chemistry** . . . . . 1
1.1 Basis Sets Background . . . . . 2
1.1.1 Gaussian Type Orbital (GTO) Basis Sets . . . . . 3
1.1.2 Common Basis Set Types . . . . . 5
1.1.3 Effective Core Potentials (ECPs) for Use with Heavy Atoms . . . . . 5
1.1.4 Suggestions for the Choice of Basis Set . . . . . 6
1.2 Density Functional Theory (DFT) . . . . . 6
1.2.1 Spin Restricted and Spin Unrestricted DFT Methods . . . . . 7
1.2.2 Wave Function Formats . . . . . 8
1.3 Geometry Optimization . . . . . 9
1.3.1 Normal-Mode Analysis . . . . . 10
1.4 An Overview of the Content of the Book . . . . . 10
1.5 Further Reading . . . . . 14
References . . . . . 14

**2 Exploring the Topological Origins of QTAIM** . . . . . 15
2.1 The Quantum Theory of Atoms in Molecules (QTAIM): Basics . . . 16
2.2 Non-euclidian Geometry for Molecules and Quantum Topology Phase Diagrams (QTPDs) . . . . . 19
2.2.1 The Structure of Quantum Topology Phase Diagrams (QTPDs) . . . . . 21
2.2.2 QTPDs and Non-nuclear Attractors (*NNA*s) . . . . . 24
2.2.3 QTPDs and the Solid State . . . . . 24
2.2.4 Hybrid QTAIM and Electrostatic Potential QTPDs . . . . . 25
2.2.5 Directed QTPDs . . . . . 27
2.3 The Number of Nearest *RCP*s (*NNRCP*s) for an Impurity *NCP* in a Metal Host Cluster . . . . . 31
2.4 Determining the Presence of Covalent Character in Closed-Shell Bonding . . . . . 32

2.5 A Measure of Metallic Character: Metallicity $\xi(r_b)$, Polarizability P and Stiffness S ..... 36
2.6 Summary ..... 40
2.7 Further Reading ..... 43
References ..... 43

**3 Bridging Scalar QTAIM and Vector-Based Next Generation QTAIM** ..... 47
3.1 Relating the Projected Density of States (PDOS) and QTAIM ..... 48
3.2 The Bond-Path Framework: Lack of Accordance of the Motion of $\rho(r_b)$ and Nuclei for Bond Torsion ..... 52
3.2.1 Torsion of Biphenyl: Detachment and Reattachment of the Bond-Path Framework ..... 54
3.2.2 The Photo-Isomerization of the Retinal Chromophore ..... 54
3.2.3 The QTAIM Interpreted Ramachandran Plot ..... 55
3.2.4 Explanation of the ($\beta_\phi$-$\beta_\psi$) and ($\beta_\phi{}^*$-$\beta_\psi{}^*$) of the Closed-Shell H--O/H---O BCPs and H---H BCPs ... 60
3.3 Summary ..... 62
3.4 Further Reading ..... 63
References ..... 63

**4 The NG-QTAIM Interpretation of the Chemical Bond** ..... 65
4.1 Construction of the Bond-Path Framework Set: Vector-Based Representation of the Chemical Bond ..... 66
4.2 Construction of the Precession K of the Bond-Path Framework Set B ..... 69
4.3 Applications of the Bond-Path Framework Set: Normal Modes of Vibration ..... 70
4.3.1 3-D Bonding Morphology of the Infra-Red Active Modes of Benzene ..... 70
4.3.2 A Vector-Based Representation of the Chemical Bond for the Normal Modes of Benzene ..... 72
4.3.3 Bond Flexing, Twisting, Anharmonicity and Responsivity for the IR-Active Modes of Benzene .... 74
4.4 Strained and Unusual Bonding Environments ..... 77
4.4.1 The Directional Bonding of [1.1.1] Propellane ..... 77
4.5 Multi-electronic States ..... 80
4.5.1 Ring-Restoring Reactions ..... 80
4.5.2 The Excited State Deactivation Reaction of Fulvene ..... 82
4.5.3 Factors Influencing the Relative Stability of the Conical Intersections of the Penta-2,4-Dieniminium Cation (PSB3) ..... 87
4.6 Summary ..... 88
4.7 Further Reading ..... 89
References ..... 89

**5 The Stress Tensor σ(r) and Ehrenfest Force F(r)** . . . . . 93
5.1 The Stress Tensor σ(r) . . . . . 94
5.1.1 The Stress Tensor σ(r) Bond-Path Framework Set $\mathsf{B}_\sigma$ . . . . . 96
5.1.2 Halogen and Hydrogen-Bonding in Halogenabenzene/$NH_3$ Complexes Compared . . . . . 98
5.1.3 Photochemical Reaction Path from Benzene to Benzvalene . . . . . 101
5.2 The Ehrenfest Force F(r): A Physically Intuitive Approach for Analyzing Chemical Interactions . . . . . 104
5.2.1 The Ehrenfest Force F(r) with Lithium . . . . . 107
5.2.2 The Ehrenfest Force F(r) Bond-Path Framework Set $\mathsf{B}_\mathrm{F}$, $\mathsf{B}_{\sigma\mathrm{F}}$ and $\mathsf{B}_{\sigma\mathrm{HF}}$ . . . . . 108
5.3 The Precessions $\mathsf{K'}_\mathrm{F}$ and $\mathsf{K}_\mathrm{F}$ Corresponding to the Ehrenfest Force F(r) . . . . . 115
5.3.1 Precessions $\mathsf{K'}_\mathrm{F}$ and $\mathsf{K}_\mathrm{F}$ of the Ehrenfest Force F(R) for the Unusual Strength of Hydrogen-Bonding . . . . . 119
5.4 Summary . . . . . 123
5.5 Further Reading . . . . . 124
References . . . . . 124

**6 The Eigenvector-Space Trajectories for Symmetry Breaking** . . . . . 127
6.1 Theoretical Background of the Eigenvector-Space Trajectories $\mathsf{T}_i(\boldsymbol{s})$; $i = \{\sigma, \rho, \mathrm{F}\}$ . . . . . 128
6.2 Numerical Considerations for Construction of the Eigen-Space Trajectories $\mathsf{T}_i(\boldsymbol{s})$; $i = \{\sigma, \rho, \mathrm{F}\}$ . . . . . 128
6.2.1 The QuantVec Program Package . . . . . 129
6.3 Applications of the Eigenvector-Space Trajectories $\mathsf{T}_i(\boldsymbol{s})$; $i =$ $\{\rho\}$: the Hessian of $\rho$(r) Trajectory $\mathsf{T}(\boldsymbol{s})$ . . . . . 132
6.3.1 Normal Modes of Vibration: Isotope Effects and Bond Coupling . . . . . 132
6.4 Applications of the Eigenvector-Space Trajectories $\mathsf{T}_i(s)$; $i =$ $\{\sigma\}$: the Stress Tensor Trajectory $\mathsf{T}_\sigma(s)$ . . . . . 134
6.4.1 Normal Modes of Vibration and Dynamic Coupling . . . . . 135
6.4.2 Covalent (Sigma) OH and Hydrogen-Bond Coupling on the $(H_2O)_5$ MP2 Potential Energy Surface . . . . . 136
6.4.3 Iso-Energetic Phenomena I: Prediction of the Flip Rearrangement in the Water Pentamer . . . . . 138
6.4.4 Iso-Energetic Phenomena II: Torquoselectivity in Competitive Ring-Opening Reactions . . . . . 140
6.5 Applications of the Eigenvector-Space Trajectories $\mathsf{T}_i(\boldsymbol{s})$; $i =$ {F}: Ehrenfest Force F(r) $\mathsf{T}_\mathrm{F}(\boldsymbol{s})$ . . . . . 141
6.5.1 Determining Photochemical Ring-Opening Reactions of Oxirane with the Ehrenfest Force F(r) . . . . . 142
6.6 Summary . . . . . 146

6.7 Further Reading . . . . . 150
References . . . . . 150

**7 Stereochemistry Beyond Chiral Discrimination** . . . . . 153
7.1 Insufficiency of Scalar Measures for Chiral Discrimination . . . . . 154
7.1.1 Location of the Unknown Helical Character Associated with Chirality . . . . . 155
7.1.2 Inducing the Required Symmetry-Breaking to Reveal Helical Character . . . . . 156
7.2 First Generation Stress Tensor Trajectories $\mathsf{T}_\sigma(s)$ . . . . . 156
7.2.1 The Choice of the Stress Tensor Trajectory $\mathsf{T}_\sigma(s)$ for Chiral Discrimination . . . . . 158
7.3 Refinements of the First Generation Stress Tensor Trajectories $\mathsf{T}_\sigma(s)$ . . . . . 160
7.3.1 Hydrogen and Deuterium Isotopomers of Glycine Compared . . . . . 161
7.3.2 Subjecting Glycine to an Electric (E)-Field . . . . . 162
7.3.3 The Chirality-Helicity Function $\mathsf{C}_{helicity}$ for Cumulenes . . . . 164
7.3.4 The Chirality with Stereoisomers for $S_N2$ Reactions . . . . . 166
7.4 Second Generation Stress Tensor Trajectories $\mathsf{T}_\sigma(s)$ . . . . . 169
7.4.1 Chiral and Steric Effects in Ethane . . . . . 169
7.4.2 Mixed Chiral and Achiral Character in Substituted Ethane . . . . . 171
7.4.3 Controlling Achiral and Chiral Properties of Alanine with an Electric Field . . . . . 179
7.4.4 Explanation of Why the *Cis*-Effect is the Exception and Not the Rule . . . . . 183
7.5 Summary . . . . . 184
7.6 Further Reading . . . . . 188
References . . . . . 188

**8 The Design of Molecular Devices** . . . . . 191
8.1 Steering Molecular Devices: With Vector-Based Measures . . . . . 192
8.2 Controlling Molecular Rotary Motors . . . . . 193
8.3 Switches: 'ON' and 'OFF' Mechanisms: Hydrogen Transfer Tautomerization . . . . . 196
8.3.1 Deformation of a Nuclear Skeleton via Hydrogen Atom Sliding . . . . . 196
8.3.2 E-Fields for Improved "ON" and "OFF" Switch Performance . . . . . 197
8.4 Switches: Ring-Opening Reactions . . . . . 200
8.5 Fatigue of Photo-Switches . . . . . 201
8.5.1 Photo-Switch Fatigue Response to External Fields Electric(E)-Fields . . . . . 202
8.6 Assembly of Electronic Devices Using Molecules . . . . . 203

8.6.1 Scoring Molecular Wires in E-fields for Molecular Electronic Devices . . . . . 205
8.6.2 Design of Emitters Exhibiting Thermally-Activated Delayed Fluorescence (TADF) . . . . . 206
8.6.3 Effect of a Static E-field on the Energy Gap $\Delta E(S_1\text{-}T_1)$ . . . . 207
8.6.4 Manipulation of the Energy Gap $\Delta E(S_1\text{-}T_1)$ with Laser Pulses . . . . . 207
8.7 Summary . . . . . 210
8.8 Further Reading . . . . . 214
References . . . . . 214

**Appendix A** . . . . . 219

**Appendix B** . . . . . 221

**Index** . . . . . 223

# Chapter 1
# Introduction to Computational Quantum Chemistry

*It doesn't matter whether a cat is black or white, as long as it catches mice.*
*Deng Xiaoping*

The calculation of wavefunctions is central to the implementation of both scalar and vector-based quantum theory of atoms in molecules (QTAIM) and will be overviewed in this chapter and forms the basis for the rest of this book. Here we do not provide a detailed overview of the historic progression of the theoretical developments of electronic theory, or very specific theoretical details not central to the calculation of the wavefunctions that we use, see Fig. 1.1. For a much more detailed and complete treatment of computational chemistry Cramer's *Essentials of Computational Chemistry* is highly recommended[1]. Almost all of quantum chemistry is based on the solution of the many-body Schrodinger equation. This solution consists of the eigenvalue, the energies typically obtained from *ab-initio* calculations, the eigenfunction, the wave-function, where $\mathbf{\Psi}(\mathbf{r}) \cdot \mathbf{\Psi} * (\mathbf{r}) = \rho(\mathbf{r})$ and is a quantum mechanical observable. It is important that we include the eigenfunctions, since they contain so much information which otherwise would be lost and because the charge density $\rho(\mathbf{r})$ is an experimental observable. Ideally, such a quantum mechanics-based theory should be able to provide a framework to make sense of future experimental findings as experimental techniques improve beyond current expectations. The task of tracking of the evolution of the electronic degrees of freedom is conventionally performed with internal coordinates, for example, bond distances, angles, dihedrals, or out-of-plane motions. This assumes a precedence of the motion of the nuclear coordinates over the electronic charge density $\boldsymbol{\rho}(\mathbf{r})$ distribution and is very insensitive to changes in the properties of $\boldsymbol{\rho}(\mathbf{r})$.

© The Author(s), under exclusive license to Springer Nature Singapore Pte Ltd. 2023

S. Jenkins and S. R. Kirk, *Next Generation Quantum Theory of Atoms in Molecules*,
Lecture Notes in Chemistry 110, https://doi.org/10.1007/978-981-99-0329-0_1

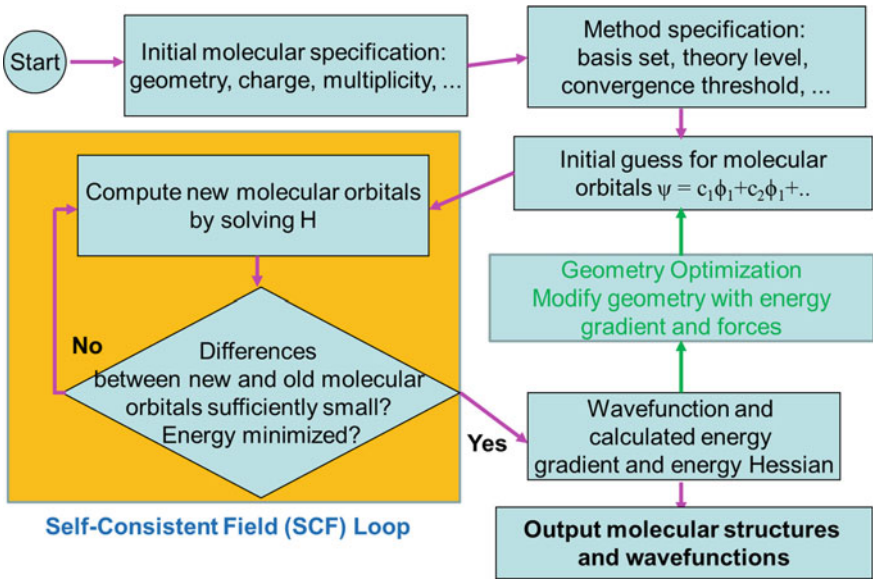
Start
Initial molecular specification: geometry, charge, multiplicity, ...
Method specification: basis set, theory level, convergence threshold, ...
Initial guess for molecular orbitals ψ = c1ϕ1+c2ϕ1+..
Compute new molecular orbitals by solving H
Geometry Optimization Modify geometry with energy gradient and forces
No
Differences between new and old molecular orbitals sufficiently small? Energy minimized?
Yes
Wavefunction and calculated energy gradient and energy Hessian
Self-Consistent Field (SCF) Loop
Output molecular structures and wavefunctions

**Fig. 1.1** Scheme of a typical self-consistent field calculation and geometry optimization procedure

## 1.1 Basis Sets Background

*In this section we explain the use of the different types of basis sets and effective core potentials (ECPs) and suggest their usage.*

A basis set is a combinations of mathematical functions used to represent atomic orbitals and are created from the linear combination of atomic orbitals (LCAO) approximation, see Fig. 1.2. Each one-electron molecular orbital $\phi$ is approximated by a linear combination of atomic orbitals $c_i$(basis functions) with expansion coefficients $c_i$:

$$\phi = c_1\chi_1 + c_2\chi_2 + c_3\chi_3 + \ldots$$

The more basis functions, the better representation of the wave function, and thus the lower energy. As the number of basis functions increases to infinity we have the best result possible corresponding to the complete basis set (CBS) limit, see Fig. 1.3. We cannot handle infinite number of basis functions, but we may be able to estimate the energy at the CBS limit.

Instead of optimizing all coefficients $c_i$, one predetermines the ratios between some selected coefficients, forming a fixed linear combination of basis functions this process is referred to a contracting the basis set. for example the following contracted basis set results in A loss in accuracy but a gain in efficiency:

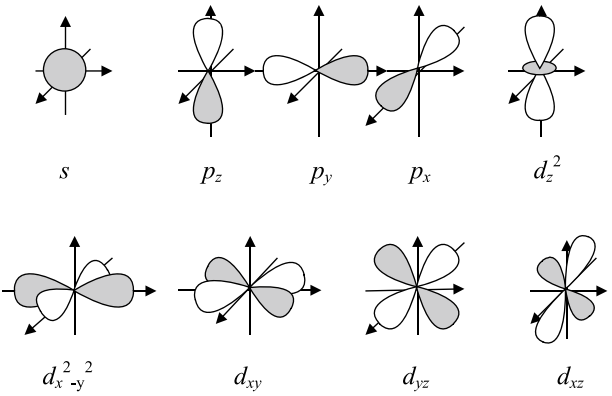


**Fig. 1.2** The employed mathematical functions describe the radial and angular distributions of electron density

**Fig. 1.3** The variation of the energy with basis set size

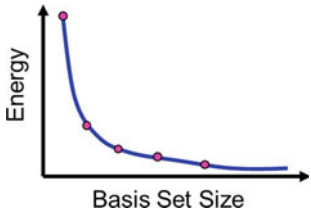


$$\phi = c_1\chi_1 + c_2\chi_2 + c_3\chi_3 + c_4\chi_4 + c_5\chi_5 + c_6\chi_6 + c_7\chi_7$$

possesses 7 coefficients ($c_1$ to $c_7$) to be optimized

$$\phi = c_1(\chi_1 + a_2\chi_2 + a_3\chi_3 + a_4\chi_4 + a_5\chi_5) + c_6\chi_6 + c_7\chi_7$$

possesses 3 coefficients ($c_1$, $c_6$ and $c_7$) to be optimized.

The contracted GTO is displayed in red and the primitive GTO is displayed in blue.

### *1.1.1 Gaussian Type Orbital (GTO) Basis Sets*

A commonly used basis set are Gaussian Type Orbital (GTOs) and although GTOs describes the radial electron distribution less satisfactorily they are easy to handle because integrations can be calculated analytically, see Fig. 1.4. A Gaussian Type Orbital (GTO) takes the form:

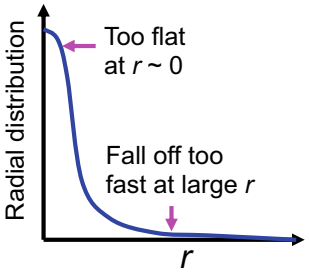


**Fig. 1.4** The variation of the radial GTO with separation $r$

$$\chi c_{\zeta,n,l,m}(r,\theta,\phi) \propto \underbrace{Y_{l,m}(q,\phi)}\,\underbrace{r^{2n-2-l}e^{zr2}}$$

A: Spherical harmonic function for angular distribution

B: Exponential function for radial distribution

Slater type orbitals (STOs) are approximated by a linear combination of $n$ primitive Gaussian functions with a minimum basis that comprises only enough functions to accommodate all electrons and are referred to as STO-$n$G and are widely used in semi-empirical calculations, especially for $n = 3$, see Fig. 1.5.

Normal split valence basis sets describe electron distribution not far away from nuclear centers. Some cases have electron distribution far away from nuclear centers e.g., anions, molecules with lone pairs of electrons, excited states, transition state. An additional $s$ function for H and He and $p$ functions for heavy atoms with very diffuse radial distributions, see Fig. 1.6.

Polarization basis functions that comprise higher angular momentum functions improves the description for anisotropic electron distribution, usually $p$ orbitals are

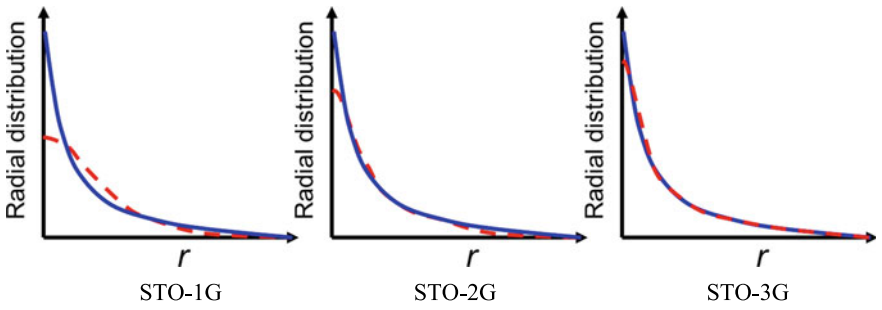


**Fig. 1.5** Distribution of the radial STO-$n$G with separation $r$

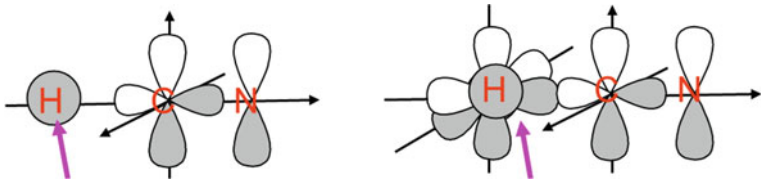


**Fig. 1.6** An anisotropic electron distribution that cannot be described by *s* orbitals (left-panel). The Anisotropic distribution in the left-panel can be better described by *p* orbitals (right-panel)

added to H and He, *d* orbitals are added to first-row atoms, *f* orbitals are added to second-row atoms.

### *1.1.2 Common Basis Set Types*

**Pople's Basis Sets**

- 3-21G

Comprises 3 primitive GTO for core electrons, 2 for inner and 1 for outer valence orbitals. Used for preliminary geometry optimization give poor results for energies.

| | |
|---|---|
| $6-31\text{G}$<br>$6-31\text{G(d)}$<br>$6-31\text{G(d, p)}$ | Common moderate basis set |
| 6–31 + G(d,p) | Good for geometry and energy |
| 6–311 + G(2df,2p) | Good for geometry and accurate energy |

**Dunning's Correlation-consistent Basis Sets**

Systematically converge the correlation energy to the basis set limit, typically with high-level electron-correlated wave function methods:

(aug)-cc-p(C)VXZ, X = D, T, Q, 5, 6, and 7.

Basis sets can also be modified and/or optimize for a particular task.

### *1.1.3 Effective Core Potentials (ECPs) for Use with Heavy Atoms*

Core electrons are chemically unimportant, but require a large number of basis functions for an accurate description of their orbitals. An effective core potential (ECP)

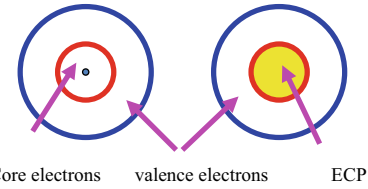


**Fig. 1.7** Schematic of the implementation of an ECP

is a linear combination of specially designed Gaussian functions that model the core electrons, i.e., the core electrons are represented by an effective potential and one treats only the valence electrons explicitly, see Fig. 1.7.

- Saves computational effort.
- Taking care of relativistic effects partly.
- Important for heavy atoms, e.g., transition metal atoms.

### *1.1.4 Suggestions for the Choice of Basis Set*

- Always a compromise between accuracy and computational cost.
- With the increase of basis set size, calculated energy will converge. We refer such a situation as the complete basis set (CBS) limit.
- Do you have anything special (anion, transition metal, transition state)?
- Use smaller basis sets for preliminary calculations and for heavy duties (e.g., geometry optimizations), and use larger basis sets to refine calculations.
- Use larger basis sets for critical atoms (e.g., atoms directly involved in bond-breaking/forming), and use smaller basis sets for unimportant atoms (e.g., atoms distant away from active site).
- Use popular and recommended basis sets. They have been tested a lot and shown to be good for certain types of calculations.

## 1.2 Density Functional Theory (DFT)

*In this section we explain the density functional theory basics.*

There is a one-to-one connection between energy E and density $\rho$: E = F[$\rho(x)$], however we do not know the functional. The central task in DFT is to find the *functional.* Thomas–Fermi-Dirac Model: Non-reacting uniform electron gas. Kohn–Sham Theory (1965): Atoms & Molecules:

$$E_{\mathrm{DFT}}[\rho] = T[\rho] + E_{\mathrm{ne}}[\rho] + J[\rho] + E_{\mathrm{xc}}[\rho]$$

$T[\rho]$ : electronic kinetic energy

$E_{ne}[\rho]$ : nuclei-electrons coulombic energy

$J[\rho]$ : electron-electrons coulombic energy

$E_{xc}[\rho]$ : electron-electrons exchange energy

DFT scaling behavior ~ $N^4$ which is expensive and there is currently systematic way to improve the accuracy. Accuracy varies from model to model and from one application area to another:

BLYP: good for metals, poor for organic compounds

B3LY: poor for metals, good for organic compounds

MPW1K: parameterized for kinetics for transition states, reaction barrier heights, poor for stable molecules.

Now improved with empirical dispersion corrections, e.g., B3LYP-D3(BJ). A model should be validated before use by testing the model on small molecules where reliable experimental data are available or high-level *ab- initio* calculations can be performed.

### *1.2.1 Spin Restricted and Spin Unrestricted DFT Methods*

For a closed-shell system, spin unrestricted and spin restricted theory methods give the same results.

For an open-shell system, spin unrestricted gives lower energy than spin restricted does, because the system is now relaxed from the restriction of forcing $\alpha$ and $\beta$ electrons in the same spatial orbitals.

Electrons have spins ($\alpha$ and $\beta$, or up and down), to identify an electron, both spatial orbitals and spin orbitals are required, see Fig. 1.8.

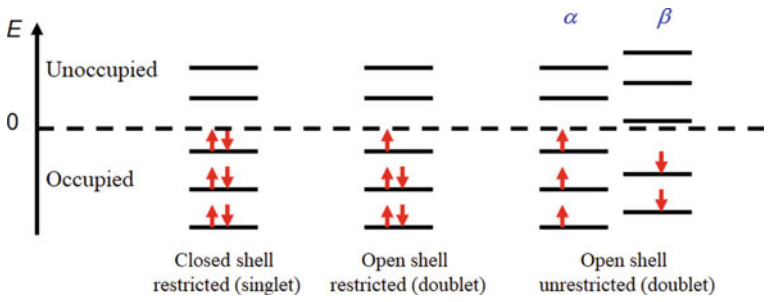


**Fig. 1.8** Schematic of $\alpha$ and $\beta$ electrons for closed shell and open shell systems

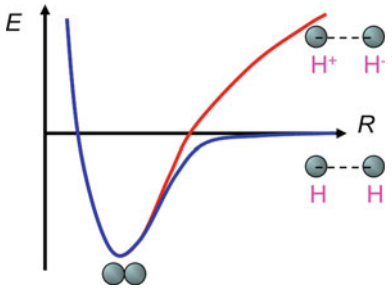


**Fig. 1.9** The dependence of the choice of spin restriction on the disassociation of the hydrogen molecule

Spin restricted: accommodate electrons of opposite spins in pairs i.e., in the same spatial orbitals.

Spin unrestricted: allow two electrons of opposite spins staying in different spatial orbitals.

A hydrogen molecule dissociates depending on the choice of spin restriction/unrestricted …

Unrestricted: two atoms

Restricted: two ions

The explanation for the differences in the dissociation of the hydrogen molecule is because the $\alpha$ and $\beta$ electrons have to be in the same spatial orbitals even if two nuclei are far away from each other, see Fig. 1.9.

### *1.2.2 Wave Function Formats*

- Molden: Can be produced by many different electron structure codes.
- WFN/WFX: Can be produced by Gaussian and a few other codes, support for ECPs in WFX only.

Support for total electronic densities and $\alpha$ and $\beta$ spin densities.

- Molden2aim can convert MOLDEN to WFN/WFX available free of charge at:

https://github.com/zorkzou/Molden2AIM

**Summary for Basis Sets**

- What is a basis set in the LCAO approximation?
- Gaussian type orbitals.
- Diffuse & polarization basis functions.
- Common basis sets.
- Effective core potentials.

- How to select basis sets.
- Typical procedure of calculations.

## 1.3 Geometry Optimization

*In this section we explain the process of obtaining the minimum energy molecular structure, see* Fig. 1.1.

The process of geometry optimization involves locating one or more of the following:

- Local Minimum Structure.

In numerical calculations, due to the finite precision, a zero gradient is not exactly zero and is smaller than a pre-defined cut-off value, loose, tight, very tight …

- Global Minimum Structure.
- Transition State Structure.
- Reaction Pathway Connecting Two Minima and Passing through the Transition State structure.

Gradient: $g_x = \partial E/\partial x$

First-order derivatives of energy w/r variables e.g., Cartesian coordinates X, Y, & Z, or internal coordinates such as bond-length and angle displacements, the negative of the gradient is called force, $F = -\partial E/\partial x$.

Stationary Point

A point on the PES where gradient is zero including minimum, maximum, and saddle points, a transition state is a first-order saddle point.

Hessian: $H_{xy} = \partial^2 E/\partial x \partial y$

A matrix of second-order derivatives of the energy with respect to variables e.g., Cartesian or internal coordinates.

**Summary for Geometry Optimizations**

Typical Tasks for Geometry Optimizations:

- Describe the PES.
- Gradient, Hessian, Minima, Maxima, Saddle Points.
- Find a local minimum.
- Steepest Descent, Conjugated gradient, Newton–Raphson.
- Restrained and Constrained Optimization e.g. A torsional scan.
- Choice of Coordinates.

### *1.3.1 Normal-Mode Analysis*

Diagonalization of the Hessian matrix to obtain vibrational frequencies, related to the eigenvalues and normal modes of vibrations referred to as eigenvectors[2]. Note: Normal-mode analysis is only meaningful at stationary points.

A normal-mode analysis also known as frequency calculation can be used to identify a stationary point.

Minimum: All frequencies are real eigenvalues of the Hessian are positive.

Maximum: All frequencies are imaginary (eigenvalues of the Hessian are negative).

Saddle point: Some frequencies are imaginary.

In particular, a saddle point with only one imaginary frequency and is called a transition state.

**Target Learning Outcomes**

- Understand the need for and limitations of the use of basis sets for the calculation of wavefunctions.
- Understand the applicability of different basis sets.
- Understand the need for different treatments for heavy elements and how to consider them.
- Understand the self-consistent nature of density functional theory (DFT).
- Know what normal modes are and their basic features.

## 1.4 An Overview of the Content of the Book

Chapters 1–8 provide *Target Learning Outcomes* and *Further Reading*, Chapters 2–8 also provide a list of the *scientific goals to be addressed*, a glossary table is provided in the summary section of Chapters 2–3, 5–8. Where applicable each chapter concludes by outlining benefits, limitations and suggestions for further investigations.

**Chapter 1**. **Introduction to Computational Quantum Chemistry**. This chapter provides a simplified version of the computational quantum chemistry sufficient to calculate the wavefunctions that are the basic input of our Quantvec NG-QTAIM software. A list of contributing BEACON group members with their thesis titles is provided along with the site to find additional contributions from BEACON group members that will not graduate until after the publication.

**Chapter 2**. **Exploring the Topological Origins of QTAIM**. Basic scalar QTAIM is provided that is sufficient to understand the later chapters in addition presenting our developments of scalar QTAIM. Activities at various levels of difficulty are provided for the readership to facilitate understanding.

**Chapter 3**. **Bridging Scalar QTAIM and Vector-Based Next Generation QTAIM**. Presents the bridge between scalar QTAIM and NG-QTAIM and explains the origins of NG-QTAIM in the form of the correspondence observed between the normal modes of vibration of cubic ice (ice Ic) and the QTAIM eigenvectors. The NG-QTAIM interpretation of the chemical bond starts with the quantification of the motion of total electronic charge density and nuclei participating in bond torsion. The examples of torsion of biphenyl and the photo-isomerization of the retinal chromophore are provided to test the degree of association of nuclei and the total electronic charge density. The QTAIM interpretation of the Ramachandran plot ($\phi$-$\psi$) includes vector-based characteristics forms a partial version of NG-QTAIM.

**Chapter 4**. **The NG-QTAIM Interpretation of the Chemical Bond**. The NG-QTAIM representation of the chemical bond that we refer to as the bond-path framework set $\mathsf{B}$ is introduced. The bond-path framework set $\mathsf{B}$ is much more sensitive to changes in the distribution of the total electronic charge density distribution than is the case for the QTAIM bond-path. We outline the construction of $\mathsf{B}$ and briefly include some of the properties of $\mathsf{B}$. The procedure to calculate the precession $\mathsf{K}$, that quantifies the wrapping of $\mathsf{B}$ around the bond-path, is presented. We consider applications of B that highlight the sensitivity to changes in $\rho(\mathbf{r})$ including the infrared active modes of benzene. The treatment of strained and unusual bonding environments includes multi-electronic states.

**Chapter 5**. **The Stress Tensor $\boldsymbol{\sigma}(\mathbf{r})$ and Ehrenfest Force $\mathbf{F}(\mathbf{r})$**. The bond-path framework set $\mathsf{B}$ is constructed for use with the stress tensor $\boldsymbol{\sigma}(\mathbf{r})$ and Ehrenfest Force $\mathbf{F}(\mathbf{r})$. The example of the torsion of ethene are used in the Hessian of $\rho(\mathbf{r})$ bond-path framework set $\mathsf{B}$ and stress tensor bond-path framework set $\mathsf{B}_{\boldsymbol{\sigma}}$. The mixed bonding character of halogen-bonding and hydrogen-bonding in halogenabenzenes includes consideration of relativistic effects, NG-QTAIM is demonstrated to be more effective than scalar QTAIM. The explosive nature of benzvalene is explained by following the photochemical reaction pathway from benzene to benzvalene. The Ehrenfest Force $\mathbf{F}(\mathbf{r})$ partitioning is outlined that includes implementation details and examples including small lithium and water clusters. The Ehrenfest Force $\mathbf{F}(\mathbf{r})$ precessions $\mathsf{K}'_{\mathbf{F}}$ and $\mathsf{K}_{\mathbf{F}}$ corresponding to the Ehrenfest Force $\mathbf{F(r)}$ are explained and applied to small water clusters to explain the unusual strength of hydrogen bonding.

**Chapter 6**. **The Eigenvector-Space Trajectories for Symmetry Breaking**. We present the theoretical background Eigenvector-space trajectories $\mathsf{T}_i(s)$ with the corresponding numerical considerations. We introduce our associated QuantVec software that is used to construct the $\mathsf{T}_i(s)$. An application of the $\mathsf{T}_i(s)$ using the Hessian of $\rho(\mathbf{r})$ for the normal modes of vibration analysis of isotope effects and bond coupling of deuterium and tritium in water is presented. An NG-QTAIM normal modes analysis of benzene of the $\mathsf{T}_i(s)$ is undertaken using the stress tensor $\boldsymbol{\sigma}(\mathbf{r})$ to provide the dynamic coupling of the C-H bonds and C–C bonds. The coupling of covalent (sigma) OH and hydrogen-bond on the $(H_2O)_5$ MP2 potential energy surface is examined and the first of two iso-energetic phenomena is considered, that of the prediction of the flip

rearrangement in $(H_2O)_5$. The iso-energetic phenomena: prediction of torquoselectivity in competitive ring-opening reactions is presented. The successful prediction of the outcome of photochemical ring-opening reactions of oxirane with the Ehrenfest Force $\mathbf{F}(\mathbf{r})$, is undertaken and consistency with a hybrid $\mathsf{T}_{\mathbf{F}\boldsymbol{\sigma}}(s)$ Ehrenfest Force $\mathbf{F}$(r) and stress tensor $\boldsymbol{\sigma}(\mathbf{r})$ is found.

**Chapter 7**. **Stereochemistry: Beyond Chiral Discrimination**. The insufficiency of all scalar chemical measures for use with chiral discrimination is explained. The unknown helical characteristics of stereoisomers as the origin of chirality are discussed along with the requirement for symmetry breaking to reveal helical character. The NG-QTAIM interpretation of chirality $\mathsf{C}_\sigma$ is presented by the construction of the first generation stress tensor trajectories. The performance of the Hessian of $\rho(\mathbf{r})$ trajectory $\mathsf{T}(s)$ and the stress tensor trajectory $\mathsf{T}_\sigma(s)$ for chiral discrimination is compared. Determination of the dependence of the chirality $\mathsf{C}_\sigma$ on an electric $\mathbf{E}$-field is undertaken as an application of first generation $\mathsf{T}_\sigma(s)$. The chirality of isotopomers of glycine is compared using the chirality-helicity function $\mathsf{C}_{helicity}$ that constitutes second generation $\mathsf{T}_\sigma(s)$. Chiral and formally achiral $S_N2$ reactions and cumulenes are investigated using the $\mathsf{C}_{helicity}$. Third generation $\mathsf{T}_\sigma(s)$ are introduced and explained and demonstrated with decorated and undecorated hydrocarbons to demonstrate the effect of atom weight of substituents and the presence of chiral mixing.

**Chapter 8**. **The Design of Molecular Devices**. We provide the necessary background to molecular devices and the relevance of NG-QTAIM. The molecular devices thought out this chapter are presented in order of decreasing nuclear motion commencing with molecular rotary motors. The 'ON' and 'OFF' mechanisms of the functioning of a switch triggered by hydrogen transfer tautomerization in the absence and presence of an applied electric ($\mathbf{E}$)-field are explained. Ring-opening reactions as switches are presented and the fatigue of switches is explained in the absence and presence of an applied $\mathbf{E}$-field. The use for the assembly of electronic devices including the scoring of molecular wires using NG-QTAIM is demonstrated. The design of emitters exhibiting thermally-activated delayed fluorescence (TADF) is provided and the unique insights gained by NG-QTAIM of the TADF emitters subject to a static $\mathbf{E}$-field and laser pulse on the energy gap $\Delta E(S_1 - T_1)$ are presented.

There are two appendices:

**Appendix A. Units of Measurement** This appendix consists of Table A1 with units of measurements. Table A2 gives prefixes that are used with these units.

**Appendix B. Mathematical Derivation** Provided for the readers convenience, separately from the main text for easier reading.

**BEACON group members post-graduate thesis**

Www.beaconresearch.org

Beacon group thesis after publication of this book may be found below in English and Chinese (Mandarin): BEACON 研究组成员发表的论文(中英文版本)可于本书出版后在以下网址下载:

https://kns.cnki.net/kns8/DefaultResult/Index?dbcode=CDMD&kw=Samantha%20Jenkins&korder=TU

https://kns.cnki.net/kns8/DefaultResult/Index?dbcode=CMFD&kw=Steven%20Robert%20Kirk&korder=TU

Xu Tianlv: 基于 "分子中的原子"量子理论框架对亚纳米团簇物理化学性质的量子拓扑学分析, 2014.

Julio Roman Maza Villegas: "Chemical and physical insights from the Eigen-properties of QTAIM, the quantum stress tensor and the Ehrenfest Force partitioning", 2015.

Xiao Chenxia: 使用量子拓扑相图对势能面提出的 "分子中的原子"量子理论观点, 2015.

Dong Jiajun: 联苯及其取代物研究中关于 QTAIM 和应力张量理论的观点, 2016.

Xu Yuning: 反应路径研究中的 "分子中的原子"理论以及应力张量理论观点, 2016.

Guo Huan: 基于 "分子中原子"和 "应力张量"理论框架对反应路径的新见解, 2017.

Hu Mingxing: 利用QTAIM以及应力张量理论探究旋转分子马达的光化学和分子的正常模式, 2017.

Yang Ping: 视网膜分子扭转路径以及开环反应研究中的 "分子中原子"和 "应力张量"理论观点, 2018.

Wang Lingling: 利用 "分子中原子"和 "应力张量"理论研究分子内相互作用和金属三明治结构 $[Sb_3Au_3Sb_3]^{3-}$, 2018.

Huang Weijie: 正常模式振动下苯环化学键以及富烯激发态的矢量表示方法, 2019.

Li Jiahui: 基于新型金、银纳米荧光复合探针的生化传感研究, 2019.

Roya Momen: "New Insight into Peptide Folding within Quantum Theory of Atoms in Molecules", 2019.

Bin Xin: 基于分子中的原子量子理论分析锥形交叉点的稳定性及开环反应, 2020.

Tian Tian: 新一代 "分子中原子"量子理论分析键的断裂及分子中同位素的区分, 2020.

Xu Tianlv: 发展下一代电子密度拓扑分析量子理论, 2020.

Alireza Azizi: “Development and Applications of Next Generation Quantum Theory of Atoms in Molecules”, 2020.

Li Shuman: 基于 “分子中原子”量子理论分析分子间弱相互作用与手性分子, 2021.

Wang Liling: 分子内相互作用及其跃迁轨道的量子化研究, 2021.

Nie Xing: 基于 “分子中原子”量子理论分析键的断裂及同位素效应, 2022.

Yang Yong: 基于 “分子中原子”量子理论分析苯和富烯化学键的性质, 2022.

## 1.5 Further Reading

An overview of computational chemistry is recommended [1], along with a text explaining how to use and draw insight from vibrational spectroscopy data using local vibrational mode theory [2]. Additional background materials for Undergraduate students are provided in simplified Chinese (Mandarin) [3].

## References

1. Cramer CJ (2004) Essentials of computational chemistry: theories and models. Wiley
2. Kraka E, Zou W, Tao Y (2020) Decoding chemical information from vibrational spectroscopy data: local vibrational mode theory. WIREs Comput Mol Sci 10:e1480
3. 张志朝主编. 向量. (中国青年出版社, 2001).[高中水平推荐阅读]

# Chapter 2
# Exploring the Topological Origins of QTAIM

**Samantha Jenkins, Steven Robert Kirk, and Dulin Yin**

*ITS THE PHYSICS!!*
*Conversation with Richard F. W. Bader, c. 2001.*

The consideration of chemical bonding is traditionally based on the use of scalar measures and in this chapter we explore, starting from the framework of the quantum theory of atoms in molecules (QTAIM), how far we can usefully proceed with scalar chemical measures. We demonstrate that Euclidian geometry should not be used to quantify the geometry of molecules since they are quantum mechanical objects and doing so reduces the understanding of the molecular dimensionality to comparison with macroscopic objects. For instance, small water clusters $(H_2O)_n$, $n \leq 6$ are known to undergo an energetic preference from planar to cluster-like morphologies for $n = 6$, where considerable debate existing on which of two $(H_2O)_6$ clusters that were candidates for the most energetically stable cluster, each of which appeared by visual inspection to be compact i.e., 3-D. Only one of these clusters was in fact 3-D when considering the quantum geometry formalism we introduced. We introduced a quantum topology phase diagram (QTPD) to better answer the question as to whether the solution sets of the Poincaré-Hopf relation of sets of isomers possessed complete sets that could be displayed in a 'phase-space'. In this way the process of forming a complete phase space would likely undercover missing QTAIM topologies. Various formalisms of the QTPD are introduced with examples. We introduced a measure to replace the use of coordination number with metallic impurity nuclei that we refer to as *NNRCP*: the number of nearest ring critical points (*RCP*s) that also serves as a reactivity measure. We pursue the total local energy density $H(\mathbf{r_b})$ as a measure of the presence of covalent bonding in strengthening weak interactions such as hydrogen-bonding and discuss the limitations of the use within scalar QTAIM. We created a real-space understanding of bond metallicity for use with molecules, clusters and solids that is particularly useful for strained and unusual bonding environments.

Section 2.1 introduces the QTAIM fundamentals. Section 2.2 explains the framework that the rest of this chapter is based on. Section 2.2 presents a non-Euclidian geometry based on QTAIM. Secttion 2.3 presents the QTPDs as the visualizations of the solution sets of the Poincaré-Hopf relation. The *NNRCP* measure is discussed in Sect. 2.3. In Sect. 2.4 the use of the total local energy density $H(\mathbf{r_b})$ as a tool to explain

© The Author(s), under exclusive license to Springer Nature Singapore Pte Ltd. 2023

S. Jenkins and S. R. Kirk, *Next Generation Quantum Theory of Atoms in Molecules*,
Lecture Notes in Chemistry 110, https://doi.org/10.1007/978-981-99-0329-0_2

"sticky" bonding and the consequent effects is demonstrated. The metallicity, bond-polarizability and bond stiffness both with QTAIM and Bader's formulation of the stress tensor $\boldsymbol{\sigma}(\mathbf{r})$ are demonstrated in Sect. 2.5. The chapter concludes in Sect. 2.6 with discussions of the benefits, limitations and suggestions further investigations for the ideas introduced. We do not consider integrated atomic properties; the interested reader is directed towards the Further Reading in Sect. 2.7.

**Scientific goals to be addressed:**

- Construct Non-Euclidian geometry for molecules and clusters to obtain an understanding of molecular geometry (1-D, 2-D, 3-D etc.) that uses QTAIM as opposed to the spatial positioning of atoms and intuition from Euclidian geometry.
- Provide a method to locate missing Poincaré-Hopf topological isomers for molecules/clusters, highly sparse structures e.g., $S_4N_4$, the solid state, hybrid QTAIM and electrostatic potential maps. In addition to providing and missing Poincaré-Hopf topological isomers of potential energy surfaces and for comparing reactions.
- Provide a more precise quantification of the degree of attachment of an impurity metal nuclear critical point (*NCP*) in a metallic host cluster than possible with the use of atomic coordination numbers.
- Determine the degree of covalent character in closed-shell bonds, e.g. hydrogen bonding.
- Provide QTAIM interpreted Hammett parameters.
- Determine metallic bond character and related measures: the metallicity $\xi(\mathbf{r_b})$, the polarizability $\mathsf{P}$ and stiffness $\mathsf{S}$.

## 2.1 The Quantum Theory of Atoms in Molecules (QTAIM): Basics

*In this section we provide the reader background developed by R. F. W. Bader and co-workers in scalar QTAIM, see also the Appendices.*

Atoms in molecules, bonds and localized electron pairs are the most fundamental concepts in chemistry. The quantum theory of atoms in molecules (QTAIM) [1] was founded by R. F. W. Bader and co-workers based on the recognition that the total electronic charge density distribution $\rho(\mathbf{r})$ plays a critical role in explaining and understanding the experimental observations of chemistry. QTAIM is uniquely and rigorously defined by the $\rho(\mathbf{r})$ distribution. QTAIM allowed us to develop a new non-Euclidean formulation of the geometry of molecules [2]. QTAIM has had many successes in prediction and correlation with experimental data [1] and in recognition of its precise basis set in quantum mechanics [1–5]. QTAIM relates various concepts of chemistry, for example chemical structure, chemical bonding and chemical reactivity, to the topology of the underlying electron-density distributions. QTAIM provides a unifying thread of physical insight in chemistry and

moved theoretical chemistry into real three dimensional space [6]. QTAIM only requires $\rho(\boldsymbol{r})$, obtained from either theory, e.g., density functional theory (DFT, time dependent (TD-DFT)), configuration interaction (HF/CIS, CASSCF and MRCI), or experiment, e.g., X-ray diffraction (XRD) [7] and 1H NMR spectroscopy data [8]. Gridded densities can now be analyzed for molecules, surfaces or solids with CRITIC2 [9–11].

We use the Quantum Theory of Atoms in Molecules (QTAIM) [12] and the stress tensor $\boldsymbol{\sigma}(\mathbf{r})$ analysis that utilizes higher derivatives of $\rho(\mathbf{r})$, in effect acting as a 'magnifying lens' on the total electronic charge density distribution $\rho(\mathbf{r})$ derived properties of the wave-function. QTAIM allows us to identify critical points in the scalar field $\rho(\mathbf{r})$ by analyzing the gradient vector field $\nabla\rho(\mathbf{r})$. The critical points can be divided into four types of topologically stable critical points according to the set of ordered eigenvalues $\lambda_1 < \lambda_2 < \lambda_3$, with corresponding eigenvectors $\underline{\mathbf{e}}_1, \underline{\mathbf{e}}_2, \underline{\mathbf{e}}_3$ of the Hessian matrix that is defined as the matrix of partial second derivatives with respect to the spatial coordinates can be diagonalized, see Appendix B. This is an eigenvalue problem whose solution corresponds to finding a rotation of the coordinate axes to a new set such that all the off-diagonal elements vanish. The trace of the Hessian matrix that corresponds to the sum of its diagonal elements, is invariant to a rotation of the coordinate system i.e., to the choice of coordinate axes. The diagonalization of the Hessian matrix of $\rho(\mathbf{r_c})$ yields principle axes and curvatures at a critical point $\mathbf{r_c}$ that correspond to the eigenvectors $(\underline{\mathbf{e}}_1, \underline{\mathbf{e}}_2, \underline{\mathbf{e}}_3)$ and eigenvalues $|\lambda_1| < |\lambda_2| < |\lambda_3|$ respectively. The signature, denoted by $\sigma$, is the algebraic sum of the signs of the eigenvalues at the critical point, i.e., the signs of the curvatures $\omega$ at the critical point. A critical point is fully characterized by the quantities $(\omega, \sigma)$. A critical point with $\omega < 3$, so that it has at least one zero curvature, is said to be degenerate and is associated with the onset of structural change. This type of critical point is unstable with respect to small changes in the charge density, such changes lead to the critical point vanishing or bifurcating into a number of non-degenerate or stable ($\omega = 3$) critical points.

The four possible signature values for critical points of rank three:

$(3, -3)$ A local maximum corresponding to a nuclear location or a non-nuclear attractor (*NNA*). All curvatures are negative and $\rho(\mathbf{r})$ is a local maximum at the bond critical point (*BCP*) or $\mathbf{r_c}$. At the site of a nucleus this is not a true critical point since the first derivative is discontinuous at the position of the nucleus as the state function must exhibit a cusp at the nuclear position: a nuclear critical point (*NCP*).

$(3, -1)$ A saddle point. Two curvatures are negative and $\rho(\mathbf{r})$ is a maximum at the *BCP* in the plane defined by their corresponding axes. The value of $\rho(\mathbf{r})$ is a minimum at the *BCP* along the third axis which is vertical to this plane. It is a necessary condition for the formation of a bound state, this type of critical point implies the existence of an atomic interaction line which means a line linking the nuclei along which the $\rho(\mathbf{r})$ is a maximum with respect to any neighbored line. In the limit that the forces on the nuclei become vanishingly small, an atomic interaction line (AIL) [13] becomes a *bond-path*, although not necessarily a chemical bond [14]. A bond within QTAIM is

referred to as a bond-path (***r***) and is defined as the extent of the path traced out by the $\underline{\mathbf{e}}_3$ eigenvector of the Hessian of the total charge density $\rho(\mathbf{r})$, passing through the *BCP*, along which $\rho(\mathbf{r})$ is locally maximal with respect to neighboring paths. Therefore, the bond-path (***r***) may possess a non-zero degree of curvature [15] and is a dimensionless ratio of the bond-path length (BPL) and geometric bond length (GBL) separating two bonded nuclei and is defined as:

$$(\mathrm{BPL} - \mathrm{GBL}) \big/ \mathrm{GBL} \tag{2.1}$$

where GBL refers to the inter-nuclear separation with the minor and major radii of bonding curvature specified by the directions of $\underline{\mathbf{e}}_2$ and $\underline{\mathbf{e}}_1$ respectively [16]. The complete set of critical points together with the network bond-paths of a molecule or cluster is referred to as the molecular graph, with the constituent atoms being referred to as nuclear critical points (*NCP*s).

(3, +1) A saddle point. Two curvatures are positive and $\rho(\mathbf{r})$ is a minimum at the *BCP* in the plane defined by their corresponding axes and is called a ring critical point (*RCP*), $\rho(\mathbf{r})$ is a maximum at the *RCP* along the third axis which is vertical to this plane. Usually, there is an *RCP* inside of a ring of chemically bonded atoms.

(3, +3) All curvatures are positive and $\rho(\mathbf{r})$ is a local minimum at the *BCP*. When numbers of rings are connected in a manner and enclose an interstitial space, a cage critical point (*CCP*) appears in the enclosed space.

The molecular graph provides an unambiguous definition of the molecular structure and can be used to locate variations in structure along a reaction path. For instance, the 2-D structural formulae, ball-and-stick rendering graph and molecular graph of the phenanthrene molecule respectively in addition to the molecular graph of tetrahedran are provided in Fig. 2.1. This polycyclic aromatic hydrocarbon molecule has a highly curved H---H *BCP* bond-path in the bay region, in contrast to dihydrogen bonding. Notice the use of the three "--- " to denote a very weak purely electrostatic *BCP*, see Eq. (2.1).

The ellipticity ε provides the relative accumulation of $\rho(\mathbf{r_b})$ in the two directions perpendicular to the bond-path at a *BCP*, defined as $\varepsilon = |\lambda_1|/|\lambda_2| - 1$ where $\lambda_1$ and $\lambda_2$ are negative eigenvalues of the corresponding $\underline{\mathbf{e}}_1$ and $\underline{\mathbf{e}}_2$ respectively. It has been deomonstrated [17, 18] that the degree of covalent character can be determined from the total local energy density $H(\mathbf{r}_\mathrm{b})$, defined as:

$$H(\mathbf{r}_\mathrm{b}) = G(\mathbf{r}_\mathrm{b}) + V(\mathbf{r}_\mathrm{b}) \tag{2.2}$$

In Eq. (2.2), where $G(\mathbf{r}_\mathrm{b})$ and $V(\mathbf{r}_\mathrm{b})$ are the local kinetic and potential energy densities at a *BCP*, respectively. A value of $H(\mathbf{r}_\mathrm{b}) < 0$ for the closed-shell interaction, $\nabla^2\rho(\mathbf{r}_\mathrm{b}) > 0$, indicates a *BCP* with a degree of covalent character and conversely $H(\mathbf{r}_\mathrm{b}) > 0$ reveals a lack of covalent character for the closed-shell *BCP*. Throughout this chapter, we use the terminology '--' and '---' to refer to closed-shell *BCP*s which by

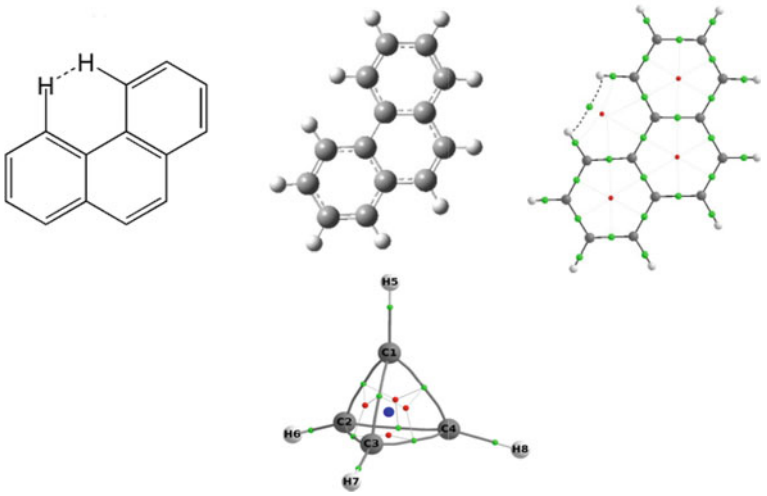


**Fig. 2.1** The 2-D structural formulae (upper-left-panel), ball-and-stick rendering (upper-middle-panel) and molecular graph (upper-right-panel) of phenanthrene, the molecular graph of tetrahedran (lower-panel), the green, red and blue spheres denoting the *BCP*s, *RCP*s and *CCP*s respectively

definition always possess values of the Laplacian $\nabla^2\rho(\mathbf{r}_b) > 0$ but possess $H(\mathbf{r}_b) < 0$ or $H(\mathbf{r}_b) > 0$ respectively.

**Activity 2.1: QTAIM basics**

- Which theory does the acronym QTAIM refer to?
- What is a critical point within QTAIM? Include the rank (ω) and signature (σ) and the four types of critical points.
- What is the name given to a bond within QTAIM?
- Within QTAIM what is a molecular graph?
- What is the meaning of the acronyms BPL and GBL?
- (More advanced) Explain why a BPL may be shorter than a GBL for molecules containing hydrogen atoms.

## 2.2 Non-euclidian Geometry for Molecules and Quantum Topology Phase Diagrams (QTPDs)

*In this section we provide the reader with the background to the (QTPDs) we developed.*

A fundamental theorem of topology is the Poincaré-Hopf relation [3] that is used universally for clusters and molecules within QTAIM to account for all the four types

of rank $\omega = 3$ critical points. The Poincaré-Hopf relation, for molecules and clusters, is expressed as:

$$n - b + r - c = 1 \tag{2.3}$$

where $n$, $b$, $r$ and $c$ are the numbers of *NCP*s, *BCP*s, *RCP*s and *CCP*s, respectively, see Eq. (2.3). A similar relation exists for the determination of the correct numbers of critical points in infinite solids modeled with periodic boundary conditions. This is sometimes referred to as the Morse relation, although the term Euler–Poincaré relation [19] is also used:

$$n - b + r - c = 0 \tag{2.4}$$

We created a non-Euclidean geometry to summarize the topology of a molecular graph created by the critical points of $\nabla\rho(\mathbf{r})$ that includes the concepts of geometry and dimensionality. This can be useful to compare the topologies of sets of isomers or reaction-pathways where the topological complexity $\sum_{brc}$ can be defined as the sum of the numbers of *BCP*s, *RCP*s and *CCP*s is also useful. This is to avoid using vague intuition from experience with Euclidean geometry and to instead quantify the topology using a quantum mechanically consistent description based on the critical points of $\nabla\rho(\mathbf{r})$. As a consequence we introduced the notation: 3-$D_{QT}$, 2-$D_{QT}$, or 1-$D_{QT}$ to refer to all possible molecular geometries within the QTAIM framework [6, 20]. The Euclidean descriptors 3-D, 2-D and 1-D and 0-D are replaced by 3-$D_{QT}$, 2-$D_{QT}$, 1-$D_{QT}$ and 0-$D_{QT}$ respectively where the subscript "QT" refers to the quantum topology origins. The presence of a *CCP* is a necessary condition for a molecular graph to be considered to be quantum topologically 3-$D_{QT}$, which implies the presence of *RCP*s, *BCP*s and *NCP*s. A molecular graph containing a *CCP* possesses a region that is completely bounded by bond-paths with an *RCP* in the plane of each enclosing face. Molecular graphs possessing 3-D Euclidean geometries can be either 2-$D_{QT}$ or 1-$D_{QT}$, but without a *CCP* they do not contain an enclosed region in the topology of the gradient of the charge density $\rho(\mathbf{r})$. Correspondingly the presence of an *RCP* is needed for a molecular graph being describable as 2-$D_{QT}$ and a *BCP* is required for a 1-$D_{QT}$ molecular graph.

**Activity 2.2: Sum rules for molecules and clusters**

- Define the Poincaré-Hopf relation for molecules and clusters.
- Define the Poincare-Hopf relation for solids.
- Define topological complexity with QTAIM, suggest an area of application.
- Write out and explain all of terms Poincaré-Hopf relation for the stable water dimer $(H_2O)_2$.
- (More advanced) Explain why satisfaction of the Poincaré-Hopf relation is a necessary but not sufficient condition to ensure all critical points in a molecule have been discovered.

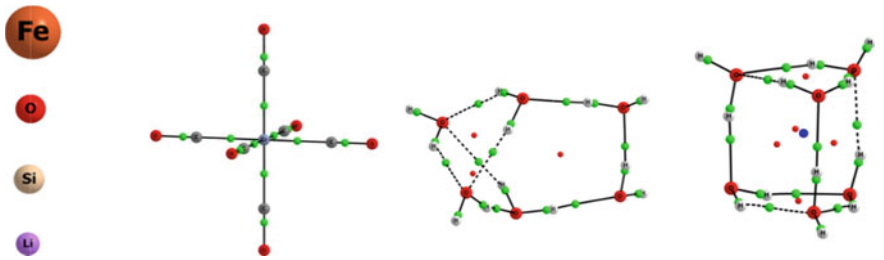


**Fig. 2.2** A selection of isolated atoms and molecular graphs, the undecorated green, red and blue spheres represent ring critical points (*RCP*s), bond critical points (*BCP*s) and cage critical points (*CCP*s) respectively

**Activity 2.3: Quantum topology**

- Quantum topology is based only on Euclidean geometry. TRUE or FALSE?
- How many quantum topological dimensions can we define? List all of them with the correct notation.
- What are the quantum topological dimensions of the molecular graphs in Fig. 2.2?
- Obtain the molecular graphs of each of the structures in Fig. 2.3 using the demo version of AIMStudio that may consider up to 12 atoms and 40 primitives, refer to Chap. 1.
- Determine the quantum topology classification as 3-$D_{QT}$, 2-$D_{QT}$, or 1-$D_{QT}$ of each of the structures in Fig. 2.3.

### *2.2.1 The Structure of Quantum Topology Phase Diagrams (QTPDs)*

For a set of isomeric molecular graphs, the number of *BCP*s and *RCP*s given by *b* and *r* respectively, contained in each molecular graph are plotted along the *x*-axis and *y*-axis, see Fig. 2.4. There is a restriction on the range in the QTPD for the topologies of isomers of a given chemical system due to the integer nature of the solution set of the Poincaré–Hopf relation. Topologically stable as well as 'missing' topologies that fall in hypothesized stable zone of QTPD may have one or more local energy minima associated with them, these missing topologies may correspond to various types of stationary points in the PES: stable minima, transition states etc. Topologically unstable solutions are increasingly unlikely to be found as molecular graphs as they contain increasing number of *CCP*s. The attempt to construct a *complete* QTPD in terms without missing topologies is referred to as a *spanning* QTPD. This is undertaken by first calculating the upper and lower boundaries of the QTPD for values of *b*, the lower boundary defined by where the number of *BCP*s and *NCP*s are equal. The upper boundary of the spanning QTPD is defined by the constructed

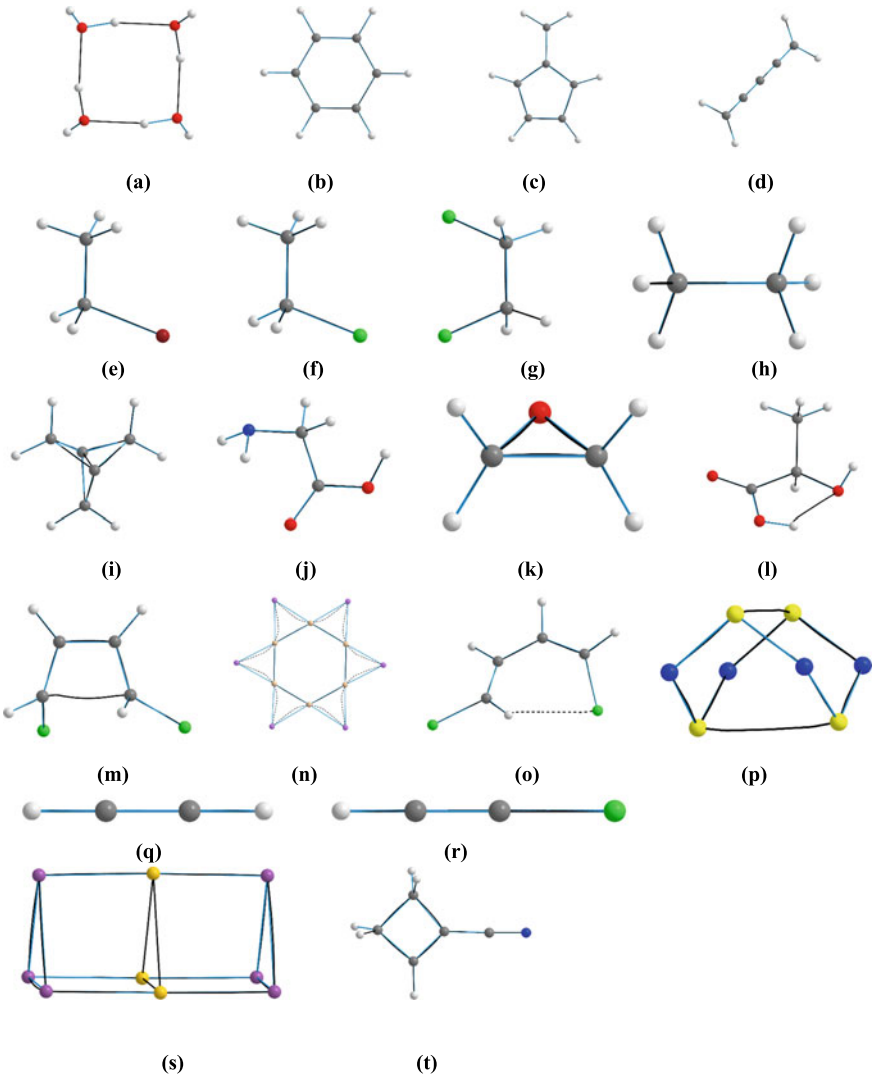


**Fig. 2.3** The $(H_2O)_4$, benzene, fulvene, [4]cumulene, monobromoethane, monochloroethene, 1,2-dichloroethane, ethane, [1,1,1] propellene, glycine, ethylene oxide, lactic acid, 1,2-dichlorocyclobutane, $Li_6Si_6$, 1,4-dichlorobutane, tetrasulfur tetranitride, ethyne, monochloroethyne, the sandwich complex $[Sb_3Au_3Sb_3]^{3-}$ and pyridine structures are presented in sub-figures **(a–t)** respectively

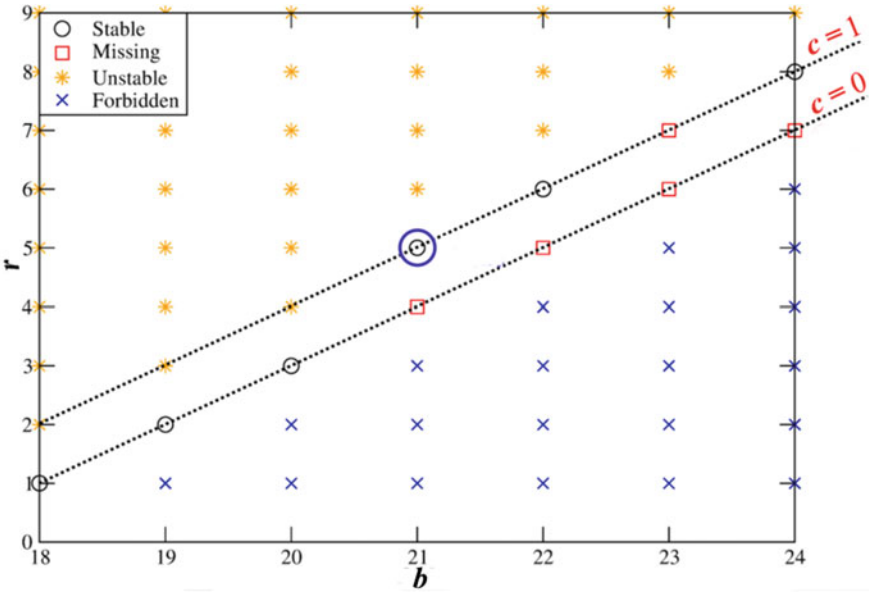


**Fig. 2.4** The spanning QTPD for the isomers of $(H_2O)_6$ molecular graphs, where $b$ and $r$ indicate the numbers of bond critical points (*BCP*s) and ring critical points (*RCP*s) respectively. The energy minimum structure corresponds to the topology ($b = 21$, $r = 5$) and is highlighted by the blue circle. The upper and lower dotted lines corresponds to topologies where the numbers of cage critical points (*CCP*s), $c = 1$ and $c = 0$ respectively. The upper boundary ($b = 24$, $r = 8$) and lower boundary ($b = 18$, $r = 1$) corresponds to a regular polyhedron and a ring structure respectively. The legend indicates the types of topologies as stable, missing, unstable or forbidden based on the known solution sets of the Poincaré-Hopf relation, see Eq. 2.1

using the topology of the simplest regular polyhedron. We do not consider QTPDs comprising string-like solutions of the Poincaré-Hopf relationship where $r = 0$.

Twenty-five conformers of $(SiO_2)_6$ were considered ten of which were new, this was undertaken by extending the $(SiO_2)_6$ QTPD by using the Poincaré-Hopf sum rules to identify the spanning set of topologies [20]. An attempt at forming a complete QTPD was aided by the introduction of a classification scheme to determine the boundary between topological stability and instability and an upper bound to the QTPD was postulated to be a regular polyhedra. We demonstrated that the four most energetically stable $(SiO_2)_6$ conformers were quantified as 2-$D_{QT}$.

We investigated the QTPDs of the *cis*- and *trans*-isomers of the cyclic contryphan-Sm peptide [7]. The regions for the cis- and trans-isomers in the QTPD only overlapped for topologies associated with the lowest energy minima of the cis- and trans-isomers. We determined the QTAIM topologies of twenty-nine 'missing' isomers and introduced a more compact form of QTPD for use with larger molecules. This simplifies the solution of the Poincaré-Hopf relation of the molecular graph of the peptide by considering each amino acid as an indivisible unit.

We created QTPDs for $(H_2O)_4$, $(H_2O)_5$ and $(H_2O)_6$ and used the QTPD to fill in missing topologies and extend the QTPD of the $(H_2O)_4$, $(H_2O)_5$ and $(H_2O)_6$ clusters and a spanning set of conformer topologies was created [6]. The spanning set of topologies comprising the QTPDs consisted of lower and upper bounds. We introduced a QTAIM topology space to replace the inconsistent use of Euclidean geometry to determine whether a cluster is 1-$D_{QT}$, 2-$D_{QT}$ or 3-$D_{QT}$.

### 2.2.2 QTPDs and Non-nuclear Attractors (NNAs)

The quantum topology phase diagrams (QTPDs) have been utilized to better understand the complexity of the topology of the $Si_6Li_6$ potential energy surface due to the presence of *NNA*s [21].

Very large amplitude vibrations of all eighteen normal modes of vibration of tetrasulfur tetranitride $S_4N_4$ were performed [22], where 11 unique topologies existing on 3-D QTPDs are found due to the presence of non-nuclear attractors (*NNA*s), see Fig. 2.5.

### 2.2.3 QTPDs and the Solid State

Earlier we suggested non-molecular/cluster applications of QTPDs could include phase transitions in solids [23] or as a tool for the discovery of new allotropes [24–26]. A variety of phases of water ice [27–29] subjected to varying pressure provides a simple demonstration of this hypothesis, see, Eq. (2.4) and Fig. 2.6 and the accompanying figure caption.

The quantum topology phase diagram is constructed by using Eq. (2.4) as a necessary but not sufficient condition on the numbers and types of critical points. Then the ratio $RCP/BCP = 1$, e.g., for ice Ic this slope is drawn and the specific data ($BCP = 16$, $RCP = 16$) point added and other points on this slope correspond to integer multiples (periodic repetitions) of the primitive unit cell. For example: for ice XI (water ice), there is a known phase transition in the applied pressure 80–85 kbar range [28] where the slope $RCP/BCP = 1$ for 80 kbar and $RCP/BCP > 1$ at a pressure of 85 kbar, see Fig. 2.6. Any solid will have differently sized primitive unit cells, therefore we only consider the *RCP*/*BCP* slope as possessing significance. The phase boundaries are delineated by solid and dotted lines and the dashed lines delineate pressure boundaries. The use of larger super-cells will enable the details of phase transitions to be followed in more detail as can be seen from the increasing separation between adjacent phase and pressure boundaries.

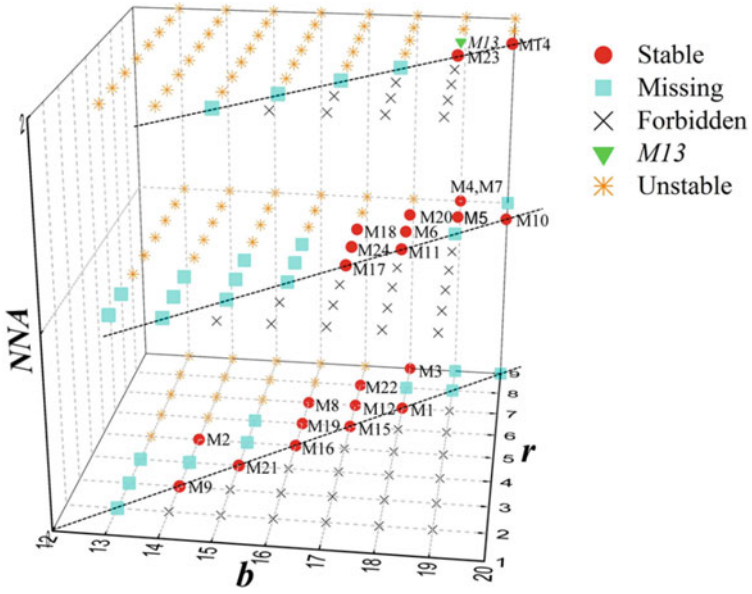


**Fig. 2.5** The 3-D QTPD with the number of *BCP*s *RCP*s and *NNA*s plotted on the X-, Y- and Z-axes respectively, the upper left regions marked with orange asterisks denotes the region of topological instability based on there being increasing more *CCP*s. The topologically stable isomers are represented as either red circles or blue squares. The topologically unstable isomer, M13 is represented by an inverted green triangle. The upper left region marked as 'Forbidden' is excluded as no valid solutions for the Poincaré-Hopf relation for $Si_6Li_6$ in that region. The three dashed lines correspond to $CCP = 0$. The X-, Y- axes correspond to the numbers of *BCP*s and *RCP*s respectively but the Z-axis represents the numbers of *NNA*s. The three dashed lines correspond to $CCP = 0$. All of the isomers correspond to stable energy minima without any imaginary frequencies

### 2.2.4 Hybrid QTAIM and Electrostatic Potential QTPDs

Hybrid QTAIM and electrostatic potential-based QTPDs were constructed for water clusters [30] using the following hybrid version of the Poincaré–Hopf relation:

$$c - r + b - n_{cp} = \chi \tag{2.5}$$

where the $\chi$ denotes the Euler characteristic, the total charge density $\rho(\mathbf{r})$ is a positive semi-definite scalar field, for which the Euler Characteristic $\chi = -1$, for any molecule or cluster and correspondingly $\chi = 0$ for a solid, see Eq. (2.5). The variables $c$, $r$, $b$ and $n_{cp}$ correspond to the number of *CCP*s, *RCP*s, *BCP*s and *NCP*s respectively.

The asymptotic topological behavior of any function is provided by the Euler characteristic. The solution space of a QTPD, unlike the terrain of potential energy surface, is more confined and has the possibility for predicting new topologies of the QTAIM, Ehrenfest or MESP fields. A pure MESP QTPD is not practical because of divergent

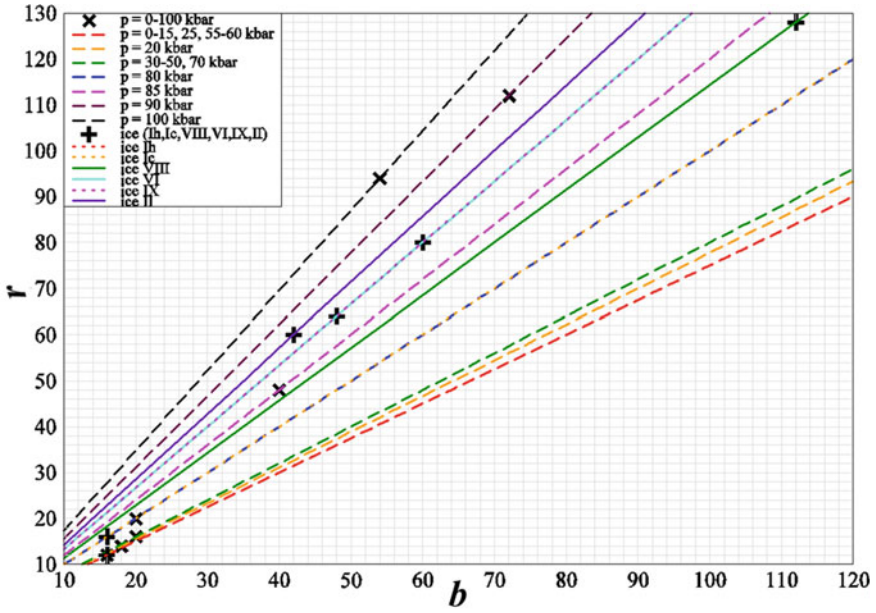


**Fig. 2.6** The solid state quantum topology phase diagram for crystalline ice phases, ice Ih, ice Ic, ice IX, ice VI, ice XI and ice VIII shown by dotted and solid lines, see the caption of Fig. 2.2 for further details. Additionally, pressure-induced phase transitions are indicated by the dashed lines for the evolution of ice XIh at 0 kbar to an ice VIII-like phase at 100kbar. The fine grid is added as a guide to the eye

chemical significance of any particular type of non-degenerate critical point as well as varying Euler characteristic values; 0, ± 1, ± 2 etc., would necessitate an additional axis to be added to a QTPD to represent each additional Euler characteristic value, see Fig. 2.7. It is practical however, to create a 'hybrid' QTAIM-MESP QTPD that can include the oxygen lone pair topologies.

The hybrid QTAIM-MESP QTPD was created from a new chemical relation $b_{\mathrm{HB}} + l \geq 2n$ for $\mathrm{W}_n$ that relates the number of hydrogen-bond bond critical points ($b_{\mathrm{HB}}$) with the number of oxygen lone pairs exclusively specified by the negative valued MESP (3, +3) critical points ($l$). The topologies of the subset $b_{\mathrm{HB}} + l = 2n$ for $\mathrm{W}_n = (\mathrm{H_2O})_n$, pointed the way to the discovery of unknown 'missing' lower energy isomers. Characterization of the structure of the QTPDs, possible with new tools, demonstrated the migration of the position of the global minimum on the spanning QTPD from the lower bound to upper bound as the $\mathrm{W}_n$, $4 \leq n \leq 10$, cluster grows in size.

*Directed* QTPDs, with respect to increase in the amplitude of each mode of vibration, were used to better understand the large-amplitude motions of the tetrasulfur tetranitride $\mathrm{S_4N_4}$ molecular graph [22], see also Sect. 2.2.5 on directed QTPDs. For directed QTPDs the order of connectivity of nodes, where the nodes are the Poincaré–Hopf

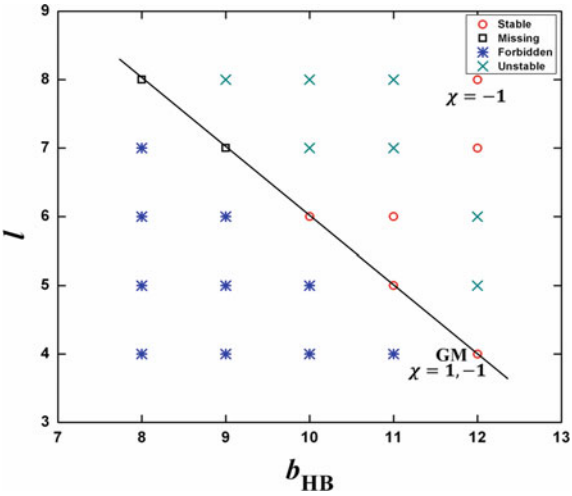


**Fig. 2.7** Hybrid-QTPDs the $(H_2O)_8$, the Euler characteristic $\chi = 0$ except where specified. The black line at the boundary of the 'forbidden' and 'stable' regions represents the solutions of the relation, $b_{HB} + l = 2n$

solutions of the molecular graphs, is important, the arrows (edges) determine the relationship between the nodes that are connected.

### *2.2.5 Directed QTPDs*

The creation of a *directed* near complete QTPDs of the $(H_2O)_5$ potential energy surface was undertaken [31]. The term 'directed' originates from the use of arrows to connect the QTPD topologies, see Fig. 2.8. The complexity of the QTPD explained the stabilizing role of the O---O *BCP*s in facilitating the $(H_2O)_5$ reaction-pathways. We explained the presence of O---O *BCP*s at all points on the $(H_2O)_5$ QTPD [32].

Reaction pathways generally comprise non-isomeric species, consequently the QTPD approach that uses sets of isomers, appears to be inaccessible. Directed QTPDs however, were used for the quantum topological resolution of catalyst proficiency where missing QTPD topologies were discovered for the inefficient Pd($\pi$-allyl)$_2$ catalyst contrasting with the efficient Ni($\pi$-allyl)$_2$ catalyst where there were no missing QTPD topologies [33], see Fig. 2.9. A typical reaction however, can be considered by associating several of the reaction species together, that we refer to as 'aggregate-isomers' to distinguish them from the individual reaction species. Any of the reaction species can be chosen as a reference-isomer and the number $n$ of *NCP*s it comprises is noted. For the remaining reaction species aggregate-isomers are created to have the same number $n$ of the *NCP*s as the reference-isomer. Following the reaction-pathway in the natural clockwise direction the components $(n, b)$ of the aggregate-isomer are added for reactants and subtracted for by-products, see Fig. 2.9. If travelling counter-clockwise around the reaction cycle the aggregate isomers are created by subtracting

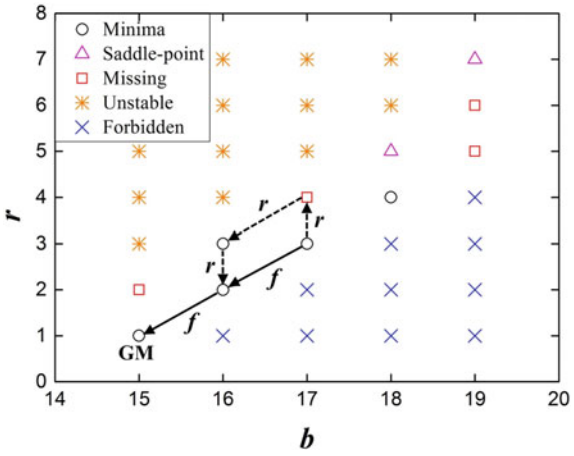


**Fig. 2.8** The 2-D 'directed' QTPD for the MP2 potential energy surface (PES) of $(H_2O)_5$ clusters with the number of *BCP*s (*b*) and *RCP*s (*r*) plotted on the x- and y- axes, respectively. The directed pathways of the nine reaction-pathways are shown for the molecular graphs, indicated by the dashed (reverse pathway) and solid black (forward pathway) arrows respectively. The topology of the global minimum is indicated by "GM"

the value *n* of the reactants whilst the value of *n* of the by-products is added. The process involves adding the number of *NCP*s (*n*) of the reactants and subtracting the number of *NCP*s (*n*) of the by-products to form the aggregate-isomer terminates on the reference-isomer. After the reference-isomer and aggregate-isomers have been constructed, the number of *BCP*s (*b*), of the aggregate-isomers must be adjusted so that the Poincaré-Hopf relation is maintained. This is attained by adding (+1) for each of the reactants and (−1) to the *BCP* total *b* for the aggregate-isomer for each of by-products added or subtracted during the reaction-cycle. For example, for a reaction cycle relative to CAT1 with $n = 17$ we have CPX + RCT2 − BP1 − BP2 and we have $1 + (-1) + (-1) = -1$, therefore, the corrected numbers of *BCP*s ($b_{raw}$) for Ni in this case is $(20) - 1 = 19$, see Fig. 2.9. Note since only difference is the presence of the Pd or Ni nucleus (*NCP*) we only present the molecular graphs for the Pd(π-allyl)$_2$ catalyst reaction cycle in Fig. 2.9.

We therefore demonstrated that the catalyzed reaction cycles can be represented as a directed QTPD where each species of the main reaction cycle forms a closed loop.

In the study of the Pd(π-allyl)$_2$ and Ni(π-allyl)$_2$ catalysts we only have 1-$D_{QT}$ reactants and by-products and so the total number of *RCP* (*r*) for the aggregate-isomer does not need to be adjusted as the 1-$D_{QT}$ reactants and by-products do not add or remove any *RCP*s. The unwanted side products for each catalyst were also considered. The QTPD corresponding to the more efficient Ni(π-allyl)$_2$ catalyst produces a reaction cycle without "missing" topologies, preferentially proceeding to desired product at 94% yield and avoiding unwanted side-product pathways. The unwanted side-products were disconnected from the major pathway by "missing" topologies

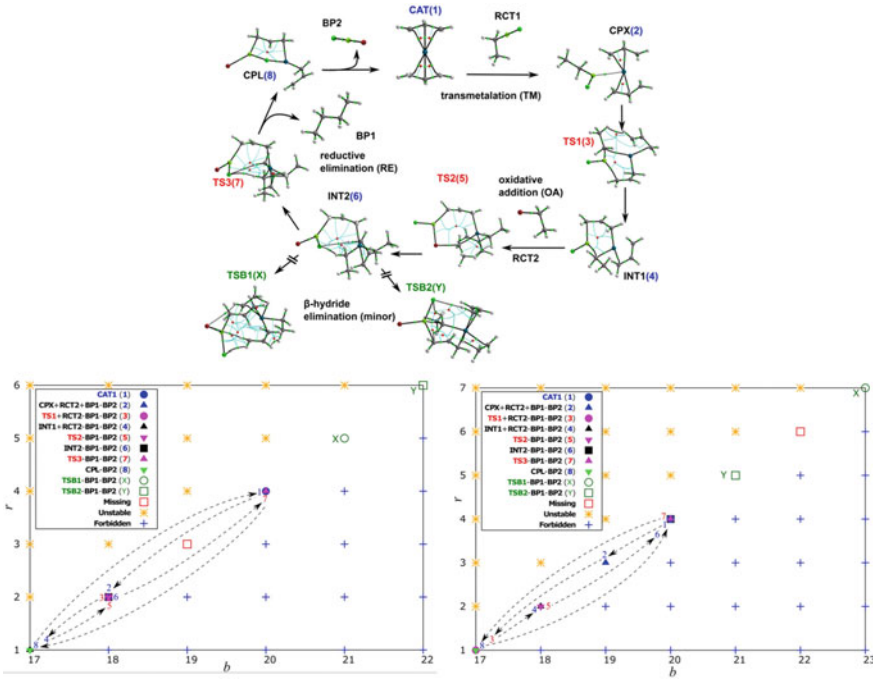


**Fig. 2.9** **Top**: The complete reaction cycle presented for the Pd(π-allyl)$_2$ catalyst reaction cycle. **Bottom**: The QTPDs for the complete reaction cycle of the Pd(π-allyl)$_2$ (left-panel) and Ni(π-allyl)$_2$ (right-panel) catalysts including the side products

on the QTPD. The converse was found for the less efficient Pd(π-allyl)$_2$ catalyst, where the main reaction pathway strongly bifurcates to final yields of 56% and 44% for product and side-product, respectively.

Very large amplitude vibrations of all of the eighteen normal modes of vibration of tetrasulfur tetranitride $S_4N_4$ were performed [22]. We found seventeen new unique QTPD topologies for the molecular graphs corresponding to the eighteen modes of vibration along with seven 'missing' topologies that are mapped onto a spanning 2-D QTPD, see Fig. 2.10. In addition, eleven unique topologies existing on 3-D QTPDs are found due to the presence of non-nuclear attractors (*NNA*s).

### Activity 2.4 Quantum topology phase diagrams

- If a molecular contains non-nuclear maximum (*NNA*) which term ($n$, $b$, $r$ or $c$) in the Poincaré-Hopf relation is that included in?
- How do we construct a QTPD when one or more *NNA*s are present.
- How do we define the lower limit of the QTPD in the absence of *NNA*s?
- How do we define the upper limit of the QTPD in the absence of *NNA*s?

Below are the QTAIM topologies for the $(H_2O)_4$ spanning QTPD:

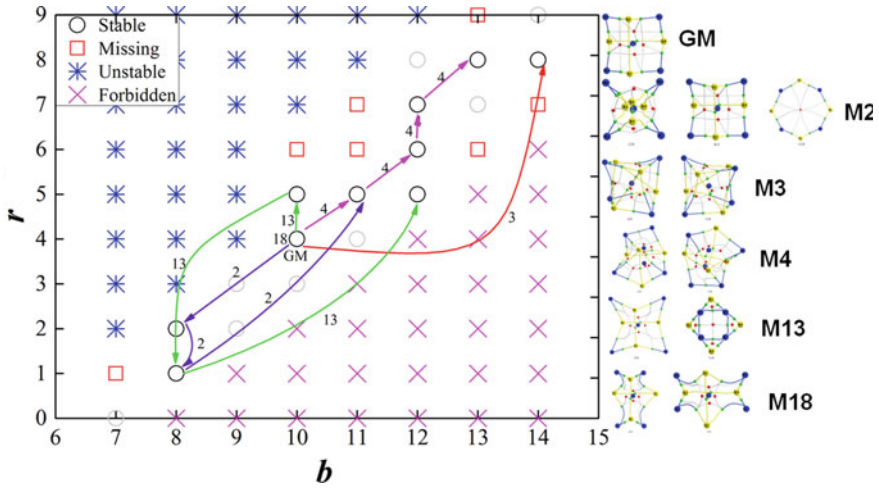


**Fig. 2.10** The 2-D QTPD of the topologically stable isomers found from the 18 normal modes of $S_4N_4$ are represented as either grey or black circles. The position of the topology of the global minimum is denoted by 'GM'. The violet, red, magenta and green arrows represent the change in topology with increasing of vibration of the modes 2–4 and mode 13, respectively, only the negative branch of the normal vibration mode 2 is relevant for the 2-D QTPD. The molecular graphs corresponds to those existing at the maximum negative and positive amplitudes shown in the left and right panels respectively

| Molecular graph | b | r | c |
|---|---|---|---|
| I | 12 | 1 | 0 |
| II | 12 | 1 | 0 |
| III | 12 | 1 | 0 |
| V | 12 | 1 | 0 |
| VI | 12 | 1 | 0 |
| VII | 12 | 1 | 0 |
| VIII | 12 | 1 | 0 |
| IV | 13 | 2 | 0 |
| A | 12 | 2 | 1 |
| B | 13 | 3 | 1 |
| C | 14 | 3 | 0 |
| IX | 14 | 4 | 1 |

- Draw this QTPD and label the axes.
- Indicate the stable and missing topologies.
- Indicate the unstable region of the QTPD.
- Indicate the forbidden region of the QTPD.
- Indicate the lower and upper bounds of the QTPD.

## 2.3 The Number of Nearest *RCP*s (*NNRCP*s) for an Impurity *NCP* in a Metal Host Cluster

*A QTAIM topology measure to replace the use of coordination number in certain circumstances.*

A quantity that can be usefully related to the QTPDs is the number of nearest *RCP*s (*NNRCP*s) for an impurity *NCP* (the nucleus) in a host cluster, previously investigated as a Pt impurity in a host cluster of $Au_6$ [34]. We calculated a basin-path set, defined as a representative set of trajectories of the charge density gradient $\nabla\rho(\mathbf{r})$ originating from the attractor (nucleus) associated with the nucleus that delimiting the atomic basin for that nucleus (*NCP*) For every *NCP* of a molecular graph. The boundaries between basin-path sets are referred to as interatomic surface paths (IAS), where a *BCP* is located along the bond-path between bonded nuclei that share a common IAS. The association with the QTPDs is made by understanding that the variations in the chemical environment of impurity Pt nucleus for a series isomers to form a QTPD. For each dopant + host $Au_6Pt$ isomer the IAS paths of the Pt nucleus may be divergent, parallel, convergent and/or enclosed depending on the how peripheral the position of the Pt nucleus is. Usually there will be *RCP*s and *BCP*s positioned alternately along the boundary of the 'impurity' atomic basin. The number of nearest neighbor ring critical points (*NNRCP)*, determined by summing the *RCP*s that lie on the bounded region of the union of inter-atomic surfaces of the impurity nucleus, $S_I(\omega)$, for *RCP*s:

$$NNRCP = \sum_{\boldsymbol{r}\in S_I(\omega)} \delta(\boldsymbol{r}), \delta(\boldsymbol{r}) = \begin{cases} 1, \nabla\rho(\boldsymbol{r}) = 0(RCP) \\ 0, elsewhere \end{cases} \tag{2.6}$$

The *NNRCP* provides the degree of association of an impurity nuclei to a host molecule, larger values indicate a higher degree of attachment and values of *NNRCP* = 0 have been found for the impurity Pt in the $Au_6$ host cluster, see Eq. (2.6).

*NNRCP*s were also used to demonstrate that the species of the main reaction cycle of the efficient Ni(π-allyl)$_2$ catalyst facilitated the desired chemical transformation whilst more effectively preventing the formation of unwanted side product as compared to the inefficient Pd(π-allyl)$_2$ catalyst [33].

The QTAIM and stress tensor $\boldsymbol{\sigma}(\mathbf{r})$ point properties are then investigated and found to be highly dependent on the mode of vibration in an investigation into the normal modes of vibration of tetrasulfur tetranitride $S_4N_4$. A considerable degree of metallicity $\xi(\mathbf{r}_b)$ is found for the S--S and S-N bonding interactions. A unique bonding feature is found for a small amplitude vibration of the most anharmonic mode (mode

2), where the S--S bond critical point (*BCP*) transforms from a closed-shell S--S *BCP* to a shared-shell S-S *BCP*.

**Activity 2.5: The Degree of attachment of an impurity nucleus in a host cluster (NNRCPs)**

Below is a table for $Au_6Pt$ of QTAIM topologies, *b*, *r* and *c*, *NNRCP* and the Pt Coordination number:

| Cluster | b | r | c | NNRCP | Pt coordination number |
|---|---|---|---|---|---|
| M6 | 16 | 13 | 3 | 5 | 4 |
| M13 | 10 | 4 | 0 | 0 | 2 |
| M14 | 14 | 10 | 2 | 3 | 3 |
| M7 | 12 | 6 | 0 | 3 | 3 |
| M2 | 16 | 10 | 0 | 10 | 6 |
| M8 | 11 | 5 | 0 | 3 | 4 |
| M9 | 15 | 12 | 3 | 3 | 3 |
| M10 | 12 | 6 | 0 | 2 | 3 |
| M11 | 14 | 11 | 3 | 1 | 2 |
| M12 | 12 | 7 | 1 | 1 | 2 |
| M1 | 12 | 6 | 0 | 6 | 6 |
| M3 | 13 | 7 | 0 | 7 | 6 |
| M4 | 14 | 9 | 1 | 6 | 5 |
| M5 | 12 | 6 | 0 | 5 | 5 |

- List the cluster names of the three most reactive clusters on the basis of the Pt Coordination number.
- List the cluster names of the single most reactive cluster on the basis of the *NNRCP*.

## 2.4 Determining the Presence of Covalent Character in Closed-Shell Bonding

*In this section we explain how we quantified the coupling between covalent (sigma) bonds and hydrogen-bonding.*

The presence of partial covalent character in hydrogen-bonding in ice Ih, that accounts for the unusual strength of the hydrogen-bonding, was first considered by Pauling [35]. Later, Isaacs et al. presented high momentum transfer inelastic (Compton) X-ray scattering studies of the hydrogen-bond in ice Ih [36]. This investigation discovered the first direct experimental evidence for covalency among neighboring molecules through the hydrogen-bonds. Existing theoretical evidence for the

unusual strength of the hydrogen-bonding in ice Ih was explained by the presence of cooperative polarization [37]. The first consideration of quantifying the covalent character of bonding within the QTAIM framework was undertaken by Cremer and Kraka where it was determined that the local potential energy $V(\mathbf{r_b})$ dominated the local kinetic energy density $G(\mathbf{r_b})$, where $\mathbf{r_b}$ indicates position of the *BCP*, see Eq. (2.2). Consequently, the total local energy density $H(\mathbf{r_b}) = V(\mathbf{r_b}) + G(\mathbf{r_b}) < 0$ for covalent bonding and $H(\mathbf{r_b}) > 0$ for closed shell-bonding such as hydrogen-bonding [38]. Earlier, one of the current authors applied the measure of covalent bonding $H(\mathbf{r_b}) < 0$ to the hydrogen-bonding in seven phases of ice and found the presence of covalent character in the hydrogen-bonding of six of the phases of ice: ice Ic, ice Ih, ice II, ice VI, ice VII and ice IX [16]. The presence of covalent character in the hydrogen-bonding of (normal) ice Ih provided consistency for the x-ray scattering studies of Isaacs et al. We also considered the covalent character of SiO solids [39] and very high pressure ice X [40], intra-molecular proton transfer [41], neutral and charged Li microclusters [42], the $(H_2O)_5$ potential energy surface [31] and the transition from planar to cluster topologies in small water clusters [6]. Later we considered the functioning of molecular rotary motors, where long lived 'sticky' (F--H) halogen-bonds on the basis of ($H(\mathbf{r_b}) < 0$) that connected the rotor and stator were found responsible for the slow dynamics trajectory [43].

The electron donating and withdrawing effect of the biphenyl molecule for any arbitrary group R was determined with our QTAIM *interpreted* Hammett parameters $a\Delta H^{\mathrm{Ham}}(\mathrm{r_b})$ where $a = 10^3$, where $H(\mathrm{r_b})$ is the total local energy and $\Delta H^{\mathrm{Ham}}(\mathrm{r_b})$ is the difference at a given *BCP* of the substituted and unsubstituted molecular graph [44]. The QTAIM and stress tensor $\boldsymbol{\sigma}(\mathbf{r})$ properties of the H--H interactions of biphenyl subjected to torsion $\varphi$, $0.0° \leq \varphi < 25.0°$, of the C4-C7 torsional bond were found to depend on *para*-substituent biphenyl, $C_{12}H_9X$, $X = N(CH_3)_2$, $NH_2$, $CH_3$, CHO, CN, $NO_2$ and $C_{12}H_9$-$Y$, $Y = SiH_3$, ZnCl, $COOCH_3$, $SO_2NH_2$, $SO_2OH$, COCl, $CB_3$, see Fig. 2.11. The QTAIM interpreted Hammett constants, $a\Delta H(\mathbf{r_b})$ yielded very good or good agreement for the $x$ groups with the Hammett *para*-, *meta*- and *ortho*- substituent constants, see Table 2.1 and Fig. 2.12. We then proceeded to present the QTAIM interpreted Hammett substituent constants of seven new biphenyl substituent groups where tabulated Hammett substituent constants were not available; $y = SiH_3$, ZnCl, $COOCH_3$, $SO_2NH_2$, $SO_2OH$, COCl, $CB_3$, see Table 2.2 and Fig. 2.13. Independent conformation is provided using the stress tensor polarizability $\mathsf{P}_\sigma$ that we introduced. The ability to identify substituent groups R that will result in a low tendency towards torsion and hence crystallization, a major cause of device damage, is vital for the selection blue emissive layers in light emitting diodes LEDs [45].

The underlying factors controlling the two possible pathways for the Dihydrocostunolide (DHCL) photochemical ring-opening reaction were investigated; the first pathway returned to the ring-closed conformation of the reactant and the second pathway progressed to the ring-opened product [47]. The optimization of the two pathways was undertaken with High-level multi-reference DFT methods were used to obtain the total density distributions $\rho(\mathbf{r})$. The chemical character of the fissile bond oscillated between closed-shell and shared-shell for the first pathway before and

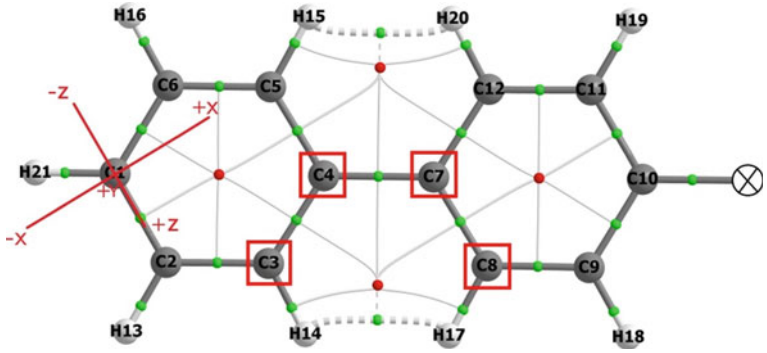


**Fig. 2.11** The representation of the molecular graphs of the *para*-substituted biphenyl that undergo the torsion φ, $C_{12}H_9$-X = *x* or *y*, where *x* = $N(CH_3)_2$, $NH_2$, $CH_3$, CHO, CN, $NO_2$ and *y* = $SiH_3$, ZnCl, $COOCH_3$, $SO_2NH_2$, $SO_2OH$, COCl, $CB_3$. The C1-C2-C3-C4-C5-C6 ring is the stator. The reaction coordinate φ is defined by the dihedral angle C3-C4-C7-C8. The C7-C8-C9-C10-C11-C12 rotor is subject to a torsion so that the nuclei comprising the substituent groups move out of the plane in an anti-clockwise direction and the H20 nuclei moves into the plane of the C1-C2-C3-C4-C5-C6 ring

**Table 2.1** The QTAIM interpretation of the Hammett substitute constants, $a\Delta H^{\mathrm{Ham}}{}_x$, $a = 10^3$, for the C-H *BCP*s and C-C *BCP*s respectively, *x* = $N(CH_3)_2$, $NH_2$, $CH_3$, CHO, CN, $NO_2$. The *para*-, *meta*- and *ortho*-, Hammett substituent constants are provided in a bold font [46]. The core-electron binding energy shifts (ΔCEBE) are provided in an italic font. The ΔCEBE are calculated, with assumptions that include the Hammett constants, for an aromatic carbon atom using the difference between the CEBE of a ring carbon of $C_6H_5$-*x* and of benzene, $C_6H_5$-H, which is the reference molecule [46]

| | $N(CH_3)_2$ | $NH_2$ | $CH_3$ | CHO | CN | $NO_2$ |
|---|---|---|---|---|---|---|
| *ΔCEBE*(*para*-) | *−0.75* | *−0.74* | *−0.25* | *0.42* | *0.57* | *0.74* |
| **Hammett(*para*-)** | **−0.83** | **−0.62** | **−0.17** | **0.47** | **0.66** | **0.78** |
| C2-H13 | −0.62 | −0.44 | −0.19 | 0.53 | 0.60 | 0.77 |
| C6-H16 | −0.62 | −0.44 | −0.05 | 0.53 | 0.60 | 0.78 |
| C1-H21 | −0.45 | −0.36 | −0.19 | 0.55 | 0.60 | 0.77 |
| *ΔCEBE*(*meta*-) | *−0.40* | *−0.34* | *−0.17* | *0.42* | *0.63* | *0.74* |
| **Hammett(*meta*-)** | **−0.21** | **0.00** | **−0.06** | **0.40** | **0.62** | **0.73** |
| C5-H15 | −0.40 | −0.36 | −0.05 | 0.30 | 0.31 | 0.36 |
| C3-H14 | −0.41 | −0.40 | −0.05 | 0.51 | 0.30 | 0.36 |
| C1-C2 | −0.35 | −0.32 | −0.04 | 0.23 | 0.28 | 0.32 |
| C6-C1 | −0.50 | −0.31 | −0.04 | 0.22 | 0.27 | 0.32 |
| *ΔCEBE*(*ortho*-) | *−0.61* | *−0.52* | *−0.28* | *0.45* | *0.67* | *0.78* |
| **Hammett(*ortho*-)** | **−0.36** | **−0.35** | **−0.17** | **0.75** | 1.06 | **0.78** |
| C8-H17 | −0.39 | −0.11 | −0.20 | 1.17 | 1.80 | 2.22 |
| C12-H20 | −0.41 | −0.11 | −0.20 | 1.09 | 1.78 | 2.21 |
| C4-C7 | 1.96 | 1.17 | 0.31 | 2.31 | 2.06 | 2.56 |

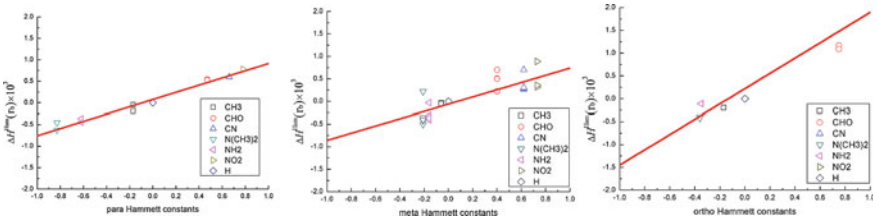


**Fig. 2.12** **Left**: The QTAIM interpreted Hammett *para*-substituent constant $a\Delta H^{\mathrm{Ham}}(\mathbf{r_b})x$, $a = 10^3$, with correlation $R = 0.989$ of the fit to a straight line. **Middle**: The QTAIM interpreted Hammett *meta*-substituent constant $a\Delta H^{\mathrm{Ham}}(\mathbf{r_b})x$, $a = 10^3$, with correlation $R = 0.900$. **Right**: The QTAIM interpreted Hammett *ortho*-substituent constant $a\Delta H^{\mathrm{Ham}}(\mathbf{r_b})x$, $a = 10^3$, with correlation $R = 0.937$

**Table 2.2** The QTAIM substituent constants, $a\Delta H^{\mathrm{Ham}}{}_{y,}$ $a = 10^3$, for the C-H *BCP*s and C-C *BCP*s respectively, where $y = SiH_3$, ZnCl, $COOCH_3$, $SO_2NH_2$, $SO_2OH$, COCl, $CB_3$

| | $SiH_3$ | ZnCl | $CO_2CH_3$ | $SO_2NH_2$ | $SO_2OH$ | COCl | $CB_3$ |
|---|---|---|---|---|---|---|---|
| C2-H13 | 0.15 | 0.19 | 0.28 | 0.55 | 0.64 | 0.75 | 0.98 |
| C6-H16 | 0.17 | 0.21 | 0.34 | 0.66 | 0.73 | 0.78 | 0.97 |
| C1-H21 | 0.20 | 0.25 | 0.37 | 0.66 | 0.75 | 0.85 | 1.04 |
| C3-H1 | 0.15 | 0.04 | 0.29 | 0.07 | 0.20 | 0.59 | 0.57 |
| C5-H15 | 0.07 | 0.02 | 0.32 | 0.34 | 0.34 | 0.53 | 0.41 |
| C1-C2 | 0.05 | 0.09 | 0.10 | 0.26 | 0.30 | 0.23 | 0.28 |
| C6-C1 | 0.11 | 0.15 | 0.11 | 0.31 | 0.29 | 0.29 | 0.43 |
| C8-H17 | −0.10 | −0.21 | 0.74 | 1.41 | 1.68 | 1.93 | 2.46 |
| C12-H20 | −0.01 | −0.19 | 0.89 | 1.43 | 1.87 | 1.64 | 2.28 |
| C4-C7 | 0.97 | 0.75 | 1.74 | 1.46 | 1.75 | 3.29 | 3.18 |

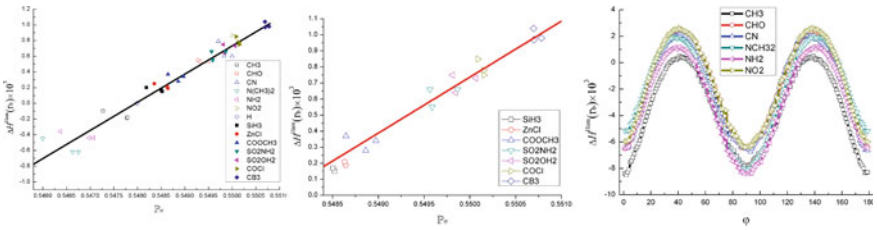


**Fig. 2.13** **Left**: The plot of the variation of the QTAIM interpreted Hammett *para*-substituent constants $\Delta H^{\mathrm{Ham}}(\mathbf{r_b}) \times 10^3$ with the stress tensor polarizability $\mathsf{P}_\sigma$ where the correlation $R = 0.969$. **Middle**: The plot of $\Delta H^{\mathrm{Ham}}(\mathbf{r_b}) \times 10^3$ for the C2-H13 *BCP*, C6-H16 *BCP* and the C1-H21 *BCP* against the stress tensor polarizability $\mathsf{P}_\sigma$ with a correlation $R = 0.977$. **Right**: The variation of $\Delta H^{\mathrm{Ham}}(\mathbf{r_b}) \times 10^3$ for the C4-C7 pivot-*BCP* with the reaction coordinate $\varphi$

after the conical intersection that steered the reaction back to reactant. This behavior was absent for the second pathway that led forward to the product. This oscillations in chemical character were caused by a "sticky" closed-shell *BCP* (on the basis of values of $H(\mathbf{r_b}) < 0$ due to leaking of covalent character from an attached sigma bond). Another example of a reaction being steered by the presence of a sticky closed-shell *BCP* was uncovered in an investigation the CHD → HT photoreaction and analyzed to determine factors influencing the CHD → HT photoreaction branching ratio [48]. This indicated that the reaction can be characterized as being pulled back towards CHD. This explained the origin of the (70:30) CHD ratio as being due to a sticky C--C *BCP*.

When constructing the QTPDs of $(H_2O)_4$, $(H_2O)_5$ and $(H_2O)_6$ we demonstrated [6] by quantifying the degree of covalent character in the hydrogen bonding ($H(\mathbf{r_b}) < 0$) that the conformers of the $(H_2O)_4$, $(H_2O)_5$ clusters are more energetically stable in less compact, planar forms, conversely the conformers of $(H_2O)_6$ are more energetically stable with compact 3-D topologies.

**Activity 2.6: Bonding types and character**

- Within QTAIM what is a shared-shell bonding interaction? State your answer in terms of the Laplacian of the total charge density distribution $\nabla^2\rho(\mathbf{r_b})$. Give an example of a bond type that is a shared-shell interaction.
- Within QTAIM what is a closed-shell bonding interaction? State your answer in terms of the Laplacian of the total charge density distribution $\nabla^2\rho(\mathbf{r_b})$. Give an example of a bond type that is a closed-shell interaction.
- Within QTAIM when can a hydrogen bond have a degree of covalent character based on $H(\mathbf{r_b})$?

## 2.5 A Measure of Metallic Character: Metallicity $\xi(\mathbf{r_b})$, Polarizability $\mathsf{P}$ and Stiffness $\mathsf{S}$

*In this section we derive the QTAIM bond metallicity measure.*

The association between covalent character and metallicity was first made in the investigation of SiO solids [39]. A measure of the topological stability of a molecular graph is provided by the ratio $|\lambda_2|/\lambda_3$ of the largest negative and the positive eigenvalues at a *BCP* [49].

In the investigation of the electron donating and withdrawing effect of the biphenyl molecule it was also discovered that effect of the addition of the *para*-substituent groups was to reduce the stress tensor polarizability $\mathsf{P}_\sigma$ at $\varphi = 90.0°$, i.e., to increase the topological stability compared to the undecorated biphenyl, see Sect. 2.4. For all values of *X* and *Y*, shorter H---H bond-path lengths corresponded to higher values of both the stiffness S and $S_\sigma$ and torsion $\varphi$. The onset of a phase transition-like behavior is found by the stress tensor stiffness $S_\sigma$, see Fig. 2.14. The atomic basins of the H---H interactions are affected by the *para*-substituent groups. A phase-transition-like

behavior for the stress tensor stiffness $S_\sigma$ is found to vary with the *para*-substituent groups.

Again using biphenyl, we used the stress tensor $\boldsymbol{\sigma}(\mathbf{r})$ within the QTAIM partitioning scheme to describe the bond-path torsion $\varphi$ that caused a change in sign of the stress tensor $\boldsymbol{\sigma}(\mathbf{r})$ eigenvalue $\lambda_{\sigma 3}$ from positive to negative of the H---H *BCP* in biphenyl for the range $5.0° \leq \varphi \leq 22.5°$, see Fig. 2.15 (left-panel). This finding which coincides with the range of the incommensurate phase transition $5° \leq \varphi \leq 21°$ determined by Benkert and collaborators. This suggests that the stress tensor $\boldsymbol{\sigma}(\mathbf{r})$ eigenvalue $\lambda_{\sigma 3}$ can be used to determine possible phase transitions where symmetry lowering is a factor, further investigations should be undertaken to test the range of applicability. Consistency was found from the QTAIM results in that the maximum in the $\underline{\mathbf{e}}_2$ H16 atomic basin-path set area at $\varphi = 5.0°$ which is the value of $\varphi$ corresponding to the maximum instability of H16 atomic basin is the QTAIM indicator of the incommensurate phase transition of the biphenyl molecular graph, see Fig. 2.15 (right-panel).

Larger values of $|\lambda_2|/\lambda_3$ indicate a 'fuzzier' a bond and relates to bond metallic character. The inequality $|\lambda_1|/\lambda_3| < 1$ holds for all closed-shell *BCP*s that are dominated by the contraction of charge away from the inter-atomic surface towards each of

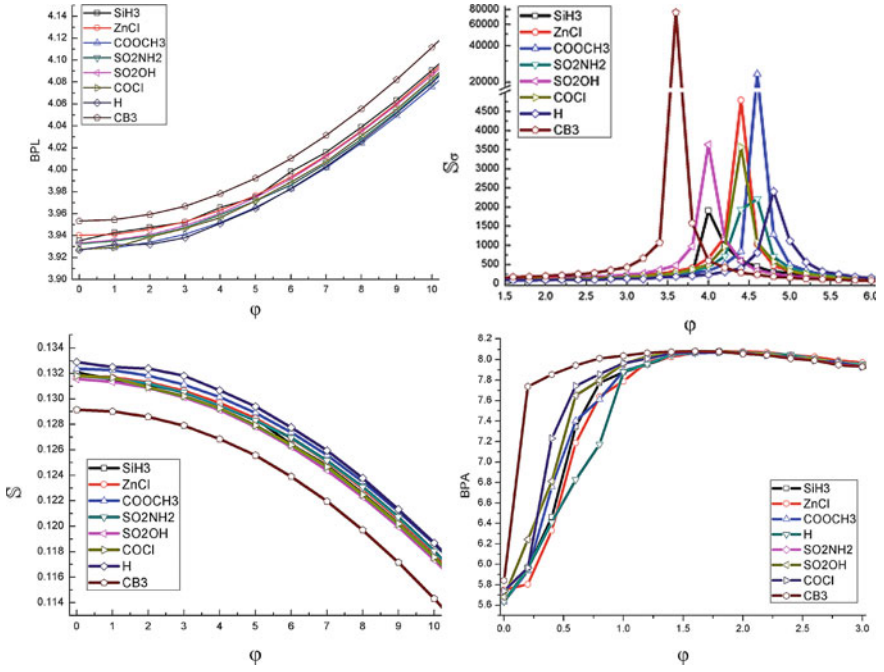


**Fig. 2.14** The variation of the H14---H17 *BCP* bond-path length (BPL), stress tensor stiffness $S_\sigma$, stiffness and basin-path set area (BPA) with the reaction coordinate $0.0° \leq \varphi \leq 10.0°$ for the substituent groups of biphenyl $C_{12}H_9Y$

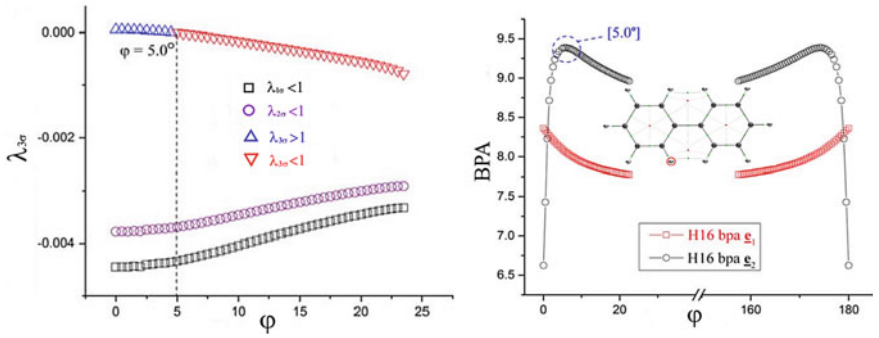


**Fig. 2.15** Variation of the stress tensor $\boldsymbol{\sigma}(\mathbf{r})$ eigenvalues $\lambda_{\sigma 1}$, $\lambda_{\sigma 2}$ and $\lambda_{\sigma 3}$ with the reaction coordinate $\varphi$ of the H---H *BCP*, notice the change in sign from (+) to (−) of the $\lambda_{\sigma 3}$ for $\varphi \geq 5.0°$ (left-panel). The basin-path set areas (BPAs) for the $\underline{\mathbf{e}}_1$ and $\underline{\mathbf{e}}_2$ eigenvectors of the H16 atomic basin comprising the bond-path of the H---H *BCP*, the H16 atom is indicated by the red circle on the inset molecular graph (right-panel)

the respective atomic basins. Larger values of $|\lambda_2|/\lambda_3|$ also correspond to a stronger tendency for the $\rho(\mathbf{r})$ to remain at the *BCP* rather than moving towards the atomic basins and results in lower values of the Laplacian $\nabla^2\rho(\mathbf{r_b})$. This observation leads directly to the concept of metallicity; the Laplacian $\nabla^2\rho(\mathbf{r_b})$ for closed shell interactions is always positive, a larger magnitude indicating a greater tendency for charge to move away from the *BCP* along the bond-path into the two atomic basins connected by the bond-path.

Therefore we can define the metallicity $\xi(\mathbf{r_b})$:

$$\xi(\mathbf{r_b}) = \rho(\mathbf{r}_b)/\nabla^2\rho(\mathbf{r}_b) \geq 1 \text{ for} \nabla^2\rho(\mathbf{r}_b) > 0 \tag{2.7}$$

Values of the metallicity $\xi(\mathbf{r_b}) \leq 1$ for closed-shell *BCP*s, correspond to non-metallic or insulating *BCP*s, see Eq. (2.7). We also examined $\xi(\mathbf{r_b})$ for very high pressure ice X [40], intra-molecular proton transfer [41], see Fig. 2.16. Values of $\xi(\mathbf{r_b})$ for a wide range of elements and compounds [50] were investigated in addition to demonstrating that the $\xi(\mathbf{r}_b)$ is inversely related to "nearsightedness" of the first-order density matrix and is suitable for closed-shell systems [51], see Fig. 2.16. The presence of $H(\mathbf{r}_b) < 0$ for closed-shell *BCP* interactions is observed for high values of the metallicity $\xi(\mathbf{r}_b) > 1$. Note, the concept of metallicity $\xi(\mathbf{r}_b)$ relates to the relative delocalization of the total electronic charge density $\rho(\mathbf{r}_b)$ [51].

Investigation of the hydrogen transfer tautomerization process yielded metallic hydrogen bonds in the benzoquinone-like core of the switch [52], see Fig. 2.17.

The metallic (i.e., $\xi(\mathbf{r}_b) \geq 1$) N10--H13 *BCP*s correlated with the relative energy $\Delta$E values demonstrating the major and minor effects of the addition of the Fe atom and UP or DOWN position of the F-substituent respectively, see Fig. 2.17. This indicated

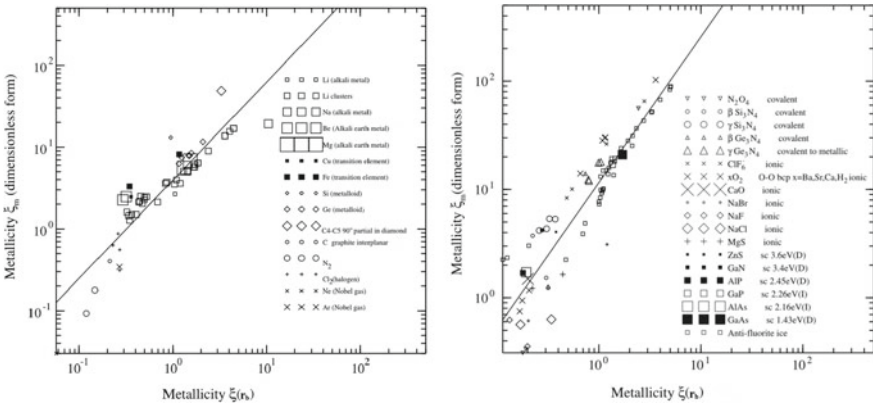


**Fig. 2.16** A plot of dimensionless metallicity $\xi_m(\mathbf{r_b})$ (left-panel) against original metallicity $\xi(\mathbf{r_b})$ for a series of elements, the correlation $R = 0.97$ for the linear fit $\xi_m(\mathbf{r_b}) = 3.93\ \xi(\mathbf{r_b})$. The corresponding plot for a series of compounds (right-panel) with correlation $R = 0.95$ for the linear fit $\xi_m(\mathbf{r_b}) = 17.18\ \xi(\mathbf{r_b})$. For each panel log–log axis are displayed for clarity

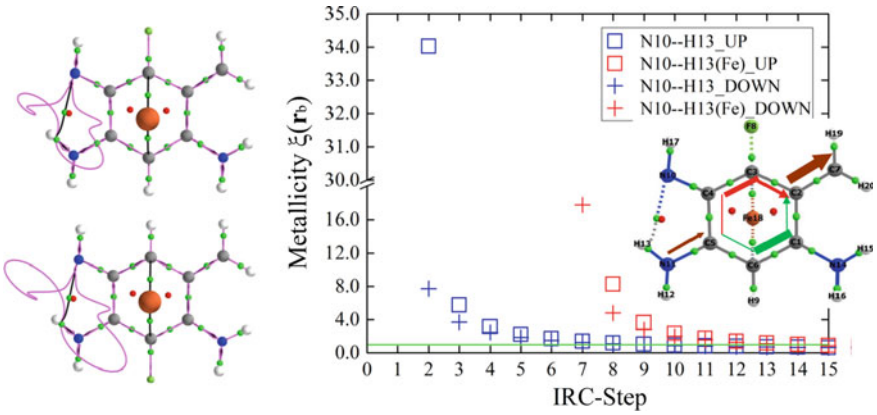


**Fig. 2.17** The variation of the metallicity $\xi(\mathbf{r}_b)$ with the IRC from the transition state at IRC-Step = 0 towards the forward minimum for N10--H13 *BCP* of the F-decorated quinone switch in the UP and DOWN positions for the undoped and Fe-doped molecular graph. The horizontal green line indicates values of metallicity $\xi(\mathbf{r}_b) = 1.0$

that the H *NCP* transfer tautomerization was facilitated by the presence of persistent metallic N10--H13 *BCP*s that were maximized in the Fe-doped switch with the F-substituent in the UP position. The effect of the metallicity $\xi(\mathbf{r}_b)$ was evident from the presence of the Fe atom that facilitates the H *NCP* transfer tautomerization by greater destabilization of the N10--H13 *BCP* bond-path that enabled the easier motion of the H *NCP*. Additional evidence of greater destabilization was found from the shorter *BCP-RCP* separation for the Fe-doped compared with undoped switch.

In an investigation into the large-amplitude motions of the tetrasulfur tetranitride $S_4N_4$ molecular graph a QTAIM polarizability $\mathsf{P}$, defined as the reciprocal of the stiffness $\mathsf{S}$, increased in proportion to the bond-path length, consistent with physical intuition. A stress tensor polarizability $\mathsf{P}_\sigma$, defined as the reciprocal of the stress tensor stiffness $\mathsf{S}_\sigma$, increased in proportion to the metallicity $\xi(\mathbf{r}_b)$ also consistent with physical intuition.

A related quantity to the metallicity $\xi(\mathbf{r}_b)$ is the charge shift ratio $\Xi(\mathbf{r}_b)$ that is defined at the *BCP* of interest:

$$\Xi(\mathbf{r}_b) = -\lambda_3/0.5(\lambda_1 + \lambda_2) \tag{2.8}$$

Earlier, we defined a bond-path *BCP* stiffness, $\mathsf{S} = |\lambda_2|/\lambda_3$ as a measure of rigidity of the bond-path [49]. The polarizability $\mathsf{P} = 1/\mathsf{S} = \lambda_3/|\lambda_2|$, where the eigenvalue ($\lambda_2$) is associated with the most preferred direction $\underline{\mathbf{e}}_2$ to reflect the facile character of the bonding rather than $|\lambda_1|/\lambda_3$ constructed from $\lambda_1$ associated with the least preferred direction $\underline{\mathbf{e}}_1$ i.e., that is less sensitive to changes in the electronic charge density $\rho(\mathbf{r})$. The polarizability $\mathsf{P} = 1/\mathsf{S} = \lambda_3/|\lambda_2|$ was found to be a more sensitive measure of charge-shift bond character e.g., to neighboring *BCP*s, than the original measure $\Xi(\mathbf{r}_b)$ that is constructed to include $\lambda_1$ in an investigation of the controversial axial 'bridgehead' bond in [1.1.1.]propellane [53], see Eq. (2.8).

## 2.6 Summary

We have presented an overview of our developments of scalar QTAIM that builds on the foundations of the topological origins of QTAIM to provide an easy to use, albeit limited, set of tools for workers using conventional (scalar QTAIM), see Table 2.3.

The QTAIM Quantum Topology Phase Diagram (QTPD) analysis is completely general and can be applied to any molecule, metals, clusters or solids. QTPDs can be used for non-isomeric species e.g., for comparing separate reactions may be formed by creating aggregate-isomers along with simple sum to ensure that the Poincaré-Hopf relation is obeyed. The hybrid-QTAIM-MESP QTPD analysis is most useful for clusters of molecules containing lone pairs and hydrogen-bonds, e.g., $NH_3$ and HCN. If a hybrid QTAIM-MESP topology possesses an Euler Characteristic $\chi = -1$ then the hybrid topology can be mapped directly *back* on the QTPD to extract the QTAIM topologies *b*, *r* and *c,* therefore, the consideration of $\chi = -1$ may be useful for identifying features of 'missing' hybrid-QTPD topologies of more energetically stable structures. The QTPD approach is not limited for use with $\rho(\boldsymbol{r})$; it could work with other scalar fields for instance the Ehrenfest Force partitioning [62] and MESP as we demonstrated in Sect. 2.2.4.

An outstanding issue for the use of QTPDs is to determine whether there are any undiscovered rules governing the structure of the QTPDs. For instance, we already determined that for sets of isomers for spanning QTPDs may have a lower limit (single

**Table 2.3** The scalar QTAIM and stress tensor $\boldsymbol{\sigma}(\mathbf{r})$ concepts that we have developed with the relevant references listed

| Scalar | Definition | Reference |
|---|---|---|
| Metallicity | $\xi(\mathbf{r_b}) = \rho(\mathbf{r}_b)/\nabla^2\rho(\mathbf{r}_b) \geq 1$ for $\nabla^2\rho(\mathbf{r}_b) > 0$ | [7, 39, 53–56] |
| Nearest neighbor *RCP*s | $NNRCP = \sum_{\boldsymbol{r}\in S_I(\omega)} \delta(\boldsymbol{r}), \delta(\boldsymbol{r}) = \begin{cases} 1, \nabla\rho(\boldsymbol{r}) = 0(RCP) \\ 0, elsewhere \end{cases}$ | [33, 34] |
| Stiffness | $\mathsf{S} = \lambda_2/\lambda_3$ | [44, 56–61] |
| Stress tensor stiffness | $\mathsf{S}_\sigma = \lvert\lambda_{1\sigma}\rvert/\lvert\lambda_{3\sigma}\rvert$ | [44, 56–58, 61] |
| Polarizability | $\mathsf{P} = \lambda_3/\lambda_2$ | [22, 56, 58] |
| Stress tensor polarizability | $\mathsf{P}_\sigma = \lvert\lambda_{3\sigma}\rvert/\lvert\lambda_{1\sigma}\rvert$ | [22, 56, 58] |
| Quantum geometry | $\{0\text{-}D_{QT}, 1\text{-}D_{QT}, 2\text{-}D_{QT}, 3\text{-}D_{QT}\}$ | [6, 8, 20, 34, 42, 43, 62] |
| Quantum topology phase diagrams | $(b, r)$ projected space of $n - b + r - c = 1$:unstable/forbidden regions | [6, 8, 20, 42, 43, 61, 62] |
| Topological complexity | $\Sigma_{brc}$ | [6, 8, 20, 61] |
| Basin-path set, basin-path set area | BPA | [44] |
| QTAIM Hammett parameters | $a\Delta H^{\mathrm{Ham}}{}_x$; $\Delta H^{\mathrm{Ham}}{}_x = H_{\mathrm{biphenyl}} - H_x$, $a = 10^3$ | [58] |

*RCP* present) and an upper bound (compact polyhedra), but are there rules beyond this perhaps on the total number of entries (Poincaré-Hopf topologies possible)?

The suggestions for further work include a method for the generation of molecular graphs from the associated QTPDs: start with the sparsest possible QTPD and use Monte Carlo methods to generate molecular graphs corresponding to neighboring points on the QTPD. Then construct rules underlying QTPDs to generate allowable topologies that could inform automated searches.

Further applications could be to use the QTPDs with the solid-state whereby the *RCP*/*BCP* slope characterizes physical phase transitions and encloses phase boundaries, this possibility was previously indicated for multiple phases of ice [8].

Another application for the solid state could be to use the QTPD to define a measure of "crystal recognition," rather than molecular recognition. The implementation would include examining the angle of separation of the *RCP*/*BCP* slopes during a phase change and investigate the effect of the rate of change of the gradient of the *RCP*/*BCP* slope. Therefore, using the example of ice IX, previously mentioned in Sect. 2.2.3, a suggested threshold that is characteristic of a phase transition is that the slope of

*RCP*/*BCP* > 1. Increases in pressure will cause more *RCP*s to form relative to the number of *BCP*s and if the same size super-cells either side of, or through, a transition of interest, the position of the data points can be continually compared to learn the dependency on the relative separation of the data points on the slope *RCP*/*BCP*. QTPDs could also, in future, be used to revisit Linus Pauling's first, third, fourth and fifth rules used to determine the crystal structures of complex ionic crystals.

One limitation of the QTPD formalism however, is that although they provides the capability of discovering missing topologies the QTPD are highly dependent on the complexities of a given potential energy surface (PES). An example of this is the hybrid-MESP-QTAIM QTPD that indicates isomers are restricted to a zone of energetic stability based on a relation between the number of lone pairs ($l$) and hydrogen-bond *BCP*s ($b_{\mathrm{HB}}$). The consequence of this is that certain combinations $l$ and $b_{\mathrm{HB}}$ are more likely to be found in, for instance, stable water clusters. Related to the dependency of the QTPD on the PES is the limitation of neglecting intermediate catastrophe critical points that lessens the ability to extract insights into topological transformations. In principle, such an intermediate QTPD could be constructed however, there would be excessively many rank 1 and rank 2 unstable catastrophe critical points rendering implementation impractical, which is also a consideration for the MESP method due to the enormous complexity of the PES and in particular that associated with structural changes. Note, a stable *BCP* is a rank 3 critical point. The QTPD is however, useful for situations where weaker and stronger chemical bonds are created from each because weaker bonds reduce the cost of the formation or destruction of the stronger chemical bonds. An example we found was that of the water $(H_2O)_5$ PES where the stronger (sigma) O-H *BCP*s exist along with the weaker hydrogen-bond H--O *BCP*s and the weakest O---O *BCP*s. The hydrogen-bond H--O *BCP*s facilitate the formation/destruction of the O-H *BCP*s and the O---O *BCP*s facilitate the formation/destruction of the hydrogen-bond H--O *BCP*s.

The *NNRCP* provides a quantitative understanding of the site reactivity of an impurity metallic nuclei host in a host cluster. Using the *NNRCP* measure a weaker condition than chemical bonding for the association of the Pt (impurity) nucleus with the $Au_6$ host. The *NNRCP* found to be more satisfactory at understanding site reactivity than the atomic coordination number. The *NNRCP* also proved useful in investigations of catalytic efficiency when comparing similar reactions that only differed in the choice of catalyst. The *NNRCP* tool has not been extensively used but the main limitation would appear to be that the range of applicability is limited to metallic impurities due to the *NNRCP* utilizing the facile nature of the $\rho(\mathbf{r})$ associated with the impurity metal atom.

The limitations of our consideration of covalent character and how it may be shared between bonding include the fact that we have not located specific bonding characteristics in *each* of the hydrogen-bond and covalent-bond that are coupled as indicated by values of $H(\mathbf{r_b}) < 0$ for the hydrogen-bond. We have also not visualized the nature of the chemical coupling in small water clusters between hydrogen-bonds and the covalent-bonds with which a hydrogen atom is shared. Further to this we have not quantified the effects of excess electron momentum transfer between adjacent covalent (sigma) and hydrogen-bonds consistent with the finding of the x-ray scattering

studies on the hydrogen-bond in ice Ih of Isaacs et al. [36]. These limitations will be addressed in Chap. 4.

**Target learning outcomes:**

Understand the limitations of chemical intuition gained from Euclidian geometry.

Understand, for a range of chemical situations, how to construct Quantum Topology Phase Diagrams (QTPDs):

- Isolated molecules or clusters.
- Molecules/clusters containing Non-Nuclear Attractors (*NNA*s).
- Solid state.
- Hybrid QTAIM and electrostatic potential QTPDs.
- Directed QTPDs for potential energy surfaces and comparing reactions.

Understand how to determine the degree of attachment of an impurity metal nuclear critical point (*NCP*) in a metallic host cluster more precisely than the coordinate number.

## 2.7 Further Reading

*Note, earlier the "Quantum Theory of Atoms in Molecules (QTAIM)" was referred to as "AIM".*

Matta and Massa et al. wrote a very readable biography on the late R. F. W. Bader, the inventor of QTAIM [63]. We recommend starting more formal reading materials on QTAIM with the Polanyi Award Lecture by R. F. W. Bader on of atoms in molecules [64], followed by the everyman derivation of QTAIM [65]. Chemical bonding within QTAIM is considered [13, 14] in addition to the quantum mechanical basis of conceptual chemistry within quantum chemistry [66–68]. Edited books on QTAIM include "The Quantum Theory of Atoms in Molecules: From Solid State to DNA and Drug Design" [69]. A introductory treatment of QTAIM was written by Popelier (this chapter) [70]. The relationship with QTAIM and experiment and interpretation of electron density distributions by Matta and Bader [71, 72].

The crystallographer Coppens developed techniques for QTAIM, namely the extraction of electron density distributions from X-ray experiment published a book on the subject [73], he also published a personal account of his extensive contributions to the field of crystallography [74].

## References

1. Bader RFW (1980) Quantum topology of molecular charge distributions. III. The mechanics of an atom in a molecule. J Chem Phys 73:2871–2883
2. Bader RFW, Nguyen-Dang TT (1981) Quantum theory of atoms in molecules–dalton revisited. In: Löwdin PO (ed) Advances in quantum chemistry, vol 14. Academic Press, pp 63–124

3. Collard K, Hall GG (1977) Orthogonal trajectories of the electron density. Int J Quantum Chem 12:623–637
4. Johnson CK (1977) Peaks, passes, pales, and pits: a tour through the critical points of interest in a density map. In: Abstracts of the American crystallographic association, vol 30. ACA Publications, Inc.
5. Smith VH, Price PF, Absar I (1977) XVI. Representations of the electron density and its topographical features. Israel J Chem 16:187–197
6. Jenkins S, Restrepo A, David J, Yin D, Kirk SR (2011) Spanning QTAIM topology phase diagrams of water isomers W4, W5 and W6. Phys Chem Chem Phys 13:11644–11656
7. Figueredo FA, Maza JR, Kirk SR, Jenkins S (2014) Quantum topology phase diagrams for the cis- and trans-isomers of the cyclic contryphan-Sm peptide. Int J Quantum Chem 114:1697–1706
8. Jenkins S (2013) Quantum topology phase diagrams for molecules, clusters, and solids. Int J Quantum Chem 113:1603–1608
9. Otero-de-la-Roza A, Blanco MA, Pendás AM, Luaña V (2009) Critic: a new program for the topological analysis of solid-state electron densities. Comput Phys Commun 180:157–166
10. Otero-de-la-Roza A, Johnson ER, Luaña V (2014) Critic2: a program for real-space analysis of quantum chemical interactions in solids. Comput Phys Commun 185:1007–1018
11. Otero-de-la-Roza A (2022) Finding critical points and reconstruction of electron densities on grids. J Chem Phys 156:224116
12. Bader RFW (1994) Atoms in molecules: a quantum theory. Oxford University Press, USA
13. Bader RFW (1998) A bond path: a universal indicator of bonded interactions. J Phys Chem A 102:7314–7323
14. Bader RFW (2009) Bond paths are not chemical bonds. J Phys Chem A 113:10391–10396
15. Jenkins S, Heggie MI (2000) Quantitative analysis of bonding in 90° partial dislocation in diamond. J Phys Condens Matter 12:10325–10333
16. Jenkins S, Morrison I (2000) The chemical character of the intermolecular bonds of seven phases of ice as revealed by ab initio calculation of electron densities. Chem Phys Lett 317:97–102
17. Kraka E (1992) Description of chemical reactions in terms of the properties of the electron density. J Mol Struct (Thoechem) 255:189–206
18. Jenkins S, Blancafort L, Kirk SR, Bearpark MJ (2014) The response of the electronic structure to electronic excitation and double bond torsion in fulvene: a combined QTAIM, stress tensor and MO perspective. Phys Chem Chem Phys 16:7115–7126
19. Johnson CK, Burnett M, Dunbar W (1996) Crystallographic topology and its applications. In: Crystallographic computing 7. International Union of Crystallography, pp 1–25
20. Jenkins S, Rong C, Kirk SR, Yin D, Liu S (2011) Spanning set of silica cluster isomer topologies from QTAIM. J Phys Chem A 115:12503–12511
21. Xiao C-X, Xu T, Maza JR, Figueredo FA, Kirk SR, Jenkins S (2014) A QTAIM perspective of the Si6Li6 potential energy surface using quantum topology phase diagrams. Chem Phys Lett 609:117–122
22. Xu Y, Xu T, Jiajun D, Kirk SR, Jenkins S (2016) A QTAIM and stress tensor perspective of large-amplitude motions of the tetrasulfur tetranitride S4N4 molecular graph. Int J Quantum Chem 116:1025–1039
23. Eberhart M (1996) From topology to geometry. Can J Chem 74:1229–1235
24. Martoňák R, Donadio D, Oganov AR, Parrinello M (2006) Crystal structure transformations in SiO2 from classical and ab initio metadynamics. Nature Mater 5:623–626
25. Oganov AR, Lyakhov AO, Valle M (2011) How evolutionary crystal structure prediction works—and why. Acc Chem Res 44:227–237
26. Boulfelfel SE, Oganov AR, Leoni S (2012) Understanding the nature of "superhard graphite." Sci Rep 2:471
27. Jenkins S, Morrison I (1999) Characterization of various phases of ice on the basis of the charge density. J Phys Chem B 103:11041–11049
28. Umemoto K, Wentzcovitch RM (2005) Low ↔ high density transformations in ice. Chem Phys Lett 405:53–57

29. Jenkins S, Kirk SR, Ayers PW (2007) The chemical character of very high pressure ice phases. In: Physics and chemistry of ice (proceedings of 11th international conference on the physics and chemistry of Ice, Bremerhaven, Germany). Royal Society of Chemistry, pp 265–272
30. Kumar A, Gadre SR, Chenxia X, Tianlv X, Kirk SR, Jenkins S (2015) Hybrid QTAIM and electrostatic potential-based quantum topology phase diagrams for water clusters. Phys Chem Chem Phys 17:15258–15273
31. Xu T, Farrell J, Xu Y, Momen R, Kirk SR, Jenkins S, Wales DJ (2016) QTAIM and stress tensor interpretation of the (H2O)5 potential energy surface. J Comput Chem 37:2712–2721
32. Xu T, Farrell J, Momen R, Azizi A, Kirk SR, Jenkins S, Wales DJ (2017) A stress tensor eigenvector projection space for the (H2O)5 potential energy surface. Chem Phys Lett 667:25–31
33. Jenkins S, Xiao C-X, Xu T, Yin D, Kirk SR, Chass GA (2015) Quantum topological resolution of catalyst proficiency. Int J Quantum Chem 115:875–883
34. Xu T, Jenkins S, Xiao C-X, Maza JR, Kirk SR (2013) The Pt site reactivity of the molecular graphs of Au6Pt isomers. Chem Phys Lett 590:41–45
35. Pauling L (1935) The structure and entropy of ice and of other crystals with some randomness of atomic arrangement. J Am Chem Soc 57:2680–2684
36. Isaacs ED, Shukla A, Platzman PM, Hamann DR, Barbiellini B, Tulk CA (1999) Covalency of the hydrogen bond in ice: a direct X-ray measurement. Phys Rev Lett 82:600–603
37. Heggie MI, Latham CD, Maynard SCP, Jones R (1996) Cooperative polarisation in ice Ih and the unusual strength of the hydrogen bond. Chem Phys Lett 249:485–490
38. Cremer D, Kraka E (1984) A description of the chemical bond in terms of local properties of electron density and energy. Croat Chem Acta 57:1259–1281
39. Jenkins S (2002) Direct space representation of metallicity and structural stability in SiO solids. J Phys Condens Matter 14:10251–10263
40. Jenkins S, Kirk SR, Ayers PW (2006) Structural and chemical character of very high pressure ice phases. In: Kuhs WF (ed) Physics and chemistry of ice (proceedings of 11th international conference on the physics and chemistry of ice, Bremerhaven, Germany), Royal Society of Chemistry, pp 265–272
41. Mitra S, Chandra A, Gashnga P, Jenkins S, Kirk S (2012) Exploring hydrogen bond in the excited state leading toward intramolecular proton transfer: detailed analysis of the structure and charge density topology along the reaction path using QTAIM. J Mol Model 18:4225–4237
42. Yepes D, Kirk SR, Jenkins S, Restrepo A (2012) Structures, energies and bonding in neutral and charged Li microclusters. J Mol Model 18:4171–4189
43. Wang L, Huan G, Momen R, Azizi A, Xu T, Kirk SR, Filatov M, Jenkins S (2017) QTAIM and stress tensor characterization of intramolecular interactions along dynamics trajectories of a light-driven rotary molecular motor. J Phys Chem A 121:4778–4792
44. Dong J, Xu Y, Xu T, Momen R, Kirk SR, Jenkins S (2016) The substituent effects on the Biphenyl H---H bonding interactions subjected to torsion. Chem Phys Lett 651:251–256
45. Hohnholz D, Schweikart K-H, Subramanian LR, Wedel A, Wischert W, Hanack M (2000) Synthesis and studies on luminescent biphenyl compounds. Synth Met 110:141–152
46. Segala M, Takahata Y, Chong DP (2006) Geometry, solvent, and polar effects on the relationship between calculated core-electron binding energy shifts ($\Delta$CEBE) and Hammett substituent ($\sigma$) constants. J Mol Struct (Thoechem) 758:61–69
47. Tian T, Xu T, Kirk SR, Filatov M, Jenkins S (2019) Next-generation quantum theory of atoms in molecules for the ground and excited state of DHCL. Chem Phys Lett 717:91–98
48. Tian T, Xu T, Kirk SR, Filatov M, Jenkins S (2019) Next-generation quantum theory of atoms in molecules for the ground and excited state of the ring-opening of Cyclohexadiene (CHD). Int J Quantum Chem 119:e25862
49. Jenkins S, Maza JR, Xu T, Jiajun D, Kirk SR (2015) Biphenyl: a stress tensor and vector-based perspective explored within the quantum theory of atoms in molecules. Int J Quantum Chem 115:1678–1690
50. Jenkins S, Ayers PW, Kirk SR, Mori-Sánchez P, Martín Pendás A (2009) Bond metallicity of materials from real space charge density distributions. Chem Phys Lett 471:174–177

51. Ayers PW, Jenkins S (2015) Bond metallicity measures. Comput Theor Chem 1053:112–122
52. Tian T, Xu T, van Mourik T, Früchtl H, Kirk SR, Jenkins S (2019) Next generation QTAIM for the design of quinone-based switches. Chem Phys Lett 722:110–118
53. Bin X, Xu T, Kirk SR, Jenkins S (2019) The directional bonding of [1.1.1]propellane with next generation QTAIM. Chem Phys Lett 730:506–512
54. Jenkins S, Kirk SR, Rong C, Yin D (2012) The cis-effect using the topology of the electronic charge density. Mol Phys 111:1–13
55. Huan G, Xu T, Momen R, Wang L, Ping Y, Kirk SR, Jenkins S, van Mourik T (2016) A QTAIM exploration of the competition between hydrogen and halogen bonding in halogenated 1-methyluracil: water systems. Chem Phys Lett 662:67–72
56. Guo H, Morales-Bayuelo A, Xu T, Momen R, Wang L, Yang P, Kirk SR, Jenkins S (2016) Distinguishing and quantifying the torquoselectivity in competitive ring-opening reactions using the stress tensor and QTAIM. J Comput Chem 37:2722–2733
57. Hu MX, Xu T, Momen R, Huan G, Kirk SR, Jenkins S, Filatov M (2016) A QTAIM and stress tensor investigation of the torsion path of a light-driven fluorene molecular rotary motor. J Comput Chem 37:2588–2596
58. Jiajun D, Maza JR, Xu Y, Xu T, Momen R, Kirk SR, Jenkins S (2016) A stress tensor and QTAIM perspective on the substituent effects of biphenyl subjected to torsion. J Comput Chem 37:2508–2517
59. Momen R, Azizi A, Wang L, Ping Y, Xu T, Kirk SR, Li W, Manzhos S, Jenkins S (2017) The role of weak interactions in characterizing peptide folding preferences using a QTAIM interpretation of the Ramachandran plot ($\phi$-$\psi$). Int J Quantum Chem 118:e25456
60. Momen R, Azizi A, Wang LL, Ping Y, Xu T, Kirk SR, Li W, Manzhos S, Jenkins S (2017) Exploration of the forbidden regions of the Ramachandran plot ($\phi$-$\psi$) with QTAIM. Phys Chem Chem Phys 19:26423–26434
61. Huang WJ, Momen R, Azizi A, Xu T, Kirk SR, Filatov M, Jenkins S (2018) Next-generation quantum theory of atoms in molecules for the ground and excited states of Fulvene. Int J Quantum Chem 118:e25768
62. Maza JR, Jenkins S, Kirk SR, Anderson JSM, Ayers PW (2013) The Ehrenfest force topology: a physically intuitive approach for analyzing chemical interactions. Phys Chem Chem Phys 15:17823–17836
63. Matta CF, Massa L, Keith TA, Richard FW (2011) Bader: a true pioneer. J Phys Chem A 115:12427–12431
64. Bader R (1998) 1997 Polanyi Award Lecture Why are there atoms in chemistry? Can J Chem 76:973–988
65. Bader RFW (2007) Everyman's derivation of the theory of atoms in molecules. J Phys Chem A 111:7966–7972
66. Bader RFW (2005) The quantum mechanical basis of conceptual chemistry. Monatsh Chem 136:819–854
67. Gillespie RJ, Popelier PLA (2001) Chemical bonding and molecular geometry: from lewis to electron densities. Oxford University Press
68. Matta CF (2017) On the connections between the quantum theory of atoms in molecules (QTAIM) and density functional theory (DFT): a letter from Richard F. W. Bader to Lou Massa. Struct Chem 28:1591–1597
69. The quantum theory of atoms in molecules: from solid state to DNA and drug design (2007). Wiley
70. Applications of topological methods in molecular chemistry, vol 22 (2016). Springer International Publishing
71. Matta CF, Bader RFW (2006) An experimentalist's reply to "What is an atom in a molecule?" J Phys Chem A 110:6365–6371
72. Matta CF, Gillespie RJ (2002) Understanding and interpreting molecular electron density distributions. J Chem Educ 79:1141
73. Coppens P (1997) X-ray charge densities and chemical bonding. Oxford University Press
74. Coppens P (2015) The old and the new: my participation in the development of chemical crystallography during 50+ years. Phys Scr 90:058001

# Chapter 3
# Bridging Scalar QTAIM and Vector-Based Next Generation QTAIM

*Without a transition, a change is just a rearrangement of the furniture. Unless transition happens, the change won't work.*
*William Bridges*

This chapter bridges conventional QTAIM, developments of which were covered in Chap. 2 and Next Generation QTAIM that is presented in Chap. 4 and the subsequent chapters.

In this chapter we start with the core concept of next generation QTAIM (NG-QTAIM) namely using the directional characteristics of QTAIM previously overlooked to understand the nature of structural deformations. The directional characteristics are extracted from the static charge density distributions and demonstrate the presence of information regarding the tendencies for molecular solids to reorganize when subject to a perturbation. This can be understood in terms of an electron following approach, i.e., that the atoms are following the directions of preferred electronic charge density accumulation. We chose the highly ordered cubic ice phase (ice Ic) for easier comparison of the motion of the phonon modes with the directions of the QTAIM eigenvectors, referred to as the Hessian of $\rho(\mathbf{r})$ eigenvectors. We then present practical uses for this electron preceding approach that the specific case of involve bond torsions.

In Sect. 3.1 we explain the origins of NG-QTAIM in the correspondence between the normal modes of vibration of cubic ice (ice Ic) and the Hessian of $\rho(\mathbf{r})$ eigenvectors. The bond-path framework that is based on the quantification of the lack of accordance of the motion of $\rho(\mathbf{r_b})$ and nuclei for bond torsion is introduced in Sect. 3.2. The torsion of biphenyl is considered in terms of the detachment and reattachment of the bond-path framework in Sect. 3.2.1. The photo-isomerization of the retinal chromophore using the bond-path is outlined in Sect. 3.2.2. The QTAIM interpretation of the Ramachandran plot ($\phi$-$\psi$) is presented in Sects. 3.2.3 and 3.2.4 that includes hydrogen bonding and H---H bonding. The chapter concludes the bridge between

© The Author(s), under exclusive license to Springer Nature Singapore Pte Ltd. 2023

S. Jenkins and S. R. Kirk, *Next Generation Quantum Theory of Atoms in Molecules*, Lecture Notes in Chemistry 110, https://doi.org/10.1007/978-981-99-0329-0_3

conventional QTAIM and NG-QTAIM in Sect. 3.4 by outlining benefits, limitations and suggestions for further investigations of the ideas introduced.

**Scientific goals to be addressed:**

- Discover the relationship between the phonon projected density of states and the Hessian of $\rho(\mathbf{r})$ eigenvectors.
- Determine the relationship between the nuclear and $\rho(\mathbf{r_b})$ motion for bond torsion.
- Quantify the detachment and reattachment of the torsioned bond-path framework of the bridging C-C bond of biphenyl.
- Determine the responsiveness to changes in the nuclear skeleton during the photo-isomerization of retinal chromophore.
- Construct the QTAIM interpreted Ramachandran plot to explore "forbidden regions" of the conventional Ramachandran plot.
- Include the weak bonds: hydrogen-bonds and H---H contacts in the QTAIM interpreted Ramachandran plot.

## 3.1 Relating the Projected Density of States (PDOS) and QTAIM

*In this section we explain the dynamic origins of NG-QTAIM.*

The procedure to find the normal modes of a set of N atoms in a relaxed structure is to systematically perturb the structure along $\pm$ ($x$, $y$, $z$) axes in a harmonic manner for the exploration the 3N degrees of freedom to find these preferred motions, i.e., normal modes of the atomic motions. In an earlier investigation on cubic ice (ice Ic), a matrix of atomic forces was constructed from the result of applying a series of harmonic shifts this was then used to construct the zone centre projected density of states (PDOS) [1]. Where projections onto the symmetric-stretch (*ss*); anti-symmetric stretch (*as*); bending (*b*); rotational ($R_x$), ($R_y$), and ($R_z$); and translational ($T_x$), ($T_y$), and ($T_z$) vibrations of the water molecule were calculated to enable the display of the intra- and inter-molecular phonon mode character [2]. The zone centre dynamical matrix associated with the ice Ic supercells is obtained [3] by a finite-difference method, based on the evaluation of the atomic forces when atoms are subjected to ($\pm$) shifts from their equilibrium positions. Each of the ionic degrees of freedom is shifted in both ($\pm$) directions about its relaxed position to obtain the rows of the dynamical matrix as follows. Expressing the total energy of the ice lattice as a Taylor expansion [4]:

$$E = E_0 + \frac{1}{2}\sum_{ij} A_{ij}u_i u_j + \frac{1}{6}\sum_{ijk} B_{ijk}u_i u_j u_k \tag{3.1}$$

where $E_0$ corresponds to the equilibrium lattice energy and $u_i$ is a general coordinate of an ion relative to the minimum energy configuration ($i$ labels both the ion and a particular Cartesian direction). $A_{ij}$ describes the harmonic response of the lattice and is used to construct the dynamical matrix from:

$$D_{ij} = \frac{1}{m_j m_j^{1/2}} A_{ij} \tag{3.2}$$

where the $m_i$ represent the ionic masses. The force on the general coordinate is written as:

$$F_i = \frac{dE}{du_i} = -\sum_j A_{ij} u_j - \frac{1}{2} \sum_{jk} B_{ijk} u_j u_k \tag{3.3}$$

Each general coordinate is independently shifted by an amount $\pm\ \Delta$ and minimizes the total energy with respect to electronic degrees of freedom to obtain forces on N atoms in this distorted configuration. Taking differences of the $F_i^{\pm \Delta m}$ we now obtain:

$$F_i^{-\Delta m} - F_i^{+\Delta m} = \Delta A_{im} \tag{3.4}$$

The applications of small shifts in opposing ($\pm$) directions ensures cancellation of any cubic terms of the expansion whilst the quartic terms are small enough to ignore. The magnitude of the ($\pm$) shift must be large enough to overcome errors in the forces due to the noise produced by grid errors and small enough to ensure that the response of the ions is still harmonic.

Consider water molecules in ice: the $z$-axis of rotation $z$-axis is perpendicular to the plane of the molecule, the $y$-axis of rotation coincides with the $C_v$ symmetry axis of the molecule, the $x$-axis of rotation is defined perpendicular to both of the other axes. Lower frequency projected phonon modes correspond to less or no distortion of the stronger sigma covalent O-H bonds, such as occurs for the symmetric-stretch ($ss$); anti-symmetric stretch ($as$); bending ($b$) vibrational modes. Therefore the rotational ($R_x$), ($R_y$), and ($R_z$) modes are the most efficient route to probe the hydrogen-bonding network.

The investigation of ice Ic provided evidence that it was possible to predict features in the PDOS from the relaxed structure that indicated information concerning the relocation of the atoms after being perturbed was already be contained within the relaxed structure; i.e., in the total charge-density distribution $\rho(\mathbf{r})$.

Later an investigation was undertaken on the phonon modes of the cubic ice phase (ice Ic) that led to the connection between the dynamic, i.e., phonon modes and static properties from the $\rho(\mathbf{r_b})$ at the hydrogen-bond critical points ($\mathbf{r_b}$) [5], see Table 3.1 and Chap. 2. The $\rho(\mathbf{r_b})$ corresponding to the bonds of a relaxed structure quantifies

**Table 3.1** The projected density of states (PDOS): symmetric stretch (*ss*), anti-symmetric stretch (*as*), bending (*b*), rotational ($R_x$), ($R_y$), and ($R_z$) and translational ($T_x$), ($T_y$), and ($T_z$) of ice Ic for the frequencies of the top (1143.17 $cm^{-1}$) and bottom (579.62 $cm^{-1}$) of the rotational band as well as the top of the stretching band (3174.60 $cm^{-1}$)

| *ss* | *as* | *b* | $R_x$ | $R_y$ | $R_z$ | $T_x$ | $T_y$ | $T_z$ |
|---|---|---|---|---|---|---|---|---|
| *1143.17* $cm^{-1}$ | | | | | | | | |
| 0.0000 | 0.0000 | 0.0000 | 0.0000 | 1.0000 | 0.0000 | 0.0000 | 0.0000 | 0.0000 |
| *579.62* $cm^{-1}$ | | | | | | | | |
| 0.0000 | 0.0000 | 0.0000 | 0.1994 | 0.0000 | 0.7394 | 0.0350 | 0.0000 | 0.0261 |
| *3174.60* $cm^{-1}$ | | | | | | | | |
| 0.9962 | 0.0007 | 0.00300 | 0.0000 | 0.0000 | 0.0000 | 0.0000 | 0.0000 | 0.0000 |

where electrons have accumulated and where they will prefer to relocate if they are perturbed that will consequently be followed by the atomic nuclei.

The motion of the phonon modes of the water molecules in Ice Ic relative to the hydrogen-bond network at the top of the rotational band (1143.17 $cm^{-1}$) are exclusively $R_y$ which corresponds to the largest distortion of the hydrogen-bond network possible for a rotational mode, see Table 3.1. The significant PDOS contributions at the bottom of the rotational band are split between $R_z$, $R_x$ and $R_z$ with the $R_z$ contribution dominant. This result can be explained by the fact that the $R_z$ mode possesses the largest component of angular momentum for an isolated water molecule, followed in order by the $R_x$ and $R_y$ vibrational modes. The top of the stretching band (3174.60 $cm^{-1}$) corresponds almost exclusively to the symmetric-stretch (*ss*) mode of the water molecule where the stretching motion is measurably confined to the covalent (sigma) O-H bond stretching motion. These correspondences for the top and bottom of the rotational band are not exact since the PDOS are constructed using the positions of the hydrogen atoms, whilst the eigenvectors are associated with the hydrogen-bond *BCP*s.

Consideration of the QTAIM 'hard' $\underline{\mathbf{e}}_\mathbf{1}$ direction corresponds almost exclusively to the $\boldsymbol{R_x}$ direction, see Table 3.2. Conversely the 'easy' ($\underline{\mathbf{e}}_\mathbf{2}$) direction demonstrates that the motion at the $R_z$ contribution is almost exclusively comprised the $\underline{\mathbf{e}}_\mathbf{2}$ eigenvector that is apparent by visual inspection of the directions of $\pm R_z$ and $\pm \underline{\mathbf{e}}_\mathbf{2}$, see Fig. 3.1. A linear combination $a\underline{\mathbf{e}}_\mathbf{1} + b\underline{\mathbf{e}}_\mathbf{2}$ of the least facile and most facile eigenvectors very closely matches the motion of the entire PDOS. The $\underline{\mathbf{e}}_\mathbf{3}$ direction corresponds to the *bond-path* direction exclusively defines the symmetric-stretch (ss) vibrational mode. The bond-path ($\boldsymbol{r}$) may possess a non-zero degree of curvature [6] and is a dimensionless ratio of the bond-path length (BPL) and geometric bond length (GBL) separating two bonded nuclei and is defined as:

$$(\mathrm{BPL} - \mathrm{GBL}) \big/ \mathrm{GBL} \tag{3.5}$$

**Table 3.2** A comparison of the "hard" ($\underline{\mathbf{e}}_1$) and "easy" ($\underline{\mathbf{e}}_2$) directions of the hydrogen-bonds with the PDOS of ice Ic. The scalar constants $a = 0.2246$ and $b = 0.7680$ were chosen for comparison with the $R_x$ and $R_z$ PDOS results respectively given in Table 3.3. The projection of the ($\underline{\mathbf{e}}_3$) direction, associated with the bond-path is included to compare with bond stretching vibration

| *ss* | *as* | *b* | $R_x$ | $R_y$ | $R_z$ | $T_x$ | $T_y$ | $T_z$ |
|---|---|---|---|---|---|---|---|---|
| | | | | $\underline{\mathbf{e}}_1$ | | | | |
| 0.0000 | 0.0000 | 0.0000 | 0.8880 | 0.0000 | 0.0000 | 0.0560 | 0.0000 | 0.0560 |
| | | | | $\underline{\mathbf{e}}_2$ | | | | |
| 0.0000 | 0.0011 | 0.0000 | 0.0000 | 0.0000 | 0.9624 | 0.0182 | 0.0000 | 0.0182 |
| | | | | $a\underline{\mathbf{e}}_1 + b\underline{\mathbf{e}}_2$ | | | | |
| 0.0000 | 0.0008 | 0.0000 | 0.1994 | 0.0000 | 0.7394 | 0.0266 | 0.0000 | 0.0266 |
| | | | | $\underline{\mathbf{e}}_3$ | | | | |
| 1.0000 | 0.0000 | 0.0000 | 0.0000 | 0.0000 | 0.0000 | 0.0000 | 0.0000 | 0.0000 |

**Table 3.3** The vector-based QTAIM and stress tensor concepts that we have developed with references listed

| Vector-based | Definition | References |
|---|---|---|
| $\rho(\mathbf{r_b})$ QTAIM facile direction | $\underline{\mathbf{e}}_2$ of the Hessian of $\rho(\mathbf{r_b})$ | [13, 14, 17–22] |
| $\rho(\mathbf{r_b})$ QTAIM least preferred direction | $\underline{\mathbf{e}}_1$ of the Hessian of $\rho(\mathbf{r_b})$ | [13, 14, 17–22] |
| Response | $\beta = arccos(\underline{\mathbf{e}}_2 \cdot \underline{\mathbf{y}})$ | [16, 19–21, 23] |
| Stress tensor response | $\beta_\sigma = arccos(\underline{\mathbf{e}}_{1\sigma} \cdot \underline{\mathbf{y}})$ | [16, 19–21, 23] |

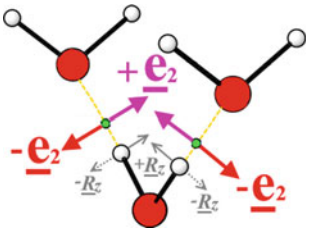


**Fig. 3.1** The $\pm\,\underline{\mathbf{e}}_2$ eigenvectors of the hydrogen-bond *BCPs* of ice Ic, indicated by the green spheres and along with the directions of the rotational ($\pm\,\boldsymbol{R}_z$) projections. The hydrogen-bonds are indicated by the yellow dashed lines. The $\pm\,\underline{\mathbf{e}}_3$ eigenvector (not shown) correspond to alignment with the hydrogen-bond path, the $\pm\,\underline{\mathbf{e}}_1$ eigenvector (not shown) is perpendicular to both the $\pm\,\underline{\mathbf{e}}_2$ and $\pm\,\underline{\mathbf{e}}_3$ eigenvectors

where GBL refers to the inter-nuclear separation with the minor and major radii of bonding curvature specified by the directions of $\underline{\mathbf{e}}_2$ and $\underline{\mathbf{e}}_1$ respectively [7].

This idea that the most preferred motion of the electrons coincides with the motion of the atoms was earlier proposed [8] that was then confirmed [9, 10] by considering the

behavior of the 'easy' direction ($\underline{\mathbf{e}}_2$ eigenvector) that indeed the direction in which electrons find it easiest to move coincided with the preferred direction of motion of the atoms [9].

## 3.2 The Bond-Path Framework: Lack of Accordance of the Motion of $\rho(\mathbf{r_b})$ and Nuclei for Bond Torsion

*In this section we explain why we introduce the bond-path framework.*

The definition of the *BCP* ellipticity ε arises from this elliptical shape and is given by the relation for the ellipticity $\varepsilon = |\lambda_1|/|\lambda_2| - 1$. For bond-paths that comprise with cylindrical symmetry, the two negative curvatures of $\rho(\mathbf{r})$ at the *BCP*, i.e., the $\lambda_1$ and $\lambda_2$ eigenvalues are of equal magnitude: $|\lambda_1| = |\lambda_2|$. A bond-path with non-zero ellipticity $\varepsilon > 0$ will possess an ellipse shaped cross-section with the long and short axes coincident with the $\underline{\mathbf{e}}_2$ and $\underline{\mathbf{e}}_1$ eigenvectors respectively. Consequently, since the eigenvalues are ordered, the charge density will be preferentially accumulated along the direction associated with the $\lambda_2$ eigenvalue, that is the $\underline{\mathbf{e}}_2$ eigenvector compared with the $\lambda_1$ eigenvalue. An example of a *BCP* with $\varepsilon > 0$ is provided for an ice VIII O---O *BCP*, see Fig. 3.2.

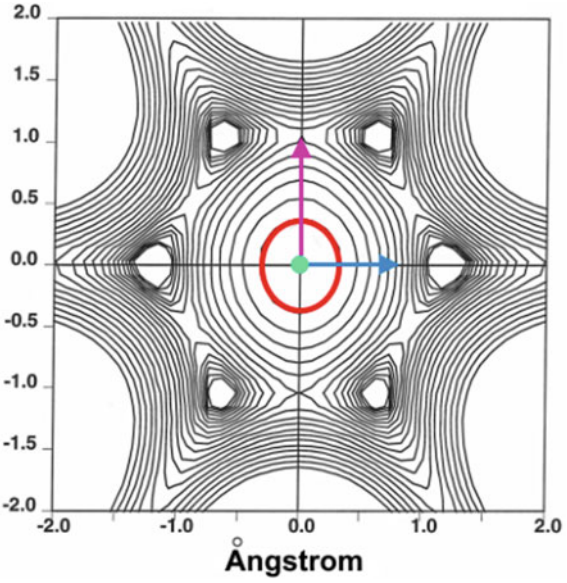


**Fig. 3.2** The plane bisecting an ice VIII O--O *BCP* (green sphere) bond-path. The ellipse (red) in the total electronic charge density $\rho(\mathbf{r})$ encloses the *BCP* and is associated with the most $\underline{\mathbf{e}}_2$ eigenvector (magenta arrow) and least $\underline{\mathbf{e}}_1$ eigenvector (cyan arrow) preferred directions of $\rho(\mathbf{r})$ [2]

The most facile, i.e., preferred direction of electron charge density accumulation determines the direction of bond motion [11] from the electron-preceding perspective where a change in the electronic charge density distribution that defines a chemical bond results in a change in atomic positions [12]. The torsion of a bond-path within QTAIM is quantified using the $\{\underline{\mathbf{e}}_1, \underline{\mathbf{e}}_2, \underline{\mathbf{e}}_3\}$ *bond-path framework* as the set of orthogonal $\underline{\mathbf{e}}_1$, $\underline{\mathbf{e}}_2$ and $\underline{\mathbf{e}}_3$ eigenvectors of the two bonded nuclei that comprise the torsional bond-path.

The directional properties derived from $\rho(\mathbf{r_b})$ at a *BCP* do not always move in accordance with the nuclei [13]. During a bond-path torsion the ellipticity ε of the torsional *BCP* attains a minimum value (i.e., $\lambda_2 \approx \lambda_1$). This simple physical connection between the ellipticity ε and bond-path torsion $\alpha$ constitutes a physically and chemically intuitive quantity where bond-path torsion plays a key role. Instead, the response $\beta$ of $\rho(\mathbf{r_b})$ to the deformation of the nuclear skeleton may depend on the electronic state or nature of the nuclei involved. A visualization of the most preferred response $\beta$ and least preferred response $\beta^*$ along with the ellipticity ε is provided in Fig. 3.3.

The response $\beta$ is defined to be the angle formed by the eigenvector $\underline{\mathbf{e}}_2$ of the torsional *BCP* projected on the *x*-*y* plane.

The response $\beta$ is defined as:

$$\beta = arc\cos(\underline{\mathbf{e}}_2 \cdot \underline{\mathbf{y}}) \tag{3.6}$$

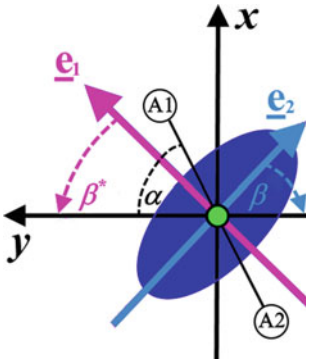


**Fig. 3.3** The blue ellipse represents the $\rho(\mathbf{r})$ of the cross-section of a bond-path with an associated *BCP* (green sphere) with non-zero ellipticity ε. The eigenvalues $\lambda_2$ and $\lambda_1$ are associated with the eigenvectors $\underline{\mathbf{e}}_2$ and $\underline{\mathbf{e}}_1$ respectively and represent the lengths of the semi-major and semi-minor axes of the blue ellipse respectively. The most and least preferred directions of $\rho(\mathbf{r})$ are indicated by the $\underline{\mathbf{e}}_2$ and $\underline{\mathbf{e}}_1$ eigenvectors respectively. The $\underline{\mathbf{e}}_3$ eigenvector defines the bond-path and connects the bonded atoms A1 and A2. The angle of mechanical twist $\boldsymbol{\alpha}$ of the methylene group and the most preferred response $\boldsymbol{\beta}$ and the least preferred response $\beta^*$

We will refer to the response $\beta$ as the most preferred (eigenvector) to distinguish it from the least preferred response $\beta^*$:

$$\beta^* = arc\cos(\underline{\mathbf{e}}_1 \cdot \mathbf{y}) \tag{3.7}$$

where $\underline{\mathbf{y}}$ is a reference vector of unit length along the **y**- axis of the global coordinate frame shown in Fig. 3.2, where it is assumed that the corresponding global frame z-axis coincides with the $\underline{\mathbf{e}}_3$ eigenvector.

### 3.2.1 *Torsion of Biphenyl: Detachment and Reattachment of the Bond-Path Framework*

An earlier investigation of biphenyl used the response $\pm\beta$ of the bond-path framework to a torsion $\alpha$ biphenyl [14]. The reaction coordinate $\alpha$, varied within the range $0.0° \leq \alpha \leq 180.0°$, the corresponding response $\pm\beta$ to this torsion $\alpha$ was $-90.0° \leq -\beta \leq -50.0°$ and $50.0° \leq +\beta \leq 90.0°$, see Fig. 3.4. The planar conformation $\alpha = 0.0°$, $\beta = -90.0°$ therefore corresponds to the maximum detachment of the $\underline{\mathbf{e}}_1$-$\underline{\mathbf{e}}_2$-$\underline{\mathbf{e}}_3$ bond-path framework from the biphenyl molecular graph. Conversely, the minimum detachment of the $\underline{\mathbf{e}}_1$-$\underline{\mathbf{e}}_2$-$\underline{\mathbf{e}}_3$ bond-path framework occurs for $\alpha = 90.0°$, where $\beta = \pm 50.0°$. As a consequence, the reaction coordinate $0.0° \leq \alpha \leq 180.0°$ describes the increase in attachment of the $\underline{\mathbf{e}}_1$-$\underline{\mathbf{e}}_2$-$\underline{\mathbf{e}}_3$ bond-path framework from the minimum at $\alpha = 0.0°$ (= 180°) to the maximum at $\alpha = 90.0°$. The expected variation, of the form $\beta \approx \alpha/2 - 90.0°$, from linear dependency between the reaction coordinate $\alpha$ and the response $\beta$ was examined. A linear variation of $\beta$ with the torsion coordinate $\alpha$ was expected since the torsional *BCP* is positioned mid-way along the torsional C4-C7 *BCP* bond-path, see the red line in Fig. 3.3. Subtle indications of a departure from the initial slope at $\alpha \approx 20°$ coincide can be explained by the annihilation of the H---H *BCP*s that correspond to the slower rate of re-attachment of the $\underline{\mathbf{e}}_1$-$\underline{\mathbf{e}}_2$-$\underline{\mathbf{e}}_3$ bond-path framework for $20.0° < \alpha < 90.0°$ and were explained by the loss of the H---H *BCP*s.

### 3.2.2 *The Photo-Isomerization of the Retinal Chromophore*

Recently, we demonstrated that the eigenvectors $\underline{\mathbf{e}}_2$ and $\underline{\mathbf{e}}_1$ were the most and least preferred directions of torsion respectively, using the photo-isomerization of the retinal chromophore subject to a torsion $\pm\alpha$ [15]. Therefore, the response $\beta$, relates to the degree of detachment of the $\underline{\mathbf{e}}_1$ and $\underline{\mathbf{e}}_2$ eigenvectors from the containing nuclear skeleton. Smaller values of $\beta$ indicate a greater degree of *alignment* (attachment) of the $\underline{\mathbf{e}}_1$ and $\underline{\mathbf{e}}_2$ eigenvectors with the containing nuclear skeleton or peptide backbone resulting in a greater responsiveness to changes in the nuclear skeleton.

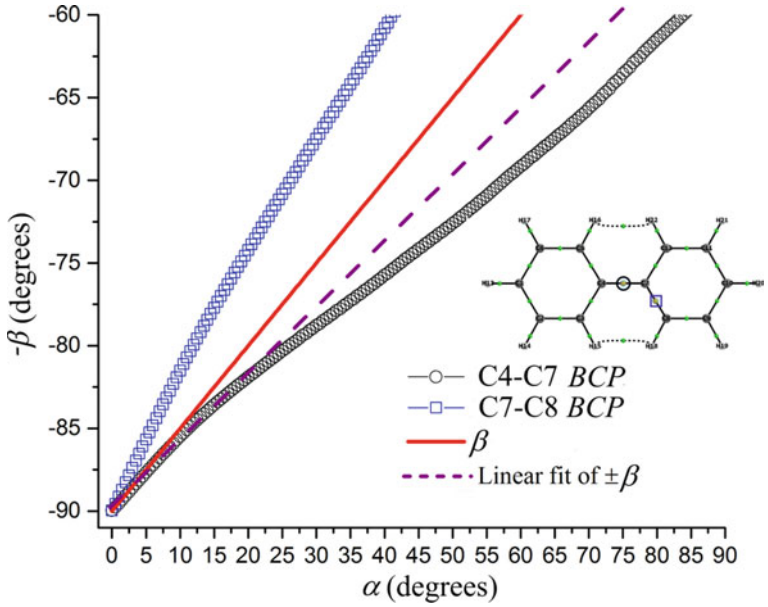


**Fig. 3.4** The variation of the reaction coordinate α with the QTAIM response $-\beta$ of the total electronic charge density $\rho(\mathbf{r}_b)$ for the torsional C4-C7 *BCP* and the neighboring C7-C8 *BCP*, shown in the inset figure. The red line has a slope with the relation $\beta = \alpha/2 - 90.0°$. The inset figure displays the biphenyl molecular graph, undecorated green and red spheres represent the bond critical points (*BCP*s) and ring critical points (*RCP*s) respectively. The torsional C4-C7 *BCP* is subjected to a torsion α, where $0.0° \leq \alpha \leq 180.0°$

The QTAIM response to a torsion $\pm\,\alpha$ increases at a faster rate for the preferred direction $\pm\,\beta$ of torsion though the conical intersection (CI) seam thus providing an alternative method to characterize the asymmetry of the $S_1$ potential energy surface, see Fig. 3.5.

### *3.2.3 The QTAIM Interpreted Ramachandran Plot*

The creation of the conventional Ramachandran plot ($\phi$-$\psi$) uses the *torsion* angles ($\phi$-$\psi$) of the backbone nuclear skeleton, therefore it would seem sensible to explore the idea of the response $\beta$ that also measures the similar *angular* detachment of the $\underline{\mathbf{e}}_1$ and $\underline{\mathbf{e}}_2$ eigenvectors to create a QTAIM interpretation of the Ramachandran plot ($\phi$-$\psi$), see Fig. 3.6.

For closed-shell *BCP*s we use the same ordering conventions used to construct Ramachandran angles $\phi$ and $\psi$, see Fig. 3.3, replacing the atomic geometry reference vector $\underline{\mathbf{y}}$, see Eqs. (3.8) and (3.9), with a unit reference vector $\underline{\boldsymbol{n}}$ where $\underline{\boldsymbol{n}} = \underline{\boldsymbol{n}}_1$

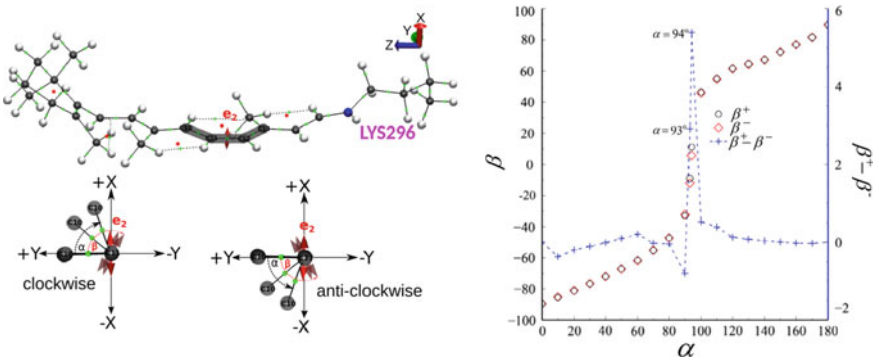


**Fig. 3.5** The molecular graph of the 11-cis retinal (left-top) for the torsion C11-C12 *BCP* is highlighted. Fragments extracted from the molecular graph viewed down the torsional bond. The computed 'clockwise' (+α), below left and 'anticlockwise' (–α) torsions (left-bottom). The torsion α occurs about the mid-point of the $C_{11}$-$C_{12}$ bond, to reach the **PSBT** isomer the C11-C12 bond vis two directions; 'clockwise' and 'anti-clockwise' corresponding to (+α) and (–α) respectively. The variation of the response $\beta^+$ (black circle) and $\beta^-$ (red diamond) with the torsion coordinate α for a rotation about the torsional C11-C12 *BCP* (right). The plot of the difference $(\beta^+ - \beta^-)$ (blue plot) for torsion coordinate α is presented on the right-hand *y*-axis. The conical intersection (CI) point is located between $\alpha = 93°$ and $\alpha = 94°$

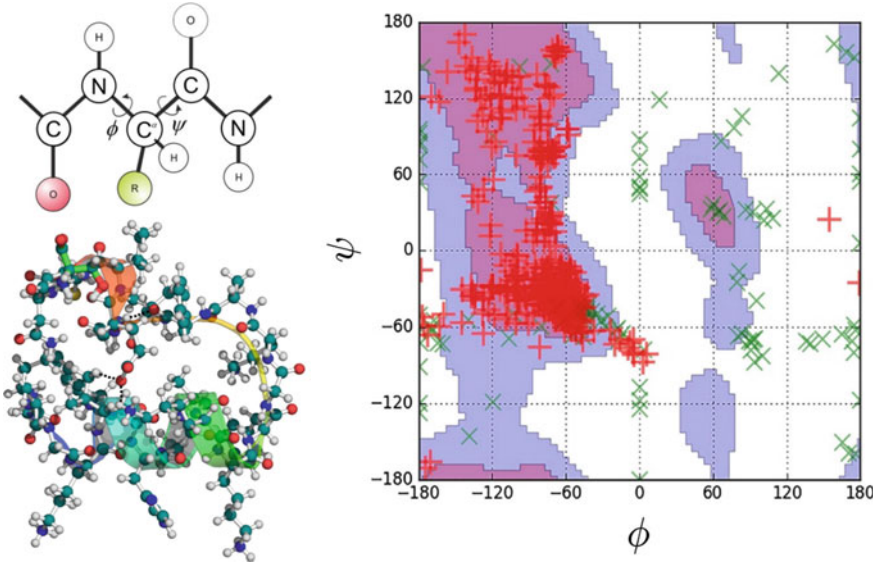


**Fig. 3.6** Conventional Ramachandran plot ($\phi-\psi$) angles $\phi$ and $\psi$ for the peptide backbone (left-top). Ball and stick renderings for the energy minimum conformer of the magainin-2 peptide (left-bottom). The Ramachandran plot ($\phi$-$\psi$) of 29 conformers of the magainin-2 peptide are presented in (right), the magenta, blue and white regions correspond to the 'favored', 'allowed' (73), 'forbidden' (76) and beta-sheet (45) regions, with the numbers of points given in the parenthesis, the green 'x' and red ' + ' indicate the glycine amino acid monomers and remaining amino acids respectively

and $\underline{\boldsymbol{n}} = \underline{\boldsymbol{n}}_{\mathbf{2}}$ for $\phi$ and $\psi$ respectively. This vector $\underline{\boldsymbol{n}}$ is derived from the local atomic geometry, specifically the normal vector to a plane through three atomic positions, see Fig. 3.3.

For closed-shell *BCP*s the most preferred responses $\beta_\phi$ and $\beta_\psi$ are defined with $\underline{\boldsymbol{v}} = \underline{\mathbf{e}}_{\mathbf{2}}$ as:

$$\beta_\phi = \arccos(\underline{\boldsymbol{v}} \cdot \boldsymbol{n}_1), \quad \beta_\psi = \arccos(\underline{\boldsymbol{v}} \cdot \underline{\boldsymbol{n}}_2) \tag{3.8}$$

The least preferred responses ${\beta_\phi}^*$ and ${\beta_\psi}^*$ are defined with $\underline{\boldsymbol{v}} = \underline{\mathbf{e}}_{\mathbf{1}}$ as:

$$\beta_\phi^* = \arccos(\underline{\boldsymbol{v}} \cdot \underline{\boldsymbol{n}}_1), \quad \beta_\psi = \arccos(\underline{\boldsymbol{v}} \cdot \underline{\boldsymbol{n}}_2) \tag{3.9}$$

Weaker interactions with longer bond-paths such as H--O/H---O *BCP*s and H---H *BCP*s closed-shell *BCP*s are likely to possess a greater *range* of $\beta$ values than rigid backbone shared-shell *BCP*s including values of $\beta$ closer to 0.0°. Conversely, larger values of $\beta$ indicate a greater degree of *detachment* of the $\underline{\mathbf{e}}_{\mathbf{1}}$ and $\underline{\mathbf{e}}_{\mathbf{2}}$ eigenvectors from the containing nuclear skeleton. The more confined and less flexible backbone shared-shell *BCP*s are likely to possess larger values of $\beta$, a known exception to this is the glycine amino acid [16] (Fig. 3.7).

The QTAIM interpretation of the Ramachandran plot $\{(\beta_\phi, {\beta_\phi}^*)\text{-}(\beta_\psi, {\beta_\psi}^*)\}$ is created from a set of 29 magainin-2 peptide conformers, see Fig. 3.8. The QTAIM Ramachandran plot $\{(\beta_\phi, {\beta_\phi}^*)\text{-}(\beta_\psi, {\beta_\psi}^*)\}$ comprised regions corresponding to the most-preferred and least-preferred regions using the $\underline{\mathbf{e}}_{\mathbf{2}}$ and $\underline{\mathbf{e}}_{\mathbf{1}}$ eigenvectors of all the back-bone *BCP*s in analogy with the 'favored' and 'allowed' regions of the conventional Ramachandran plot ($\phi$-$\psi$). The glycine amino acid monomer was

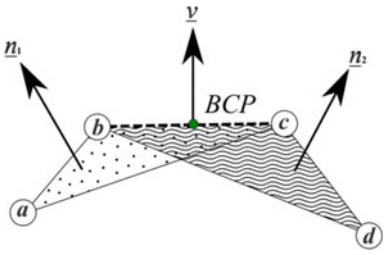


**Fig. 3.7** The schematic for defining the QTAIM analogous Ramachandran angles ($\phi$-$\psi$), i.e., the responses ($\beta_\phi$,$\beta_\psi$) and (${\beta^*}_\phi$,${\beta^*}_\psi$), for the closed-shell *BCP*s. The QTAIM most preferred response ($\beta_\phi$,$\beta_\psi$) and the least preferred response (${\beta^*}_\phi$,${\beta^*}_\psi$) are defined using a vector $\underline{\boldsymbol{v}}$ and unit-length plane normal vectors $\underline{\boldsymbol{n}}_{\mathbf{1}}$ and $\underline{\boldsymbol{n}}_{\mathbf{2}}$ in planes defined by atoms *a*, *b*, *c* and *b*, *c*, *d* respectively. The plane normal vectors $\underline{\boldsymbol{n}}_{\mathbf{1}}$ and $\underline{\boldsymbol{n}}_{\mathbf{2}}$ are used as reference directions analogously to the unit vector $\underline{\mathbf{y}}$ and define $\phi$ and $\psi$ respectively, see Fig. 3.3, Eqs. (3.6) and (3.7). We select atoms a and *d*, the closest backbone shared-shell bonded atoms to atoms *b* and *c* respectively that comprise the *b*−*c* bond-path of the *b*-*c* *BCP*. If the *a*-*b* bond-path length is greater than *c*-*d* bond-path length, the order of the atom labels *a*-*b*-*c*-*d* is reversed

found to occupy the largest extent of the QTAIM Ramachandran plot compared with the remaining backbone peptide bonds. The facile character of the glycine amino acid monomer indicated by the response $\{(\beta_\phi, \beta_\phi{}^*)\text{-}(\beta_\psi, \beta_\psi{}^*)\}$ was greater than for the other amino acids and was comparable to that of the hydrogen bonding, explaining the flexibility of the magainin-2 backbone. The hybrid QTAIM-Ramachandran plots highlight how the glycine amino acid monomer largely occupies the 'forbidden' region on the Ramachandran plot. In addition, the new hybrid QTAIM-Ramachandran plots contained regions that can be associated with concepts familiar from the conventional Ramachandran plot such as the 'forbidden', 'allowed', 'beta sheet' inside of the 'allowed' regions. For example, we created the hybrid QTAIM-Ramachandran plots of the backbone shared-shell *BCPs* for the complete set of magainin-2 peptide molecular graphs $\{(\beta_\psi, \beta_\psi{}^*)\text{-}\psi\}$ and $\{\phi\text{-}(\beta_\phi, \beta_\phi{}^*)\}$ in Figs. 3.9 and 3.10 respectively. We additionally created the corresponding mixed hybrid QTAIM-Ramachandran plots $\{\phi\text{-}(\beta_\psi, \beta_\psi{}^*)\}$ and $\{(\beta_\phi, \beta_\phi{}^*)\text{-}\psi\}$ in Figs. 3.11 and 3.12 respectively.

The QTAIM interpreted Ramachandran plot ($\phi$-$\psi$) comprises a non-trivial mapping between the pure QTAIM interpreted Ramachandran plot $\{(\beta_\phi, \beta_\phi{}^*)\text{-}(\beta_\psi, \beta_\psi{}^*)\}$ values of the backbone shared-shell *BCP*s and the conventional Ramachandran plot ($\phi$-$\psi$). This mapping was non-trivial because the $\{(\beta_\phi, \beta_\phi{}^*)\text{-}(\beta_\psi, \beta_\psi{}^*)\}$ values that are defined by the $\underline{\mathbf{e}}_2$ and $\underline{\mathbf{e}}_1$ eigenvectors are derived from $\rho(\mathbf{r_b})$ are *independent* of the definition of the $\phi$ and $\psi$ angles of the Ramachandran plot ($\phi$-$\psi$) that are based solely on atomic geometries. The pure QTAIM interpreted Ramachandran plot $\{(\beta_\phi, \beta_\phi{}^*)\text{-}(\beta_\psi, \beta_\psi{}^*)\}$ created from all of the backbone shared-shell *BCP*s

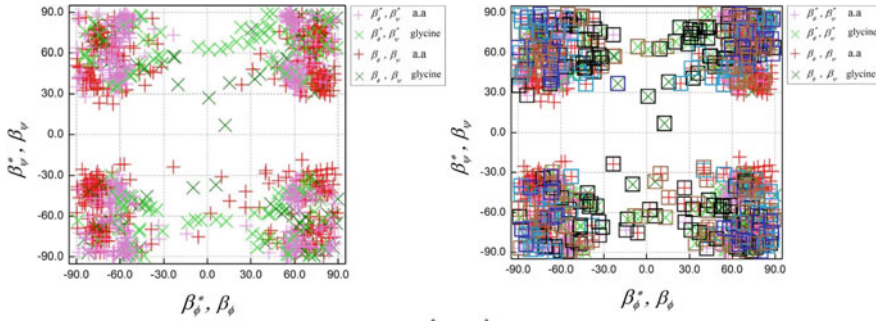


**Fig. 3.8** QTAIM interpreted Ramachandran plots $\{(\beta_\phi, \beta_\phi{}^*)\text{-}(\beta_\psi, \beta_\psi{}^*)\}$ (left panel) of the backbone shared-shell *BCPs* for the set of 29 magainin-2 peptide molecular graphs. When the nomenclature (x-y) is used the "-" is to be interpreted as a hyphen and not a subtraction sign, the ',' indicates that the bracketed quantities are superimposed onto the same axes. The pale green crosses indicate the $\beta_\phi{}^*$ and $\beta_\psi{}^*$ (the least preferred responses), the dark green crosses represent the $\beta_\phi$ and $\beta_\psi$ (the most preferred responses) for the glycine amino acid *BCP*s. The corresponding quantities for the remaining amino acids are given by the pink ($\beta_\phi{}^*$ and $\beta_\psi{}^*$) and red ($\beta_\phi$ and $\beta_\psi$) pluses respectively. In the right panel we superimpose on the $\{(\beta_\phi, \beta_\phi{}^*)\text{-}(\beta_\psi, \beta_\psi{}^*)\}$ plot the black, brown, pale blue and dark blue squares that indicate the 'forbidden', 'allowed', 'beta sheet' inside of the 'allowed' region but close to beta-sheet region from the conventional Ramachandran plot ($\phi$-$\psi$) respectively

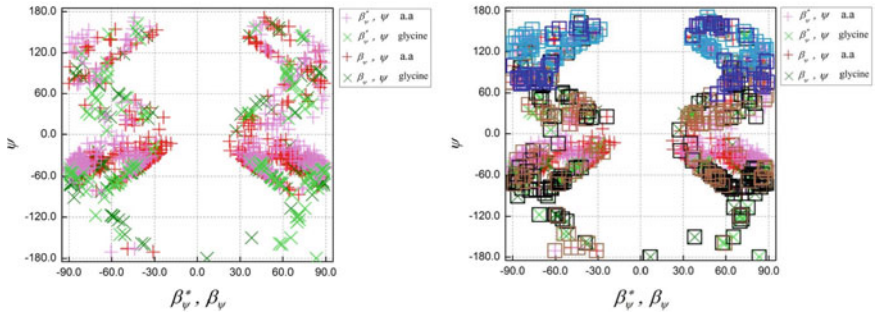

**Fig. 3.9** Hybrid QTAIM interpreted Ramachandran plots $\{(\beta_\psi, \beta_\psi{}^*)\text{-}\psi\}$ of the backbone shared-shell *BCPs* for the complete set of magainin-2 peptide molecular graphs are presented, see the caption of Fig. 3.7 for further details

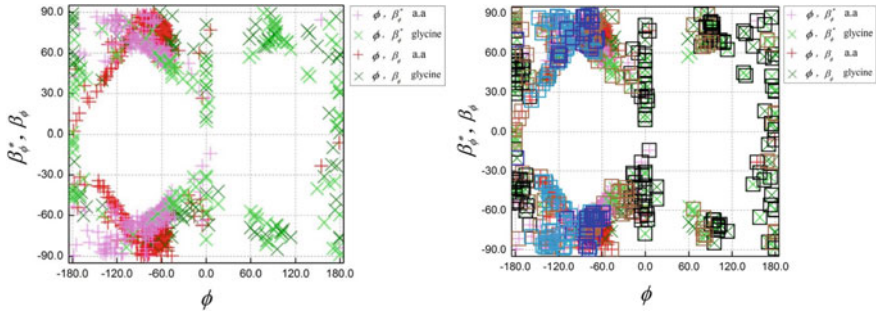

**Fig. 3.10** Hybrid QTAIM interpreted Ramachandran plots $\{\phi\text{-}(\beta_\phi, \beta_\phi{}^*)\}$ of the backbone shared-shell *BCPs* for the complete set of magainin-2 peptide molecular graphs, see the figure caption of Fig. 3.8 for further details

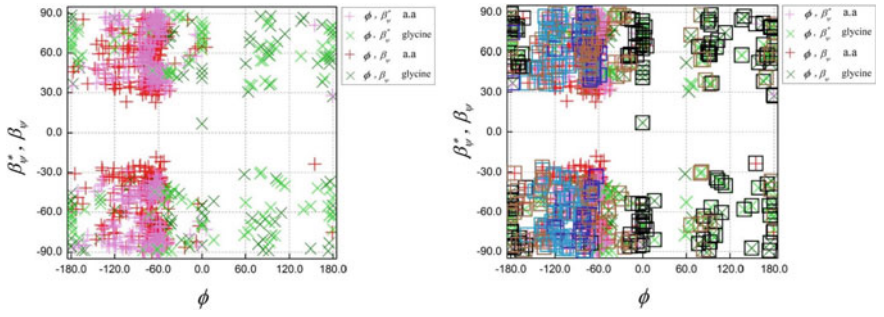

**Fig. 3.11** Mixed hybrid QTAIM interpreted Ramachandran plots $\{\phi\text{-}(\beta_\psi, \beta_\psi{}^*)\}$ of the backbone shared-shell *BCPs* for the complete set of magainin-2 peptide molecular graphs, see the figure caption of Fig. 3.8 for further details

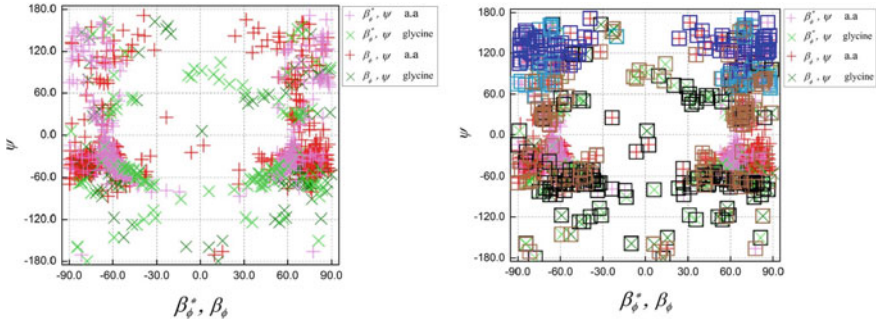


**Fig. 3.12** Mixed hybrid QTAIM interpreted Ramachandran plots $\{(\beta_\phi, \beta_\phi{}^*)\text{-}\psi\}$ of the backbone shared-shell *BCPs* for the complete set of magainin-2 peptide molecular graphs, see the figure caption of Fig. 3.11 for further details

does however contain unoccupied regions, demonstrating the effect of the peptide backbone in restricting and confining the $\underline{\mathbf{e}}_2$ and $\underline{\mathbf{e}}_1$ eigenvectors of the backbone shared-shell *BCP*s that creates unoccupied regions in the pure QTAIM interpreted Ramachandran plot $\{(\beta_\phi, \beta_\phi{}^*)\text{-}(\beta_\psi, \beta_\psi{}^*)\}$.

### 3.2.4 *Explanation of the $(\beta_\phi\text{-}\beta_\psi)$ and $(\beta_\phi{}^*\text{-}\beta_\psi{}^*)$ of the Closed-Shell H--O/H---O BCPs and H---H BCPs*

The H--O *BCP*s (note two dashes "--") that possess a degree of covalent character $(H(\mathbf{r_b}) < 0)$ all possess greater values of the stiffness S than do the purely electrostatic H---O *BCP*s or H---H *BCP*s (note three dashes "---") that possess $H(\mathbf{r_b}) > 0$, in line with expectations from physical intuition, see the square symbols, see Fig. 3.13 and Chap. 2.

The distribution of data points for $(\beta_\phi\text{-}\beta_\psi)$ and $(\beta_\phi{}^*\text{-}\beta_\psi{}^*)$ is complementary for the H--O/H---O *BCP*s and H---H *BCP*s. Therefore regions that are characteristic for $(\beta_\phi\text{-}\beta_\psi)$ and $(\beta_\phi{}^*\text{-}\beta_\psi{}^*)$, that can be seen examination of Fig. 3.13 and also Eqs. (3.7) and (3.8). There is a clustering of the $(\beta_\phi{}^*\text{-}\beta_\psi{}^*)$ in the vicinity of $\beta_\phi{}^* = 0.0°$ for the H--O *BCP*s and H---O *BCP*s. This finding is explained by the inherent asymmetry present in the construction of the $(\beta_\phi\text{-}\beta_\psi)$ and $(\beta_\phi{}^*\text{-}\beta_\psi{}^*)$; the bond-path length of the first nearest neighbor shared-shell *BCP* used in the construction of $\beta_\phi$ is shorter than that for $\beta_\psi$, see Fig. 3.7. The nearest neighbors, either side, of the H---H *BCP*s are generally shared-shell C-H *BCP*s consequently the $(\beta_\phi\text{-}\beta_\psi)$ and $(\beta_\phi{}^*\text{-}\beta_\psi{}^*)$ values for the H---H *BCP*s are distributed rather more symmetrically than is the case for the H--O *BCP*s and H---O *BCP*s,

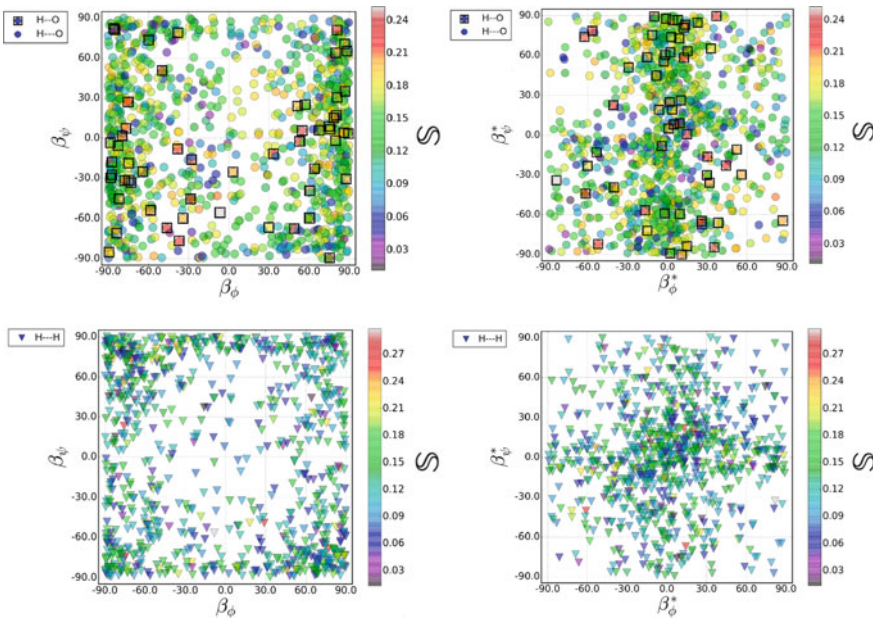


**Fig. 3.13** Plots of the $\beta_\phi$ versus $\beta_\psi$ with the distribution of stiffness S of the H--O *BCP*s, H---O *BCP*s (top-left) for the molecular graph of complete set of twenty-nine conformers of the magainin-2 peptides. The corresponding quantity for the $\beta_\phi{}^*$ versus $\beta_\psi{}^*$ of the H--O *BCP*s, H---O *BCP*s (top-right). The data points surrounded by squares represent values of the total local energy density $H(\mathbf{r_b}) < 0$. Plots of the responses $\beta_\phi$ versus $\beta_\psi$ with the distribution of stiffness S of the H---H *BCP*s (bottom-left). The corresponding quantity for the least preferred responses ($\beta_\phi{}^*$-$\beta_\psi{}^*$) of the H---H *BCP*s (bottom-right)

In addition, greater values of the stiffness S the (stronger) H--O *BCP*s are associated with values of $\beta_\phi{}^*$ located closer to $\beta_\phi{}^* = 0.0°$ than for the (purely electrostatic) H--O *BCP*s. Similarly, the stiffness S values of the H---O *BCP*s are generally greater than those of the very long and weak H–-H *BCP*s.

The absence of steric hindrance of the glycine amino acid results in a broad scatter of $\{(\beta_\phi,\beta_\phi{}^*)$-$(\beta_\psi,\beta_\psi{}^*)\}$values including lower values of $\beta_\psi$. This explains why the presence of four glycine amino acid monomers **G**I**G**KWLHSAKKF**G**KAFV**G**EIMNS, results in the Magainin-2-2 peptide backbone being more flexible and therefore more prone to folding than the backbone of the lycosin peptide conformer RK**G**WFKAMKSIAKFIAKEKLKEHL where linear backbone conformations exist.

## 3.3 Summary

We have presented the initial accidental discovery that led to the future development of Next Generation QTAIM (NG-QTAIM) by comparing the projected density of states (PDOS) phonon modes of vibration of the highly ordered cubic ice (Ic) with the Hessian of $\rho(\mathbf{r})$ eigenvectors. This 'experiment' in combining the dynamical and static properties of highly ordered cubic ice provided an important demonstration of the need for a much more in-depth understanding of the eigenvectors that would potentially provide a wealth of new chemical insight, see Table 3.3.

Further useful comparisons of the Hessian of $\rho(\mathbf{r_b})$ eigenvectors and the PDOS are extremely limited, consequently, this analysis is only applicable to very simple spectra produced by using the PDOS in addition to using a highly symmetrical structure and therefore this analysis is not useful in practice. In addition, the analysis could not directly relate the PDOS and the Hessian of $\rho(\mathbf{r_b})$ eigenvectors due to the using the atomic positions and *BCP*s respectively, consequently a linear combination $a\underline{\mathbf{e}}_{\mathbf{1}} + b\underline{\mathbf{e}}_{\mathbf{2}}$ of the least facile and most facile eigenvectors were required.

The bond-path framework arose from the realization that for a bond subjected to a torsion there is a lack of accordance of the motion of $\rho(\mathbf{r_b})$ and nuclei as the torsion progresses. We discovered that during the torsion process the $\underline{\mathbf{e}}_{\mathbf{1}}$ and $\underline{\mathbf{e}}_{\mathbf{2}}$ eigenvectors at the *BCP* can detach and reattach with the nuclear skeleton. This enabled new insights to be obtained the role of the H---H bonding into the topological stability of biphenyl.

We were to use the bond-path framework to quantify the asymmetry of the potential energy surface (PES) and probe the conical intersection (CI) associated with the 11-cis retinal torsion to separate out the properties of the ground state $S_0$ and first excited state $S_1$.

The creation of a QTAIM interpreted Ramachandran plot uniquely enabled the creation of such a plot for closed-shell *BCP*s (H---H, H---O and H--O) in addition to shared-shell *BCP*s. Benefits of the QTAIM Ramachandran plot:

- The ability to explore the forbidden regions of the conventional Ramachandran plot due to the inclusion of closed-shell *BCP*s (H--O/H---O hydrogen-bond *BCP*s and H---H *BCP*s).
- Quantification of the steric hindrance of the glycine amino acid that is known to be lower than for other amino acids, in terms of lower values of $\beta_{\psi}$ that are comparable to that of the hydrogen bonding.
- Provided an explanation as to why the magainin-2 peptide backbone, that comprises four glycine acid monomers, is highly flexible compared with the larger lycosin peptide that contains only one glycine acid monomer.

The limitation of the bond-path framework is only being able to consider situations where bond torsions about a *BCP*. This limitation is overcome in Chap. 4 where we introduce the bond-path framework *set*.

**Target learning outcomes:**

- Understand the relationship between the projected density of states (PDOS) and QTAIM.
- Understand the consequences of the lack of accordance of the motion of $\rho(\mathbf{r_b})$ and nuclei for bond torsion.
- Detachment and reattachment of the bond-path framework via the torsion of the bridging C-C *BCP* of biphenyl.
- Differences in the QTAIM properties at the conical intersection (C.I) for the photo-isomerization of the retinal chromophore.
- Understand the QTAIM interpreted Ramachandran plot.
- Explanation of the ($\beta_\phi$-$\beta_\psi$) and ($\beta_\phi$*-$\beta_\psi$*) of the closed-shell H--O/H---O *BCP*s and H---H *BCP*s.

## 3.4 Further Reading

The first systematic attempt to understand the amino acid sequences and arrangements was carried out by Ramachandran and co-workers who created the Ramachandran plot [24].

The review of Harekrushna Sahoo presents recent advancements in optical techniques of Förster resonance energy transfer (FRET) in association that provides a way to understand the detailed mechanisms in different biological systems at the molecular level [25].

## References

1. Jenkins S, Morrison I (2001) The dependence on structure of the projected vibrational density of states of various phases of ice as calculated by ab initio methods. J Phys Condens Matter 13:9207–9229
2. Jenkins S (1999) Ab initio studies of the static and dynamic properties of phases of H2O ICE. University of Salford
3. Ackland GJ, Warren MC, Clark SJ (1997) Practical methods in ab initio lattice dynamics. J Phys Condens Matter 9:7861–7872
4. Dolling G (1976) The calculation of phonon frequencies. In: Gilat G (ed) Methods in computational physics: advances in research and applications, vol 15. Elsevier, pp 1–40
5. Jenkins S, Kirk SR, Cote AS, Ross DK, Morrison I (2003) Dependence of the normal modes on the electronic structure of various phases of ice as calculated by ab initio methods. Can J Phys 81(7):225–231

6. Jenkins S, Heggie MI (2000) Quantitative analysis of bonding in 90° partial dislocation in diamond. J Phys Condens Matter 12:10325–10333
7. Jenkins S, Morrison I (2000) The chemical character of the intermolecular bonds of seven phases of ice as revealed by ab initio calculation of electron densities. Chem Phys Lett 317:97–102
8. Bone RGA, Bader RFW (1996) Identifying and analyzing intermolecular bonding interactions in van der Waals molecules. J Phys Chem 100:10892–10911
9. Jenkins S, Heggie MI (2000) Quantitative analysis of bonding in 90° partial dislocation in diamond. J Phys Condens Matter 12:10325–10333
10. Ayers PW, Jenkins S (2009) An electron-preceding perspective on the deformation of materials. J Chem Phys 130:154104–154104–11
11. Li JH, Huang WJ, Xu T, Kirk SR, Jenkins S (2018) Stress tensor eigenvector following with next-generation quantum theory of atoms in molecules. Int J Quantum Chem 119:e25847
12. Nakatsuji H (1974) Common nature of the electron cloud of a system undergoing change in nuclear configuration. J Am Chem Soc 96:24–30
13. Jenkins S, Blancafort L, Kirk SR, Bearpark MJ (2014) The response of the electronic structure to electronic excitation and double bond torsion in fulvene: a combined QTAIM, stress tensor and MO perspective. Phys Chem Chem Phys 16:7115–7126
14. Jenkins S, Maza JR, Xu T, Jiajun D, Kirk SR (2015) Biphenyl: A stress tensor and vector-based perspective explored within the quantum theory of atoms in molecules. Int J Quantum Chem 115:1678–1690
15. Maza JR, Jenkins S, Kirk SR (2016) 11-cis retinal torsion: a QTAIM and stress tensor analysis of the S1 excited state. Chem Phys Lett 652:112–116
16. Momen R, Azizi A, Wang L, Ping Y, Xu T, Kirk SR, Li W, Manzhos S, Jenkins S (2017) The role of weak interactions in characterizing peptide folding preferences using a QTAIM interpretation of the Ramachandran plot ($\phi$-$\psi$). Int J Quantum Chem 118:e25456
17. Figueredo FA, Maza JR, Kirk SR, Jenkins S (2014) Quantum topology phase diagrams for the cis- and trans-isomers of the cyclic contryphan-Sm peptide. Int J Quantum Chem 114:1697–1706
18. Huan G, Xu T, Momen R, Wang L, Ping Y, Kirk SR, Jenkins S, van Mourik T (2016) A QTAIM exploration of the competition between hydrogen and halogen bonding in halogenated 1-methyluracil: water systems. Chem Phys Lett 662:67–72
19. Hu MX, Xu T, Momen R, Huan G, Kirk SR, Jenkins S, Filatov M (2016) A QTAIM and stress tensor investigation of the torsion path of a light-driven fluorene molecular rotary motor. J Comput Chem 37:2588–2596
20. Jiajun D, Maza JR, Xu Y, Xu T, Momen R, Kirk SR, Jenkins S (2016) A stress tensor and QTAIM perspective on the substituent effects of biphenyl subjected to torsion. J Comput Chem 37:2508–2517
21. Guo H, Morales-Bayuelo A, Xu T, Momen R, Wang L, Yang P, Kirk SR, Jenkins S (2016) Distinguishing and quantifying the torquoselectivity in competitive ring-opening reactions using the stress tensor and QTAIM. J Comput Chem 37:2722–2733
22. Xu T, Farrell J, Xu Y, Momen R, Kirk SR, Jenkins S, Wales DJ (2016) QTAIM and stress tensor interpretation of the (H2O)5 potential energy surface. J Comput Chem 37:2712–2721
23. Momen R, Azizi A, Wang LL, Ping Y, Xu T, Kirk SR, Li W, Manzhos S, Jenkins S (2017) Exploration of the forbidden regions of the Ramachandran Plot ($\phi$-$\psi$) with QTAIM. 19:26423–26434. https://doi.org/10.1002/qua.25006
24. Ramachandran GN, Ramakrishnan C, Sasisekharan V (1963) Stereochemistry of polypeptide chain configurations. J Mol Biol 7:95–99
25. Sahoo H (2011) Förster resonance energy transfer—a spectroscopic nanoruler: principle and applications. J Photochem Photobiol C Photochem Rev 12:20–30

# Chapter 4
# The NG-QTAIM Interpretation of the Chemical Bond

*In most gardens' the Tiger-lily said, 'they make the beds too soft - so that the flowers are always asleep.'*
*Lewis Carroll*

In this chapter we present the NG-QTAIM representation of the chemical bond, the bond-path framework set $\mathsf{B}$. The bond-path framework set $\mathsf{B}$ is constructed from the $\underline{\mathbf{e}}_1$ and $\underline{\mathbf{e}}_2$ eigenvectors, in contrast to conventional (scalar) QTAIM that is only constructed using the $\underline{\mathbf{e}}_3$ eigenvector. Consequently, $\mathsf{B}$ is much more sensitive to changes in the distribution of the total electronic charge density distribution $\rho(\mathbf{r})$ than is the case for the QTAIM bond-path. In Sect. 4.1 we outline the construction of the bond-path framework set $\mathsf{B}$ and briefly include some of the possible geometrical properties of $\mathsf{B}$. The procedure to calculate the precession $\mathsf{K}$ of $\mathsf{B}$ is described in Sect. 4.2. In Sect. 4.3 we consider the applications of $\mathsf{B}$ that highlight the sensitivity to changes in $\rho(\mathbf{r})$. This includes the infrared active modes of benzene in Sects. 4.3.1–4.3.3. The treatment of strained and unusual bonding environments is accommodated in Sect. 4.4. The provision for including multi-electronic states is detailed in Sect. 4.5. The summary of the chapter is presented in Sect. 4.6 by outlining benefits, limitations and suggestions for further investigations of the ideas introduced. Further reading materials are provided in Sect. 4.7.

**Scientific goals to be addressed:**

- Develop a bonding framework $\mathsf{B}$ in terms of the least/least easy directions of accumulation of $\rho(\mathbf{r})$.
- Develop a directional nature of the chemical bond based on the degree of wrapping $\mathsf{K}$ of $\mathsf{B}$ around the bond-path.to include strained and unusual bonding environments.
- Development a bonding framework $\mathsf{B}$ that is not dependent on relative motion of atoms that includes photochemistry.

© The Author(s), under exclusive license to Springer Nature Singapore Pte Ltd. 2023

S. Jenkins and S. R. Kirk, *Next Generation Quantum Theory of Atoms in Molecules*, Lecture Notes in Chemistry 110, https://doi.org/10.1007/978-981-99-0329-0_4

## 4.1 Construction of the Bond-Path Framework Set: Vector-Based Representation of the Chemical Bond

*In this section we present and explain the construction of the bond-path framework set. See* Chap. 5 *for definitions and examples of the bond-path framework set $B_\sigma$ and $B_F$ implementations of the stress tensor $\boldsymbol{\sigma}(\boldsymbol{r})$ and Ehrenfest Force $\boldsymbol{F}(\boldsymbol{r})$ respectively.*

A bond within QTAIM is referred to as the bond-path ($\boldsymbol{r}$) and is defined as the extent of the path traced out by the $\underline{\mathbf{e}}_3$ eigenvector of the Hessian of the total charge density $\rho(\mathbf{r})$, passing through the *BCP*, along which $\rho(\mathbf{r})$ is locally maximal with respect to neighboring paths. Therefore the bond-path ($\boldsymbol{r}$) may possess a non-zero degree of curvature [1] and is a dimensionless ratio separating two bonded nuclei and is defined as:

$$(\text{BPL} - \text{GBL})/\text{GBL} \tag{4.1}$$

where the geometric bond length (GBL) refers to the inter-nuclear separation with the minor and major radii of bonding curvature specified by the directions of $\underline{\mathbf{e}}_2$ and $\underline{\mathbf{e}}_1$ respectively [2]. The NG-QTAIM definition of a bond considers the bond-path framework set $\mathsf{B}$ to comprise the bond-path ($\boldsymbol{r}$) defined by the eigenvector $\underline{\mathbf{e}}_3$, two paths swept out by the $\underline{\mathbf{e}}_2$ and $\underline{\mathbf{e}}_1$ eigenvectors. This three-stranded interpretation of the chemical bond is more complete than minimal definition of bonding ($\underline{\mathbf{e}}_3$) provided by the bond-path ($\boldsymbol{r}$) because it comprises all three of the $\{\underline{\mathbf{e}}_1, \underline{\mathbf{e}}_2, \underline{\mathbf{e}}_3\}$ eigenvectors.

The name for the $\{\boldsymbol{q}, \boldsymbol{q}'\}$ path-packet is used in reference to the orbital-like envelope that the pair of $\boldsymbol{q}$ and $\boldsymbol{q}'$ paths form along the bond-path ($\boldsymbol{r}$) on a QTAIM or Ehrenfest Force $\mathbf{F}(\mathbf{r})$ molecular graph [3], see Chap. 7. This more complete definition of the bond-path ($\boldsymbol{r}$) within NG-QTAIM is referred to as the bond-path framework set $\mathsf{B}\{(\boldsymbol{p}, \boldsymbol{p}'), (\boldsymbol{q}, \boldsymbol{q}'), (\boldsymbol{r})\}$ for a ground state total charge density distribution $\rho(\mathbf{r})$.

The properties of the bond-path framework set $\mathsf{B}$ are much more responsive to deformations in $\rho(\mathbf{r})$ than the QTAIM bond-path ($\boldsymbol{r}$) (black lines), see Sect. 4.2. A benefit of the bond-path framework set $\mathsf{B}$ is that it visualizes the admixture of double or single or ionic character of a bond along an *entire* length of the bond-path ($\boldsymbol{r}$), rather than only returning a single number at the *BCP* [3–19]. The $\boldsymbol{p}$, $\boldsymbol{q}$ and $\boldsymbol{r}$ paths are constructed from the values of the least ($\underline{\mathbf{e}}_1$) and most ($\underline{\mathbf{e}}_2$) preferred directions of electronic charge density accumulation $\rho(\mathbf{r})$ along the bond-path ($\boldsymbol{r}$). The $\boldsymbol{q}$ path (equivalently $\boldsymbol{q}_\sigma$ or $\boldsymbol{q}_\mathbf{F}$) is always defined to be longer than the $\boldsymbol{q}'$ (equivalently $\boldsymbol{q}_\sigma{}'$ or $\boldsymbol{q}_\mathbf{F}{}'$) paths. Conversely, the $\boldsymbol{p}$ ($\boldsymbol{p}_\sigma$ or $\boldsymbol{p}_\mathbf{F}$ for the stress tensor $\boldsymbol{\sigma}(\mathbf{r})$ or Ehrenfest force $\mathbf{F}(\mathbf{r})$ respectively) is always defined to be the shorter of the two paths associated with the $\underline{\mathbf{e}}_1$ eigenvector. For very curved bond-paths $\boldsymbol{p}$ may be shorter than $\boldsymbol{r}$ (the bond-path length), so we only chose $\boldsymbol{p}'$. Two paths ($\boldsymbol{q}$ and $\boldsymbol{q}'$) that comprise the path-packet are associated with the most preferred (facile) $\underline{\mathbf{e}}_2$ and -$\underline{\mathbf{e}}_2$ eigenvectors respectively because $\underline{\mathbf{e}}_2 \equiv -\underline{\mathbf{e}}_2$ lie in the same plane for the same point on the bond-path ($\boldsymbol{r}$), see

Eq. (4.2), similarly for ($\boldsymbol{p}$ and $\boldsymbol{p'}$) associated with the least preferred $\pm$ $\underline{\mathbf{e}}_{\mathbf{1}}$ eigenvectors, see Fig. 4.1. This is because the $\underline{\mathbf{e}}_{\mathbf{1}}$, $\underline{\mathbf{e}}_{\mathbf{2}}$ and $\underline{\mathbf{e}}_{\mathbf{3}}$ eigenvectors are defined within the ranges $-90°$ to $+90°$ ($-\pi/2$ to $+\pi/2$ radians) as opposed to 0°–180° (0–π radians).

The ellipticity ε is the scaling factor used due to the universal chemical interpretation of the ellipticity ε in the construction of the $\{\boldsymbol{q}, \boldsymbol{q'}\}$ and $\{\boldsymbol{p}, \boldsymbol{p'}\}$ path-packets, where $\boldsymbol{r}$ is constructed from ($\underline{\mathbf{e}}_{\mathbf{3}}$):

$$\begin{aligned} \boldsymbol{p}_{\mathrm{i}} &= \boldsymbol{r}_i + \boldsymbol{\varepsilon}_i \underline{\mathbf{e}}_{1,\mathbf{i}}, \quad \boldsymbol{p'}_i = \mathbf{r}_{\mathbf{i}} - \boldsymbol{\varepsilon}_i \underline{\mathbf{e}}_{1,\mathbf{i}} \\ \boldsymbol{q}_{\mathrm{i}} &= \boldsymbol{r}_i + \boldsymbol{\varepsilon}_i \underline{\mathbf{e}}_{2,\mathbf{i}} \quad \boldsymbol{q'}_i = \mathbf{r}_{\mathbf{i}} - \boldsymbol{\varepsilon}_i \underline{\mathbf{e}}_{2,\mathbf{i}} \end{aligned} \tag{4.2}$$

The $\{\boldsymbol{q}, \boldsymbol{q'}\}$ path-packet can be used along the bond-path on a QTAIM, Ehrenfest Force $\mathbf{F(r)}$ or hybrid molecular graph [3]. A pair of paths ($\boldsymbol{q}$ and $\boldsymbol{q'}$) that comprise the

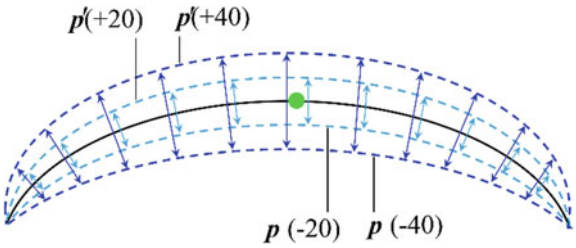


**Fig. 4.1** A sketch, not to scale, of the $\{\boldsymbol{p}, \boldsymbol{p'}\}$ path-packets illustrating that for the highly curved bond-path ($\boldsymbol{r}$) the $\boldsymbol{p}$ path may be shorter than $\boldsymbol{r}$ path arising for bond-path subjected to a varying electric-field e.g. $\pm$ 20 $\times$ $10^{-4}$ a.u and $\pm$ 40 $\times$ $10^{-4}$ a.u indicated by the figures in parenthesis

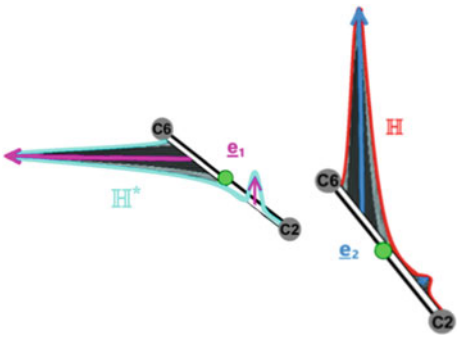


**Fig. 4.2** The pale-blue line (left) represents the path, referred to as the eigenvector-following path with length $\mathsf{H}^*$, swept out by the tips of the scaled $\underline{\mathbf{e}}_{\mathbf{1}}$ eigenvectors, shown in magenta. The red path (right) corresponds to $\mathsf{H}$, constructed from the path swept out by the tips of the scaled $\underline{\mathbf{e}}_{\mathbf{2}}$ eigenvectors, shown in mid-blue. The pale-blue and mid-blue arrows representing the $\underline{\mathbf{e}}_{\mathbf{1}}$ and $\underline{\mathbf{e}}_{\mathbf{2}}$ eigenvectors are scaled by the ellipticity ε respectively, where the vertical scales are exaggerated for visualization purposes, see Eq. (4.3). The green sphere indicates the position of a given *BCP*

path-packet are associated with the most preferred (facile) $\underline{\mathbf{e}}_{\mathbf{2}}$ and -$\underline{\mathbf{e}}_{\mathbf{2}}$ eigenvectors respectively. This is because $\underline{\mathbf{e}}_{\mathbf{2}} \equiv -\underline{\mathbf{e}}_{\mathbf{2}}$ lie in the same plane for the same point on the bond-path ($\boldsymbol{r}$), see Eq. (4.2), similarly for ($\boldsymbol{p}$ and $\boldsymbol{p'}$) associated with the least preferred $\pm\,\underline{\mathbf{e}}_{\mathbf{1}}$ eigenvectors. This explained by the fact that the $\underline{\mathbf{e}}_{\mathbf{1}}$, $\underline{\mathbf{e}}_{\mathbf{2}}$ and $\underline{\mathbf{e}}_{\mathbf{3}}$ eigenvectors only exist within the ranges $-90°$ to $+90°$ ($-\pi/2$ to $+\pi/2$ radians) as opposed to 0°–180° (0–π radians).

In the limit of vanishing ellipticity $\varepsilon = 0$, *for all* steps $i$ along the bond-path ($\boldsymbol{r}$) then $\mathsf{B}$ = BPL, see Fig. 4.2, the lengths of the $\boldsymbol{p}$ and $\boldsymbol{q}$ paths are defined as the *eigenvector-following paths* $\mathsf{H}^*$ or $\mathsf{H}$:

$$\mathsf{H}^* = \sum_{i=1}^{n-1} |\boldsymbol{p}_{i+1} - \boldsymbol{p}_{i,}|,$$
$$\mathsf{H} = \sum_{i=1}^{n-1} |\boldsymbol{q}_{i+1} - \boldsymbol{q}_{i}| \tag{4.3}$$

Analogous to the bond-path curvature, see Eq. (4.1), we can define dimensionless, *fractional* versions of the eigenvector-following path length $\mathsf{H}$ where several forms are possible and not limited to the following:

$$\mathsf{H}_{\mathrm{f}} = (\mathrm{H}{-}\mathrm{BPL})/\mathrm{BPL} \tag{4.4}$$

$$\mathsf{H}_{\mathrm{f}\theta\mathrm{min}} = (\mathsf{H} - \mathsf{H}_{\theta\mathrm{min}})/\mathsf{H}_{\theta\mathrm{min}} \tag{4.5}$$

where $\mathrm{H}_{\theta\mathrm{min}}$ is defined as the length swept out by the scaled $\underline{\mathbf{e}}_{\mathbf{2}}$ eigenvectors using value of the torsion θ at the energy minimum, with similar expressions for $\mathsf{H}^*_{\mathrm{f}}$ and $\mathsf{H}^*_{\mathrm{f}\theta\mathrm{min}}$ can both be derived using the $\underline{\mathbf{e}}_{\mathbf{1}}$ eigenvectors defined by Eqs. (4.4) and (4.5) respectively.

For a non-torsional bond-path ($\boldsymbol{r}$) distortion motion comprising bond-paths with negligible curvature the $\{\underline{\mathbf{e}}_{\mathbf{1}}, \underline{\mathbf{e}}_{\mathbf{2}}, \underline{\mathbf{e}}_{\mathbf{3}}\}$ bond-path framework there is no relative change of the $\lambda_1$ and $\lambda_2$ eigenvalues for all values of the scaling factor $\varepsilon_i$. Additionally, because $\mathsf{H}$ and $\mathsf{H}^*$ are defined by the distances swept out by the $\underline{\mathbf{e}}_{\mathbf{2}}$ tip path points, $\boldsymbol{q}_{\mathbf{i}} = \boldsymbol{r}_{\boldsymbol{i}} + \varepsilon_i \underline{\mathbf{e}}_{\mathbf{2},i}$ and $\boldsymbol{p}_{\mathbf{i}} = \boldsymbol{r}_{\boldsymbol{i}} + \varepsilon_i \underline{\mathbf{e}}_{\mathbf{1},i}$ respectively, one has $\mathsf{H} = \mathsf{H}^*$ provided that identical scaling factor $\varepsilon_i$ is used in Eq. (4.3).

We consider the bond-path framework for photochemistry e.g. for the ground state ($S_0$), first ($S_1$), second ($S_2$) and *n*th exited states:

$$\mathsf{B}_0 = \{(\boldsymbol{p}_{\mathbf{0}}, \boldsymbol{p'}_{\mathbf{0}}),\ (\boldsymbol{q}_{\mathbf{0}}, \boldsymbol{q'}_{\mathbf{0}}),\ (r_0)\}$$
$$\mathsf{B}_1 = \{(\boldsymbol{p}_{\mathbf{1}}, \boldsymbol{p'}_{\mathbf{1}}),\ (\boldsymbol{q}_{\mathbf{1}}, \boldsymbol{q'}_{\mathbf{1}}),\ (r_1)\}$$
$$\mathsf{B}_2 = \{(\boldsymbol{p}_{\mathbf{2}}, \boldsymbol{p'}_{\mathbf{2}}),\ (\boldsymbol{q}_{\mathbf{2}}, \boldsymbol{q'}_{\mathbf{2}}),\ (r_2)\}$$
$$\ldots$$

$$\ldots$$

$$\mathsf{B}_n = \{(\boldsymbol{p}_n, \boldsymbol{p'}_n),\ (\boldsymbol{q}_n, \boldsymbol{q'}_n),\ (\boldsymbol{r}_n)\} \tag{4.6}$$

Each state contributes a total of five unique paths to the bond-path framework set comprising two path packets to Eq. (4.6), e.g. for the ground state $S_0$ the bond-path framework set $B_0$ comprises the five paths: $\boldsymbol{p_0}$, $\boldsymbol{p'_0}$, $\boldsymbol{q_0}$, $\boldsymbol{q'_0}$ and $\boldsymbol{r_0}$ and two path-packets: $\{\boldsymbol{p_0}, \boldsymbol{p'_0}\}$ and $\{\boldsymbol{q_0}, \boldsymbol{q'_0}\}$. If we consider the $S_1$ and $S_2$ states in addition to $S_0$ there are a total of fifteen paths and six path-packets.

## 4.2 Construction of the Precession K of the Bond-Path Framework Set B

*In this section we present and explain the construction of the precession of the bond-path framework set. See* Chap. 5 *for definitions and examples of the precession* $K_{\boldsymbol{\sigma}}$ *and* $K_{\boldsymbol{F}}$ *implementations of the stress tensor* $\boldsymbol{\sigma}(\boldsymbol{r})$ *and Ehrenfest Force* $\boldsymbol{F}(\boldsymbol{r})$ *respectively.*

Using $n$ points $\boldsymbol{r}_i$ along the bond path $\boldsymbol{r}$ (associated with eigenvector $\underline{\mathbf{e}}_3$) and defining $\varepsilon_i$ as the ellipticity at this point, one can draw vectors $\boldsymbol{q}_i$ and $\boldsymbol{p}_i$, scaled by $\varepsilon_i$, originating at this point. The tips of these vectors ($\boldsymbol{q}_i$ and $\boldsymbol{p}_i$) define the paths $\boldsymbol{p}$ and $\boldsymbol{q}$. The form of $\boldsymbol{p}_i$ and $\boldsymbol{q}_i$ is defined by Eq. (4.2).

We define the extent to which the $\{\boldsymbol{p}, \boldsymbol{p'}\}$ path-packet constructed from the $\underline{\mathbf{e}}_1$ eigenvector wraps i.e. undergoes a *precession* about a bond-path, see Fig. 4.3. For the $\{\boldsymbol{p}, \boldsymbol{p'}\}$ path-packet, defined by the $\underline{\mathbf{e}}_1$ eigenvector, we wish to follow the extent to which the $\{\boldsymbol{p}, \boldsymbol{p'}\}$ path-packet precesses about the bond-path by defining the *precession* K for bond-path-rigidity [20–22]:

$$\mathsf{K} = 1 - \cos^2\alpha, \quad \text{where } \cos\alpha = \underline{\mathbf{e}}_1 \cdot \underline{\mathbf{u}} \quad \text{and} \quad 0 \le \mathsf{K} \le 1 \tag{4.7}$$

where $\underline{\mathbf{u}}$ defines the *BCP* $\rightarrow$ *RCP* (bond critical point to ring critical point) path. Considering the extremes of K, with $\alpha$ defined by Eq. (4.7), for $\mathsf{K} = 0$, there is maximum alignment of the *BCP* $\rightarrow$ *RCP* path with the $\underline{\mathbf{e}}_1$ eigenvector, the least facile direction. For $\mathsf{K} = 1$ we have the maximum degree of alignment with the $\underline{\mathbf{e}}_2$ eigenvector, the most facile direction. In other words, $\mathsf{K} = 0$ and $\mathsf{K} = 1$ indicate bond-paths with the lowest and highest tendencies towards bond-path-flexibility, respectively. The precession K is determined relative to the *BCP*, in either direction along the bond-path towards the nuclei at either end of the bond-path using an arbitrarily small spacing of $\underline{\mathbf{e}}_1$ eigenvectors. The *BCP* indicates minimum facile character, i.e. bond-path-rigidity when the precession K of the $\{\boldsymbol{p}, \boldsymbol{p'}\}$ path-packet about the bond-path $\pm\ \underline{\mathbf{e}}_1$ eigenvector is parallel to $\underline{\mathbf{u}}$. By following the variation of the precession K we can quantify the degree of facile character of a *BCP* along an entire extent of the bond-path, see Fig. 4.3.

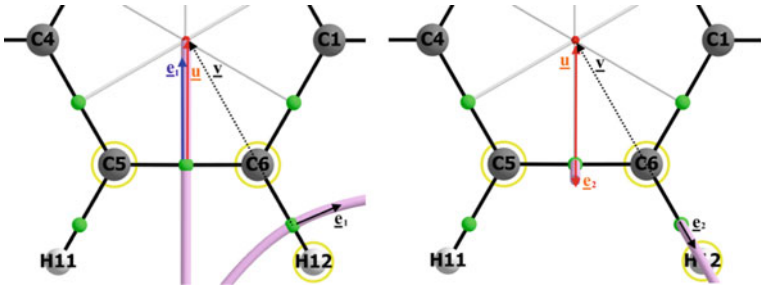


**Fig. 4.3** The $\{\boldsymbol{p}, \boldsymbol{p}'\}$ precession $\mathsf{K}$ construction (left panel) and $\{\boldsymbol{q}, \boldsymbol{q}'\}$ path-packet precession $\mathsf{K}'$ (right panel) for the C5-C6 *BCP* and C6-H12 *BCP* of benzene molecular graph, where the $\underline{\mathbf{u}}$ is a unit vector (red arrow) along the $BCP \rightarrow RCP$ path are denoted by the grey line. The vector $\underline{\mathbf{v}}$ is a unit vector (black arrow) defined to be aligned parallel to the normal vector of the plane of the relaxed benzene molecule. The pale magenta line indicates the interatomic surface paths (IAS) that originate at the *BCP*. The $\underline{\mathbf{e}}_1$ eigenvector (blue arrow) and $\underline{\mathbf{e}}_2$ eigenvector (magenta arrow), the $\pm$ signs of $\underline{\mathbf{e}}_1$ and $\underline{\mathbf{e}}_2$ are chosen to form the right handed orthogonal set $\{\underline{\mathbf{e}}_1, \underline{\mathbf{e}}_2, \underline{\mathbf{e}}_3\}$. The undecorated red and green spheres indicate the locations of the bond critical points (*BCP*s) and ring critical points (*RCP*s) respectively

## 4.3 Applications of the Bond-Path Framework Set: Normal Modes of Vibration

*In this section we provide a series of investigations the infra-red active normal modes of benzene.*

### *4.3.1 3-D Bonding Morphology of the Infra-Red Active Modes of Benzene*

We use the bond-path framework set $\mathsf{B}$, to follow variations in the 3-D morphology of all bonds for the four infra-red (IR) active normal modes of benzene [4]. We find 3-D distortions including bond-stretching/compression, bond-torsion and bond-curving. We considered fractional measures including $\mathrm{H}_{\mathrm{f}\theta\mathrm{min}}$ and $\mathrm{H}_{\mathrm{f}}$ to quantify these variations away from linearity of the bond, see Eqs. (4.4) and (4.5) respectively.

For all four infra-red (IR) active normal modes; mode 5, mode 14, mode 21 and mode 18, the C-H *BCP* bond-paths possess values of $\mathsf{H}$ that are virtually indistinguishable with the bond-path lengths BPLs because all of the C-H *BCP*s possess low ellipticity values $\varepsilon$ for the benzene C-H *BCP*s. This is seen from the expression for the from Eq. (4.3) that determines the eigenvector-following path length $\mathsf{H}$, see Fig. 4.4. Only the C-H *BCP*s of the highest frequency mode 28 have linear variations of the BPL with respect to the amplitude. The reason is that for mode 28 the C-H bond-paths are distorted linearly i.e. bond stretching/compression, without a significant bond-path torsion due to the absence of zero bond-path curvature throughout the duration of

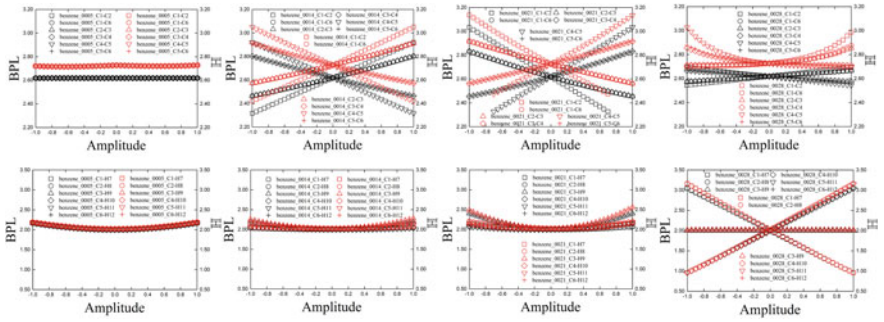


**Fig. 4.4** The variation of the BPL (black) and the eigenvector-following path length H (red) of the C-C *BCPs* (top) and C-H *BCP*s (bottom) with amplitude for the four benzene infrared (IR) active modes

the normal mode. The presence of non-zero variations in the bond-path curvature of mode 21 were apparent from the molecular graphs of the maximum ± amplitudes of the normal modes of vibration of our earlier work [23].

Inspection of the fractional eigenvector-following path length $H_f$, for the C-C *BCP*s and C-H *BCP*s revealed a magnification of the features of the IR benzene normal modes, see Fig. 4.5.

The variations of the newly introduced eigenvector-following path lengths and $H^*$ and H captured the corresponding torsional (twisting) bond-path motions as determined by the presence of non-linear variations of $H^*$ and H with amplitude. We found small differences in the eigenvector-following path lengths and $H^*$ and H for the presence of bond-path torsion that occur for non-linear variations of H with amplitude are due to slight variations from linearity of a bond-path ($r$). The $H_f$ and $H_{f\theta min}$ were found to be useful in magnifying the non-linear variations of H with amplitude whereas the bond-path curvature was not found to usefully magnify the variations of the BPL, see

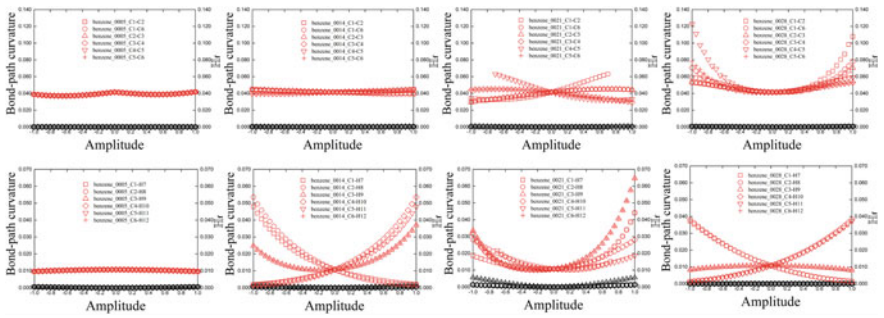


**Fig. 4.5** The variation of the bond-path curvature (black) and the eigenvector-following path length $H_f$ (red) of the C-C *BCPs* (top) and C-H *BCP*s (bottom) with amplitude for the four IR active modes of benzene

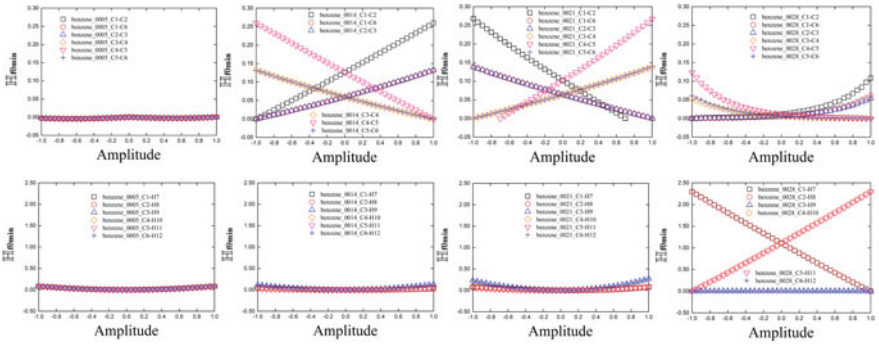


**Fig. 4.6** The variation of the $H_{f\theta min}$ of the C-C *BCPs* with amplitude for the four IR active normal modes of benzene

Figs. 4.5 and 4.6 respectively. This is due to the inability of the BPL and consequently bond-path curvature to detect the presence of torsion of the BPL. This is explained by the fact that $\mathsf{H}^*$ and $\mathsf{H}$ are defined using all three $\underline{\mathbf{e}}_1$, $\underline{\mathbf{e}}_2$ and $\underline{\mathbf{e}}_3$ eigenvectors. In contrast only the $\underline{\mathbf{e}}_3$ eigenvector is used to define the bond-path.

We demonstrated the ability of $\mathsf{H}$ to sensitively identify torsional features in the IR active modes of benzene not accessible to either conventional analysis using molecular geometries or the BPL. Therefore we introduced a new bond-by-bond measure to establish bond-path torsion without the need to use either dihedral angles or reference directions. In future, experimentalists could revisit vibrational spectra where there is poor agreement with the corresponding calculated spectra obtained from conventional *ab-initio* treatments. Then discrepancies between the experiment spectra and calculated spectra can now be understood in terms of previously unaccounted-for 3-D bond-path distortions including bond-path twisting.

### *4.3.2 A Vector-Based Representation of the Chemical Bond for the Normal Modes of Benzene*

The molecular graph for the four infra-red (IR) active normal modes of benzene demonstrates the non-linear character of the bond-paths, see Fig. 4.7 [24].

The lengths of the $\boldsymbol{q}$-paths defined by $\mathsf{H}$ of each of the four IR active benzene normal modes demonstrated that the C-C *BCP* and C-H *BCP* bond-paths were non-linear due to the presence of bond-path curving and bond-path twisting and Sect. 4.3.1. This finding demonstrated the inadequacy of the assumption of the presence of constantly

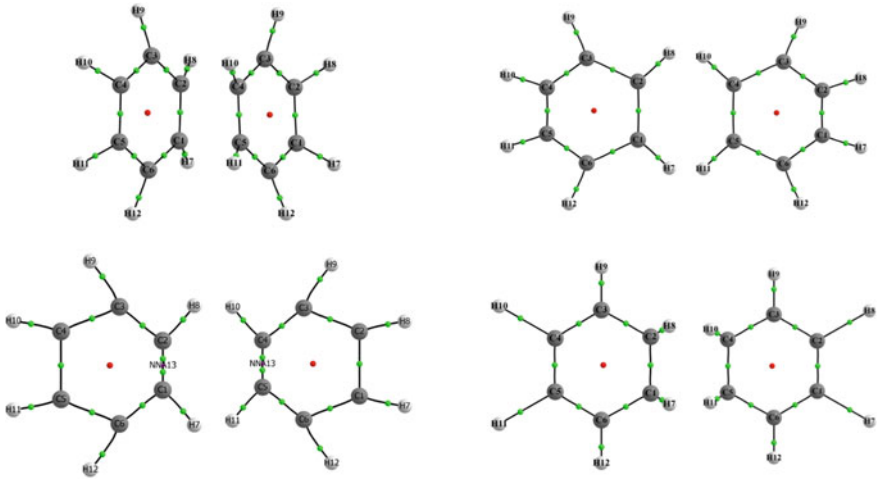

**Fig. 4.7** Molecular graphs of the four infrared active modes of benzene; mode 5 (721.568 $cm^{-1}$), mode 14 (1097.691 $cm^{-1}$), mode 21 (1573.927 $cm^{-1}$) and mode 28 (3298.320 $cm^{-1}$). The left and right panels correspond to the (-) and (+) extrema of the normal modes of vibrations, undecorated green and red spheres represent the *BCP*s and *RCP*s respectively

C-C and C-H linear bonds for the four IR active benzene normal modes. The assumption of bond linearity, used by current mathematical models for analyzing experimental vibrational spectra, relies on the erroneous *ad-hoc* addition of anharmonic terms to correct the resulting spectra.

The ***p-***, ***q-*** and ***r***-paths corresponding to mode 5, the lowest frequency IR active mode of benzene, remain similar to the bond-path frame-work set B of the relaxed benzene, compare Fig. 4.8 with molecular graphs in Fig. 4.6. In particular, we notice that the *q*-paths, corresponding to the easy direction of $\rho(\mathbf{r})$ motion, remains in the plane of the benzene ring throughout the normal mode of vibration. We also note for mode 5 that despite the considerable flexing of the C-H *BCP* bond-paths at the extremes of the amplitude ($\pm 1$) that the B associated with the C-H *BCP*s again maintain a similar appearance to the relaxed B due to the lack of C-H *BCP* bond-path curving and twisting.

We see for mode 14 that the dominance of the ***q***- over the ***p***-paths is maintained in the plane of the benzene ring, although the C-H *BCP* bond-path flexing can also be seen and results in an increase in the deviation of the ***p-*** and ***q-***paths from bond-path (***r***), compared with the relaxed benzene.

The ***p-*** and ***q-***paths of mode 21 are associated with greater distortion of the C-C *BCP* bond-paths than is the case for mode 5 and mode 14, as a consequently the ***p***-paths are more apparent in the plane of the benzene ring. The effect of the mode 21 is enough to induce a non-nuclear attractor (*NNA*) in the compressed C-C *BCP* bond-path, that may occur in electron deficient or strained [25, 26] bonding environments.

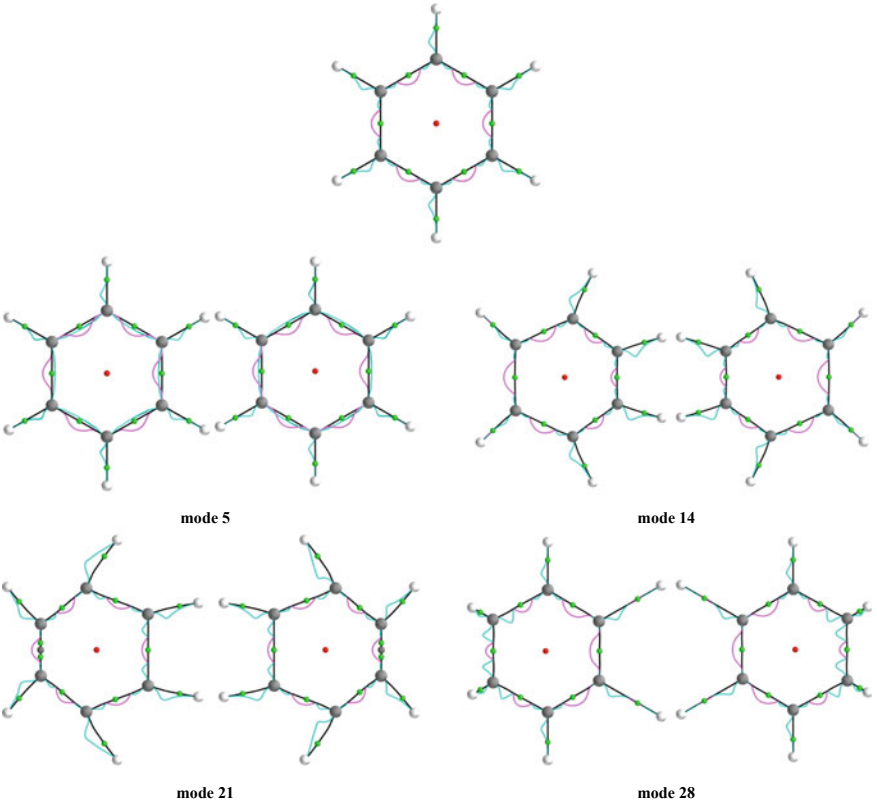


**Fig. 4.8** The bond-path frame-work set $\mathsf{B}$ corresponding to the relaxed benzene structure (top) for the views for the $\boldsymbol{p}$-(pale-blue) and $\boldsymbol{q}$-(magenta) paths with a magnification factor of $\times$ 5. The corresponding bond-path ($\boldsymbol{r}$) is indicated by the black line. The corresponding pairs of plots for each of the four indicated infrared (IR) active mode with the amplitudes $-1.0$ (left-panel) and $+$ 1.0 (right-panel)

### *4.3.3 Bond Flexing, Twisting, Anharmonicity and Responsivity for the IR-Active Modes of Benzene*

Bond Flexing, Twisting, Anharmonicity and Responsivity for the IR-active modes of Benzene [20] were earlier considered where 'anharmonicity' is not to be confused with force-constants, is determined from the relative *BCP* shifts that quantify the sliding of $\underline{\mathbf{e}}_3$, defined at the *BCP*. 'anharmonicity' refers to a non-linear response. For the case of the IR-active modes of benzene, values of $\mathsf{K} = 0$ and $\mathsf{K} = 1$ also indicate bond-paths with the lowest and highest tendencies towards IR-responsivity respectively.

The relative positions ($-\Delta\mathrm{Q}$ and $+\Delta\mathrm{Q}$) along the bond-path are where the precession $\mathsf{K}$ jumps from $\mathsf{K} =$ minimum to $\mathsf{K} = 1$ in a.u. for the amplitudes $= -1.0$ and $+1.0$,

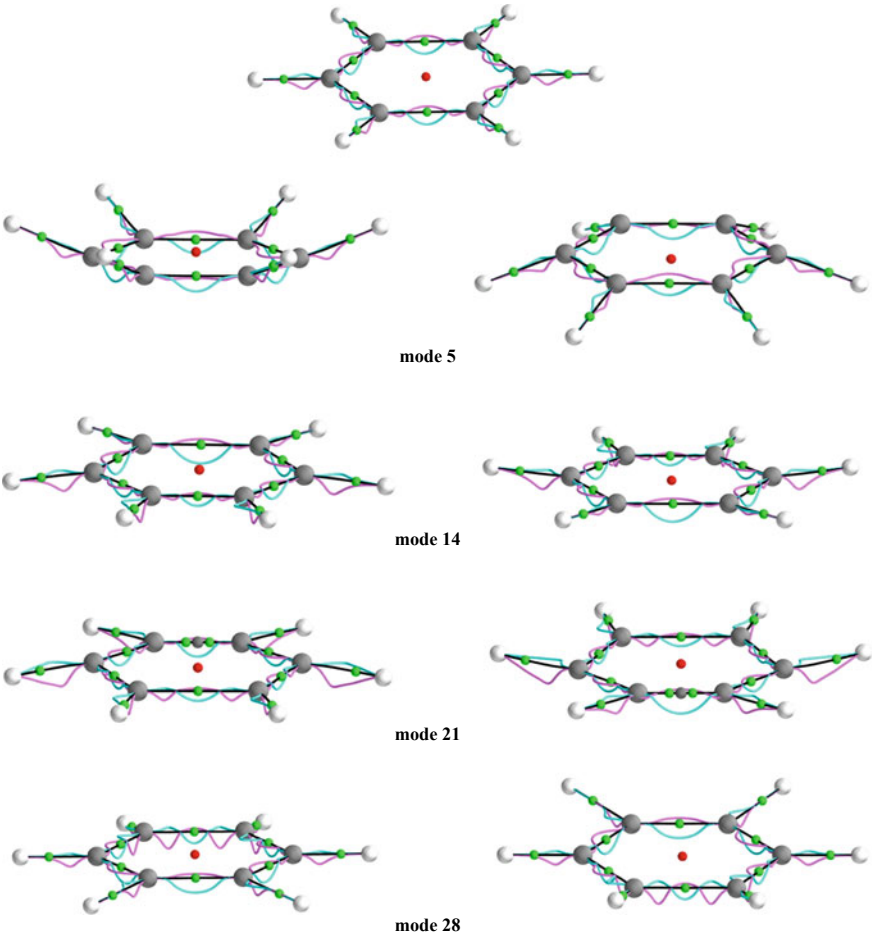


**Fig. 4.9** The corresponding side views of the relaxed benzene structure (top) and the four indicated infrared (IR) active modes, see Fig. 4.7 for further details

see Table 4.1. The IR-active mode 5 for amplitudes $\pm$ 1.0 the K (and K′) profiles of the C-C *BCP* bond-paths possessed a harmonic-like morphology. This was explained by the non-planar molecular graph of IR-active mode 5, where the *RCP* (red sphere) is visible the side view, see Fig. 4.10. Conversely, the other three IR-active modes as well as the relaxed benzene possess step-like K (and K′) profiles for the C-C *BCP* bond-paths and planar molecular graphs, see Fig. 4.11. The values of the relative position along the bond-path ($-\Delta$Q and $+\Delta$Q) for the C-C *BCP* bond-paths do not relate to the *BCP* shifts, e.g. see the entries for the C1-C2 *BCP* for the IR-active mode 14 presented in Table 4.1. For mode 21, the presence of the non-nuclear attractors (*NNA*s) [27, 28] for both the C1-C2 *BCP* bond-path (amplitude $= +1.0$) and C4-C5 *BCP* (amplitude $= -1.0$) bond-path results in values of $\pm$ $\Delta$Q comparable to the

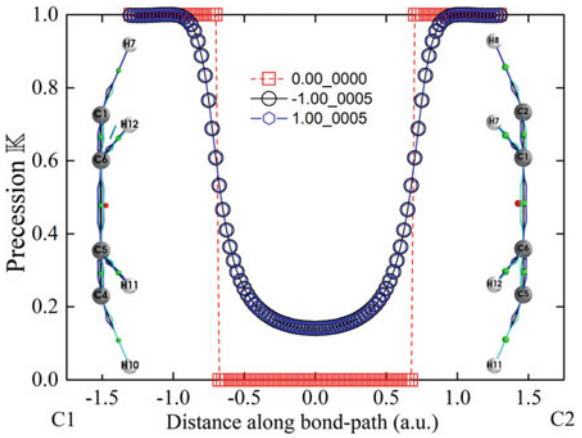


**Fig. 4.10** The variation of the precession K along the C-C *BCP* bond-paths of the benzene IR-active mode 5 for the amplitudes of vibration −1.0 (black), 0.0 (red) and + 1.0(blue). The $\{\boldsymbol{p}, \boldsymbol{p}'\}$ path-packets are superimposed onto the molecular graph and shown on the insets for amplitude -1.0 (left) and +1.0 (right). Bond critical points (*BCP*s) are located at a distance = 0.0 a.u along the bond-path, the ring critical point (*RCP*) is visible as the red sphere located outside of the plane of the benzene ring

relaxed benzene and symmetrical precession K (and K′) profiles. Conversely, for mode 21 the bond-paths without an *NNA* possess a greater range of the values of ± ΔQ and asymmetrical precession K (and K′) profiles. The effect of the *NNA*s on the torsion of the bond-path can be determined by examination of the precession K profile and the relative positions along the bond-path ± ΔQ of the jumps in K. The presence of the *NNA*s results in K profiles and values of ± ΔQ that are the most similar to the relaxed benzene.

The initial **U** (non-responsive) value for the C1-C2 *BCP* bond-path of mode 28 with amplitude = − 1.0 indicates a complete lack of IR-responsivity, see Table 4.1 and Fig. 4.11. For the C-H *BCP* bond-paths the converse relation between K and K′ does not hold since the H atom is not anchored and can therefore move.

The lack of dependency of the relative positions along the bond-path ± ΔQ of the jumps in K and the C-C *BCP* shifts is explained by the orthogonality of $\{\underline{\mathbf{e}}_1, \underline{\mathbf{e}}_2, \underline{\mathbf{e}}_3\}$, therefore $\underline{\mathbf{e}}_3$ will move with the *BCP* independently of the $\{\boldsymbol{p}, \boldsymbol{p}'\}$ and $\{\boldsymbol{q}, \boldsymbol{q}'\}$ path-packets that are constructed from the $\underline{\mathbf{e}}_1$ and $\underline{\mathbf{e}}_2$ respectively.

For mode 5 in the form of the 'harmonic' K profile is consistent with the zero values for the relative C-C *BCP* shifts indicate no change in chemical character due to the absence of change of the charge density $\rho(\mathbf{r})$ distribution [29]. The cause of this is the C-H *BCP* bond-paths flex out the plane of the benzene ring that results in the ring critical point (*RCP*) being located outside of the $C_6$ ring. Additionally, the minimum value of the C-C bond-path K profile of mode 5 is non-zero, unlike the other three IR-active modes. This indicates a lower degree of shared-shell character for mode

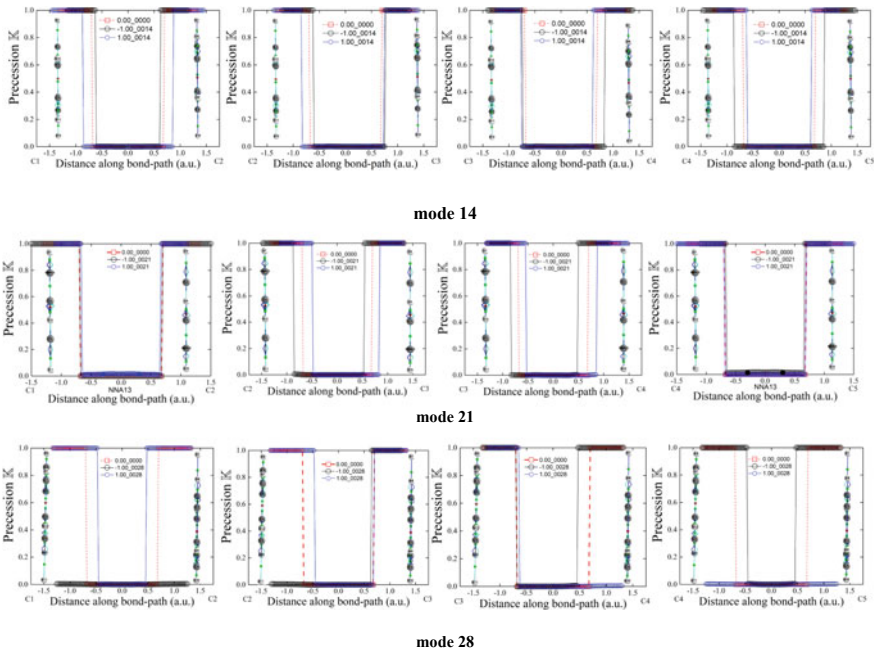


**Fig. 4.11** The variation of the precession K along the C-C *BCP* bond-paths of three of the benzene IR-active modes, also see Fig. 4.9

5, lower IR-responsivity and a more pliable response of the bond-path than for the C-C *BCP* bond-paths of the other three modes. The C-H *BCP* bond-path K profiles are non-zero and much closer to $K = 1.0$ than is the case for the C-C *BCP* bond-path K profiles, therefore the C-H *BCP* bond-paths are more flexible and pliable than the C-C *BCP* bond-paths.

## 4.4 Strained and Unusual Bonding Environments

*In this section we consider a selection of bonding environments particularly in need of a directional approach provided by NG-QTAIM.*

### *4.4.1 The Directional Bonding of [1.1.1] Propellane*

The influence on the bonding environment on the controversial axial C1--C2 *BCP* of [1.1.1]propellane molecule was determined with the bond-path framework sets B, see Fig. 4.12. The axial C1-C2 *BCP* bond-path was determined to be of single bond

**Table 4.1** The symmetry inequivalent *BCP* values of the relative partial benzene bond-path lengths Δ(C-*BCP*/*NNA*) = ΔA, Δ(*NNA*/*BCP*-C/H) = ΔB with the Δ(BPL), ΔGBL and the relative position along the bond-path that precession K jumps from K = minimum to K = 1 (−ΔQ and + ΔQ) in a.u. for the amplitudes = − 1.0 and +1.0 of the infrared (IR) benzene each of the four IR-active modes are presented. The Δ(C-*BCP*/*NNA*) and Δ(*BCP*/*NNA*-C/H) were calculated by subtracting off the relaxed benzene values. For the relaxed benzene −Q and +Q values are −0.700 and 0.700 respectively. [a] IR-active mode 5: the values of ± ΔQ were estimated as half way up the slope of the non-step-like variation in the K profile. [b]IR-active mode 21: '*NNA*' indicates the presence of a non-nuclear attractor (*NNA*) .[c]IR-active mode 28: the C-C *BCP* bond-paths that are unresponsive are indicated by '**U**'

| *BCP* | −1.0 | | | +1.0 | | |
|---|---|---|---|---|---|---|
| | (ΔA, ΔB) | ΔBPL (ΔGBL) | (+ΔQ, −ΔQ) | (ΔA, ΔB) | ΔBPL (ΔGBL) | (+ΔQ, −ΔQ) |
| *IR-active mode 5*[a], $\nu = 721.57\ cm^{-1}$ | | | | | | |
| C1-C2 | (0.000, 0.000) | 0.000(0.000) | (0.037, −0.037) | (0.000, 0.000) | 0.000(0.000) | (0.037, − 0.037) |
| C1-H7 | (0.116, 0.047) | 0.169(0.163) | (---, ---) | (0.116, 0.047) | 0.169(0.163) | (---, ---) |
| *IR-active mode 14*, $\nu = 1097.69\ cm^{-1}$ | | | | | | |
| C1-C2 | (−0.151, −0.151) | −0.302(−0.302) | (−0.071, 0.071) | (0.152, 0.152) | 0.303(0.303) | (0.175, −0.175) |
| C2-C3 | (0.085, 0.101) | 0.185(0.184) | (−0.075, 0.075) | (0.085, 0.101) | 0.185(0.184) | (0.050, −0.150) |
| C3-C4 | (−0.065, −0.090) | − 0.154(−0.154) | (0.150, −0.050) | (−0.065, −0.090) | −0.154(−0.154) | (−0.075, −0.075) |
| C4-C5 | (0.152, 0.152) | 0.303(0.303) | (0.175, −0.175) | (−0.151, −0.151) | −0.302(−0.302) | (−0.071, 0.071) |
| C1-H7 | (0.002, 0.030) | 0.034(0.031) | (---, ---) | (0.071, −0.004) | 0.069(0.067) | (---, ---) |
| C3-H9 | (0.134, 0.052) | 0.195(0.185) | (---, ---) | (0.134, 0.052) | 0.195(0.185) | (---, ---) |
| C5-H11 | (0.027, −0.006) | 0.069(0.067) | (---, ---) | (0.002, 0.030) | 0.034(0.031) | (---, ---) |
| *IR-active mode 21*[b], $\nu = 1573.93\ cm^{-1}$ | | | | | | |
| C1-C2 | (0.208, 0.208) | 0.416(0.416) | (0.000, 0.000) | (−0.208, −0.208)*NNA* | −0.415(−0.415) | (−0.028, 0.028) |
| C2-C3 | (0.187, 0.026) | 0.215(0.213) | (−0.150, −0.175) | (−0.177, 0.012) | −0.164(−0.165) | (0.150, 0.200) |
| C3-C4 | (0.012, −0.177) | −0.164(−0.165) | (−0.200, −0.150) | (0.026, 0.187) | 0.215(0.213) | (0.175, 0.150) |
| C4-C5 | (−0.208, −0.208) *NNA* | −0.415(−0.415) | (−0.028, 0.028) | (0.208, 0.208) | 0.416(0.416) | (0.000, 0.000) |

(continued)

**Table 4.1** (continued)

| *BCP* | −1.0 | | | +1.0 | | |
|---|---|---|---|---|---|---|
| | (ΔA, ΔB) | ΔBPL (ΔGBL) | (+ΔQ, −ΔQ) | (ΔA, ΔB) | ΔBPL (ΔGBL) | (+ΔQ, −ΔQ) |
| C1-H7 | (0.112, 0.027) | 0.145(0.138) | (---, ---) | (0.048, 0.021) | 0.074(0.067) | (---, ---) |
| C3-H9 | (0.286, 0.102) | 0.405(0.381) | (---, ---) | (0.286, 0.102) | 0.405(0.381) | (---, ---) |
| C5-H11 | (0.009, 0.021) | 0.074(0.067) | (---, ---) | (0.112, 0.027) | 0.145(0.138) | (---, ---) |
| *IR-active mode 28*$^e$, $\nu = 3298.32\ \mathrm{cm}^{-1}$ | | | | | | |
| C1-C2 | (−0.037, −0.037) | −0.074(−0.075) | (**U**, **U**) | (0.038, 0.038) | 0.078(0.076) | (−0.225, 0.225) |
| C2-C3 | (0.014, −0.059) | −0.044(−0.045) | (−0.050, **U**) | (0.027, 0.021) | 0.049(0.048) | (0.000, 0.225) |
| C3-C4 | (0.021, 0.027) | 0.049(0.048) | (−0.225, 0.000) | (−0.059, 0.014) | −0.044(−0.045) | (**U**, 0.050) |
| C4-C5 | (0.152, 0.152) | 0.303(0.303) | (−0.225, 0.225) | (0.019, 0.019) | 0.038(0.038) | (**U**, **U**) |
| C1-H7 | (0.639, 0.386) | 1.047(1.024) | (---, ---) | (−0.648, −0.377) | −1.042(−1.024) | (---, ---) |
| C3-H9 | (0.009, −0.008) | 0.000(0.000) | (---, ---) | (0.009, −0.008) | 0.000(0.000) | (---, ---) |
| C5-H11 | (−0.648, −0.377) | −1.042(−1.024) | (---, ---) | (0.639, 0.386) | 1.047(1.024) | (---, ---) |

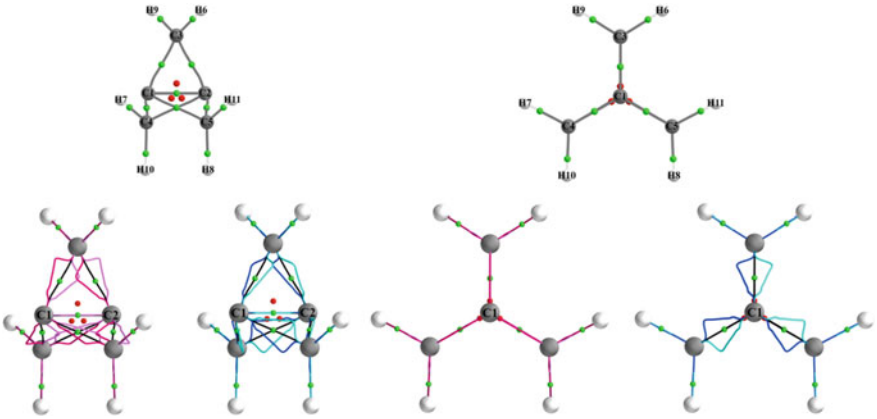

**Fig. 4.12** Two views (top-panel) of the [1.1.1]propellane molecular graphs with atomic numbering scheme, the undecorated green and red spheres denote the bond critical points (*BCPs*) and ring critical points (*RCPs*) respectively. The bond-path framework set B (bottom-panel) is presented with the $\boldsymbol{p}$(dark-blue), $\boldsymbol{p}'$(light-blue) and $\boldsymbol{q}$(dark-magenta, $\boldsymbol{q}'$(light-magenta) paths at the MP2/cc-pVTZ theory level corresponding to the views in the top-panel

character along the entirety of the bond-path [8]. The influence of the single bond character of the axial C1--C2 *BCP* on the neighboring symmetry inequivalent C1-C3 bonding was indicated by the transmission of single bond character determined by the B. These results were found to be consistent for the MP2, CCSD and B3LYP theory levels.

## 4.5 Multi-electronic States

*In this section we consider the multi-stranded bond-path framework set that occurs for excited states, see* Sect. 4.1 *and in particular* Eq. (4.6).

### *4.5.1 Ring-Restoring Reactions*

A photochemical pathway between two conformers (switch positions) are connected may be initiated by a laser pulse that transfers the electronic wave-packet to an excited electronic state. Consequently, an ultra-fast return to the ground state ensured a rapid switching process, where the ultra-fast transfer was mediated by C.I.s, for instance the ring-opening of photochromic (1,3-cyclohexadiene) CHD → HT (1,3,5-hexatriene) [10].

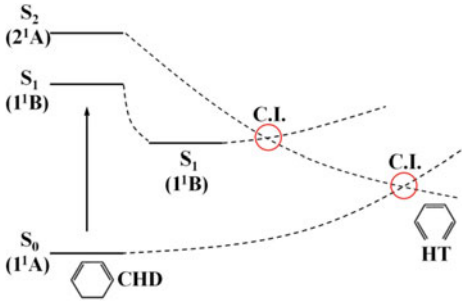


**Fig. 4.13** Scheme of photochemical ring-opening reaction of CHD

The quantum chemical factors underlying the branching ratio (70:30) of the (1,3-cyclohexadiene) CHD → HT (1,3,5-hexatriene) photochemical ring-opening reaction experimentally observed were examined, see Fig. 4.13. High-level multi-reference DFT method was used to optimize the ring-opening reaction path. These calculations yielded a (60:40) CHD → HT photoreaction branching ratio which is in better agreement with the experimental value of (70:30) than results obtained from the CASSCF method. A bonding interaction was subsequently found between the ends of the fissile σ-bond of CHD that steered the ring-opening reaction predominantly in the direction of restoration of the ring for the $S_1$ *and* $S_0$ electronic states.

The factors underlying two possible pathways were explored; the first pathway returned to the ring-closed conformation of the reactant and the second pathway progressed to the ring-opened product. Oscillations in the chemical character of the fissile bond were found for the first pathway before and after the conical intersection that steered the reaction back to react. Several *additional* C.I.s along the $S_1/S_0$ seam were optimized with the bond-path C5-C6 *BCP* in the range of 1.9 Å to 2.5 Å, the C.I. points covered a sufficiently large energy range; up to 150 kcal/mol above the MECI point, see Fig. 4.14 (bottom). The corresponding $H(\mathbf{r_b})$ values presented for the additional points along the C.I. seam demonstrated that for bond-path lengths of 2.5 Å the closed-shell C5--C6 *BCP* possesses a degree of covalent character i.e. $H(\mathbf{r_b}) < 0$. As a consequence the closed-shell C5--C6 *BCP* was regarded as "sticky" and resistant to moving towards the HT product until $H(\mathbf{r_b}) > 0$, see Fig. 4.14 (bottom).

The bond-path framework set $\mathsf{B} = \{(\boldsymbol{p_0}, \boldsymbol{p_1}), (\boldsymbol{q_0}, \boldsymbol{q_1}), \boldsymbol{r}\}$ for the CHD → HT photoreaction was determined and used to demonstrate that the strong shared-shell C5-C6 *BCP* acquires closed-shell *BCP* character early on in the reaction process and this process starts closer CHD for the $S_1$ state than for the $S_0$ state, see Fig. 4.15.

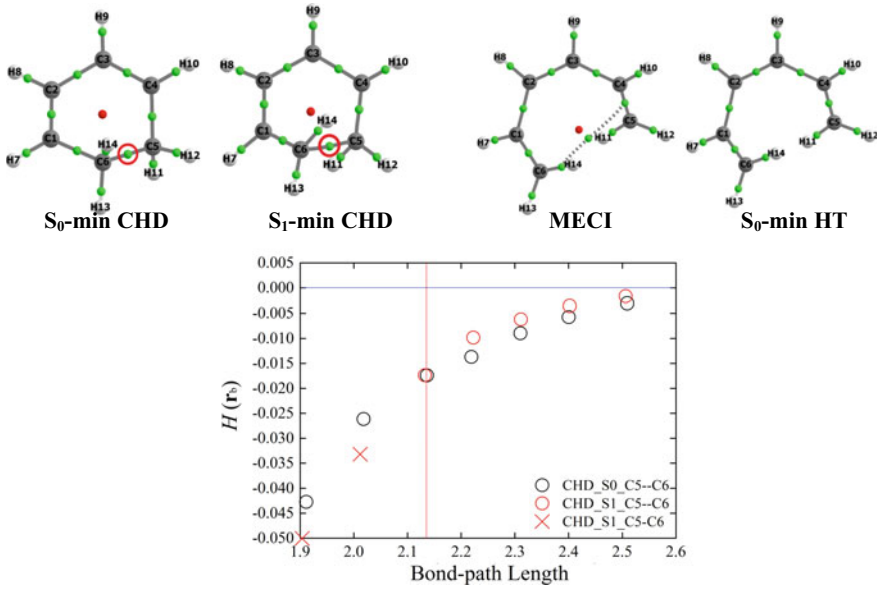


**Fig. 4.14** The molecular graphs (top) for the CHD (FC-closed), CHD (C.I.) temporary state and HT (FC-open) configurations (top); with the ring-opening C5-C6 *BCP* being indicated by a red circle. Note, the C1-C5 bond in the grey-scale sketches corresponds to the C4--C6 *BCP* of the molecular graph. The variation of local total energy density $H(\mathbf{r_b})$ (bottom) for $S_0$ (black) and $S_1$ (red) with the bond-path length (Å) of the closed-shell C5--C6 *BCP* (circle) and shared-shell C5-C6 *BCP* (cross) for the of the CHD molecular graph

### *4.5.2 The Excited State Deactivation Reaction of Fulvene*

NG-QTAIM provided a quantitative 3-D rendering of the all of the bonding for both the ground state ($S_0$) and first excited state ($S_1$) of fulvene consistent with the use of the Lewis structures [6]. This followed on from earlier work that only considered the torsion bond C2-C6 *BCP* bond-path, see Fig. 4.16 [7]

NG-QTAIM however, proved to be useful in quantifying and visualizing bonding in the $S_0$ and $S_1$ states as existing on a continuous spectrum rather than as the simplified extremes presented on the Lewis structures. This was undertaken with both the QTAIM bond-path framework sets $B_{0,1}$, see Fig. 4.17.

NG-QTAIM was used to visualize and quantify the rearrangement of $\rho(\mathbf{r})$ for the $S_0 \rightarrow S_1$ ($S_{01}$) and $S_0 \rightarrow S_2$ ($S_{02}$) natural transition orbital (NTO) $\rho(\mathbf{r})$ densities for fulvene in response to an applied torsion [31].

A greater rearrangement of the total charge density $\rho(\mathbf{r})$ for the $S_0 \rightarrow S_1$ ($S_{01}$) transition at the CI ($\theta = 64.3°$) than at $\theta = 64.3°$ for the $S_0 \rightarrow S_2$ ($S_{02}$) transition was indicated by the greater ellipticity $\varepsilon$ of the $S_0 \rightarrow S_1$ ($S_{01}$) transition. The scalar QTAIM bond-path length (BPL) and associated BPL curvatures were not useful because they

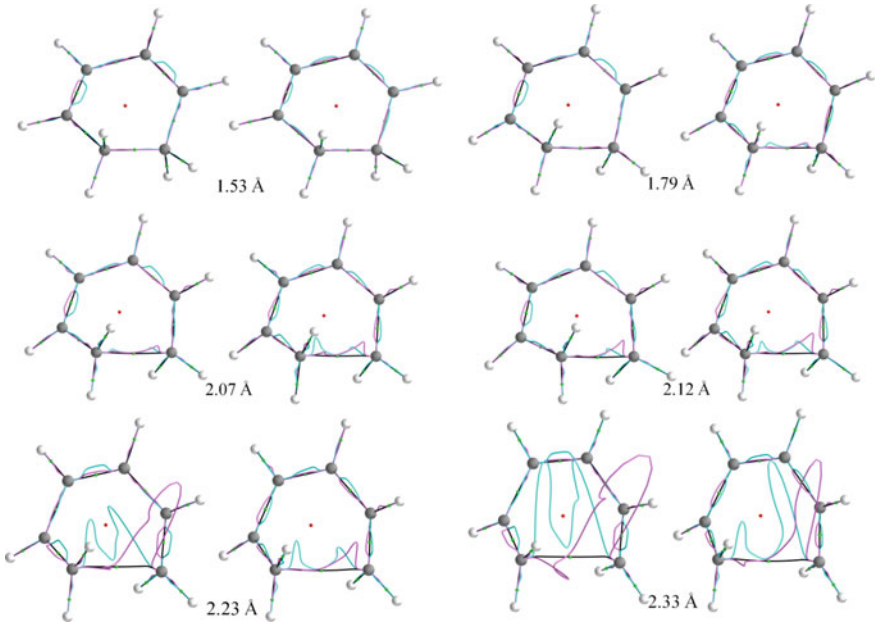


**Fig. 4.15** The $\boldsymbol{p_0}$- and $\boldsymbol{q_0}$-paths for the $S_0$ state (left panel) and corresponding $\boldsymbol{p_1}$- and $\boldsymbol{q_1}$-paths $S_1$ state (right panel) electronic states of the C5-C6 *BCP* bond-path for the CHD → HT photoreaction molecular graph subjected to the bond-length R(C5-C6) distortion for 1.53 Å, 1.79 Å, 2.07 Å, 2.12 Å, 2.23 Å and 2.33 Å

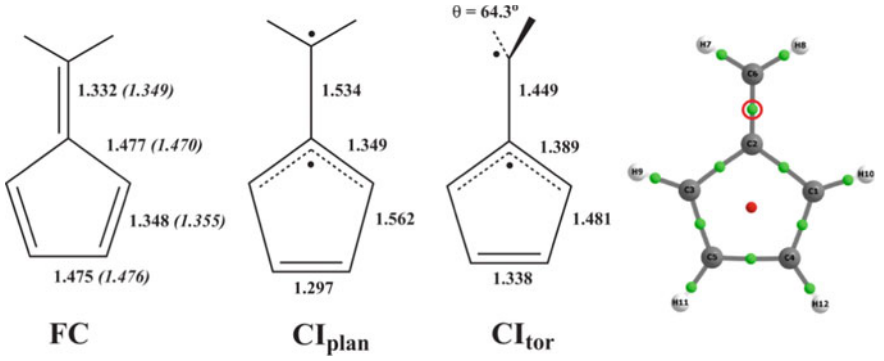


**Fig. 4.16** Geometries of the FC point ($S_0$ state) and the two conical intersections, $CI_{planar}$ and $CI_{tor}$, optimized in this work. Key geometric parameters (in Å) are shown. In parentheses, the gas phase experimental data from [30]. Lewis structures of the $S_0$ (FC) and $S_1$ ($CI_{planar}$ and $CI_{tor}$) states are shown. Atom labeling scheme (right panel) corresponding to the molecular graph and the torsion C2-C6 *BCP* is indicated by a red circle

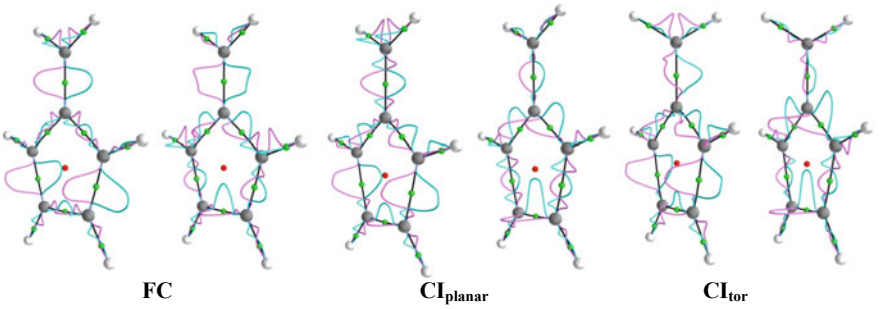


**Fig. 4.17** The Hessian of $\rho(\mathbf{r})$ bond-path frame-work set $B_{0,1}$ with $(\boldsymbol{p}_0, \boldsymbol{q}_0)$-paths (left panels) for $S_0$ and $(\boldsymbol{p}_1, \boldsymbol{q}_1)$-paths (middle-panels) for the $S_1$ states are presented with $(\boldsymbol{p}_0, \boldsymbol{p}_1)$-paths (pale-blue) and $(\boldsymbol{q}_0, \boldsymbol{q}_1)$-paths (magenta) with a magnification factor of $\times$ 5. for torsion $\theta = 64.3°$the FC (left), $CI_{planar}$ (middle) and $CI_{tor}$ (right)

were unable to distinguish the $S_0$, $S_1$, $S_2$ electronic states or the $S_0 \rightarrow S_1$ ($S_{01}$) and $S_0 \rightarrow S_2$ ($S_{02}$) transitions. This demonstrated the insufficiency scalar QTAIM due to the lacks the directional information required to describe the rearrangement of $\rho(\mathbf{r})$.

The $\{\boldsymbol{q_{01}}, \boldsymbol{q_{01}}'\}$ path-packet for the $S_0 \rightarrow S_1$ ($S_{01}$) NTO densities corresponding to the large peak in the bond-path ellipticity $\varepsilon$ profile that envelopes the $S_{01}$ C2-C6 *BCP*, is longer compared with that of the $\{\boldsymbol{q_{02}}, \boldsymbol{q_{02}}'\}$ for the $S_{02}$, $S_0 \rightarrow S_2$ ($S_{02}$) NTO densities see Fig. 4.18. The extent of the C2-C6 *BCP* motion is much lower for the $S_0 \rightarrow S_1$ ($S_{01}$) transition compared with the $S_0 \rightarrow S_2$ ($S_{02}$) transition. The hindering effect on the C2-C6 *BCP* for the $S_{01}$ transition results in a greater extent of the $\{\boldsymbol{q}, \boldsymbol{q}'\}$ path-packet, due to piling up of the ($S_{01}$) NTO charge density $\rho(\mathbf{r})$. The *NCP-BCP* separation ratio for the $S_1$ state 'swaps' from a value of $< 0.5$ to value $> 0.5$ at a value of torsion $\theta = 53.74°$: correspondingly, the C2-*BCP* separation ratio goes from a value $> 0.5$ to a value $> 0.5$, see the inset of Fig. 4.19 (left-panel). This symmetrization effect does not occur for the states $S_0$, $S_2$ or the transitions $S_{01}$ or $S_{02}$ Fig. 4.19 (right panel). From this we hypnotized that the symmetrization of the position of the *BCP* of the torsional C2-C6 *BCP* along the containing C2-C6 *BCP* bond-path was determined to be characteristic of the presence of a conical intersection (CI) for the $S_0 \rightarrow S_1$ ($S_{01}$) transition. A CI was found for the $S_0 \rightarrow S_1$ ($S_{01}$) but not for the $S_0 \rightarrow S_2$ ($S_{02}$) transition, therefore this symmetrization effect may be associated with the presence of a CI along a reaction pathway.

We determined the precessions $\mathsf{K}$ and $\mathsf{K}'$ of the $\{\boldsymbol{p}, \boldsymbol{p}'\}$ and $\{\boldsymbol{q}, \boldsymbol{q}'\}$ path-packets for the excited state deactivation reaction of fulvene that includes the tendencies towards bond-path-rigidity and bond-path-flexibility [22]. An asymmetry is found for the $S_1$ state resulting in non-linear variation the bond-path-rigidity $\mathsf{K}$ as a function of the torsion coordinate $\theta$. The $S_1$ state at torsion $\theta = 0.0°$ was found to uniquely possess the possible maximum bond-path-rigidity, along the entire bond-path but subsequently dropped lower than for the $S_0$ state at the conical intersection indicating photo-excitation facilitated the torsion.

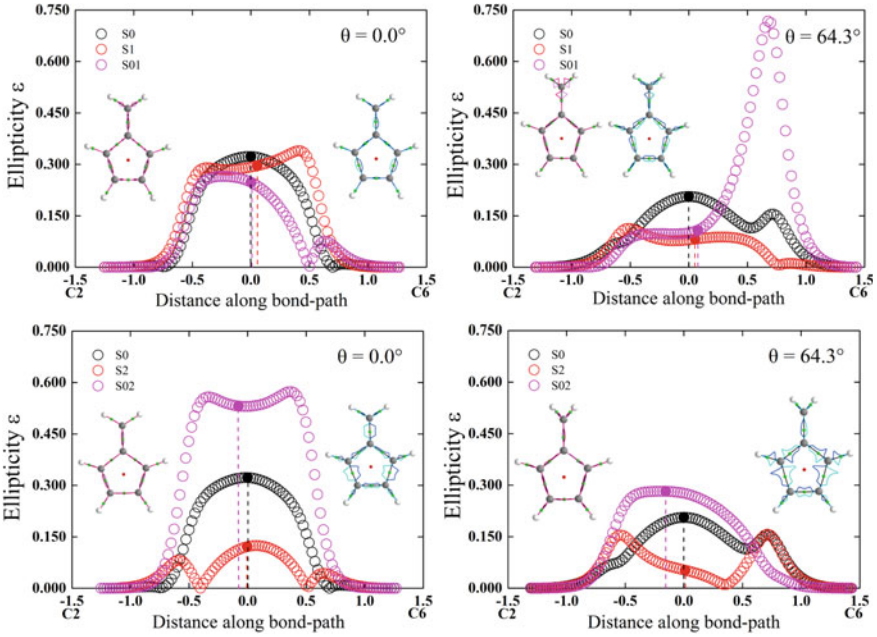


**Fig. 4.18** The variations of the bond-path ellipticity ε profiles of the bond-path ($\boldsymbol{r}$) of the torsional C2-C6 *BCP* corresponding to the electronic states: $S_0$, $S_1$ and $S_{01}$ (top) and $S_0$, $S_2$ and $S_{02}$ (bottom). The vertical dashed lines indicate the position of the *BCP* for each electronic state. The insets correspond to the {$\boldsymbol{q}$(dark-magenta), $\boldsymbol{q'}$(light-magenta)} and {$\boldsymbol{p}$(dark-blue), $\boldsymbol{p'}$(light-blue)}

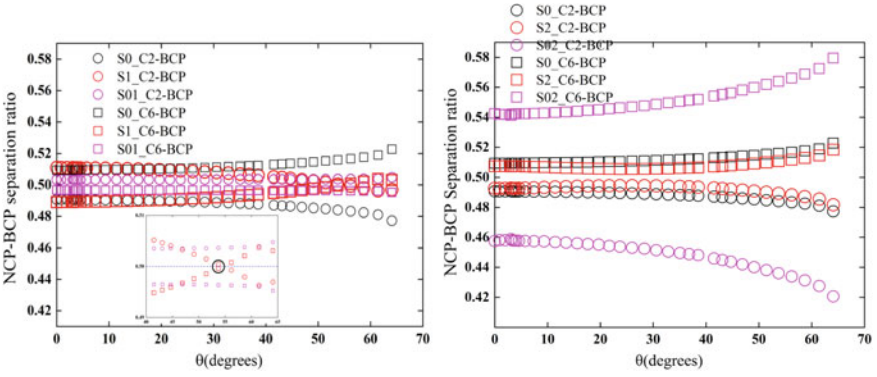


**Fig. 4.19** The variation of the *NCP-BCP* separation ratio with torsion θ for the $S_0 \rightarrow S_1$ ($S_{01}$) (left) and $S_0 \rightarrow S_2$ ($S_{02}$) (right) transitions

Due to the torsion C2-C6 *BCP* bond-path not being in the same plane as an *RCP* a slightly different approach to calculation of the precession $\mathsf{K}'$ of the $\{\boldsymbol{q}, \boldsymbol{q}'\}$ path-packets was taken compared with Sect. 4.2, The precession $\mathsf{K}'$ of the $\{\boldsymbol{q}, \boldsymbol{q}'\}$ path-packets defined by the $\underline{\mathbf{e}}_2$ eigenvector, about the bond-path, $\beta = (\pi/2 - \alpha)$ and $\alpha$ is defined by Eq. (4.8) and the right panel of Fig. 4.20, we can write an expression $\mathsf{K}'$ for the bond-path-flexibility:

$$\mathrm{K}' = 1 - \cos^2\beta, \quad \text{where} \cos\beta = \underline{\mathbf{e}}_2 \cdot \underline{\mathbf{u}}, \ \beta = (\pi/2 - \alpha) \text{ and } 0 \leq \mathrm{K}' \leq 1 \qquad (4.8)$$

For $\mathsf{K}' = 0$ and $\mathsf{K} = 1$ correspond to a maximum and minimum degree of facile character respectively. Therefore values of $\mathsf{K}' = 0$ and $\mathsf{K}' = 1$ indicated bond-paths with the lowest and highest tendencies towards bond-path-flexibility respectively, see Fig. 4.21. Since the C-H *BCP* bond-path is not anchored and may move out of the plane of the $C_5$ ring of the fulvene molecule graph, consequently the $\mathsf{K}$ and $\mathsf{K}'$ will not necessarily be converses of each other as will be the case for C-C *BCP* bond-paths.

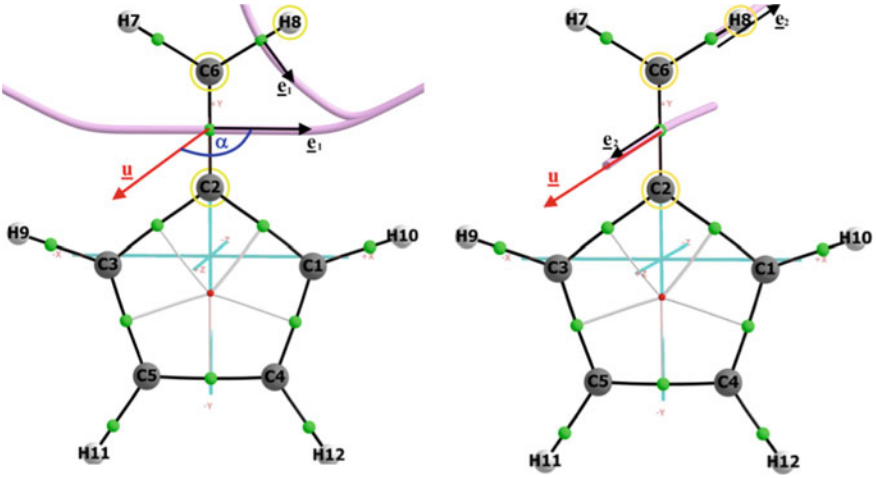


**Fig. 4.20** The $\{\boldsymbol{p}, \boldsymbol{p}'\}$ precession $\mathsf{K}$ construction (left panel) and $\{\boldsymbol{q}, \boldsymbol{q}'\}$ path-packet precession $\mathsf{K}'$ (right panel) for the C2-C6 *BCP* and C6-H8 *BCP* of fulvene, where the $\underline{\mathbf{u}}$ is a unit vector (red arrow) directed parallel to the initial orientation of the $\underline{\mathbf{e}}_2$ eigenvector and the normal vector to the fulvene $C_5$ ring. The pale magenta line indicates the interatomic surface paths (IAS) that originate at the *BCP*. The $\underline{\mathbf{e}}_1$ eigenvector and $\underline{\mathbf{e}}_2$ eigenvector, the $\pm$ signs of $\underline{\mathbf{e}}_1$ and $\underline{\mathbf{e}}_2$ are chosen to form the right handed orthogonal set $\{\underline{\mathbf{e}}_1, \underline{\mathbf{e}}_2, \underline{\mathbf{e}}_3\}$

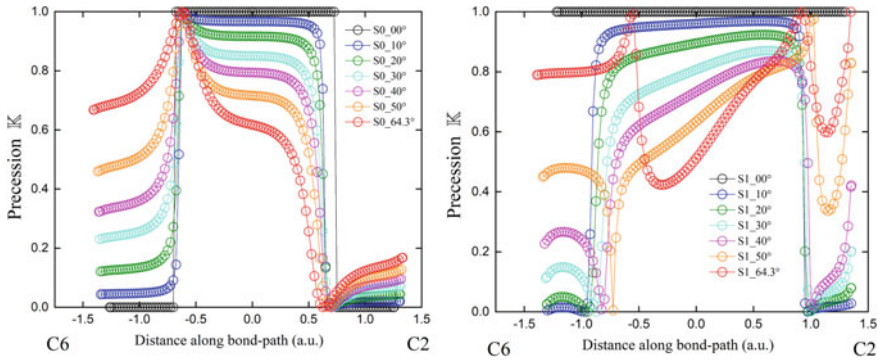


**Fig. 4.21** The variation of the precession $\mathsf{K}$ along the fulvene torsion C2-C6 *BCP* bond-path for $S_0$ (left-panel) and $S_1$ (right-panel) electronic states for values of the torsion $\theta = 0.0°$ (FC) to $\theta = 64.3°$ ($CI_{tor}$)

### 4.5.3 *Factors Influencing the Relative Stability of the Conical Intersections of the Penta-2,4-Dieniminium Cation (PSB3)*

The bond-path framework set $\mathsf{B}$ enabled a more balanced treatment of the covalent and ionic contributions of the ground ($S_0$) and the ($S_1$) excited electronic states of PSB3 by providing a directional representation of the chemical bond [15]. The mix of covalent (diradical) and ionic electronic configurations was precisely established by quantifying the most preferred ($\underline{\mathbf{e}}_2$) directions of the accumulation of $\rho(\mathbf{r})$ from the $\{\boldsymbol{q}, \boldsymbol{q}'\}$ path-packets along the bond-path ($\boldsymbol{r}$). The $\{\boldsymbol{q}, \boldsymbol{q}'\}$ path-packets provided a 'bond-localized orbital-like' directional interpretation of bonding. The reason to determine the ionicity/covalency mix of the $S_0$ and the $S_1$ states is that this defines the geometries at which crossings between the $S_1$ and $S_0$ states, the conical intersections (C.I.), occur.

Using $\mathsf{B}$, obtained from multi-reference DFT calculations where the dynamic correlation is included from the outset, demonstrated that the iconicity of the excited state of PSB3 increased considerably as compared with the widely accepted view based on the CASSCF calculations. The increased iconicity of the $S_1$ state resulted in reverting the energetic stability of the C.I.s corresponding to torsion about the C1-C2 *BCP* and C10-N12 *BCP*, see Fig. 4.22. The electronic structure of PSB3 near the C10-N12 *BCP* C.I. is much more ionic than could be expected from CASSCF and this led to the destabilization of this C.I. compared to the C1-C2 *BCP* C.I.; that has considerable implications for the mechanism of photoisomerization of PSB3.

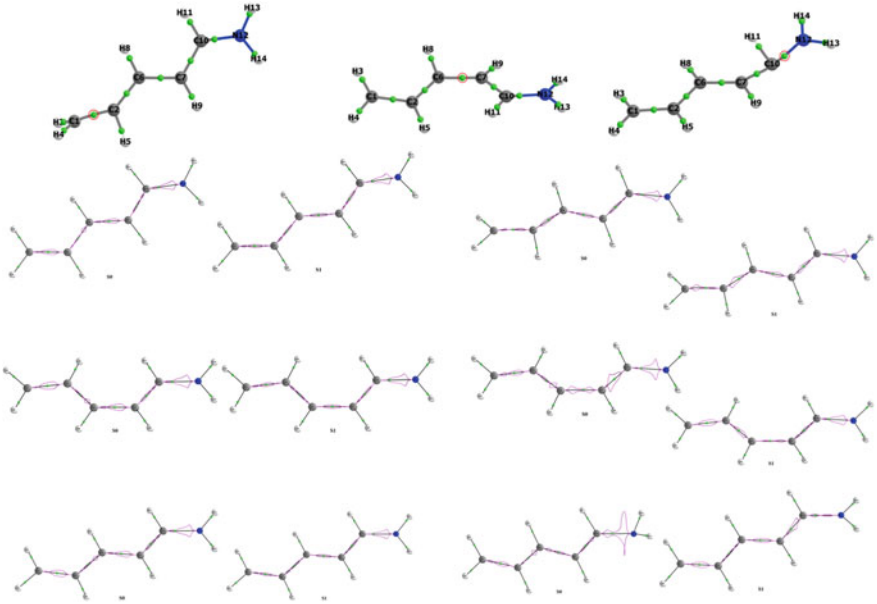

**Fig. 4.22** The atomic numbering scheme and the $\{\boldsymbol{q}, \boldsymbol{q}'\}$-path-packets for the $S_0$ (left) and $S_1$ (right) states at a value of the torsion $\theta = 0.0°$ (left-panels) along and $\theta = 90.0°$ (right-panels) of the backbone bond-path ($\boldsymbol{r}$) corresponding to the torsional C1-C2 *BCP* (top-panels), C6-C7 *BCP* (middle-panels) and C10-N12 *BCP* (bottom-panels). The undecorated green spheres indicate the position of the *BCPs*

## 4.6 Summary

The NG-QTAIM interpretation of the chemical bond: the bond-path frame-work set B provides a consistent 3-D chemical definition of a molecule returning much more information than the scalar QTAIM molecular graph.

The bond-path frame-work set B and associated precession K been demonstrated to be suitable for the analysis of dynamic and static charge density distributions, both in the ground state and multi-excited states, in addition to natural transition orbitals (NTOs).

The dynamic phenomena include normal modes of vibration, ring restoring reactions and photochemical reaction pathways. The static phenomena include strained and unusual bonding environments including comparing the SR-ZORA Hamilton and effective core potentials (ECPs) for relativistic effects.

In Chap. 5 we use will use consider the stress tensor $\boldsymbol{\sigma}(\mathbf{r})$ and Ehrenfest Force $\mathbf{F}(\mathbf{r})$. The stress tensor version of the bond-path-framework $B_\sigma$ is better than is the Hessian version B. The Ehrenfest Force $\mathbf{F}(\mathbf{r})$ is able to solve covalent bond and hydrogen bond coupling in addition to understanding the nature of non-nuclear attractors (*NNA*s).

**Target learning outcomes**:

- Understand the differences of the NG-QTAIM representation of the chemical bond and scalar QTAIM.
- Understand the wrapping of bond-path framework set B: the precession K.
- Understand the bond-path framework set B in terms of least/least easy directions of accumulation of $\rho(\mathbf{r})$
- Understand the treatment of dynamic and static bonding environments.
- Understand the construction of B for excited states and natural transition orbitals (NTOs).

## 4.7 Further Reading

A recent review by E. Kraka et al., on modern vibrational spectroscopy can provide information about the electronic structure of a molecule, the strength of its bonds and its conformational flexibility is encoded in the normal vibrational modes [32].

Basic details of the reasons for the unusual structure of [1.1.1]propellane were earlier considered [33].

Conical intersections (C.I.s) are known to be the core feature of organic photochemistry: background is provided [34]. We include several articles on the electrocyclic ring-opening photoreaction of 1,3-cyclohexadiene (CHD) to 1,3,5,-hexatriene (HT) because it is a prototypical reaction relevant for many photochemical ring-opening processes important for synthetic organic chemistry and biochemistry [35–39].

Thorough theoretical investigations of the interplay in PSB3 between the diradicaloid [40] and (zwitter-)ionic states that occur along the path to $S_1/S_0$ C.I.s have been undertaken [41–50].

Earlier firstly identified fulvene as a potential benchmark [51] and secondly demonstrated that the interpolation along the crossing seam linked the critical points of the projected $S_1/S_0$ gradient are recommended [52].

M. Filatov has written a chapter on density functional (DFT) methods for excited states that we have used throughout this book [53].

## References

1. Jenkins S, Heggie MI (2000) Quantitative analysis of bonding in 90° partial dislocation in diamond. J Phys Condens Matter 12:10325–10333
2. Jenkins S, Morrison I (2000) The chemical character of the intermolecular bonds of seven phases of ice as revealed by ab initio calculation of electron densities. Chem Phys Lett 317:97–102

3. Azizi A, Momen R, Kirk SR, Jenkins S (2019) 3-D bond-paths of QTAIM and the stress tensor in neutral lithium clusters, Lim (m = 2–5), presented on the Ehrenfest force molecular graph. Phys Chem Chem Phys 22:864–877
4. Huang WJ, Xu T, Kirk SR, Jenkins S (2018) The 3-D bonding morphology of the infra-red active normal modes of benzene. Chem Phys Lett 710:31–38
5. Li JH, Huang WJ, Xu T, Kirk SR, Jenkins S (2018) Stress tensor eigenvector following with next-generation quantum theory of atoms in molecules. Int J Quantum Chem 119:e25847
6. Huang WJ, Xu T, Kirk SR, Filatov M, Jenkins S (2018) QTAIM and stress tensor bond-path framework sets for the ground and excited states of fulvene. Chem Phys Lett 713:125–131
7. Huang WJ, Momen R, Azizi A, Xu T, Kirk SR, Filatov M, Jenkins S (2018) Next-generation quantum theory of atoms in molecules for the ground and excited states of Fulvene. Int J Quantum Chem 118:e25768
8. Bin X, Xu T, Kirk SR, Jenkins S (2019) The directional bonding of [1.1.1]propellane with next generation QTAIM. Chem Phys Lett 730:506–512
9. Xu T, Momen R, Azizi A, van Mourik T, Früchtl H, Kirk SR, Jenkins S (2019) The destabilization of hydrogen bonds in an external E-field for improved switch performance. J Comput Chem 40:1881–1891
10. Tian T, Xu T, Kirk SR, Filatov M, Jenkins S (2019) Next-generation quantum theory of atoms in molecules for the ground and excited state of the ring-opening of cyclohexadiene (CHD). Int J Quantum Chem 119:e25862
11. Tian T, Xu T, Kirk SR, Filatov M, Jenkins S (2019) Next-generation quantum theory of atoms in molecules for the ground and excited state of DHCL. Chem Phys Lett 717:91–98
12. Bin X, Azizi A, Xu T, Kirk SR, Filatov M, Jenkins S (2019) Next-generation quantum theory of atoms in molecules for the photochemical ring-opening reactions of oxirane. Int J Quantum Chem 119:e25957
13. Tian T, Xu T, van Mourik T, Früchtl H, Kirk SR, Jenkins S (2019) Next generation QTAIM for the design of quinone-based switches. Chem Phys Lett 722:110–118
14. Wang L, Azizi A, Xu T, Kirk SR, Jenkins S (2019) Explanation of the role of hydrogen bonding in the structural preferences of small molecule conformers. Chem Phys Lett 730:206–212
15. Bin X, Momen R, Xu T, Kirk SR, Filatov M, Jenkins S (2019) A 3-D bonding perspective of the factors influencing the relative stability of the S1/S0 conical intersections of the penta-2,4-dieniminium cation (PSB3). Int J Quantum Chem 119:e25903
16. Malcomson T, Azizi A, Momen R, Xu T, Kirk SR, Paterson MJ, Jenkins S (2019) Stress tensor eigenvector following with next-generation quantum theory of atoms in molecules: excited state photochemical reaction path from benzene to benzvalene. J Phys Chem A 123:8254–8264
17. Li S, Xu T, van Mourik T, Früchtl H, Kirk SR, Jenkins S (2019) Halogen and hydrogen bonding in halogenabenzene/$NH_3$ complexes compared using next-generation QTAIM. Molecules 24:2875
18. Li S, Azizi A, Kirk SR, Jenkins S (2020) An explanation of the unusual strength of the hydrogen bond in small water clusters. Int J Quantum Chem 120:e26361
19. Azizi A, Momen R, Früchtl H, van Mourik T, Kirk SR, Jenkins S (2020) Next-generation QTAIM for scoring molecular wires in E-fields for molecular electronic devices. J Comput Chem 41:913–921
20. Yang Y, Xu T, Kirk SR, Jenkins S (2021) Bond flexing, twisting, anharmonicity and responsivity for the infrared-active modes of benzene. Int J Quantum Chem 121:e26584
21. Nie X, Yang Y, Xu T, Kirk SR, Jenkins S (2021) Fatigue and fatigue resistance in S1 excited state diarylethenes in electric fields. Int J Quantum Chem 121:e26527
22. Mahara B, Azizi A, Yang Y, Filatov M, Kirk SR, Jenkins S (2021) Bond-path-rigidity and Bond-path-flexibility of the ground state and first excited state of Fulvene. Chem Phys Lett 766:138339
23. Hu MX, Xu T, Momen R, Azizi A, Kirk SR, Jenkins S (2017) The normal modes of vibration of benzene from the trajectories of stress tensor eigenvector projection space. Chem Phys Lett 677:156–161

24. Huang WJ, Azizi A, Xu T, Kirk SR, Jenkins S (2018) A vector-based representation of the chemical bond for the normal modes of benzene. Int J Quantum Chem 118:e25698
25. Bader RFW, Slee TS, Cremer D, Kraka E (1983) Description of conjugation and hyperconjugation in terms of electron distributions. J Am Chem Soc 105:5061–5068
26. Yepes D, Kirk SR, Jenkins S, Restrepo A (2012) Structures, energies and bonding in neutral and charged Li microclusters. J Mol Model 18:4171–4189
27. Azizi A, Momen R, Kirk SR, Jenkins S (2020) 3-D bond-paths of QTAIM and the stress tensor in neutral lithium clusters, Lim (m = 2–5), presented on the Ehrenfest force molecular graph. Phys Chem Chem Phys 22:864–877
28. Azizi A, Momen R, Xu T, Kirk SR, Jenkins S (2018) Non-nuclear attractors in small charged lithium clusters, Limq (m = 2–5, q = ±1), with QTAIM and the Ehrenfest force partitioning. Phys Chem Chem Phys 20:24695–24707
29. Tian T, Xu T, Kirk SR, Rongde IT, Tan YB, Manzhos S, Shigeta Y, Jenkins S (2020) Intramolecular mode coupling of the isotopomers of water: a non-scalar charge density-derived perspective. Phys Chem Chem Phys 22:2509–2520
30. Baron PA, Brown RD, Burden FR, Domaille PJ, Kent JE (1972) The microwave spectrum and structure of fulvene. J Mol Spectrosc 43:401–410
31. Wang L, Azizi A, Xu T, Filatov M, Kirk SR, Paterson MJ, Jenkins S (2020) The role of the natural transition orbital density in the S0 → S1 and S0 → S2 transitions of Fulvene with next generation QTAIM. Chem Phys Lett 751:137556
32. Kraka E, Zou W, Tao Y (2020) Decoding chemical information from vibrational spectroscopy data: Local vibrational mode theory. WIREs Comput Mol Sci 10:e1480
33. Newton MD, Schulman JM (1972) Theoretical studies of tricyclo[1.1.1.01,3]pentane and bicyclo[1.1.1]pentane. J Am Chem Soc 94:773–778
34. Robb MA (2014) In this molecule there must be a conical intersection. Adv Phys Org Chem 48:189–228
35. Fuß W, Schmid WE, Trushin SA (2000) Time-resolved dissociative intense-laser field ionization for probing dynamics: femtosecond photochemical ring opening of 1,3-cyclohexadiene. J Chem Phys 112:8347–8362
36. Hofmann A, Vivieriedle RD (2000) Quantum dynamics of photoexcited cyclohexadiene introducing reactive coordinates. J Chem Phys 112:5054–5059
37. Garavelli M, Celani P, Fato M, Bearpark MJ, Smith BR, Olivucci M, Robb MA (1997) Relaxation paths from a conical intersection: the mechanism of product formation in the cyclohexadiene/hexatriene photochemical interconversion. J Phys Chem A 101:2023–2032
38. Celani P, Ottani S, Olivucci M, Bernardi F, Robb MA (1994) What happens during the picosecond lifetime of 2A1 Cyclohexa-1,3-diene? A CAS-SCF Study of the Cyclohexadiene/Hexatriene Photochemical Interconversion. J Am Chem Soc 116:10141–10151
39. Celani P, Bernardi F, Robb MA, Olivucci M (1996) Do photochemical ring-openings occur in the spectroscopic state? $^1B_2$ pathways for the cyclohexadiene/hexatriene photochemical interconversion. J Phys Chem 100:19364–19366
40. Abe M (2013) Diradicals. Chem Rev 113:7011–7088
41. Tuna D, Lefrancois D, Wolański Ł, Gozem S, Schapiro I, Andruniów T, Dreuw A, Olivucci M (2015) Assessment of approximate coupled-cluster and algebraic-diagrammatic-construction methods for ground- and excited-state reaction paths and the conical-intersection seam of a retinal-chromophore model. J Chem Theory Comput 11:5758–5781
42. Zen A, Coccia E, Gozem S, Olivucci M, Guidoni L (2015) Quantum Monte Carlo treatment of the charge transfer and diradical electronic character in a retinal chromophore minimal model. J Chem Theory Comput 11:992–1005
43. Garavelli M, Celani P, Bernardi F, Robb MA, Olivucci M (1997) The $C_5H_6NH_{2+}$ protonated Shiff Base: an ab initio minimal model for retinal photoisomerization. J Am Chem Soc 119:6891–6901
44. Garavelli M, Bernardi F, Robb MA, Olivucci M (1999) The short-chain acroleiniminium and pentadieniminium cations: towards a model for retinal photoisomerization. A CASSCF/PT2 study. J Mol Struct THEOCHEM 463:59–64

45. Huix-Rotllant M, Filatov M, Gozem S, Schapiro I, Olivucci M, Ferré N (2013) Assessment of density functional theory for describing the correlation effects on the ground and excited state potential energy surfaces of a retinal chromophore model. J Chem Theor Comput 9:3917–3932
46. Xu X, Gozem S, Olivucci M, Truhlar DG (2013) Combined self-consistent-field and spin-flip Tamm-Dancoff density functional approach to potential energy surfaces for photochemistry. J Phys Chem Lett 4:253–258
47. Gozem S, Krylov AI, Olivucci M (2013) conical intersection and potential energy surface features of a model retinal chromophore: comparison of EOM-CC and multireference methods. J Chem Theory Comput 9:284–292
48. Gozem S, Huntress M, Schapiro I, Lindh R, Granovsky AA, Angeli C, Olivucci M (2012) Dynamic electron correlation effects on the ground state potential energy surface of a retinal chromophore model. J Chem Theory Comput 8:4069–4080
49. Gozem S, Melaccio F, Lindh R, Krylov AI, Granovsky AA, Angeli C, Olivucci M (2013) Mapping the excited state potential energy surface of a retinal chromophore model with multireference and equation-of-motion coupled-cluster methods. J Chem Theor Comput 9:4495–4506
50. Gozem S, Melaccio F, Valentini A, Filatov M, Huix-Rotllant M, Ferré N, Frutos LM, Angeli C, Krylov AI, Granovsky AA, Lindh R, Olivucci M (2014) Shape of multireference, equation-of-motion coupled-cluster, and density functional theory potential energy surfaces at a conical intersection. J Chem Theory Comput 10:3074–3084
51. Bearpark MJ, Bernardi F, Olivucci M, Robb MA, Smith BR (1996) Can Fulvene S1 decay be controlled? A CASSCF study with MMVB dynamics. J Am Chem Soc 118:5254–5260
52. Bearpark MJ, Blancafort L, Paterson MJ (2006) Mapping the intersection space of the ground and first excited states of fulvene. Mol Phys 104:1033–1038
53. Filatov M, Ensemble DFT (2015) Approach to excited states of strongly correlated molecular systems. in density-functional methods for excited states. In: Ferré N, Filatov M, Huix-Rotllant M (eds). Springer International Publishing, pp 97–124

# Chapter 5
# The Stress Tensor σ(r) and Ehrenfest Force F(r)

*Great results can be achieved with small force.*
*Sun Tzu*

In this chapter we build on the NG-QTAIM representation of the chemical bond presented in Chap. 4, the bond-path framework set $\mathsf{B}$. The bond-path framework set $\mathsf{B}$ was constructed to be applicable for use with the stress tensor $\boldsymbol{\sigma}(\mathbf{r})$ and Ehrenfest Force $\mathbf{F}(\mathbf{r})$. In Sect. 5.1 we outline the basics of the stress tensor $\boldsymbol{\sigma}(\mathbf{r})$, explaining its relationship to the Hessian of $\rho(\mathbf{r})$ partitioning and construction of the stress tensor bond-path framework set $\mathsf{B}_{\boldsymbol{\sigma}}$. In Sect. 5.1.1 we provide an example using the torsion of ethene to compare the used in the Hessian of $\rho(\mathbf{r})$ bond-path framework set $\mathsf{B}$ and stress tensor bond-path framework set $\mathsf{B}_{\boldsymbol{\sigma}}$. In Sect. 5.1.2 we consider the mixed bonding character of halogen-bonding and hydrogen-bonding in halogenabenzene and include consideration of relativistic effects. The photochemical reaction path from benzene to benzvalene was investigated and $\mathsf{B}_{\boldsymbol{\sigma}}$ was particularly useful at explaining the explosive nature of benzvalene. In Sect. 5.2 the Ehrenfest Force $\mathbf{F}(\mathbf{r})$ partitioning was outlined including the implementation details. In Sects. 5.2.1–5.2.2 examples including small lithium and water clusters are examined. The Ehrenfest Force $\mathbf{F}(\mathbf{r})$ precessions $\mathsf{K}'_{\mathbf{F}}$ and $\mathsf{K}_{\mathbf{F}}$ corresponding to the Ehrenfest Force $\mathbf{F}(\mathbf{r})$ are explained in Sect. 5.3. In Sect. 5.3.1 Ehrenfest Force $\mathbf{F}(\mathbf{r})$ precessions $\mathsf{K}'_{\mathbf{F}}$ and $\mathsf{K}_{\mathbf{F}}$ are applied to small water clusters. The summary of the chapter was presented in Sect. 5.4 by outlining benefits, limitations and suggestions for further investigations of the ideas introduced. Further reading materials are provided in Sect. 5.5.

**Scientific goals to be addressed:**

- Explore differences between the Hessian of $\rho(\mathbf{r})$, the stress tensor $\boldsymbol{\sigma}(\mathbf{r})$ and the Ehrenfest Force $\mathbf{F}(\mathbf{r})$.
- Consider the competition between halogen and hydrogen bonding.
- Explain the explosive character of benzvalene in terms of the bonding.
- Explore the origins of non-nuclear attractors (*NNA*s) in lithium.
- Explain why the average hydrogen-bond strength in $(H_2O)_6$ is lower than for $(H_2O)_4$.

© The Author(s), under exclusive license to Springer Nature Singapore Pte Ltd. 2023

S. Jenkins and S. R. Kirk, *Next Generation Quantum Theory of Atoms in Molecules*,
Lecture Notes in Chemistry 110, https://doi.org/10.1007/978-981-99-0329-0_5

- Visualize and explain the nature of the two-way donation of sigma and hydrogen-bond character.

## 5.1 The Stress Tensor σ(r)

In this work we use the definition of the stress tensor proposed by Bader to investigate the stress tensor properties within QTAIM [1]. The quantum stress tensor $\boldsymbol{\sigma}(\mathbf{r})$ was used to characterize the mechanics of the forces acting on the electron density distribution in open systems, defined as:

$$\boldsymbol{\sigma}(\mathbf{r}) = -\frac{1}{4}\left[\left(\frac{\partial^2}{\partial \mathbf{r}_i \partial \mathbf{r}_j{}'} + \frac{\partial^2}{\partial \mathbf{r}_i{}' \partial \mathbf{r}_j} - \frac{\partial^2}{\partial \mathbf{r}_i \partial \mathbf{r}_j} - \frac{\partial^2}{\partial \mathbf{r}_i{}' \partial \mathbf{r}_j{}'}\right) \cdot \gamma\left(\mathbf{r}, \mathbf{r}'\right)\right]_{\mathbf{r}=\mathbf{r}'} \tag{5.1}$$

where $\gamma(\mathbf{r},\mathbf{r}')$ is the one-body density matrix,

$$\gamma\left(\mathbf{r}, \mathbf{r}'\right) = N \int \Psi(\mathbf{r}, \mathbf{r}_2, \ldots, \mathbf{r}_N)\Psi^*\left(\mathbf{r}', \mathbf{r}_2, \ldots, \mathbf{r}_N\right)\mathrm{d}\mathbf{r}_2 \cdots \mathrm{d}\mathbf{r}_N \tag{5.2}$$

The stress tensor is then any quantity $\boldsymbol{\sigma}(\mathbf{r})$, that satisfies Eq. (5.1) since one can add any divergence free tensor to the stress tensor without violating this definition [1–3].

A small cube of fluid flowing in 3-D space the stress $\Pi(x, y, z, t)$, a rank-3 tensor field, has nine components [4] of these the three diagonal components $\Pi_{xx}$, $\Pi_{yy}$, and $\Pi_{zz}$ correspond to normal stress. A negative value for these normal components corresponds to a compression of the cube, conversely a positive value corresponds to a pulling or tension, where more negative/positive values correspond to increased compression/tension of the cube. Diagonalization of the stress tensor $\boldsymbol{\sigma}(\mathbf{r})$, returns the principal electronic stresses $\Pi_{xx}$, $\Pi_{yy}$, and $\Pi_{zz}$ in the form of the stress tensor eigenvalues $\lambda_{1\sigma}$, $\lambda_{2\sigma}$, $\lambda_{3\sigma}$, with associated eigenvectors $\underline{\mathbf{e}}_{\mathbf{1}\sigma}$, $\underline{\mathbf{e}}_{\mathbf{2}\sigma}$, $\underline{\mathbf{e}}_{\mathbf{3}\sigma}$. The stress tensor $\boldsymbol{\sigma}(\mathbf{r})$ eigenvalues $\lambda_{1\sigma}$, $\lambda_{2\sigma}$, $\lambda_{3\sigma}$, and eigenvectors $\underline{\mathbf{e}}_{\mathbf{1}\sigma}$, $\underline{\mathbf{e}}_{\mathbf{2}\sigma}$, $\underline{\mathbf{e}}_{\mathbf{3}\sigma}$ are generally calculated within the QTAIM partitioning, although the Ehrenfest Force partitioning has also been used, see Sect. 5.2.

The normal modes of vibration of nuclei are used in the *electron-following* picture to understand chemical properties [5–8]. The eigenvectors of the stress tensor $\boldsymbol{\sigma}(\mathbf{r})$ are used in the *electron-preceding* picture where chemical reactions are guided by changes in electronic charge density distribution [9]. In the electron-preceding picture movements of the bonds, rather than the nuclei, was used to quantify changes to the molecular structure (i.e. molecular graph).

The stress tensor usually $\boldsymbol{\sigma}(\mathbf{r})$ has one tensile eigenvector $\underline{\mathbf{e}}_{\mathbf{3}\sigma}$ with associated eigenvalue ($0 < \lambda_{3\sigma}$) and two compressive eigenvectors $\underline{\mathbf{e}}_{\mathbf{1}\sigma}$ and $\underline{\mathbf{e}}_{\mathbf{2}\sigma}$ with corresponding eigenvalues ($\lambda_{1\sigma} < \lambda_{2\sigma} < 0$) at a *BCP*. The stress tensor $\boldsymbol{\sigma}(\mathbf{r})$ however, may have *three* compressive eigenvectors ($\lambda_{1\sigma} < \lambda_{2\sigma} < \lambda_{3\sigma} < 0$) for topologically unstable *BCP*s as

was the case for the H---H *BCP*s in biphenyl subjected to a torsion [10]. The tensile eigenvector describes the pull of the nuclei on the electrons towards the center of the bond-path. The compressive eigenvectors describes the attraction of electrons along the bond-path. The most negative of the compressive stress tensor eigenvectors $\underline{\mathbf{e}}_{\mathbf{1\sigma}}$ is therefore the most compressive and is usually, although not always, associated with the Hessian of $\rho(\mathbf{r})$ $\underline{\mathbf{e}}_{\mathbf{2}}$ eigenvector where the *BCP* ellipticity $\varepsilon > 0$. The eigenvalues of the stress tensor are ordered ($\lambda_{1\sigma} < \lambda_{2\sigma} < 0$) at a *BCP* and $\lambda_{1\sigma}$ has the largest associated compressive stress. Consequently, the $\underline{\mathbf{e}}_{\mathbf{1\sigma}}$ direction, for a *BCP* subjected to a bond torsion perturbation, corresponds to the direction of maximum response, i.e. the most "preferred" direction, of the $\rho(\mathbf{r_b})$ in the plane perpendicular to the bond-path**.** Conversely, the corresponding $\underline{\mathbf{e}}_{\mathbf{2\sigma}}$ direction corresponds to the direction of minimum response of the $\rho(\mathbf{r_b})$ and hence the least preferred direction. The concept of maximum and minimum response of the $\rho(\mathbf{r_b})$ is central to the understanding of the stress tensor trajectories at that covered in detail in Chap. 6.

Sufficient bond migration could result in a topological catastrophe indicating significant changes that often occur in chemical reactions [11–16].

The NG-QTAIM use of the stress tensor more closely relates to the profound work of Tachibana et al. [17–21], who used the stress tensor's "spindle structure" to determine electron pairing and covalent bonding. This previous work by Bader et al. and Tachibana et al. provides strong support for building chemical concepts using the stress tensor.

The NG-QTAIM implementation of the stress tensor $\boldsymbol{\sigma}(\mathbf{r})$ is closer to the spirit of Tachibana's work in that it is not limited *BCP* but occupies the space above *and* below along the entire extent of the bond-path, thereby more closely resembling the spindle structure of Tachibana.

The earlier attempt [22] with the phonon modes of ice assumed, in an over simplification, that there was a one-to-one mapping between the QTAIM least preferred $\underline{\mathbf{e}}_{\mathbf{1}}$ and most preferred $\underline{\mathbf{e}}_{\mathbf{2}}$ directions of motions of the electronic charge density and the stress tensor $\underline{\mathbf{e}}_{\mathbf{1\sigma}}$ and $\underline{\mathbf{e}}_{\mathbf{2\sigma}}$ eigenvectors [9] or even only the eigenvalues [23]. Later investigations clearly demonstrated a lack of one-to-one mapping between the eigenvectors and eigenvalues of QTAIM and the stress tensor [24, 25]. This confusion was due to the accidental and occasional coincidence of the Hessian of $\rho(\mathbf{r})$ $\underline{\mathbf{e}}_{\mathbf{2}}$ and stress tensor $\underline{\mathbf{e}}_{\mathbf{2\sigma}}$ eigenvector directions for asymmetrical bonds where the BCP was not located at the bond-path mid-point. These misleading results occurred as a consequence of the use of the stress tensor within the QTAIM partitioning where for the stress tensor $\boldsymbol{\sigma}(\mathbf{r})$ *BCP*s the $-\nabla\boldsymbol{\sigma}(\mathbf{r_b}) \neq 0$ unlike the QTAIM result $\nabla\rho(\mathbf{r_b}) = 0$. This led us to realize the need to track the eigenvectors the QTAIM and stress tensor $\boldsymbol{\sigma}(\mathbf{r})$ eigenvectors along the entire bond-path rather than only at the *BCP*.

### 5.1.1 The Stress Tensor σ(r) Bond-Path Framework Set $\mathbf{B}_\sigma$

Recent investigations using ethene developed an in depth understanding of the *directional* character of the stress tensor i.e. the $\underline{\mathbf{e}}_{1\sigma}$ and $\underline{\mathbf{e}}_{2\sigma}$ eigenvectors [26].

We see that the variation of the ellipticity $\boldsymbol{\varepsilon}$ of the C1-H3 *BCP* is rather similar to that of the stress tensor ellipticity $\varepsilon_{\sigma H}$ that could mislead the reader into thinking that the *scalar* QTAIM and stress tensor $\boldsymbol{\sigma}(\mathbf{r})$ behaviors are also similar and therefore that QTAIM can be used as an approximation of the stress tensor $\boldsymbol{\sigma}(\mathbf{r})$, see Fig. 5.3. It may be expected that the *symmetrical* C1-C2 *BCP* bond-path that the QTAIM and stress tensor $\boldsymbol{\sigma}(\mathbf{r})$ properties would be more similar than for the asymmetrical C1-H3 *BCP* bond-path. This may be expected on the basis of the greater matching of the locations of the C1-C2 *BCP* between the QTAIM and stress tensor $\boldsymbol{\sigma}(\mathbf{r})$ than for the corresponding locations of the C1-H3 *BCP*. Examination of the variations of the QTAIM ellipticity ε and the stress tensor $\boldsymbol{\sigma}(\mathbf{r})$ ellipticities $\varepsilon_{\sigma H}$ and $\varepsilon_\sigma$ however, shows that this not the case, see Fig. 5.1.

Consideration of the QTAIM and stress tensor eigenvectors along the *entire* bond-path rather than *only* at the *BCP*, avoids such misleading results. An additional consequence of the mismatch in the positions of $\nabla\rho(\mathbf{r_b}) = 0$ and $-\nabla\boldsymbol{\sigma}(\mathbf{r_b}) = 0$ is that the stress tensor properties derived from the stress tensor eigenvalues will be

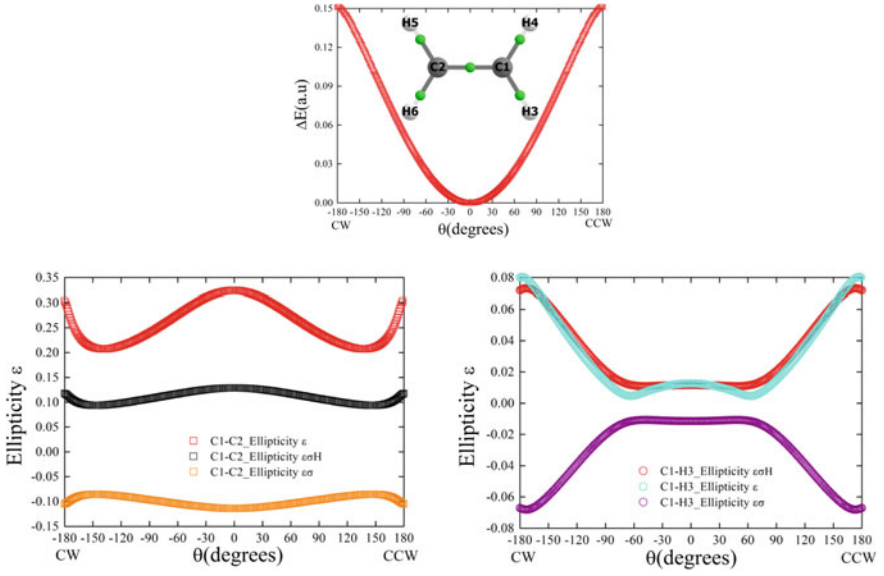


**Fig. 5.1** The variation of the relative energy ΔE (in a.u.) of the ethene with the torsion θ, $-180.0° \leq \theta \leq +180.0°$ (top) with inset figure of the molecular graph of the ethene with the atom labelling scheme, where green spheres indicate the *BCP*s. The variation of the three versions ellipticity $\varepsilon = |\lambda_1|/|\lambda_2| - 1$, $\varepsilon_{\sigma H} = |\lambda_{1\sigma}|/|\lambda_{2\sigma}| - 1$ and $\varepsilon_\sigma = |\lambda_{2\sigma}|/|\lambda_{1\sigma}| - 1$, for the C1-C2 *BCP* (bottom-left) with the torsion θ, with the corresponding values for the C1-H3 *BCP* (bottom-right)

sensitive to small variations. A consequences of this sensitivity to small variations was the ability to use $\lambda_{3\sigma} < 0$ as a measure of topological instability or approaching phase transition [27, 28].

We demonstrated that the stress tensor $\boldsymbol{\sigma}(\mathbf{r})$, used within the QTAIM partitioning scheme, with an adapted version of the 3-D *vector-based* interpretation of the chemical bond $\mathsf{B} = \{\boldsymbol{p}, \boldsymbol{q}, \boldsymbol{r}\}$ of the form $\mathsf{B}_\sigma = \{\boldsymbol{p}_\sigma, \boldsymbol{q}_\sigma, \boldsymbol{r}\}$ to follow changes in the directional properties of the stress tensor $\boldsymbol{\sigma}(\mathbf{r})$ that is robust to large torsions.

The Hessian of $\rho(\mathbf{r})$ bond-path framework set $\mathsf{B} = \{\boldsymbol{p}, \boldsymbol{q}, \boldsymbol{r}\}$ and the stress tensor $\boldsymbol{\sigma}(\mathbf{r})$ versions, $\mathsf{B}_\sigma = \{\boldsymbol{p}_\sigma, \boldsymbol{q}_\sigma, \boldsymbol{r}\}$ and $\mathsf{B}_{\sigma\mathrm{H}} = \{\boldsymbol{p}_{\sigma\mathbf{H}}, \boldsymbol{q}_{\sigma\mathbf{H}}, \boldsymbol{r}\}$ where each of the three constituent paths display the network of most preferred and least preferred directions of motion of the associated bond-paths and *BCP*s, see Fig. 5.2. The construction of $\mathsf{B}_\sigma = \{\boldsymbol{p}_\sigma, \boldsymbol{q}_\sigma, \boldsymbol{r}\}$ that uses $\varepsilon_\sigma \leq 0$ possesses $\boldsymbol{p}_\sigma$ and $\boldsymbol{q}_\sigma$ paths more closely resemble the $\boldsymbol{p}$ and $\boldsymbol{q}$ from the Hessian of $\rho(\mathbf{r})$ than the $\boldsymbol{p}_{\sigma\mathbf{H}}$ and $\boldsymbol{q}_{\sigma\mathbf{H}}$ path. The reason for the counterintuitive result that $\varepsilon_\sigma \leq 0$ is more useful is because the 'easy' direction for the stress tensor $\boldsymbol{\sigma}(\mathbf{r})$ is determined by the most compressible $\lambda_{1\sigma}$ i.e. associated with the longest axis of the ellipse, whereas for the Hessian of $\rho(\mathbf{r})$ the 'easy' direction, (longest axis of the ellipse) is associated with the $\lambda_2$ eigenvalue.

The importance of considering a 3-D vector-based bonding measure was demonstrated by the fact that the $\boldsymbol{p}_\sigma$, $\boldsymbol{q}_\sigma$ paths and $\boldsymbol{p}_{\sigma\mathbf{H}}$, $\boldsymbol{q}_{\sigma\mathbf{H}}$ paths twist about the *BCP* for the asymmetrical C-H *BCP* bond-path $\boldsymbol{r}$ and the ellipticity profiles $\varepsilon$, $\varepsilon_\sigma$ and $\varepsilon_{\sigma\mathrm{H}}$

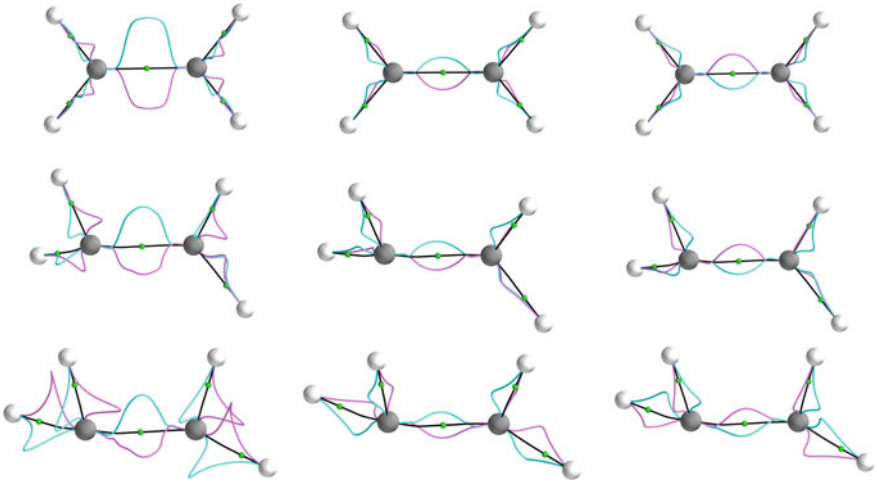

**Fig. 5.2** The bond-path framework sets $\mathsf{B} = \{\boldsymbol{p}, \boldsymbol{q}, \boldsymbol{r}\}$ (left-panels), $\mathsf{B}_\sigma = \{\boldsymbol{p}_\sigma, \boldsymbol{q}_\sigma, \boldsymbol{r}\}$ (middle-panels) and $\mathsf{B}_{\sigma\mathrm{H}} = \{\boldsymbol{p}_{\sigma\mathbf{H}}, \boldsymbol{q}_{\sigma\mathbf{H}}, \boldsymbol{r}\}$ (right-panels) showing magnified (×5) $\boldsymbol{p}$, $\boldsymbol{p}_\sigma$ and $\boldsymbol{p}_{\sigma\mathbf{H}}$ paths (pale-blue) and $\boldsymbol{q}$, $\boldsymbol{q}_\sigma$ and $\boldsymbol{q}_{\sigma\mathbf{H}}$ paths (magenta). The $\boldsymbol{r}$ path i.e. bond-path (black) corresponding ethene rotated in the clockwise (CW) direction for values of the torsion $\theta = 0.0°$ (top), 90.0° (middle) and 150.0° (bottom)

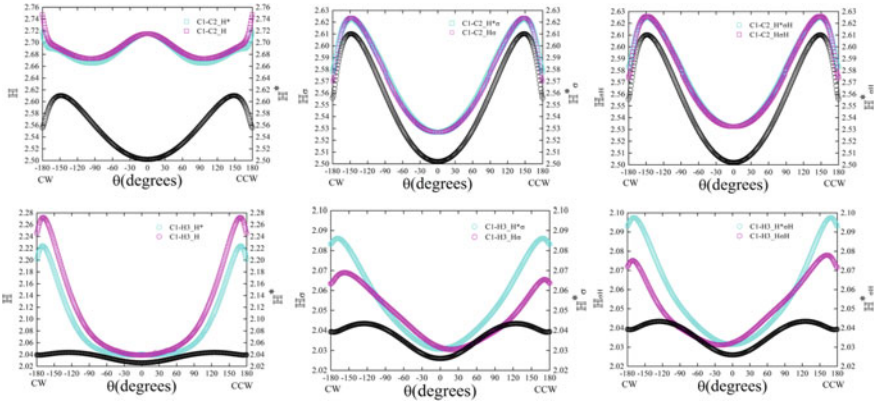


**Fig. 5.3** The variation of the $H$, $H_\sigma$ and $H_{\sigma H}$ of the C1-C2 *BCP* with torsion θ: are denoted by the pale-blue plot lines in the left, middle and right panels respectively. The corresponding values for $H^*$, $H^*_\sigma$ and $H^*_{\sigma H}$ and the bond-path lengths (BPL) are denoted by the magenta and black plot lines respectively, see Fig. 5.1 for the atom labelling scheme

profiles for the C1-H3 and C2-H6 *BCP* display peak values well away from the location of the associated *BCP*s.

For the Hessian of $\rho(\mathbf{r})$ the most preferred 'easy' direction $\underline{\mathbf{e}}_{\mathbf{2}}$ is determined on the basis of the ease of $\rho(\mathbf{r_b})$ accumulation. Conversely, the least preferred direction was found to be $\underline{\mathbf{e}}_{\mathbf{1}}$ for the Hessian of $\rho(\mathbf{r})$ and $\underline{\mathbf{e}}_{\mathbf{2\sigma}}$ for the stress tensor $\boldsymbol{\sigma}(\mathbf{r})$. For the stress tensor $\boldsymbol{\sigma}(\mathbf{r})$ we have found that the $\underline{\mathbf{e}}_{\mathbf{1\sigma}}$ eigenvector corresponds to the most preferred 'easy' direction on the basis of ease of compressibility. This finding was demonstrated using stress tensor trajectory formalism $T_\sigma(s)$ in partnership with the potential energy surface to prove that the $\underline{\mathbf{e}}_{\mathbf{2\sigma}}$ eigenvector was the least preferred direction of $\rho(\mathbf{r_b})$ accumulation and therefore that the $\underline{\mathbf{e}}_{\mathbf{1\sigma}}$ eigenvector was the most preferred direction, see this chapter. Additional support for the most and least preferred directions for the stress tensor $\boldsymbol{\sigma}(\mathbf{r})$ being defined by the $\underline{\mathbf{e}}_{\mathbf{1\sigma}}$ and $\underline{\mathbf{e}}_{\mathbf{2\sigma}}$ eigenvectors respectively was provided by the fact that the values for $H_\sigma{}^* > H_\sigma$ and $H_{\sigma H}{}^* > H_{\sigma H}$ consistent with previous findings from QTAIM that the preferred path has the longer associated eigenvector following path length, see Sect. 5.1 and Fig. 5.3. The least preferred stress tensor $\underline{\mathbf{e}}_{\mathbf{2\sigma}}$ eigenvector was indicated by the presence of asymmetrical variations of $H_\sigma$ and $H_{\sigma H}$ with the applied torsion θ.

### 5.1.2 *Halogen and Hydrogen-Bonding in Halogenabenzene/$NH_3$ Complexes Compared*

NG-QTAIM highlighted the competition between hydrogen-bonding and halogen-bonding for the recently proposed (Y = Br, I, At): halogenabenzene: $NH_3$ complex

[29]. NG-QTAIM demonstrated for X = (F, Cl, Br, I, At): 1-methyluracil: $H_2O$ that the effective core potentials (ECPs) are unreliable which was evident from the excessively high levels of metallic character, $\xi(\mathbf{r_b}) > 1$, in contrast to the complete absence of metallic character with SR-ZORA, see Table 5.1. The use of ECPs also indicated a halogen-bond Cl--O *BCP* is present; however the Cl--O *BCP* was not present with SR-ZORA calculations and instead a Cl--H *BCP* was present.

Differences between using the SR-ZORA Hamiltonian and effective core potentials (ECPs) to account for relativistic effects, in terms of on *BCP* and bond-path properties, with increased atomic mass were demonstrated, see Table 5.2.

**Table 5.1** SR-ZORA results for the eigenvector following path lengths (H,H′), bond-path length (BPL), geometric bond-length (GBL) and ($H_\sigma$, $H'_\sigma$), metallicity $\xi(\mathbf{r_b})$ and the total local energy density $H(\mathbf{r_b})$ in a.u. for the (Y = Cl, Br, I, At): $NH_3$ system. Note the use of the bond notations "--" (closed-shell *BCP*) and "--" (shared-shell *BCP*)

| *BCP* | (H, H′) | (BPL, GBL) | ($H_\sigma$, $H'_\sigma$) | $\xi(\mathbf{r})_\mathbf{b}$ | $H(\mathbf{r_b})$ |
|---|---|---|---|---|---|
| | | | **Cl-$NH_3$** | | |
| $C_3$--$H_{14}$ | (5.390, 5.202) | (4.927, 4.864) | (5.024, 4.928) | 0.351 | 0.001 |
| $N_{12}$-$H_{14}$ | (2.161, 2.154) | (1.877, 1.914) | (1.897, 1.897) | −0.198 | −0.481 |
| $C_3$--$H_8$ | (2.317, 2.298) | (2.007, 2.036) | (2.051, 2.039) | −0.274 | −0.299 |
| $C_4$-$C_3$ | (3.105, 3.095) | (2.586, 2.585) | (2.648, 2.631) | −0.324 | −0.375 |
| $Cl_2$-$C_3$ | (3.876, 3.831) | (3.421. 3.396) | (3.999, 3.983) | −0.862 | −0.123 |
| | | | **Br-$NH_3$** | | |
| $C_3$--$H_{14}$ | (6.297, 5.619) | (5.125, 4.991) | (5.347, 5.097) | 0.329 | 0.001 |
| $Br_2$--$N_{12}$ | (6.429, 6.376) | (6.107, 6.091) | (6.137, 6.133) | 0.286 | 0.001 |
| $N_{12}$-$H_{14}$ | (2.157, 2.149) | (1.876, 1.913) | (1.896, 1.896) | −0.198 | −0.482 |
| $C_3$-$H_8$ | (2.294, 2.275) | (2.008, 2.037) | (2.051, 2.038) | −0.276 | −0.297 |
| $C_4$-$C_3$ | (3.062, 3.054) | (2.587, 2.585) | (2.646, 2.627) | −0.325 | −0.374 |
| $Br_2$-$C_3$ | (3.895, 3.859) | (3.691, 3.666) | (3.716, 3.713) | −1.103 | −0.088 |
| | | | **I-$NH_3$** | | |
| $I_2$--$N_{12}$ | (6.213, 6.195) | (5.986, 5.970) | (6.588, 6.584) | 0.346 | 0.001 |
| $C_3$-$H_8$ | (2.250, 2.231) | (2.010, 2.039) | (2.045, 2.035) | −0.279 | −0.295 |
| $C_4$-$C_3$ | (3.007, 3.002) | (2.589, 2.587) | (2.641, 2.624) | −0.329 | −0.369 |
| $I_2$-$C_3$ | (4.363, 4.334) | (4.025, 4.004) | (4.640, 4.638) | −2.200 | −0.061 |
| | | | **At-$NH_3$** | | |
| At6--$N_{12}$ | (6.160, 6.142) | (5.927, 5.914) | (5.948, 5.943) | 0.357 | 0.001 |
| $C_5$-$H_8$ | (2.257, 2.238) | (2.014, 2.043) | (2.051, 2.041) | −0.280 | −0.292 |
| $C_4$-$C_5$ | (2.963, 2.957) | (2.593, 2.591) | (2.644, 2.626) | −0.329 | −0.367 |
| At6-$C_5$ | (4.636, 4.616) | (4.235, 4.208) | (4.272, 4.270) | −22.03 | −0.046 |

**Table 5.2** The difference Δ{(ECP) – (SR-ZORA)} for the Δ(H, H′), Δ(BPL), Δ(GBL), Δ($\mathsf{H}_\sigma$, $\mathsf{H}'_\sigma$), Δξ($\mathbf{r_b}$) and Δ$H$($\mathbf{r_b}$) in a.u. of the (X = Cl, Br, I, At): 1-methyluracil: $NH_3$ system, see the caption of Table 5.1 for further details

| *BCP* | Δ(H, H′) | Δ(BPL, GBL) | Δ($\mathsf{H}_\sigma$, $\mathsf{H}_\sigma$′) | Δξ($\mathbf{r_b}$) | $H$($\mathbf{r_b}$) |
|---|---|---|---|---|---|
| | | | **Cl-$NH_3$** | | |
| $C_3$--$H_{14}$ | (−0.013, 0.006) | (−0.005, 0.000) | (−0.013, 0.000) | −0.012 | 0.000 |
| $N_{12}$-$H_{14}$ | (0.005, 0.004) | (−0.006, 0.000) | (−0.005, −0.005) | 0.010 | −0.042 |
| $C_3$-$H_8$ | (0.048, 0.045) | (−0.004, 0.000) | (0.004, 0.001) | 0.028 | −0.043 |
| $C_4$-$C_3$ | (0.093, 0.090) | (0.001, 0.000) | (0.009, 0.008) | 0.039 | −0.043 |
| $Cl_2$-$C_3$ | (0.120, 0.104) | (0.006, 0.000) | (0.061, 0.076) | 0.117 | −0.008 |
| | | | **Br-$NH_3$** | | |
| $C_3$--$H_{14}$ | (−0.042, −0.045) | (−0.002, 0.000) | (−0.016, 0.008) | −0.005 | 0.000 |
| $Br_2$--$N_{12}$ | (−0.003, 0.034) | (0.000, 0.000) | (0.007, −0.007) | −0.012 | 0.001 |
| $N_{12}$-$H_{14}$ | (0.009, 0.008) | (−0.005, 0.000) | (−0.005, −0.005) | 0.010 | −0.042 |
| $C_3$-$H_8$ | (0.037, 0.035) | (−0.003, 0.000) | (0.002, 0.000) | 0.029 | −0.044 |
| $C_4$-$C_3$ | (0.082, 0.080) | (0.000, 0.000) | (0.007, 0.007) | 0.039 | −0.043 |
| $Br_2$-$C_3$ | (0.088, 0.075) | (0.005, 0.000) | (0.008, 0.009) | 0.081 | −0.001 |
| | | | **I-$NH_3$** | | |
| $I_2$--$N_{12}$ | (−0.142, −0.139) | (−0.003, 0.000) | (0.051, 0.054) | −0.007 | 0.000 |
| $C_3$-$H_8$ | (−0.019, −0.017) | (−0.002, 0.000) | (−0.004, −0.004) | 0.026 | −0.039 |
| $C_4$-$C_3$ | (−0.030, −0.029) | (0.000, 0.000) | (−0.004, −0.003) | 0.032 | −0.036 |
| $I_2$-$C_3$ | (−0.203, −0.205) | (−0.001, 0.000) | (0.047. 0.047) | 0.355 | −0.003 |
| | | | **At-$NH_3$** | | |
| At6--$N_{12}$ | (−0.154, −0.153) | (−0.002, 0.000) | (1.312, 1.316) | −0.015 | 0.000 |
| $C_5$-$H_8$ | (−0.006, −0.007) | (−0.002, 0.000) | (−0.003, −0.004) | 0.026 | −0.039 |
| $C_4$-$C_5$ | (−0.012, −0.011) | (0.000, 0.000) | (−0.003, −0.003 | 0.031 | −0.035 |
| At6-$C_5$ | (−0.305, −0.309) | (0.000, 0.000) | (1.293, 1.293) | −0.320 | −0.001 |

Subtle details of the competition between halogen-bonding and hydrogen-bonding were observed, indicating the presence of mixed chemical character. The use of SR-ZORA indicated that ECPs overestimated the topological stability of the halogen-bonding and on particular for (X = Cl): 1-methyluracil: $H_2O$ this resulted in the Cl--O halogen-bond being replaced by a Cl--H hydrogen-bond. Additionally, the use of SR-ZORA reduced or removed spurious features of $\mathsf{B}$ on the site of the halogen atoms for the stress tensor $\mathsf{B}_\sigma$, see Fig. 5.5.

The competition between halogen-bonding and hydrogen-bonding is demonstrated to favor hydrogen-bonding for the lightest halogen atom Y = Cl. Conversely, halogen-bonding is favored for the heaviest halogen atoms Y = I and At. Intermediate behavior was found for Y = Br, where contains halogen-bonding and hydrogen-bonding are present. Halogen-bonding was absent from Y = Cl and Y = I, At comprised only halogen-bonding.

The increasingly mixed chemical character of the hydrogen-bonding present for Y = Cl, Br was presence of double peaks in the $\{\boldsymbol{q}, \boldsymbol{q}'\}$ and stress tensor $\{\boldsymbol{q}_\sigma, \boldsymbol{q}_\sigma{}'\}$ path-packets was only evident with the use of SR-ZORA, see Figs. 5.4 and 5.5 respectively. The mix of chemical character demonstrated the competition between hydrogen-bonding and halogen-bonding. This was evident as the stronger double peak apparent for Y = Br that indicated that the hydrogen-bonding is more polarized and strained than for the Y = Cl hydrogen-bond.

### *5.1.3 Photochemical Reaction Path from Benzene to Benzvalene*

We used NG-QTAIM to follow the entire bond-path to better understand the short chemical half-life of photo-chemical reaction associated with of the formation of benzvalene from benzene, see Fig. 5.6 [30]. This was undertaken in terms of the competition between the formation of unstable new strong C-C bonding that also destabilizes nearest neighbor C-C bonds. The formation of benzvalene from benzene was unusual in that it resulted in two additional *shared-shell* C-C *BCPs*, compared with the benzene molecular graph. The formation of additional closed-shell *BCP*s as a result of a reaction process is common and occurs to maximize the bonding density to increase the favorability of a reaction. The formation of shared-shell *BCP*s however, was the first time the authors have observed this process. The explosive character of benzvalene was indicated by the unusual tendency of the strong shared-shell C-C *BCP*s to rupture as easily as weak closed-shell C-C *BCP*s.

The topological instability of the strong shared-shell C-C *BCP*s was explained by the existence of measures that previously have only been observed in weak closed-shell C-C *BCP*s including twisted $\{\boldsymbol{p}, \boldsymbol{p}'\}$ and$\{\boldsymbol{q}, \boldsymbol{q}'\}$ path-packets. The use of the stress tensor $\boldsymbol{\sigma}(\mathbf{r})$ was also used as it better highlighted differences in the in the $\{\boldsymbol{p}, \boldsymbol{p}'\}$ and$\{\boldsymbol{q}, \boldsymbol{q}'\}$ path-packets for the various electronic states than did the Hessian of $\rho(\mathbf{r})$ $\{\boldsymbol{p}, \boldsymbol{p}'\}$ and$\{\boldsymbol{q}, \boldsymbol{q}'\}$ path-packets. This is seen from the orientation of the large and twisted $\{\boldsymbol{q}, \boldsymbol{q}'\}$ path-packets relative to the short *RCP-BCP* lines that is therefore favorable to the coalescence of the associated *BCP* and *RCP*, see Fig. 5.6 (bottom).

The presence of significant double bond character for vertical excitation benzene $S_0 \rightarrow S_1$vert is indicated by the magnitude of the symmetrical $\{\boldsymbol{q}, \boldsymbol{q}'\}$ path-packets of the C-C *BCPs*, see Fig. 5.6. A 1% decrease in lengths of the $\{\boldsymbol{q}, \boldsymbol{q}'\}$ path-packets, defined by the lengths (H, H′), occurs for this vertical excitation, see Table 5.3. An increase/decrease in (H, H′) value was associated with an increase/decrease in the double bond character for a shared-shell *BCP* and an increased/decreased tendency to rupture for a closed-shell *BCP*. For the benzene $S_1$vert $\rightarrow$ $S_1$opt reaction step the inter-nuclear separation (GBL) increases as expected which yielded an identical geometry and bond-path length from conventional QTAIM, indicated by GBL and

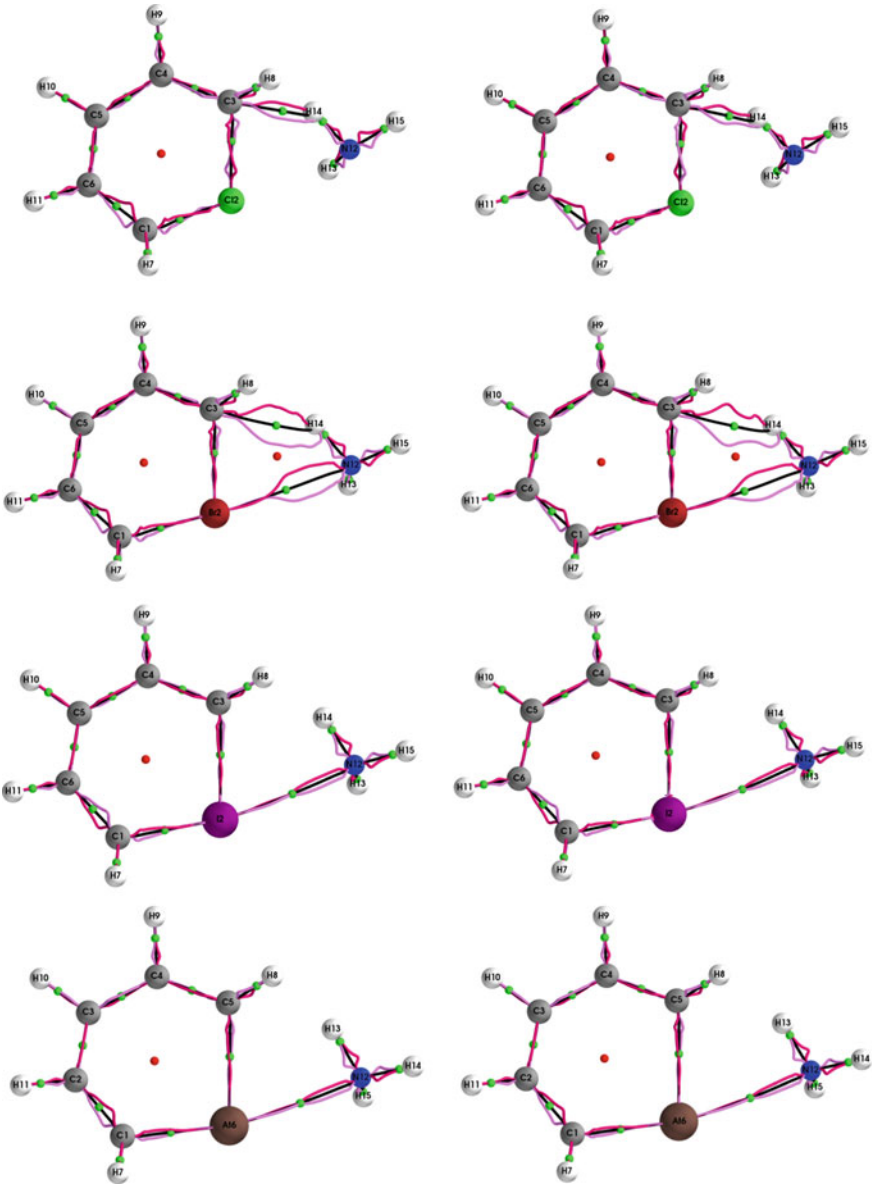

**Fig. 5.4** The $\{q, q'\}$ path-packets, with $q$ (dark-magenta) and $q'$(light-magenta) for the (Y = Cl, Br, I, At): halogenabenzene: $NH_3$ system are presented in sub-figure **(a–d)** respectively, calculated using ECPs (left panels) and with the SR-ZORA Hamiltonian (right panels)

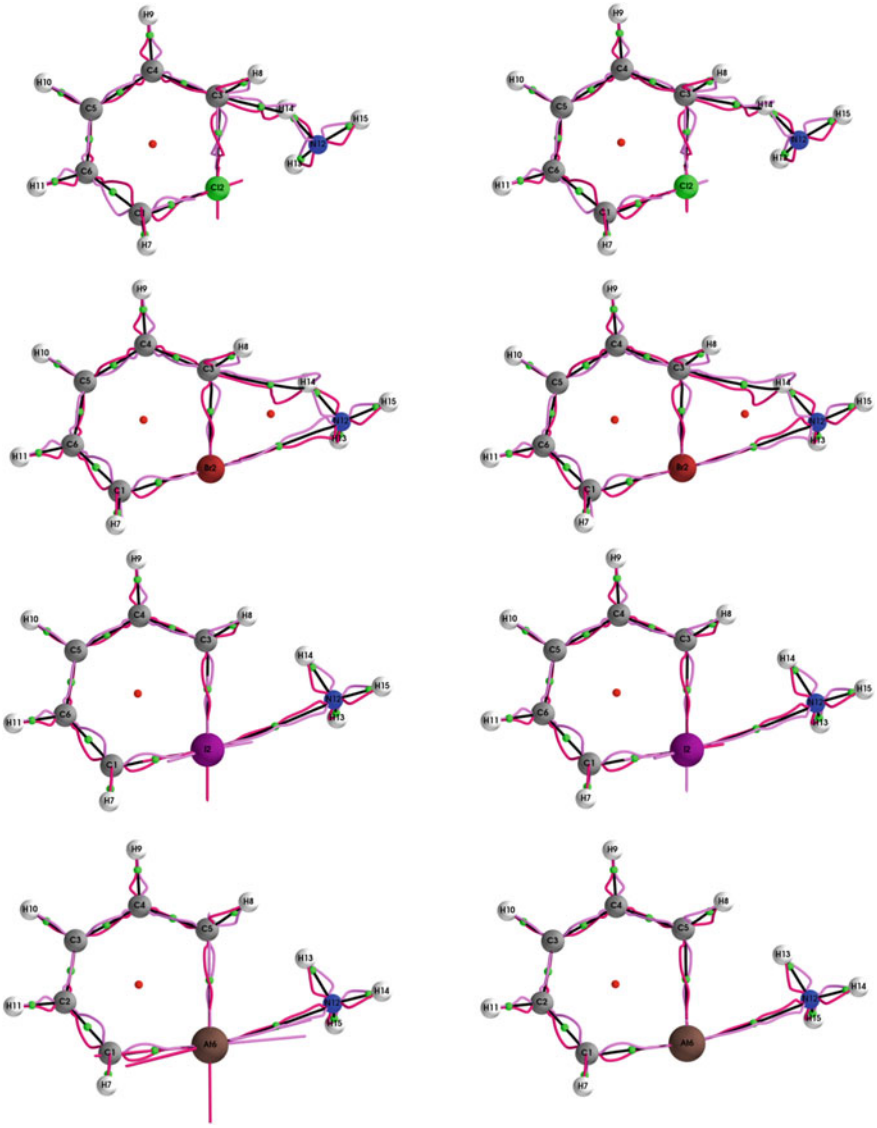

**Fig. 5.5** The $\{q_\sigma, q_\sigma'\}$ path-packets with a magnification factor of × 5 for the (Y = Cl, Br, I, At): halogenabenzene: $NH_3$ system are presented in sub-figure **(a–d)** respectively, see the caption of Fig. 5.5 for further details

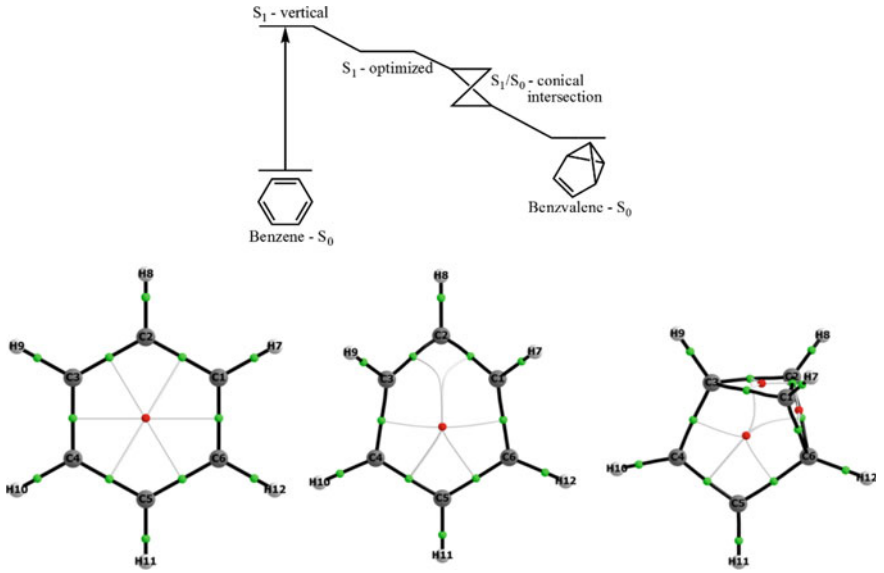


**Fig. 5.6** The photochemical formulation of benzvalene from benzene (top). The benzene $S_0$, benzene $S_1$vert and benzene $S_1$opt (bottom-left), benzvalene $S_0/S_1$ContInt (bottom-middle) and benzvalene $S_0$ (bottom-right) molecular graphs, the bond-path (***r***) is indicated by the black lines with the undecorated green and red spheres representing the bond critical point (*BCP*s) and ring critical points (*RCP*s), respectively, with the white lines indicating the *RCP-BCP* paths

BPL respectively, see Table 5.3. Therefore the NG-QTAIM length measures are demonstrated be more sensitive than conventional QTAIM.

## 5.2 The Ehrenfest Force F(r): A Physically Intuitive Approach for Analyzing Chemical Interactions

The Ehrenfest Force $\mathbf{F}(\mathbf{r})$ Topology [31] can be proposed in terms of the molecular Coulomb potential integral equation or in terms of the divergence of the quantum stress tensor. The latter form of $\mathbf{F}(\mathbf{r})$ allows us to map onto a surface integral $\mathbf{S}(\mathbf{r})$ using the Gauss's theorem as an integration of the force density, over the basin of an atom $\Omega$:

$$\mathbf{F}(\Omega) = -N \oint_{\Omega} \mathrm{d}S(\mathbf{r}, \Omega) \cdot \boldsymbol{\sigma}(\mathbf{r}) \tag{5.1}$$

Thus the quantum stress tensor $\boldsymbol{\sigma}(\mathbf{r})$ can be used to determine the force exerted on each element of the atomic surface, $S(\mathbf{r},\Omega)$, and its product with an element of the surface gives the force acting on this region [32, 33]. As a comparison with the examination of

**Table 5.3** The eigenvector following path lengths (H, H′) and (H*, H*′) of the associated with the $\{q, q'\}$ and $\{p, p'\}$ path-packets respectively, along with the bond-path lengths (BPL) and geometric bond lengths (GBL) in Ångstrom, see the caption of Figs. 5.6 and 5.7 for further details

| *BCP* | Benzene $S_0$ | | | Benzene $S_1$ vert | | | |
|---|---|---|---|---|---|---|---|
| | (H, H′) | (H*, H*′) | (BPL, GBL) | (H, H′) | (H*, H*′) | (BPL, GBL) | |
| C1-C2 | (1.458, 1.458) | (1.458, 1.458) | (1.396, 1.396) | (1.441, 1.441) | (1.441, 1.441) | (1.396, 1.396) | |
| Benzene $S_1$ opt | | | | | | | |
| | (H, H′) | (H*, H*′) | (BPL, GBL) | | | | |
| | (1.482, 1.482) | (1.482, 1.482) | (1.435, 1.435) | | | | |
| Benzvalene $S_0/S_1$ ConInt | | | | Benzvalene $S_0$ | | | |
| | (H, H′) | (H*, H*′) | (BPL, GBL) | (H, H′) | (H*, H*′) | (BPL, GBL) | |
| C1-C2 | (1.506, 1.485) | (1.491, 1.499) | (1.462, 1.454) | (1.545, 1.544) | (1.535, 1.556) | (1.482, 1.462) | |
| C2-C3 | (1.505, 1.484) | (1.491, 1.498) | (1.462, 1.454) | (1.767, 1.690) | (1.704, 1.747) | (1.514, 1.503) | |
| C3-C4 | (1.545, 1.541) | (1.542, 1.544) | (1.467, 1.466) | (1.537, 1.536) | (1.534, 1.539) | (1.513, 1.512) | |
| C4-C5 | (1.511, 1.499) | (1.501, 1.510) | (1.395, 1.395) | (1.539, 1.539) | (1.523, 1.555) | (1.343, 1.342) | |
| C5-C6 | (1.508, 1.496) | (1.498, 1.507) | (1.395, 1.395) | (1.538, 1.537) | (1.535, 1.540) | (1.515, 1.514) | |
| C6-C1 | (1.548, 1.544) | (1.545, 1.547) | (1.467, 1.466) | (1.878, 1.795) | (1.804, 1.859) | (1.520, 1.510) | |
| C1-C3 | (----, ----) | (----, ----) | (----, ----) | (2.014, 1.939) | (1.931, 2.005) | (1.562, 1.552) | |
| C2-C6 | (----, ----) | (----, ---) | (---, ----) | (1.846, 1.767) | (1.775, 1.829) | (1.520, 1.510) | |

the gradient of the electron density in the QTAIM theory, a complementary scheme can be proposed from the investigation of the primitive amount of the Ehrenfest Force, the Ehrenfest potential, $V^{\mathrm{F}}(\mathbf{r})$, using the definition:

$$\mathbf{F}(\mathbf{r}) = -\nabla V^{\mathrm{F}}(\mathbf{r}) \tag{5.2}$$

Alongside the condition that the potential energy of interaction of an electron located at an infinite distance from a molecule is zero:

$$\underbrace{\lim}_{|\mathbf{r}|\to\infty} V^{\mathrm{F}}(\mathbf{r}) = 0 \tag{5.3}$$

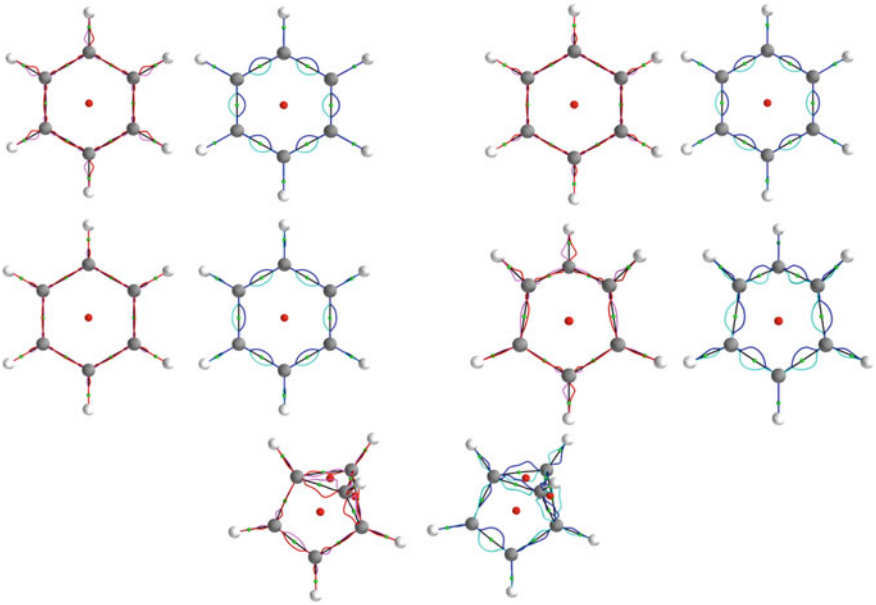

**Fig. 5.7** The stress tensor $\mathsf{B}_{\sigma 0,1} = \{(\boldsymbol{p_{\sigma 0}}, \boldsymbol{p_{\sigma 1}}), (\boldsymbol{q_{\sigma 0}}, \boldsymbol{q_{\sigma 1}}), (\boldsymbol{r_0}, \boldsymbol{r_1})\}$ for the benzene $S_0$ (top-left), benzene $S_1$ vert (top-right) and benzene $S_1$ opt (middle-left), benzvalene $S_0/S_1$ ConInt (middle-right) and benzvalene $S_0$ (bottom). The $\boldsymbol{q}_\sigma$(magenta), $\boldsymbol{q'}_\sigma$(red) and $\boldsymbol{p}_\sigma$(light-blue), $\boldsymbol{p'}_\sigma$(dark-blue) paths are shown molecular graph a magnification factor of × 5 is used

Using this analogy we can follow the trajectories of $\mathbf{F}(\mathbf{r})$ that terminate at points where $\mathbf{F}(\mathbf{r}) = 0$. One can then calculate inter-atomic Ehrenfest Force surfaces which satisfy the zero-flux condition $\mathbf{F}(\mathbf{r})\cdot\mathbf{n}(\mathbf{r}) = 0$, therefore the Ehrenfest Hessian may also be defined as $\nabla\nabla \cdot \boldsymbol{\sigma}(\mathbf{r})$. The Ehrenfest $\mathbf{F}(\mathbf{r})$ *BCP* can be characterized similarly to the critical points (CP) of the electron density distribution in QTAIM as long as at the Ehrenfest *BCP*s all the force applied on an electron are balanced [9] ($\mathbf{F}(\mathrm{r}) = 0$).

The advantage of using the Ehrenfest partitioning is to gain physically meaning for a capping surface at a threshold value of $V^{\mathbf{F}}(\mathbf{r})$, that it is the outer boundary of molecule. We can use, for example, the ionization potential $V_\mathrm{I}$ to define the molecular boundary using [34]:

$$V^{\mathbf{F}}(\mathbf{r}) = -V_\mathrm{I} \tag{5.4}$$

Ionization energy $E_\mathrm{I}$, or ionization potential $V_\mathrm{I}$, is the minimum amount of necessary energy to completely remove an electron to infinity from the neutral atom that can be determined from experiment. Within QTAIM however, the somewhat arbitrary conventional definition of the molecular boundary uses a threshold of 0.001 a.u. for the electron density.

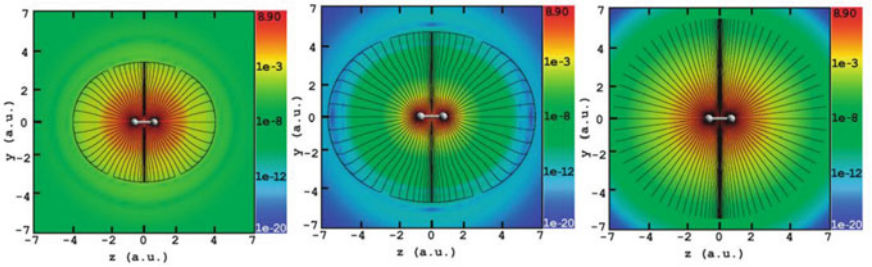


**Fig. 5.8** Ehrenfest force $\mathbf{F}(\mathbf{r})$ plots of the inter-nuclear YZ plane computed using the three different basis sets for the $H_2$ molecule taken from [31]. The color scale plot in the background shows the normalized negative values for the magnitude of the divergence of the stress tensor, $\mathbf{F}(\mathbf{r})$. The three panels were constructed using (left-panel) aug-cc-pVQZ, (middle-panel) ANO-RCC and (right-panel) ANO-RCC in the form of the pVDZ basis with the selected range of exponents. The spurious artifacts are apparent as the boundary lines that terminate the field lines in the left and middle but not right panel

The difficulties of the computation of the Ehrenfest force $\mathbf{F}(\mathbf{r})$ were considered in detail during a previous investigation by some of the current authors [31], attributing the spurious artifacts to the diffuse GTOs used in basis sets, see Fig. 5.8. In the work by Tachibana et al. [35] the effect of the basis sets expansion on the electronic stress tensor calculations was investigated and compared with the exact wave function for the ion $H + 2$. The outcome was the demonstration that the calculations for *cc*-pV5Z and *cc*-pV6Z basis sets are in close agreement with the *spindle* form of the exact wave function. Additionally, the effect of the basis sets on the stress tensor, by calculating the profiles of the magnitude of the attractive $\mathbf{F}(\mathbf{r})$ for the H and $H_2$ ground states, was demonstrated by other Pendas et al. [36], see Fig. 5.8. The expanded basis set aug-*cc*-pV5Z was found to provide the best agreement with the exact computation of $\mathbf{F}(\mathbf{r})$. Hernández-Trujillo and co-workers suggested in 2007 that spurious artifacts are pushed into the bonding regions upon close-approach of the nuclei [32] in the $\mathbf{F}(\mathbf{r})$ calculations if GTOs with s and p functions with exponents of order of $10^5$ and $10^3$ were used. In contrast to conventional basis sets such as pV6Z which have exponent values of order $10^3$ and $10^1$ respectively. We decided to use the extended relativistic Atomic Natural Orbital (ANO-RCC) GTO basis sets developed by Ross and collaborators [37–39]. These basis sets possessed the key feature of being highly focused at the nuclei and were averaged over several atomic states, positive and negative ions and atoms in an external electric field.

### *5.2.1 The Ehrenfest Force F(r) with Lithium*

The investigation of the stress tensor $\boldsymbol{\sigma}(\mathbf{r})$ on the Ehrenfest Force $\mathbf{F}(\mathbf{r})$ molecular graph was undertaken with neutral lithium $Li_m$ ($m = 2 - 5$) clusters [40].

### 5.2.2 *The Ehrenfest Force F(r) Bond-Path Framework Set* $\mathsf{B}_F$, $\mathsf{B}_{\sigma F}$ *and* $\mathsf{B}_{\sigma HF}$

Using NG-QTAIM removes the need to use the engineered ANO-RCC basis sets because we are only use the location of the *BCP* and not the location or numbers of the *RCP* and *CCP* critical points. Variant $\{\boldsymbol{p}_{\mathrm{FA}}, \boldsymbol{p}_{\mathrm{FA}}'\}$, $\{\boldsymbol{p}_{\mathrm{FB}}, \boldsymbol{p}_{\mathrm{FB}}'\}$ and $\{\boldsymbol{q}_{\mathrm{FA}}, \boldsymbol{q}_{\mathrm{FA}}'\}$, $\{\boldsymbol{q}_{\mathrm{FB}}, \boldsymbol{q}_{\mathrm{FB}}'\}$ path-packets were generated based on the $\mathbf{F}(\mathbf{r})$ Hessian matrix eigenvectors and the definition of the Ehrenfest Force $\mathbf{F}(\mathbf{r})$ ellipticity $\varepsilon_{\mathrm{FA}} = (|\lambda_{1\mathrm{F}}|/|\lambda_{2\mathrm{F}}|) - 1$ and $\varepsilon_{\mathrm{FB}} = (|\lambda_{2\mathrm{F}}|/|\lambda_{2\mathrm{F}}|) - 1$.

The Hessian of $\rho(\mathbf{r})$ and the stress tensor $\boldsymbol{\sigma}(\mathbf{r})$ were also calculated at each point along the bond-path. This allowed the Hessian of $\rho(\mathbf{r})$ eigenvectors to be 'transplanted' onto the $\mathbf{F}(\mathbf{r})$ along with the $\mathbf{F}(\mathbf{r})$ bond-path definition, in the construction of the $\mathsf{B}_{\mathrm{F}}$, $\mathsf{B}_{\sigma\mathrm{F}}$ and $\mathsf{B}_{\sigma\mathrm{HF}}$. Note the subscript "$_{\mathrm{F}}$" is used to indicate the placement on the $\mathbf{F}(\mathbf{r})$ molecular graph.

In addition we calculated the Hessian of $\rho(\mathbf{r})$ eigenvectors on the associated QTAIM molecular graph ($\{\boldsymbol{q}, \boldsymbol{q}'\}$, $\{\boldsymbol{p}, \boldsymbol{p}'\}$, $\boldsymbol{r}$) and on the Ehrenfest Force $\mathbf{F}(\mathbf{r})$ molecular graph ($\{\boldsymbol{q}_{\rho\mathrm{F}}, \boldsymbol{q}_{\rho\mathrm{F}}'\}$, $\{\boldsymbol{p}_{\rho\mathrm{F}}, \boldsymbol{p}_{\rho\mathrm{F}}'\}$, $\boldsymbol{r}_{\mathbf{F}}$). Two variants of the stress tensor $\boldsymbol{\sigma}(\mathbf{r})$ on the QTAIM molecular graph ($\{\boldsymbol{q}_{\sigma\rho}, \boldsymbol{q}_{\sigma\rho}'\}$, $\{\boldsymbol{p}_{\sigma\rho}, \boldsymbol{p}_{\sigma\rho}'\}$, $\boldsymbol{r}$) and ($\{\boldsymbol{q}_{\sigma\mathrm{H}\rho}, \boldsymbol{q}_{\sigma\mathrm{H}\rho}'\}$, $\{\boldsymbol{p}_{\sigma\mathrm{H}\rho}, \boldsymbol{p}_{\sigma\mathrm{H}\rho}'\}$, $\boldsymbol{r}$) and on the Ehrenfest Force $\mathbf{F}(\mathbf{r})$ molecular graph ($\{\boldsymbol{q}_{\sigma\mathrm{F}}, \boldsymbol{q}_{\sigma\mathrm{F}}'\}$, $\{\boldsymbol{p}_{\sigma\mathrm{F}}, \boldsymbol{p}_{\sigma\mathrm{F}}'\}$, $\boldsymbol{r}_{\mathbf{F}}$) and ($\{\boldsymbol{q}_{\sigma\mathrm{HF}}, \boldsymbol{q}_{\sigma\mathrm{HF}}'\}$, $\{\boldsymbol{p}_{\sigma\mathrm{HF}}, \boldsymbol{p}_{\sigma\mathrm{HF}}'\}$, $\boldsymbol{r}_{\mathbf{F}}$).

We were able to display the stress tensor $\boldsymbol{\sigma}(\mathbf{r})$ ($\mathsf{B}_{\sigma\mathrm{F}}$ and $\mathsf{B}_{\sigma\mathrm{HF}}$) on the Ehrenfest Force $\mathbf{F}(\mathbf{r})$ molecular graph. This was because of the matching of the locations of the Ehrenfest $\mathbf{F}(\mathbf{r})$ *BCP*s and stress tensor $\boldsymbol{\sigma}(\mathbf{r})$ *BCP*s on the $\mathbf{F}(\mathbf{r})$ molecular graph from the condition $\mathbf{F}(\mathbf{r}) = -\nabla \cdot \boldsymbol{\sigma}(\mathbf{r}) = 0$ at the *BCP*. Conversely, the Hessian of $\rho(\mathbf{r})$ partitioning cannot be used to display the stress tensor $\boldsymbol{\sigma}(\mathbf{r})$ ($\mathsf{B}_{\sigma\rho}$ and $\mathsf{B}_{\sigma\mathrm{H}\rho}$) on the QTAIM molecular graph due to a mis-match in the location of the QTAIM and stress tensor $\boldsymbol{\sigma}(\mathbf{r})$ *BCP*s.

Prior to this the stress tensor $\boldsymbol{\sigma}(\mathbf{r})$ had only been computed within QTAIM partitioning scheme, see Fig. 5.9. The nature of the stress tensor $\boldsymbol{\sigma}(\mathbf{r})$ was undertaken by exploring evidence for the existence of the non-nuclear attractors (*NNA*) character in neutral clusters in addition of the topologically stabilizing effect of the presence of *NNA*s. Due to the lack of scalar-field or vector-field for the stress tensor $\boldsymbol{\sigma}(\mathbf{r})$ it is not possible to construct an exclusive $\boldsymbol{\sigma}(\mathbf{r})$ partitioning, in contrast to the QTAIM (scalar-field $\rho(\mathbf{r})$) and Ehrenfest Force $\mathbf{F}(\mathbf{r})$ (vector-field $\boldsymbol{\sigma}(\mathbf{r})$) partitioning schemes.

We explored evidence for the existence of the *NNA* character in $\mathrm{Li}_m$ ($m = 2 - 5$) clusters as well as the topologically stabilizing effect of the presence of *NNA*s to get closer to the true nature of the stress tensor $\boldsymbol{\sigma}(\mathbf{r})$. We discovered that all of the QTAIM $\mathrm{Li}_m$ ($m = 2 - 5$) molecular graphs contained at least one *NNA* and none of the corresponding $\mathbf{F}(\mathbf{r})$ molecular graphs from contained *NNA*s.

Displaying the stress tensor ($\mathsf{B}_{\sigma\mathrm{F}}$ and $\mathsf{B}_{\sigma\mathrm{FH}}$), using the stress tensor $\boldsymbol{\sigma}(\mathbf{r})$ eigenvectors, on the Ehrenfest Force $\mathbf{F}(\mathbf{r})$ molecular graphs is a better choice to display the character

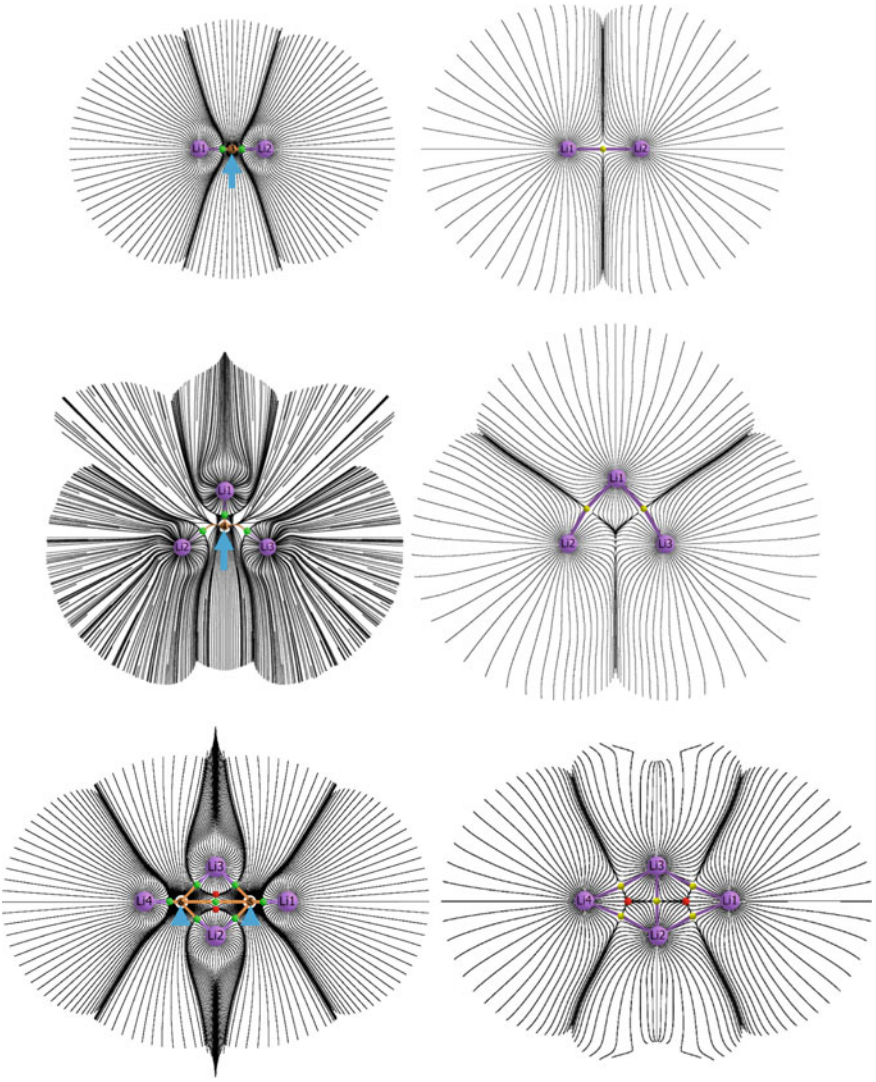


**Fig. 5.9** The QTAIM $\nabla\rho(\mathbf{r})$ (left-panel) and Ehrenfest Force $\mathbf{F}(\mathbf{r})$ $\nabla\rho(\mathbf{r}) \cdot \boldsymbol{\sigma}(\mathbf{r})$ (right-panel) trajectory maps are superimposed onto the corresponding molecular graph for neutral lithium $Li_m$ ($m = 2 - 5$) clusters. The purple spheres represent the lithium nuclear critical points (*NCP*s), the brown and green represent QTAIM non-nuclear attractors (*NNA*s) and bond critical points (*BCP*s) respectively. The blue arrows indicate the location of the *NNA*s. The corresponding *BCP*s in the Ehrenfest Force $\mathbf{F}(\mathbf{r})$ trajectory maps are indicated by the yellow spheres

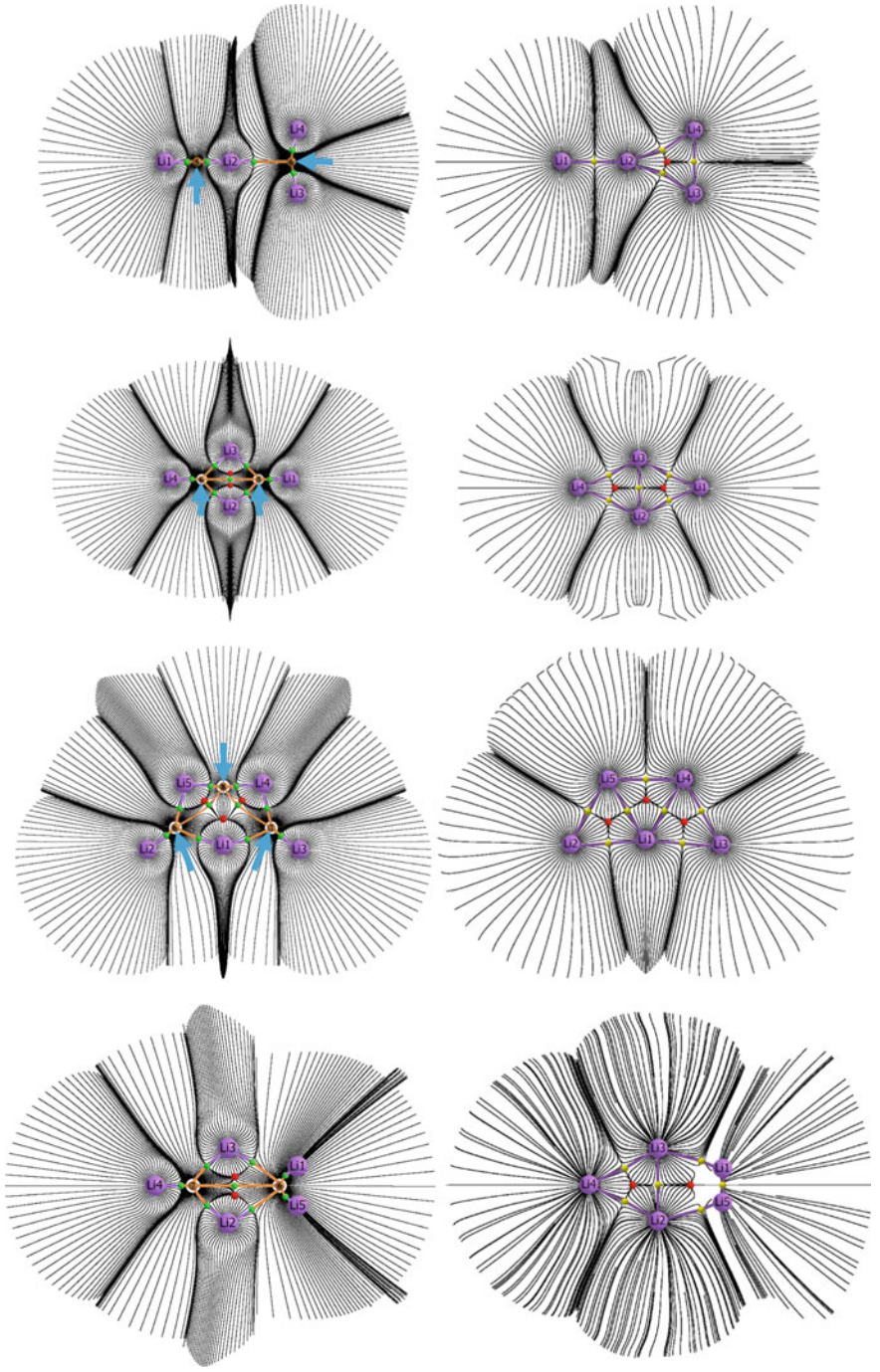

**Fig. 5.9** (continued)

of the stress tensor $\boldsymbol{\sigma}(\mathbf{r})$ than the QTAIM molecular graph, see Fig. 5.10. This is due to the matching of the locations of the Ehrenfest $\mathbf{F}(\mathbf{r})$ *BCP*s and stress tensor $\boldsymbol{\sigma}(\mathbf{r})$ *BCP*s on the $\mathbf{F}(\mathbf{r})$ molecular graph from the condition $\mathbf{F}(\mathbf{r}) = -\nabla \cdot \boldsymbol{\sigma}(\mathbf{r}) = 0$ at the *BCP*. Conversely, the use of the QTAIM partitioning to display the stress tensor ($\mathsf{B}_{\sigma}$ and $\mathsf{B}_{\sigma F}$) is not practical since there is a mis-match in the location of the QTAIM and stress tensor $\boldsymbol{\sigma}(\mathbf{r})$ *BCP*s.

We also displayed the $\mathsf{B}_{F}$, using the Hessian of $\rho(\mathbf{r})$ eigenvectors and stress tensor ($\mathsf{B}_{\sigma F}$ and $\mathsf{B}_{\sigma HF}$), using the stress tensor $\boldsymbol{\sigma}(\mathbf{r})$ eigenvectors and Ehrenfest Force $\mathbf{F}(\mathbf{r})$ ($\mathsf{B}_{FA}$ and $\mathsf{B}_{FB}$) all using the Ehrenfest Force $\mathbf{F}(\mathbf{r})$ partitioning schemes. This was chosen to isolate the effect of the eigenvalues and eigenvectors of the QTAIM and Ehrenfest Force $\mathbf{F}(\mathbf{r})$ molecular graphs, except for the case of the $Li_2$ dimer, due to the different in bonding connectivities.

The *NNA* character corresponded to isolated peaks in the path-packets either side of the *BCP*, consequently we concluded there was significant *NNA* character for the $\mathsf{B}_{\sigma F}$ and $\mathsf{B}_{\sigma HF}$ calculated on the Ehrenfest Force $\mathbf{F}(\mathbf{r})$ molecular graphs. The corresponding $\mathsf{B}_{F}$, using the Hessian of $\rho(\mathbf{r})$ eigenvectors on the $\mathbf{F}(\mathbf{r})$ molecular

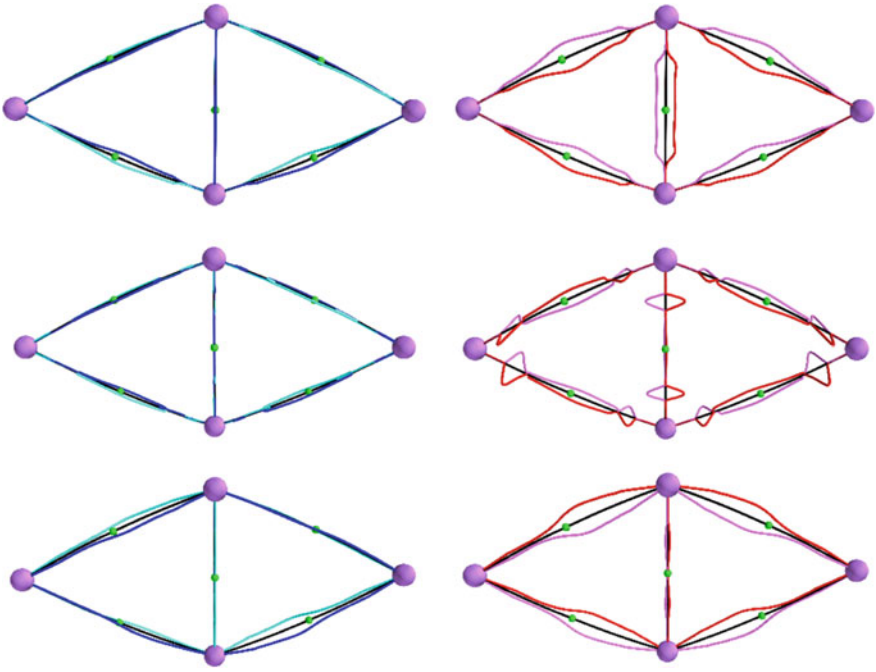

**Fig. 5.10** The $\{\boldsymbol{p}_F, \boldsymbol{p}_F{}'\}$ and $\{\boldsymbol{q}_F, \boldsymbol{q}_F{}'\}$ path-packets (top-panel), using the Hessian of $\rho(\mathbf{r})$ eigenvectors and eigenvalues. The corresponding results for the $\{\boldsymbol{p}_{\sigma F}, \boldsymbol{p}_{\sigma F}{}'\}$ and $\{\boldsymbol{q}_{\sigma F}, \boldsymbol{q}_{\sigma F}{}'\}$ path-packets (middle-panel), using the stress tensor ellipticity $\varepsilon_{\sigma} = |\lambda_{2\sigma}|/|\lambda_{1\sigma}| - 1$and the $\{\boldsymbol{p}_{FA}, \boldsymbol{p}_{FA}{}'\}$ and $\{\boldsymbol{q}_{FA}, \boldsymbol{q}_{FA}{}'\}$ path-packets, using the Ehrenfest Force $\mathbf{F}(\mathbf{r})$ ellipticity $\varepsilon_{FA} = (|\lambda_{1F}|/|\lambda_{2F}|) - 1$. All results are calculated on the Ehrenfest Force $\mathbf{F}(\mathbf{r})$ molecular graphs for $Li_4$

graph and both choices of the Ehrenfest Force $\mathbf{F}(\mathbf{r})$ ($\mathsf{B}_{\mathrm{FA}}$ and $\mathsf{B}_{\mathrm{FB}}$) only indicated a low level of *NNA* character. Therefore, we found that the $\mathsf{B}_{\mathrm{F}}$, using the Hessian of $\rho(\mathbf{r})$ eigenvectors, is presented on the Ehrenfest Force $\mathbf{F}(\mathbf{r})$ molecular graph was more similar to the Ehrenfest Force $\mathbf{F}(\mathbf{r})$ ($\mathsf{B}_{\mathrm{FA}}$ and $\mathsf{B}_{\mathrm{FB}}$) than to the stress tensor ($\mathsf{B}_{\boldsymbol{\sigma}\mathrm{F}}$ and $\mathsf{B}_{\boldsymbol{\sigma}\mathrm{FH}}$) presented on the Ehrenfest Force $\mathbf{F}(\mathbf{r})$ molecular graph.

The compression of the Li1-Li2 QTAIM and Ehrenfest Force $\mathbf{F}(\mathbf{r})$ $Li_2$ bond-paths led to the rupturing process of the *BCP-NNA-BCP* annihilation where further compression led to the annihilation of the *NNA* resulting in a single *BCP* as was found for bond-path stretching, see Fig. 5.11.

Sufficient stretching Li1-Li2 QTAIM and Ehrenfest Force $\mathbf{F}(\mathbf{r})$ bond-paths to annihilate the *NNA* results in visibly twisted path-packets. The persistence of the $Li_2$ bond-path torsion, determined by the stress tensor path-packets, was increased with large stretching distortions and indicated an extremely strained and electron deficient environment of $\rho(\mathbf{r})$. Therefore, the increase in bond-path torsion i.e. topological instability, after the rupture of the *NNA* demonstrated the topologically stabilizing effect of the *NNA*.

We endeavored to understand the unusual strength of hydrogen-bonding in water in terms of the coupling that occurs between the hydrogen-bond and the associated covalent bond that donates a degree of covalent character [41]. We used the $\mathsf{B}_{\mathbf{F}}$ to visualize provide insight into the previous phenomena associated with the easy direction ($\underline{\mathbf{e}}_{\mathbf{2F}}$) of the Ehrenfest Force $\mathbf{F}(\mathbf{r})$ eigenvectors on the coupling, between covalent (sigma) and hydrogen-bonds. see Fig. 5.12. This phenomena occurred only for hydrogen-bonds that possessed values of the total local energy density $H(\mathbf{r_b}) < 0$ [31]. The presence of coplanar $\{\boldsymbol{q}_{\mathrm{F}}, \boldsymbol{q}_{\mathrm{F}}'\}$ path-packets for covalent and hydrogen-bonds provided a check to demonstrate that the $\underline{\mathbf{e}}_{\mathbf{2F}}$ and not just at the *BCP*. Where hydrogen-bonding did not couple to a covalent (sigma) bond ($H(\mathbf{r_b}) > 0$) the corresponding $\{\boldsymbol{q}, \boldsymbol{q}'\}$ path-packets of the hydrogen-bond and covalent (sigma) bond were twisted relative to each other.

The Ehrenfest Force $\mathbf{F}(\mathbf{r})$ eigenvectors calculated on the Ehrenfest Force $\mathbf{F}(\mathbf{r})$ molecular graph yielded the phenomenon of collinear ($\underline{\mathbf{e}}_{\mathbf{2F}}$) most preferred eigenvectors between covalent (sigma) and hydrogen-bonds for $H(\mathbf{r_b}) < 0$, the Hessian of $\rho(\mathbf{r})$ eigenvectors did not. The morphology of the H-*BCP* segment of path-packets for all the hydrogen-bonds for the Hessian of $\rho(\mathbf{r})$ and the stress tensor $\boldsymbol{\sigma}(\mathbf{r})$, for both two variants, possessed very small profiles. Conversely, the corresponding H-*BCP* path-packet segment of the Ehrenfest Force $\mathbf{F}(\mathbf{r})$ were large and provides of the conditions necessary to visualize the effects of transfer of $\rho(\mathbf{r})$. The other condition being collinearity of the covalent (sigma) and hydrogen-bond path-packets determined by the eigenvectors. The Ehrenfest Force $\mathbf{F}(\mathbf{r})$ provides an understanding of the forces on the electrons, e.g. $\mathbf{F}(\mathbf{r}) = 0$ at the Ehrenfest Force $\mathbf{F}(\mathbf{r})$ *BCP*. The coplanar $\{\boldsymbol{q}, \boldsymbol{q}'\}$ path-packets in the region between the covalent (sigma) and hydrogen-bond *BCP*s were used to explain the relative ease of electron momentum transfer from the hydrogen atom of a sigma bond to the hydrogen-bond. This information was not extractable using the Hessian of $\rho(\mathbf{r})$ eigenvectors.

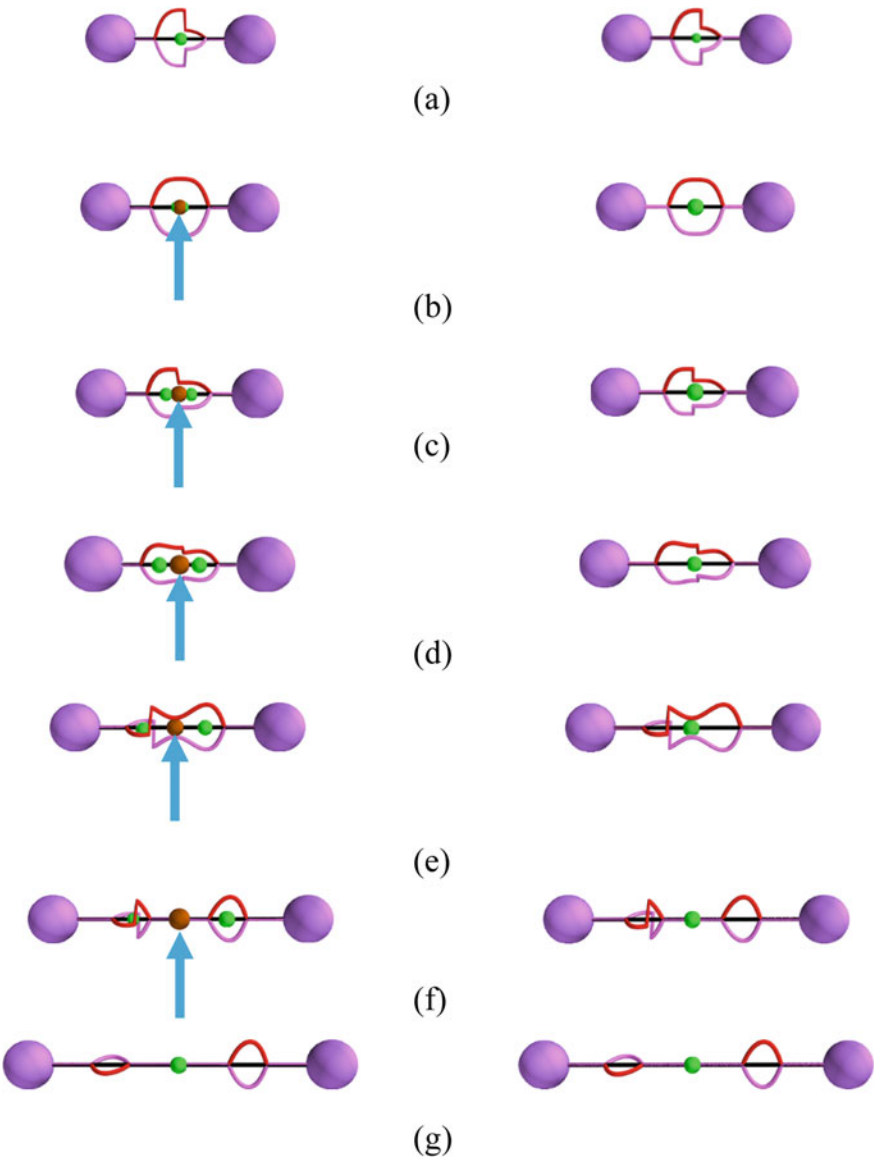


**Fig. 5.11** The $\{q_\sigma, q_\sigma{}'\}$ (left-panels) and $\{q_{\sigma F}, q_{\sigma F}{}'\}$path-packets (right-panels) calculated on the QTAIM and Ehrenfest $\mathbf{F}(\mathbf{r})$ $Li_2$ molecular graphs with the applied compression and stretching distortions sub-figure **(e)** corresponds to the undistorted molecular graph, corresponding to Table 5.4, the blue arrows indicate the location of the *NNA*s

**Table 5.4** Distances in a.u. corresponding to the compression and stretching distortions of the QTAIM $Li_2$ molecular graphs and the corresponding Ehrenfest Force **F**(**r**) molecular graphs, see Fig. 6.8, the values for the molecular graph corresponding to the relaxed geometry are indicated by sub-figure (**e**) displayed with the italic font

| | Li1--Li2 | $L_{i1}$-*NNA3* | *NNA3-BCP* |
|---|---|---|---|
| (**a**) | 3.8248 | --- | --- |
| (**b**) | 4.0248 | 2.0124 | 0.0956 |
| (**c**) | 4.2248 | 2.1124 | 0.3006 |
| (**d**) | 4.6248 | 2.3124 | 0.5229 |
| (**e**) | *5.1036* | *2.5518* | *0.7273* |
| (**f**) | 6.1036 | 3.0518 | 1.0762 |
| (**g**) | 7.1036 | --- | --- |

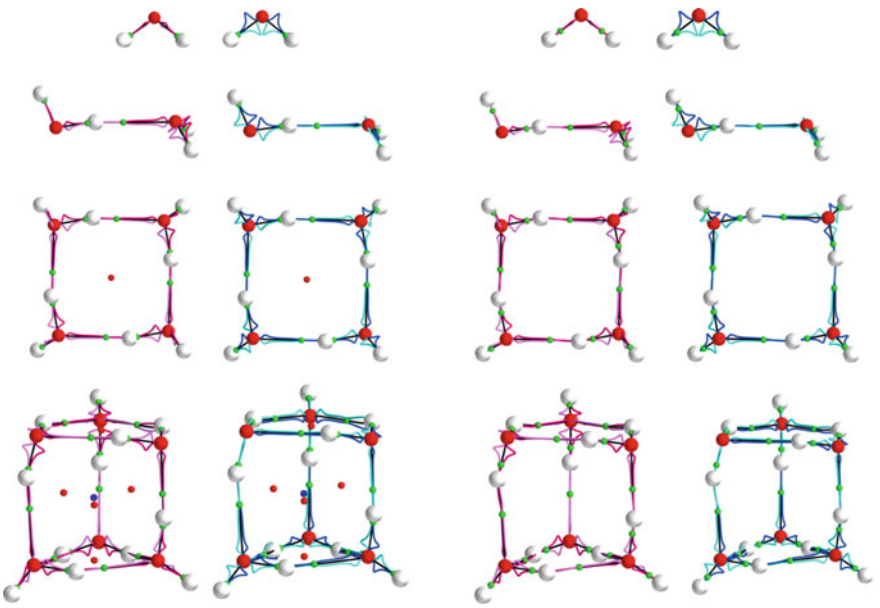

**Fig. 5.12** The Hessian of $\rho(\mathbf{r})$ bond-path framework set $\mathsf{B} = (\{\boldsymbol{q}, \boldsymbol{q}'\}, \{\boldsymbol{p}, \boldsymbol{p}'\}, \boldsymbol{r})$ and QTAIM on the Ehrenfest **F**(**r**) molecular graph bond-path framework set $\mathsf{B}_{\rho F} = (\{\boldsymbol{q}_{\rho F}, \boldsymbol{q}_{\rho F}'\}, \{\boldsymbol{p}_{\rho F}, \boldsymbol{p}_{\rho F}'\}, \boldsymbol{r}_F)$ for the $H_2O$, $(H_2O)_2$, $(H_2O)_4$ and $(H_2O)_6$ are presented. The '$_{\rho F}$' and '$\boldsymbol{r}_F$' refers to using the Hessian of $\rho(\mathbf{r})$ eigenvectors on the Ehrenfest Force **F**(**r**) molecular graph, with $\boldsymbol{q}$, $\boldsymbol{q}_{\rho F}$ (dark-magenta), $\boldsymbol{q}'$, $\boldsymbol{q}_{\rho F}{}'$ (light-magenta), $\boldsymbol{p}$, $\boldsymbol{p}_{\rho F}$ (dark-blue) and $\boldsymbol{p}'$, $\boldsymbol{p}'_{\rho F}$ (light-blue)

An earlier scalar QTAIM investigation into the unusually strong hydrogen-bonding in water ice found that hydrogen-bond *BCP*s possessed a degree of covalent character [42, 43] in confirmation of the X-ray diffraction work by Isaacs et al. [44]. E. D. Isaacs determined the presence of excess electron momentum on the shared hydrogen atom. The earlier scalar QTAIM work could not *explain why* this coupling occurred but only

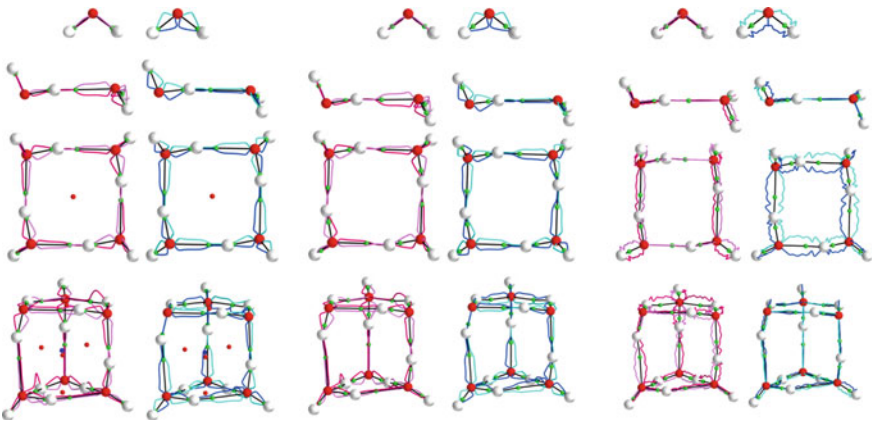

**Fig. 5.13** The stress tensor $\boldsymbol{\sigma}(\mathbf{r})$ on the QTAIM molecular graph bond-path framework set $B_{\sigma\rho} = (\{q_{\sigma\rho}, q_{\sigma\rho}'\}, \{p_{\sigma\rho}, p_{\sigma\rho}'\}, r)$ (left-panels) and stress tensor $\boldsymbol{\sigma}(\mathbf{r})$ on the Ehrenfest $\mathbf{F}(\mathbf{r})$ molecular graph $B_{\sigma F} = (\{q_{\sigma F}, q_{\sigma F}'\}, \{p_{\sigma F}, p_{\sigma F}'\}, r_F)$ (middle-panels) and with a magnification factor of $\times$ 5 for the $H_2O$, $(H_2O)_2$, $(H_2O)_4$ and $(H_2O)_6$, the stress tensor $\boldsymbol{\sigma}(\mathbf{r})$ ellipticity $\varepsilon_{\sigma} = |\lambda_{2\sigma}|/|\lambda_{1\sigma}| - 1$ is used. The $B_{FB} = (\{q_{FB}, q_{FB}'\}, \{p_{FB}, p_{FB}'\}, r_F)$ (right-panels) with Ehrenfest Force $\mathbf{F}(\mathbf{r})$ ellipticity $\varepsilon_{FB} = (|\lambda_{2F}|/|\lambda_{1F}|) - 1$

provided a visualization of coupling of the hydrogen-bonds in $(H_2O)_6$ acquire less covalent-bond character compared with those of $(H_2O)_4$, but did not fully quantity this effect, see Fig. 5.13 and Table 5.5 [45]. Later this effect was quantified using the Ehrenfest Force $\mathbf{F}(\mathbf{r})$ precessions $B_F$ within NG-QTAIM. This was undertaken specifically to provide insight into the net electron momentum transfer between the coupling hydrogen-bond *BCP* and covalent-bond *BCP* due to the forces on the electrons are zero at the *BCP* for the $\mathbf{F}(\mathbf{r})$ atomic partitioning.

## 5.3 The Precessions $K'_F$ and $K_F$ Corresponding to the Ehrenfest Force F(r)

When the $\underline{\mathbf{e}}_{2F}$ eigenvector, the subscript '$_F$' denotes the Ehrenfest Force, aligns along the *BCP* $\rightarrow$ *RCP* path the corresponding bond-path will rupture when the *BCP* and *RCP* coalesce. This process usually unfolds more readily for a hydrogen-bond compared with a covalent-bond. The precession $K'_F$ of the $\{q_F, q_F'\}$ path-packet, constructed with the $\underline{\mathbf{e}}_{2F}$ eigenvector, about the bond-path: With $\beta = (\pi/2 - \alpha)$ and $\alpha$ defined by Eq. (5.5), we can write an expression for $K'_F$:

$$K'_F = 1 - \cos^2\beta, \quad \text{where } \cos\beta = e_{2F} \cdot u,\ \beta = (\pi/2 - \alpha) \text{ and } 0 \leq K'_F \leq 1 \qquad (5.5)$$

**Table 5.5** Total local energy $H(\mathbf{r_{bF}})$ and the Ehrenfest $\underline{\mathbf{e}}_{\mathbf{1F}}$ and $\underline{\mathbf{e}}_{\mathbf{2F}}$ eigenvector components at the Ehrenfest *BCP*s for the $H_2O$, $(H_2O)_2$, $(H_2O)_4$ and $(H_2O)_6$ molecular graphs, as well as the vector dot product between the hydrogen-bond *BCP* $\underline{\mathbf{e}}_{\mathbf{1F}}$ and $\underline{\mathbf{e}}_{\mathbf{2F}}$ eigenvectors and those of its collinear sigma *BCP*. Hydrogen-bond *BCP*s with a degree of covalent character, $H(\mathbf{r_{bF}}) < 0$ are highlighted in bold font. The remaining sigma-bonds that do not share a hydrogen atom with hydrogen-bond with associated *BCP*s are presented in an italic font, with $\underline{\mathbf{e}}_{\mathbf{1F}}$(H--O)·$\underline{\mathbf{e}}_{\mathbf{1F}}$(O-H) and $\underline{\mathbf{e}}_{\mathbf{2F}}$(H--O)·$\underline{\mathbf{e}}_{\mathbf{2F}}$(O-H) values shown as *N.A*

| *BCP* | $H(\mathbf{r_{bF}})$ | | $\underline{\mathbf{e}}_{\mathbf{1F}}$ | | $\underline{\mathbf{e}}_{\mathbf{1F}}$(H--O)·$\underline{\mathbf{e}}_{\mathbf{1F}}$(O--H) | $\underline{\mathbf{e}}_{\mathbf{2F}}$ | | | $\underline{\mathbf{e}}_{\mathbf{2F}}$(H--O)·$\underline{\mathbf{e}}_{\mathbf{2F}}$(O-H) |
|---|---|---|---|---|---|---|---|---|---|
| | | | | | $H_2O$ | | | | |
| O1-$H_2$ | −0.5524 | 0.0000 | 0.6391 | 0.7692 | *N.A* | 1.0000 | 0.0000 | 0.0000 | *N.A* |
| O1-$H_3$ | −0.5524 | 0.0000 | −0.6391 | 0.7692 | | 1.0000 | 0.0000 | 0.0000 | |
| | | | | | $(H_2O)_2$ | | | | |
| $H_2$--$O_6$ | 0.0012 | 0.0321 | 0.0578 | −0.9978 | 0.9787 | −0.0024 | −0.9983 | −0.0579 | −0.9995 |
| $O_3$-$H_2$ | −0.5353 | 0.2336 | 0.0233 | −0.9720 | | 0.0052 | 0.9997 | 0.0252 | |
| *$O_3$-$H_1$* | *−0.5537* | *−0.8594* | *−0.0274* | *−0.5106* | *N.A* | *0.0434* | *−0.9989* | *−0.0195* | *N.A* |
| *$O_6$-$H_5$* | *−0.5513* | *0.2670* | *0.6584* | *−0.7037* | | *0.8726* | *0.1447* | *0.4665* | |
| | | | | | $(H_2O)_4$ | | | | |
| **$H_4$--$O_1$** | **−0.0030** | **0.7208** | **−0.6932** | **−0.0039** | **0.9877** | **0.0019** | **−0.0037** | **1.0000** | **0.9999** |
| $O_5$-H4 | −0.4990 | 0.8204 | −0.5718 | 0.0027 | | 0.0071 | 0.0150 | 0.9999 | |
| *O1-H3* | *−0.5536* | *−0.0150* | *−0.7523* | *−0.6587* | *N.A* | *0.9979* | *−0.0525* | *0.0372* | *N.A* |
| | | | | | $(H_2O)_6$ | | | | |
| **$H_{11}$--$O_4$** | **−0.0031** | **0.2556** | **−0.9648** | **−0.0621** | **0.9677** | **0.0041** | **0.0653** | **−0.9979** | **−0.9980** |
| $O_{10}$-$H_{11}$ | −0.4988 | 0.4855 | −0.8742 | −0.0023 | | 0.0016 | −0.0018 | 1.0000 | |
| **$H_{17}$--$O_{13}$** | **−0.0013** | **−0.2945** | **−0.9445** | **−0.1458** | **0.8224** | **0.9555** | **−0.2889** | **−0.0587** | **0.9879** |
| $O_{16}$-$H_{17}$ | −0.5074 | −0.1155 | −0.8997 | 0.4209 | | 0.9896 | −0.1407 | −0.0294 | |
| **$H_9$--$O_1$** | **−0.0001** | **0.7969** | **−0.5140** | **0.3174** | **0.8155** | **0.5493** | **0.8352** | **−0.0267** | **0.9864** |
| $O_7$-H9 | −0.5152 | 0.7090 | −0.6525 | −0.2676 | | 0.6776 | 0.7355 | 0.0021 | |

(continued)

**Table 5.5** (continued)

| *BCP* | $H(\mathbf{r}_{bF})$ | | $\underline{\mathbf{e}}_{1F}$ | | $\underline{\mathbf{e}}_{1F}$(H--O)·$\underline{\mathbf{e}}_{1F}$(O--H) | $\underline{\mathbf{e}}_{2F}$ | | | $\underline{\mathbf{e}}_{2F}$(H--O)·$\underline{\mathbf{e}}_{2F}$(O-H) |
|---|---|---|---|---|---|---|---|---|---|
| **$H_2$--$O_{16}$** | **−0.0089** | **0.3517** | **−0.9313** | **−0.0947** | **0.9622** | **0.0540** | **0.1212** | **−0.9912** | **0.9359** |
| $O_1$-$H_2$ | −0.4653 | 0.4436 | −0.8819 | 0.1596 | | −0.0734 | −0.2132 | −0.9743 | |
| $H_{14}$--$O_7$ | 0.0013 | 0.3802 | −0.8983 | −0.2203 | 0.4491 | 0.0377 | 0.2531 | −0.9667 | −0.3569 |
| $O_{13}$-$H_{14}$ | −0.5323 | 0.3753 | −0.5279 | 0.7618 | | −0.0349 | 0.8133 | 0.5808 | |
| $H_{15}$--$O_{10}$ | 0.0017 | 0.0436 | 0.6116 | −0.7900 | 0.4177 | 0.9735 | 0.1517 | 0.1712 | 0.2922 |
| $O_{13}$-$H_{15}$ | −0.5353 | 0.8544 | 0.5126 | −0.0847 | | 0.1363 | −0.0640 | 0.9886 | |
| $H_{18}$--$O_{10}$ | 0.0019 | −0.0123 | −0.6737 | −0.7389 | −0.4083 | 0.9821 | 0.1307 | −0.1355 | 0.1584 |
| $O_{16}$-$H_{18}$ | −0.5391 | 0.8128 | 0.5825 | 0.0080 | | 0.0265 | −0.0233 | −0.9994 | |
| $H_6$--$O_7$ | 0.0020 | −0.6794 | −0.4616 | 0.5704 | 0.3607 | 0.6549 | −0.0308 | 0.7551 | 0.5462 |
| $O_4$-$H_6$ | −0.5420 | 0.4362 | −0.6329 | 0.6397 | | 0.7918 | 0.6077 | 0.0614 | |
| $H_5$--$O_1$ | 0.0014 | −0.2518 | −0.5198 | −0.8164 | 0.8969 | 0.9373 | 0.0792 | −0.3395 | 0.9558 |
| $O_4$-$H_5$ | −0.5321 | 0.1235 | −0.7306 | −0.6715 | | 0.9163 | 0.3437 | −0.2055 | |
| *$O_7$-$H_8$* | *−0.5542* | *0.6981* | *0.4886* | *0.5233* | | *0.0111* | *0.7235* | *−0.6902* | |
| *$O_{10}$-$H_{12}$* | *−0.5542* | *0.7412* | *0.6710* | *0.0173* | *N.A* | *0.0959* | *−0.0803* | *−0.9921* | *N.A* |
| *$O_1$-$H_3$* | *−0.5543* | *0.7454* | *−0.1762* | *−0.6429* | | *0.3530* | *0.9224* | *0.1566* | |

Note that there are separate expressions for the $\underline{\mathbf{u}}$ unit vector for the hydrogen-bond *BCP* bond-path ($\underline{\mathbf{u}}_{\text{H--O}}$) and for the covalent O-H bond *BCP* bond-path ($\underline{\mathbf{u}}_{\text{O-H}}$), see Fig. 5.14. Values of $\mathsf{K'}_{\mathbf{F}} = 0$ and $\mathsf{K'}_{\mathbf{F}} = 1$ for an entire bond-path indicate the lowest and highest tendencies towards bond-path-rigidity respectively: $\mathsf{K'}_{\mathbf{F}} = 0$ and $\mathsf{K'}_{\mathbf{F}} = 1$ define minimum and maximum covalent-bond character, respectively. Considering the extremes, $\mathsf{K'}_{\mathbf{F}} = 1$ corresponds to the maximum alignment of the *BCP* → *RCP* path with the $\underline{\mathbf{e}}_{\mathbf{1F}}$ eigenvector, the least facile direction, i.e. the most covalent-bond-like and for $\mathsf{K'}_{\mathbf{F}} = 0$, we have the maximum degree of alignment with the $\underline{\mathbf{e}}_{\mathbf{2F}}$ eigenvector, the most facile direction, that is least covalent-bond-like. The precession $\mathsf{K}_{\mathbf{F}}$, of the $\{\boldsymbol{p}_{\mathbf{F}}, \boldsymbol{p}_{\mathbf{F}}'\}$ path-packet constructed with the $\underline{\mathbf{e}}_{\mathbf{1F}}$ eigenvector, enables the extent to which the $\{\boldsymbol{p}_{\mathbf{F}}, \boldsymbol{p}_{\mathbf{F}}'\}$ path-packet precesses about the bond-path and is defined by the *precession* $\mathsf{K}_{\mathbf{F}}$:

$$\mathsf{K}_{\mathbf{F}} = 1 - \cos^2\alpha, \text{ where } \cos\alpha = \mathrm{e}_{1\mathrm{F}} \cdot \mathrm{u} \quad \text{and} \quad 0 \leq \mathsf{K}_{\mathbf{F}} \leq 1 \tag{5.6}$$

The precession of the $\{\boldsymbol{p}_{\mathbf{F}}, \boldsymbol{p}_{\mathbf{F}}'\}$ path-packet is defined when for alignment of the $\pm\underline{\mathbf{e}}_{\mathbf{1F}}$ eigenvector with $\underline{\mathbf{u}}_{\text{O--H}}$ or $\underline{\mathbf{u}}_{\text{H-O}}$, that coincides with the *BCP* → *RCP* path. Therefore the *BCP* will have minimum facile character, i.e. bond-path-rigidity. For the two extremes, $\mathsf{K}_{\mathbf{F}} = 0$, where α is defined by Eq. (5.6), the maximum alignment of the *BCP* → *RCP* path with the $\underline{\mathbf{e}}_{\mathbf{1F}}$ eigenvector, the least facile direction, i.e. least

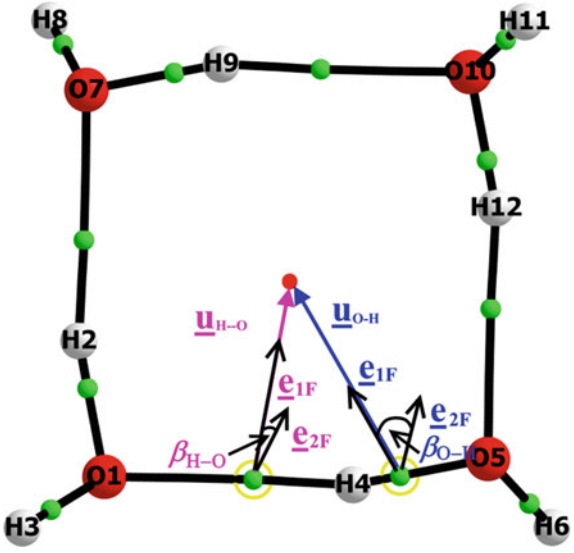


**Fig. 5.14** The Ehrenfest Force $\mathbf{F}(\mathbf{r})$ $\{\boldsymbol{q}_{\mathbf{F}}, \boldsymbol{q}_{\mathbf{F}}'\}$ path-packet precession $\mathsf{K'}_{\mathbf{F}}$ for the sigma O1-H4 *BCP* and hydrogen-bond H4-O5 *BCP* shown for the $(H_2O)_4$ cluster, where the $\underline{\mathbf{u}}_{\mathbf{H--O}}$ (magenta arrow) and $\underline{\mathbf{u}}_{\mathbf{O-H}}$ (blue arrow) are unit vectors directed parallel to the initial orientation of the *BCP-RCP* direction. The undecorated red and green spheres indicate the locations of the QTAIM ring (*RCP*) and Ehrenfest Force $\mathbf{F}(\mathbf{r})$ bond critical points (*BCP*s) respectively

hydrogen-bond-like and for $K_F = 1$, we have the maximum degree of alignment with the $\underline{\mathbf{e}}_{2F}$ eigenvector, the most facile direction, that is least hydrogen-bond-like. Therefore, $K_F = 0$ and $K_F = 1$ define minimum and maximum covalent-bond character respectively. The presence of hydrogen-bond *BCP* and covalent-bond *BCP* coupling was determined by quantifying the relative orientation of the Hessian of $\rho(\mathbf{r})$ $\{\boldsymbol{q}, \boldsymbol{q}'\}$ or Ehrenfest Force $\mathbf{F}(r)$ $\{\boldsymbol{q}_F, \boldsymbol{q}_F'\}$ path-packets in an extended region around both sides of each *BCP* along the containing bond-path. The precession $K'_F$ provided a quantification of the directional chemical character as a result of the coupling, or lack of, between the hydrogen-bond *BCP* and covalent-bond *BCP*.

The construction of precessions $K'_F$ and $K_F$along the $\mathbf{F}(\mathbf{r})$ bond-path was undertaken using $\mathbf{F}(\mathbf{r})$ eigenvectors. The $\mathbf{F}(\mathbf{r})$ eigenvectors display a slow variation with bond-path location when close to the $\mathbf{F}(\mathbf{r})$ (3, −1) *BCP*. Closer to nuclei the character of these eigenvectors changes to show substantial oscillations in direction. Therefore cutoffs were established in terms of fractional distance traced along the bond-path from *BCP* to the nucleus of 65% and 80% for the covalent-bond and the hydrogen-bond respectively. In tracing out the $K'_F$ and $K_F$ for locations on the bond-path with fractional distances greater than the cutoff values, the $\mathbf{F}(\mathbf{r})$ eigenvectors used to construct the $K'_F$ and $K_F$ are assumed constant between their values at the cutoff and the terminating nucleus.

### 5.3.1 *Precessions $K'_F$ and $K_F$ of the Ehrenfest Force F(R) for the Unusual Strength of Hydrogen-Bonding*

The Ehrenfest Force $\mathbf{F}(\mathbf{r})$ precessions $K'_F$, was used to explain why hydrogen-bonds are weaker in the $(H_2O)_6$ cluster than for the $(H_2O)_4$ cluster: the chemical coupling present in $(H_2O)$ results in maximum hydrogen-bond like character ($K'_F = 1.0$) for both the hydrogen-bond *BCP*s *and* the covalent-bond *BCP*s [46]. The behavior of the Hessian of $\rho(\mathbf{r})$ $K'$ was found to be inconsistent, e.g. the values of $K'$ for the covalent-bond *BCP*s are very low and high respectively for the O13-H15 *BCP* and O16-H18 *BCP*, see Fig. 5.15 (left-panel). In contrast, the Ehrenfest Force $\mathbf{F}(\mathbf{r})$ precessions $K'_F$: for the $(H_2O)_4$ cluster, all four hydrogen bonds were equivalent, there was strong covalent-bond like character for both the hydrogen-bond *BCP*s and covalent-bond *BCP*s, see Fig. 5.15 (right-panel).

Using the Ehrenfest Force $\mathbf{F}(\mathbf{r})$, the separations (A + D), in Table 5.7 of the hydrogen-bond-*BCP* and covalent-bond *BCP* decrease with increase in the magnitude of $H(\mathbf{r_b})$ < 0, the exception being the H9--O1 *BCP* and O7-H9 *BCP* pair that possess a smaller than expected $H(\mathbf{r_b}) < 0$ value was explained by the proximity of the 'dangling' O7-H8 *BCP* to the O7-H9 *BCP*. There is complete agreement however, with the trend of reduction of the *BCP* separations (A + D) with the reduction in the differences in the ratios $\Delta\{Q_{rel}{}^{H\text{--}O}, Q_{rel}{}^{O\text{-}H}\}$. Conversely, for Hessian of $\rho(\mathbf{r})$ eigenvectors no such correlation was found, see Table 5.6. It can be noticed for both the Hessian

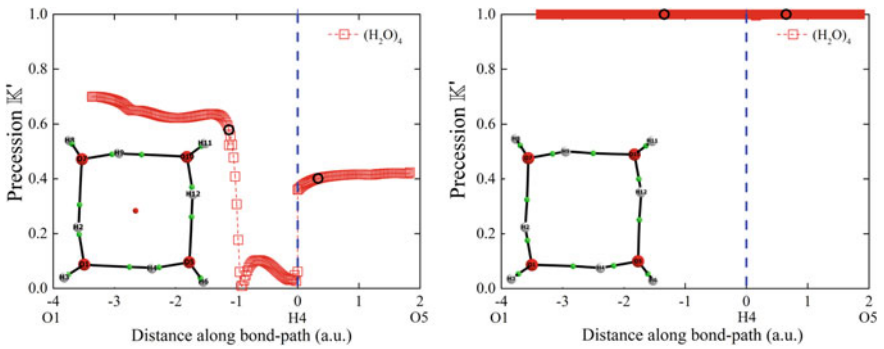


**Fig. 5.15** The $\mathsf{K}'$ of the Hessian of $\rho(\mathbf{r})$ (left panel) and $\mathsf{K}'$ of Ehrenfest Force $\mathbf{F(r)}$ (right panel) path-packets are for the $(H_2O)_4$ are presented, the value of the Ehrenfest Force $\mathbf{F}(\mathbf{r})$ dot product at the *BCP*s $\underline{\mathbf{e}}_{\mathbf{2F}}\mathbf{(H\text{--}O)}\cdot\underline{\mathbf{e}}_{\mathbf{2F}}\mathbf{(O\text{--}H)} = 0.9999$ corresponding to the right panel, see Table 5.5. The inserts correspond to the Hessian of $\rho(\mathbf{r})$ (left-panel) and Ehrenfest Force $\mathbf{F(r)}$ (right-panel) $(H_2O)_4$ molecular graphs, where the undecorated green, red and blue spheres representing the bond critical points (*BCPs*), ring critical points (*RCPs*)

of $\rho(\mathbf{r})$ and the Ehrenfest Force $\mathbf{F}(\mathbf{r})$ that only the hydrogen-bond $H_2\text{--}O_{16}$ *BCP* bond-path was shorter for $(H_2O)_6$ than was the case for the representative hydrogen-bond H4--O1 *BCP* in $(H_2O)_4$, see Tables 5.6 and 5.7. The hydrogen-bond H11--O4 *BCP* bond-path in $(H_2O)_6$ possesses a bond-path length (BPL) closest to that of the $(H_2O)_4$ representative H4--O1 *BCP* bond-path. Therefore, to provide an NG-QTAIM comparison of the topological strength of the $(H_2O)_6$ and $(H_2O)_4$ clusters that these of these hydrogen-bond *BCP*s will be used to provide a good basis for comparison.

The precession $\mathsf{K}'_{\mathbf{F}}$ quantified the dependency of the chemical character on the degree of coupling of the covalent (sigma) and hydrogen-bonds. Examination of the precession $\mathsf{K}'_{\mathbf{F}}$ of pairs of non-coupling covalent (sigma) and hydrogen-bonds for the $(H_2O)_6$ cluster provided a consistency check. This was undertaken by the location of prototypical $\mathsf{K}'_{\mathbf{F}}$ profiles that corresponded to low values ($\mathsf{K}'_{\mathbf{F}} \leq 0.2$) and high values ($\mathsf{K}'_{\mathbf{F}} \geq 0.8$) respectively, see Fig. 5.16.

It was discovered for the first time, that a greater degree of coupling ($H(\mathbf{r_b}) < 0$ for a hydrogen-bond *BCP*) for a given water cluster between pairs of covalent (sigma) and hydrogen-bonds correlated well with a shorter separation (A + D) between the corresponding *BCP*s. Perfect correlation was found between the *BCP* separations (A + D) and the difference ratios $\Delta\{Q_{rel}{}^{H\text{--}O}, Q_{rel}{}^{O\text{-}H}\}$ calculated from the $\mathsf{K}'_{\mathbf{F}}$ profiles, whereby shorter *BCP* separations (A + D) correlated perfectly with smaller $\Delta\{Q_{rel}{}^{H\text{--}O}, Q_{rel}{}^{O\text{-}H}\}$, see Table 5.7. Therefore, the lowest values of $\Delta\{Q_{rel}{}^{H\text{--}O}, Q_{rel}{}^{O\text{-}H}\}$ were regarded as providing a measure of 'matching' between the covalent (sigma) and hydrogen-bonds. A higher degree of matching i.e. the lower

**Table 5.6** The bond-path length (BPL), partial bond-path lengths H-*BCP* = A, *BCP*--O = B, O-*BCP* = C and *BCP*-H = D, of the symmetry inequivalent QTAIM *BCP* values of the hydrogen-bond and covalent-bond in atomic units (a.u). The ratios $Q_{rel}{}^{H\text{--}O} = Q/Q_{max}(H\text{-}O)$ and $Q_{rel}{}^{O-H} = Q/Q_{max}(O\text{-}H)$ are calculated by dividing the area Q under each precession $K'_F$ plot by the theoretical limit $Q_{max}$ defined as $K_F = 1$ along the entire bond-path. H--O and O-H correspond to the hydrogen-bond *BCP* bond-path and the covalent-bond *BCP* bond-path respectively. The absolute difference in the ratios $Q_{rel}{}^{H\text{--}O}$ and $Q_{rel}{}^{O-H}$ waspresented as $\Delta(Q_{rel}{}^{H\text{--}O}, Q_{rel}{}^{O\text{-}H})$

| *BCP* | H--O(BPL,A,B) | O-H(C,D) | A + D | $Q_{rel}{}^{H\text{--}O}$, $Q_{rel}{}^{O\text{-}H}$ ($\Delta\{Q_{rel}{}^{H\text{--}O}, Q_{rel}{}^{O\text{-}H}\}$) |
|---|---|---|---|---|
| **$(H_2O)_4$** | | | | |
| $H_4$--$O_1$,$O_5$-$H_4$ | 3.379, 1.137, 2.242 | 1.504, 0.333 | 1.470 | 0.469, 0.409 (0.060) |
| **$(H_2O)_6$** | | | | |
| $H_{18}$--$O_{10}$, $O_{16}$-$H_{18}$ | 4.228, 1.637, 2.591 | 1.466, 0.342 | 1.979 | 0.199, 0.854 (0.655) |
| $H_{15}$--$O_{10}$, $O_{13}$-$H_{15}$ | 3.963, 1.462, 2.501 | 1.470, 0.341 | 1.803 | 0.200, 0.099 (0.101) |
| $H_{17}$--$O_{13}$, $O_{16}$-$H_{17}$ | 3.571, 1.242, 2.329 | 1.495, 0.337 | 1.579 | 0.272, 0.856 (0.584) |
| $H_9$--$O_1$, $O_7$-$H_9$ | 3.548, 1.229, 2.319 | 1.493, 0.333 | 1.562 | 0.173, 0.667 (0.494) |
| $H_{11}$--$O_4$, $O_{10}$-$H_{11}$ | 3.403, 1.145, 2.258 | 1.503, 0.334 | 1.479 | 0.355, 0.845 (0.490) |
| $H_2$--$O_{16}$, $O_1$-$H_2$ | 3.204, 1.040, 2.164 | 1.527, 0.336 | 1.376 | 0.324, 0.725 (0.401) |

**Table 5.7** The bond-path length (BPL), partial water cluster bond-path lengths for the Ehrenfest Force **F**(**r**) symmetry inequivalent hydrogen-bond *BCP* and covalent-bond *BCP* values and the ratios $Q_{rel}{}^{H\text{--}O}$, $Q_{rel}{}^{O\text{-}H}$ and the absolute difference ($\Delta\{Q_{rel}{}^{H\text{--}O}, Q_{rel}{}^{O\text{--}H}\}$) being presented in the parenthesis, see the caption of Table 5.6 for further details

| *BCP* | H--O(BPL,A,B) | O--H(C,D) | | A + D | $Q_{rel}{}^{H\text{--}O}$, $Q_{rel}{}^{O\text{-}H}$ ($\Delta\{Q_{rel}{}^{H\text{--}O}$, $Q_{rel}{}^{O\text{-}H}\}$) | $H(\mathbf{r_b})$ |
|---|---|---|---|---|---|---|
| **$(H_2O)_4$** | | | | | | |
| $H_4$--$O_1$, $O_5$-$H_4$ | 3.359, 1.345, 2.014 | 1.207, 0.648 | | 1.993 | 1.000, 0.999 (0.001) | −0.0030 |
| **$(H_2O)_6$** | | | | | | |
| $H_{18}$--$O_{10}$, $O_{16}$-$H_{18}$ | 4.166, 1.798, 2.366 | 1.189, 0.638 | | 2.436 | 0.940, 0.077 (0.863) | 0.0019 |
| $H_{15}$--$O_{10}$, $O_{13}$-$H_{15}$ | 3.935, 1.632, 2.301 | 1.190, 0.639 | | 2.271 | 0.931, 0.163 (0.768) | 0.0017 |
| $H_{17}$--$O_{13}$, $O_{16}$-$H_{17}$ | 3.549, 1.431, 2.117 | 1.204, 0.647 | | 2.078 | 0.669, 0.891 (0.222) | −0.0013 |
| $H_9$--$O_1$, $O_7$-$H_9$ | 3.526, 1.417, 2.109 | 1.200, 0.645 | | 2.062 | 0.628, 0.744 (0.116) | −0.0001 |
| $H_{11}$--$O_4$, $O_{10}$-$H_{11}$ | 3.384, 1.357, 2.027 | 1.207, 0.649 | | 2.006 | 0.685, 0.780 (0.095) | −0.0031 |
| $H_2$--$O_{16}$, $O_1$-$H_2$ | 3.186, 1.279, 1.907 | 1.222, 0.658 | | 1.937 | 0.073, 0.070 (0.003) | −0.0089 |

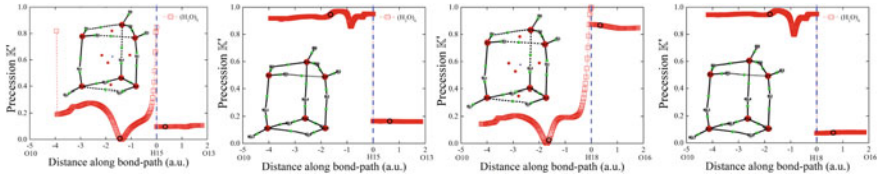


**Fig. 5.16** The precession $\mathsf{K}'$ of the Hessian of $\rho(\mathbf{r})$ and $\mathsf{K}'$ of the Ehrenfest Force **F(r)** path-packets for the $(H_2O)_6$ cluster that correspond to low values of the Ehrenfest Force **F**(**r**) dot product at the *BCP*s $\underline{\mathbf{e}}_{\mathbf{2F}}$**(H--O)**·$\underline{\mathbf{e}}_{\mathbf{2F}}$**(O-H)** = 0.292 (O10-H15-O13) and 0.158 (O10--H18-O16). The inserts are the corresponding QTAIM and Ehrenfest Force **F(r)** $(H_2O)_6$ molecular graphs, see the caption of Fig. 5.15 for further details

values of $\Delta\{Q_{rel}{}^{H\text{--}O}, Q_{rel}{}^{O\text{-}H}\}$ was considered a measure of the relative ease of electron momentum transfer from the hydrogen atom of a sigma-bond to the hydrogen-bond. Furthermore, for the smallest separation (A + D) of the *BCP*s the degree of coupling between covalent (sigma) and hydrogen-bond increases between the pairs of covalent (sigma) and hydrogen-bonds for the $(H_2O)_6$ cluster. This occurred to the extent that the hydrogen-bond $H_2$--$O_{16}$ *BCP* possesses $\mathsf{K}'_{\mathbf{F}} \leq 0.2$, characteristic of a covalent-bond.

Favorable conditions for chemical coupling i.e. electron momentum transfer occurred for larger *BCP* separations where $H(\mathbf{r_b}) < 0$ resulting in e.g. the covalent-bond O10-H11 *BCP* with a value of $\mathsf{K}'_{\mathbf{F}} \geq 0.8$. This value of $\mathsf{K}'_{\mathbf{F}}$ was high enough to be considered to be hydrogen-bond-like, indicating the coupling has significantly altered the directional character of the covalent-bond *BCP*, see Fig. 5.17 the Hessian of $\rho(\mathbf{r})$ precession $\mathsf{K}'_{\mathbf{F}}$ results were provided in parallel but did not display any covalent-bond and hydrogen-bond coupling effects. This was in contrast to the Ehrenfest Force **F**(**r**) where, by definition, the forces on the electrons **F**(**r**) = 0 at the Ehrenfest Force **F**(**r**) *BCP*s.

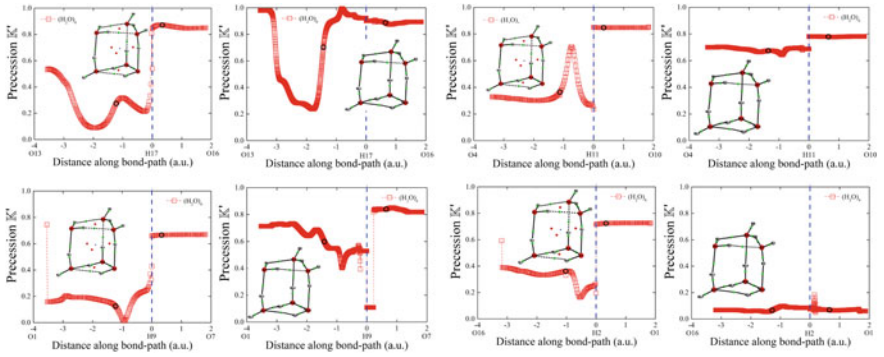


**Fig. 5.17** The $\mathsf{K}'$ of the Hessian of $\rho(\mathbf{r})$ and $\mathsf{K}'_{\mathbf{F}}$ of the Ehrenfest Force **F(r)** path-packets for $(H_2O)_6$ that correspond to high values at the *BCP*s of the dot product $\underline{\mathbf{e}}_{\mathbf{2F}}$**(H--O)**·$\underline{\mathbf{e}}_{\mathbf{2F}}$**(O-H)** ≥ 0.94, see the caption of Fig. 5.16 for further details

## 5.4 Summary

We explained the basics of the stress tensor $\boldsymbol{\sigma}(\mathbf{r})$ within the NG-QTAIM framework. We demonstrated that assuming the stress tensor eigenvectors calculated at the scalar QTAIM *BCP*s are equivalent an over simplification by considering the bond-path framework set $\mathsf{B}$ for ethene. Visual inspection of the three-stranded paths $\mathsf{B}$ with the $\mathsf{B}_{\sigma}$ and $\mathsf{B}_{\sigma\mathrm{H}}$ overturned previous assumptions of the presence of an $\underline{\mathbf{e}}_{\mathbf{1}} \rightarrow \underline{\mathbf{e}}_{\mathbf{1}\sigma}$ and $\underline{\mathbf{e}}_{\mathbf{2}} \rightarrow \underline{\mathbf{e}}_{\mathbf{2}\sigma}$ mapping. This was undertaken for the ethene molecule subjected to a torsion $\theta$, $-150.0° \leq \theta \leq +150.0°$ and inspecting which of $\mathsf{B}_{\sigma}$ or $\mathsf{B}_{\sigma\mathrm{H}}$ most closely resembled $\mathsf{B}$ by overlaying the $\mathsf{B}$, $\mathsf{B}_{\sigma}$ and $\mathsf{B}_{\sigma\mathrm{H}}$ onto three separate sets of the molecular graph. This visual inspection clearly indicated that the $\mathsf{B}_{\sigma}$ and not $\mathsf{B}_{\sigma\mathrm{H}}$ provided the most consistent mapping being $\underline{\mathbf{e}}_{\mathbf{1}} \rightarrow \underline{\mathbf{e}}_{\mathbf{2}\sigma}$ and $\underline{\mathbf{e}}_{\mathbf{2}} \rightarrow \underline{\mathbf{e}}_{\mathbf{1}\sigma}$. [26] We outlined the basic implementation of the Ehrenfest Force $\mathbf{F}(\mathbf{r})$ including the difficulties of calculating the Ehrenfest Force $\mathbf{F}(\mathbf{r})$ partitioning to return the complete spurious free topology for use with QTAIM. These difficulties focused on the requirement to engineer the ANO-RCC basis set to remove spurious artifacts. We discovered that using the Ehrenfest Force $\mathbf{F}(\mathbf{r})$ with NG-QTAIM did not require any additional basis set engineering so that it was sufficient to use more convenient basis sets. In particular the bond-path framework sets $\mathsf{B}_{\mathbf{F}}$, $\mathsf{B}_{\sigma\mathrm{F}}$ and $\mathsf{B}_{\sigma\mathrm{HF}}$ may be transplanted to molecular graphs from the QTAIM or Ehrenfest Force $\mathbf{F}(\mathbf{r})$ partitioning, see Table 5.8. In Chap. 6 we construct eigenvector-space trajectories $\mathsf{T}_i(\boldsymbol{s})$ for iso-energetic phenomena.

**Table 5.8** The NG-QTAIM concepts bond-path framework set and precessions listings of the locations of examples

| *Bond-path framework* | *Eigenvectors* | *Most facile* | *Least facile* | *Chapter (section)* |
|---|---|---|---|---|
| $\mathsf{B}$ Hessian of $\rho(\mathbf{r})$ | $\{\underline{\mathbf{e}}_{\mathbf{1}}, \underline{\mathbf{e}}_{\mathbf{2}}, \underline{\mathbf{e}}_{\mathbf{3}}\}$ | $\underline{\mathbf{e}}_{\mathbf{2}}$ | $\underline{\mathbf{e}}_{\mathbf{1}}$ | Chapter 5 (5.1.2) |
| $\mathsf{B}_{\sigma}$ Stress tensor $\boldsymbol{\sigma}(\mathbf{r})$ | $\{\underline{\mathbf{e}}_{\mathbf{1}\sigma}, \underline{\mathbf{e}}_{\mathbf{2}\sigma}, \underline{\mathbf{e}}_{\mathbf{3}\sigma}\}$ | $\underline{\mathbf{e}}_{\mathbf{1}\sigma}$ | $\underline{\mathbf{e}}_{\mathbf{2}\sigma}$ | Chapter 5 (5.1.3) |
| $\mathsf{B}_{\mathbf{F}}$ Ehrenfest force $\mathbf{F}(\mathbf{r})$ | $\{\underline{\mathbf{e}}_{\mathbf{1F}}, \underline{\mathbf{e}}_{\mathbf{2F}}, \underline{\mathbf{e}}_{\mathbf{3F}}\}$ | $\underline{\mathbf{e}}_{\mathbf{2F}}$ | $\underline{\mathbf{e}}_{\mathbf{1F}}$ | Chapter 5 (5.3.1) |
| *Precession* | *Bond-path character* | *Extremal-values* | | |
| | | 0.0 | 1.0 | |
| $\mathsf{K}$ Hessian of $\rho(\mathbf{r})$ | | | | |
| | | Benzene IR-responsivity | | Chapter 4 (**4.3.3**) |
| | | Rigidity | | Chapter 4 (**4.5.2**) |
| | | Fatigue | | Chapter 8 (**8.5.1**) |
| | | Covalent | | Chapter 8 (**8.6.3**) |
| $\mathsf{K}_{\mathbf{F}}$ Ehrenfest force $\mathbf{F}(\mathbf{r})$ | | | | |
| | | **Covalent** | | Chapter 5 (**5.3.1**) |

**Target learning outcomes:**:

- Determine the reasons for the differences between the stress tensor $\boldsymbol{\sigma}(\mathbf{r})$ and the Hessian of $\rho(\mathbf{r})$ and the Ehrenfest Force $\mathbf{F}(\mathbf{r})$.
- Understand why NG-QTAIM can consider the competition between halogen and hydrogen bonding.
- Understand why the bonding of benzvalene leads to explosive character.
- Determine the circumstances for which lithium clusters do not contain non-nuclear attractors (*NNA*s).
- Understand the unusual strength of hydrogen-bonding in ice.

## 5.5 Further Reading

On the stress tensor, we recommend reading the works of A. Tachibana who has made highly significant contributions in the area [18, 21, 47–49].

## References

1. Bader RFW (1980) Die allgemeinen Prinzipien der Wellenmechanik. J Chem Phys 73:2871–2883
2. Anderson JSM, Ayers PW, Hernandez JIR (2010) How ambiguous is the local kinetic energy?†. J Phys Chem A 114:8884–8895
3. Anderson JSM, Ayers PW (2011) Quantum theory of atoms in molecules: results for the SR-ZORA Hamiltonian. J Phys Chem A 115:13001–13006
4. Wyatt RE (2006) Quantum dynamics with trajectories. Springer, Berlin
5. Nichols J, Taylor H, Schmidt P, Simons J (1990) Walking on potential energy surfaces. J Chem Phys 92:340–346
6. Banerjee A, Adams N, Simons J, Shepard R (1985) Search for stationary points on surfaces. J Phys Chem 89:52–57
7. Simons J, Joergensen P, Taylor H, Ozment J (1983) Walking on potential energy surfaces. J Phys Chem 87:2745–2753
8. Nakatsuji H (1974) Common nature of the electron cloud of a system undergoing change in nuclear configuration. J Am Chem Soc 96:24–30
9. Ayers PW, Jenkins S (2009) An electron-preceding perspective on the deformation of materials. J Chem Phys 130:154104
10. Jenkins S, Maza JR, Xu T, Jiajun D, Kirk SR (2015) Biphenyl: a stress tensor and vector-based perspective explored within the quantum theory of atoms in molecules. Int J Quant Chem 115:1678–1690
11. Bader RFW (1994) Atoms in molecules: a quantum theory. Clarendon Press
12. Bader RFW, Laidig KE (1991) The prediction and calculation of properties of atoms in molecules. J Mol Struct (Thoechem) 234:75–80
13. Bader RFW, Nguyen-Dang TT, Tal Y (1979) Quantum topology of molecular charge distributions. II. Molecular structure and its change. J Chem Phys 70:4316–4329
14. Bader RFW, Anderson SG, Duke AJ (1979) Quantum topology of molecular charge distributions. 1. J Am Chem Soc 101:1389–1395
15. Bader RFW, Tal Y, Anderson SG, Nguyen-Dang TT (1980) Quantum topology: theory of molecular structure and its change. Isr J Chem 19:8–29

16. Tal Y, Bader RFW, Nguyen-Dang TT, Ojha M, Anderson SG (1981) Quantum topology. IV. Relation between the topological and energetic stabilities of molecular structures. J Chem Phys 74:5162–5167
17. Tachibana A (2001) Electronic energy density in chemical reaction systems. J Chem Phys 115:3497–3518
18. Tachibana A (2004) Spindle structure of the stress tensor of chemical bond. Int J Quant Chem 100:981–993
19. Tachibana A (2005) A new visualization scheme of chemical energy density and bonds in molecules. J Mol Model 11:301–311
20. Szarek P, Tachibana A (2007) The field theoretical study of chemical interaction in terms of the Rigged QED: new reactivity indices. J Mol Model 13:651–663
21. Szarek P, Sueda Y, Tachibana A (2008) Electronic stress tensor description of chemical bonds using nonclassical bond order concept. J Chem Phys 129:094102
22. Jenkins S, Kirk SR, Côté AS, Ross DK, Morrison I (2003) Dependence of the normal modes on the electronic structure of various phases of ice as calculated by ab initio methods. Can J Phys 81:225–231
23. Guevara-García A, Echegaray E, Toro-Labbe A, Jenkins S, Kirk SR (2011) Pointing the way to the products? Comparison of the stress tensor and the second-derivative tensor of the electron density. J Chem Phys 134:234106
24. Xu T, Farrell J, Momen R, Azizi A, Jenkins S (2017) A stress tensor eigenvector projection space for the $(H_2O)_5$ potential energy surface. Chem Phys Lett 667:25–31
25. Xu T, Wang L, Ping Y, Mourik TV, Früchtl H, Kirk SR, Jenkins S (2018) Quinone-based switches for candidate building blocks of molecular junctions with QTAIM and the stress tensor. Int J Quantum Chem 118(16):e25676
26. Li JH, Huang WJ, Xu T, Kirk SR, Jenkins S (2018) Stress tensor eigenvector following with next-generation quantum theory of atoms in molecules. Int J Quant Chem 119:e25847
27. Jenkins S, Maza JR, Xu T, Kirk SR (2015) Biphenyl: a stress tensor and vector-based perspective explored within the quantum theory of atoms in molecules. Int J Quant Chem 115:1678–1690
28. Jiajun D, Xu Y, Xu T, Momen R, Kirk SR (2016) The substituent effects on the biphenyl H---H bonding interactions subjected to torsion. 651, 251–256
29. Li S, Xu T, van Mourik T, Früchtl H, Kirk SR, Jenkins S (2019) Halogen and hydrogen bonding in halogenabenzene/$NH_3$ complexes compared using next-generation QTAIM. Molecules 24:2875
30. Malcomson T, Azizi A, Momen R, Xu T, Kirk SR, Paterson MJ, Jenkins S (2019) Stress tensor eigenvector following with next-generation quantum theory of atoms in molecules: excited state photochemical reaction path from benzene to benzvalene. J Phys Chem A 123:8254–8264
31. Maza JR, Jenkins S, Kirk SR, Anderson JSM, Ayers PW (2013) The Ehrenfest force topology: a physically intuitive approach for analyzing chemical interactions. Phys Chem Chem Phys 15:17823–17836
32. Hernández-Trujillo J, Cortés-Guzmán F, Fang D-C, Bader RFW (2006) Forces in molecules. Faraday Discuss 135:79–95; discussion 125–149, 503–506
33. Dem'yanov P, Polestshuk P (2012) A bond path and an attractive ehrenfest force do not necessarily indicate bonding interactions: case study on M2X2 (M=Li, Na, K; X=H, OH, F, Cl). Chem A Eur J 18:4982–4993
34. Davidson ER, Hagstrom SA, Chakravorty SJ, Umar VM, Fischer CF (1991) Ground-state correlation energies for two- to ten-electron atomic ions. Phys Rev A 44:7071–7083
35. Ichikawa K, Wagatsuma A, Kusumoto M, Tachibana A (2010) Electronic stress tensor of the hydrogen molecular ion: comparison between the exact wave function and approximate wave functions using Gaussian basis sets. J Mol Struct (Thoechem) 951:49–59
36. Pendás AM, Hernández-Trujillo J (2012) The Ehrenfest force field: topology and consequences for the definition of an atom in a molecule. J Chem Phys 137:134101–134101–9
37. Widmark P-O, Malmqvist P-Å, Roos BO (1990) Density matrix averaged atomic natural orbital (ANO) basis sets for correlated molecular wave functions. Theoret Chim Acta 77:291–306

38. Roos BO, Veryazov V, Widmark P-O (2004) Relativistic atomic natural orbital type basis sets for the alkaline and alkaline-earth atoms applied to the ground-state potentials for the corresponding dimers. Theor Chem Acc 111:345–351
39. Roos BO, Lindh R, Malmqvist P-Å, Veryazov V, Widmark P-O (2005) New relativistic ANO basis sets for transition metal atoms. J Phys Chem A 109:6575–6579
40. Azizi A, Momen R, Kirk SR, Jenkins S (2019) 3-D bond-paths of QTAIM and the stress tensor in neutral lithium clusters, Lim (m = 2–5), presented on the Ehrenfest force molecular graph. Phys Chem Chem Phys 22:864–877
41. Li S, Azizi A, Kirk SR, Jenkins S (2020) An explanation of the unusual strength of the HYDROGEN BOND in small water clusters. Int J Quantum Chem 120:e26361
42. Cremer D, Kraka E (1984) In conceptual approaches in quantum chemistrymodels and applications. Croat Chem Acta 57:1259
43. Rozas I, Alkorta I, Elguero J (2000) Behavior of Ylides containing N, O, and C atoms as hydrogen bond acceptors. J Am Chem Soc 122:11154–11161
44. Isaacs ED, Shukla A, Platzman PM, Hamann DR, Barbiellini B, Tulk CA (1999) Covalency of the hydrogen bond in ice: a direct X-ray measurement. Phys Rev Lett 82:600–603
45. Wang L, Azizi A, Xu T, Kirk SR, Jenkins S (2019) Explanation of the role of hydrogen bonding in the structural preferences of small molecule conformers. Chem Phys Lett 730:206–212
46. Xing H, Yang Y, Nie X, Xu T, Kirk SR, Jenkins S (2021) Understanding chemical coupling in cyclic versus compact water clusters with the Ehrenfest Force. Chem Phys Lett 781:138983
47. Ichikawa K, Nozaki H, Komazawa N, Tachibana A (2012) Theoretical study of lithium clusters by electronic stress tensor. AIP Adv 2:042195
48. Tachibana A (2014) Electronic stress tensor of chemical bond. Indian J Chem Sect A Inorganic Phys Theor Anal Chem 53:1031–1035
49. Nozaki H, Ikeda Y, Ichikawa K, Tachibana A (2015) Electronic stress tensor analysis of molecules in gas phase of CVD process for GeSbTe alloy. J Comput Chem 36:1240–1251

# Chapter 6
# The Eigenvector-Space Trajectories for Symmetry Breaking

*I call our world Flatland, not because we call it so, but to make its nature clearer to you, my happy readers, who are privileged to live in Space.*
*Edwin A. Abbott*

In this chapter we firstly provide the theoretical background Eigenvector-space trajectories $\mathsf{T}_i(\boldsymbol{s})$ and the corresponding numerical considerations including the associated QuantVec software required for their construction in Sects. 6.1 and 6.2 respectively. In Sect. 6.3 we provide an application of the $\mathsf{T}_i(\mathbf{s})$ based on QTAIM, i.e. using the Hessian of $\rho(\mathbf{r})$ for the normal modes of vibration analysis of isotope effects and bond coupling of deuterium in water. An NG-QTAIM normal mode analysis of benzene is used as an application of $\mathsf{T}_i(\boldsymbol{s})$ using the stress tensor $\boldsymbol{\sigma}(\mathbf{r})$ to provide the dynamic coupling of the C-H bonds and C-C bonds in Sect. 6.4.1. The coupling of covalent (sigma) OH and hydrogen-bonds on the $(H_2O)_5$ MP2 potential energy surface is examined in Sect. 6.4.2. In Sect. 6.4.3 the first of two iso-energetic phenomena is considered, that of the prediction of the flip rearrangement in the water pentamer. The second of two iso-energetic phenomena: prediction of torquoselectivity in competitive ring-opening reactions is presented in Sect. 6.4.4. In Sect. 6.5 we provide an application of the $\mathsf{T}_i(\boldsymbol{s})$ to predict the photochemical ring-opening reactions of oxirane with the Ehrenfest Force $\mathbf{F}(\mathbf{r})$ where consistency with a hybrid $\mathsf{T}_{\mathbf{F}\boldsymbol{\sigma}}(\mathbf{s})$ Ehrenfest Force $\mathbf{F}(\mathbf{r})$ and stress tensor $\boldsymbol{\sigma}(\mathbf{r})$ is found. In Sect. 6.6 we conclude by summarizing the importance of directional quantum chemical measures for providing new insight into investigations of normal modes analysis, ring-opening reactions and isoenergetic phenomena.

**Scientific goals to be addressed:**

- Construct eigenvector-space trajectories $\mathsf{T}_i(\mathbf{s})$ for iso-energetic phenomena in addition to other non-stereochemistry applications.
- Determine isotope effects and bond coupling for water and benzene with normal modes.
- Predict torquoselectivity in competitive ring-opening reactions.
- Prediction of the flip rearrangement isomers in the water pentamer.
- Predict the products of photochemical ring-opening reactions.

© The Author(s), under exclusive license to Springer Nature Singapore Pte Ltd. 2023

S. Jenkins and S. R. Kirk, *Next Generation Quantum Theory of Atoms in Molecules*, Lecture Notes in Chemistry 110, https://doi.org/10.1007/978-981-99-0329-0_6

## 6.1 Theoretical Background of the Eigenvector-Space Trajectories $\mathsf{T}_i(s)$; $i = \{\sigma, \rho, \mathrm{F}\}$

*In this section we provide the necessary theoretical background to the $T_i(s)$, see also* Chap. 3, *Sect. 3.2.*

Eigenvector-space trajectories $\mathsf{T}_i(s)$; $i = \{\sigma,\rho,\mathbf{F}\}$ are constructed using the stress tensor $\boldsymbol{\sigma}(\mathbf{r})$ $\{\pm\underline{\mathbf{e}}_{1\sigma}, \pm\underline{\mathbf{e}}_{2\sigma}, \pm\underline{\mathbf{e}}_{3\sigma}\}$, the Hessian of $\rho(\mathbf{r})$ $\{\pm\underline{\mathbf{e}}_1, \pm\underline{\mathbf{e}}_2, \pm\underline{\mathbf{e}}_3\}$ and Ehrenfest Force $\mathbf{F}(\mathbf{r})$ Hessian $\{\pm\underline{\mathbf{e}}_{1\mathrm{F}}, \pm\underline{\mathbf{e}}_{2\mathrm{F}}, \pm\underline{\mathbf{e}}_{3\mathrm{F}}\}$ eigenvectors, respectively, with corresponding reference coordinate frames referred to as $\mathsf{U}_\sigma$-space, $\mathsf{U}_\rho$-space or $\mathsf{U}_\mathbf{F}$-space. Usually, the reference coordinate frame is chosen to correspond to the minimum energy geometry, the associated trajectories, $\mathsf{T}_\sigma(s)$, $\mathsf{T}_\rho(s)$ and $\mathsf{T}_\mathbf{F}(s)$, are defined as ordered sets of points with sequence parameter *s*. For a given *BCP*, the coordinates associated with each of the points are calculated by evaluating the components of the shift vector $\mathbf{dr} = \mathbf{r_b}(s) - \mathbf{r_b}(s\text{-}1)$, $s > 0$, where $\mathbf{r_b}$ indicates the location of the *BCP*, from the previous step to the current step, resulting in the tracking of the *BCP* in the corresponding eigenvector reference coordinate frame. Every *BCP* shift vector **dr** is mapped to a *point*, e.g. for the construction of the stress tensor $\mathsf{T}_\sigma(s)$ we have $\{(\underline{\mathbf{e}}_{1\sigma}.\mathbf{dr}),(\underline{\mathbf{e}}_{2\sigma}.\mathbf{dr}),(\underline{\mathbf{e}}_{3\sigma}.\mathbf{dr})\}$ in sequence, forming the $\mathsf{T}_\sigma(s)$ and also for the $\mathsf{T}_\rho(s)$ and $\mathsf{T}_\mathbf{F}(s)$.

The eigenvector-space trajectory $\mathsf{T}_i(s)$ is constructed without *BCP* torsions from an ordered sequence of points by tracking a *BCP* in the $\mathsf{U}_i$-space; $i = \{\sigma, \rho, \mathbf{F}\}$.

## 6.2 Numerical Considerations for Construction of the Eigen-Space Trajectories $\mathsf{T}_i(s)$; $i = \{\sigma, \rho, \mathrm{F}\}$

*In this section we outline the data denoising and smoothing filters implemented in our software suite QuantVec.*

Central to the concept of the eigen-space trajectories $\mathsf{T}_i(s)$, $i = \{\sigma, \rho, \mathbf{F}\}$, is the concept of a monotonically increasing sequence parameter *s*, which may take the form of an increasing integer sequence (0, 1, 2, 3,…) in applications where a set of discrete numbered steps are involved, or a continuous real number. The 3-D $\mathsf{T}_i(s)$ are defined as an ordered set of points, whose sequence is described by the parameter *s* where we use an integer step number for *s*, for the particular case of the stress tensor trajectory $\mathsf{T}_\sigma(s)$, see Fig. 6.1. We first choose to associate $s = 0$ with a specific reference molecular graph, often the energy minimum structure. For a given *BCP*, the coordinates associated with each of the points are calculated by evaluating the components of the shift vector $\mathbf{dr} = \mathbf{r_b}(s) - \mathbf{r_b}(s\text{-}1)$ where $\mathbf{r_b}$ indicates the location of the *BCP*, from the previous step to the current step in the reference coordinate frame defined by the eigenvectors $\underline{\mathbf{e}}_{1\sigma}, \underline{\mathbf{e}}_{2\sigma}, \underline{\mathbf{e}}_{3\sigma}$ in the case of the stress tensor trajectory $\mathsf{T}_\sigma(s)$. It has been observed that the magnitudes of the steps **dr** tend to slowly decrease toward

the end of $\mathsf{T}_i(\boldsymbol{s})$ paths. Note: for displaying the $\mathsf{T}_i(\boldsymbol{s})$, large steps, which can occur at the beginning or end of a $\mathsf{T}_i(\boldsymbol{s})$, may swamp the appearance of the. To solve this problem we temporarily filter these steps before including them back in to correctly calculate the $\mathsf{U}_\mathbf{f}$ space trajectory $\mathsf{T}_i(\boldsymbol{s})$ length $\mathsf{L}_\sigma$. To solve this we temporarily filter these steps before including them back in to correctly calculate the $\mathsf{T}_i(\boldsymbol{s})$. The calculation of the $\mathsf{T}_i(\boldsymbol{s})$ is made simpler if the code which produces the list of structures corresponding to points along each step of the torsion or pathway generates these structures at regularly-spaced points. Therefore, with this desirable characteristic is that there are few or no large changes or 'spikes' in the magnitude of the *BCP* shift vector **dr** i.e. $\boldsymbol{\Delta}\mathbf{dr}$, between path step $s$ and $s + 1$. Such 'spike' anomalies occur because some path-following algorithms may employ occasional small predictor-corrector steps that are at least an order of magnitude smaller than standard steps. With NG-QTAIM it is observed that such intermittent relatively small steps in turn cause very small shifts **dr** to be interspersed between longer runs of larger changes, causing 'spike' noise in the otherwise smooth $\mathsf{T}_i(\boldsymbol{s})$. Such 'spikes', which usually only consist of a single spurious point deviating from the locally smooth stress tensor trajectory, can result in large spurious contributions to the $\mathsf{T}_i(\boldsymbol{s})$ and may be safely filtered. We implemented the following denoising strategies to remove spikes from the $\mathsf{T}_i(\boldsymbol{s})$:

I. If the percentage deviation $\Delta\mathbf{dr}$ of the magnitude of the **dr** from a moving average calculated along the $\mathsf{T}_i(\boldsymbol{s})$ exceeds 50%, the current point is filtered out as a 'spike'.
II. Abrupt changes in direction in the $\mathsf{T}_i(\boldsymbol{s})$, e.g. turning by more than 60° from one $\mathsf{T}_i(\boldsymbol{s})$ step to the next cause the current point to be labelled as a 'spike'.
III. When the above rules (I and II) are used together, this combination is referred to as the 'turn' filter. These rules can be repeatedly applied across multiple 'passes' through the $\mathsf{T}_i(\boldsymbol{s})$ data as necessary.

The data smoothing filter that we use is that of Kolmogorov-Zurbenko [1]: this is referred to as the 'avg' filter.

### *6.2.1 The QuantVec Program Package*

Wavefunctions from first-order density matrices expressed in an MO basis using Gaussian-type primitives in the WFX/WFN file format are used as input for the QuantVec program package, see Fig. 6.2. The open-source Molden2AIM code [2] can convert to WFX/WFN the widely-used MOLDEN-format. QuantVec will be used to extract the QTAIM, stress tensor $\boldsymbol{\sigma}(\mathbf{r})$ and Ehrenfest force $\mathbf{F}(\mathbf{r})$ partitioning eigenvector-derived properties. The NG-QTAIM interpretation of the chemical bond, the bond-path framework set $\mathsf{B}$ and precessions $\mathsf{K}$, beyond the capabilities of scalar QTAIM, have explained anisotropic directional chemical phenomena using the most preferred directions of bond deformation: bond coupling effects explaining the

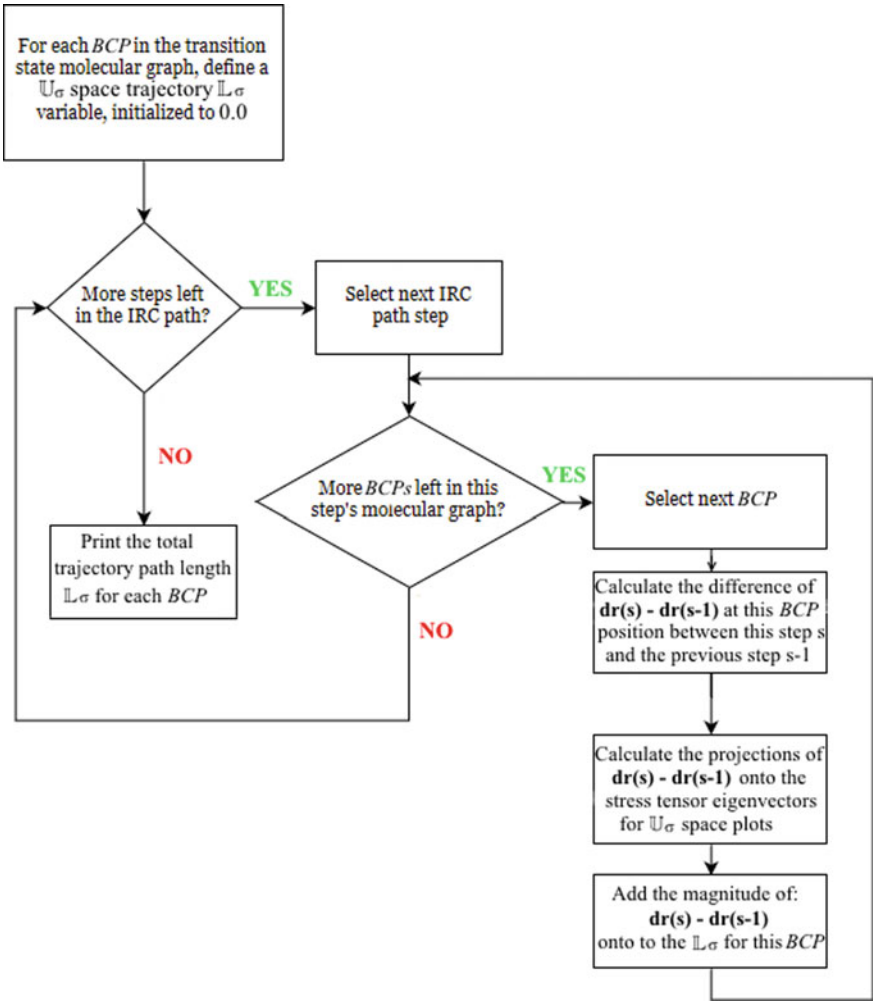
For each BCP in the transition state molecular graph, define a $\mathbb{U}_\sigma$ space trajectory $\mathbb{L}_\sigma$ variable, initialized to 0.0
More steps left in the IRC path?
YES
Select next IRC path step
NO
Print the total trajectory path length $\mathbb{L}_\sigma$ for each BCP
More BCPs left in this step's molecular graph?
YES
Select next BCP
NO
Calculate the difference of dr(s) - dr(s-1) at this BCP position between this step s and the previous step s-1
Calculate the projections of dr(s) - dr(s-1) onto the stress tensor eigenvectors for $\mathbb{U}_\sigma$ space plots
Add the magnitude of: dr(s) - dr(s-1) onto to the $\mathbb{L}_\sigma$ for this BCP

**Fig. 6.1** The procedure to generate the stress tensor trajectory $\mathsf{T}_\sigma(s)$ in $U_\sigma$ space

strength of hydrogen bonding in water [3], the direction of photoreactions [4], molecular switch function [5–8], scoring of molecular wires [9], controversial bonding environments e.g. [1.1.1.]propellane [10] and non-nuclear attractors [11]. The stress tensor trajectory $\mathsf{T}_\sigma(s)$ analysis has been used for iso-energetic phenomena: stereochemistry of achiral and chiral species, reactions and chiral discrimination [12–14], predict reaction pathways in competitive ring-opening reactions [15, 16], rotors [17], permutation-inversion isomers [18] and photochemistry [16, 19, 20] by providing the necessary symmetry-breaking. Python scripts produce tables in text or CSV form and the interactive GUI produces bitmap/vector images or the.x3d 3-D model format. The first beta-version of the QuantVec code can be obtained upon request. Quantvec

preserves data provenance information as metadata, is designed to be extendable and requires only modest computational resources.

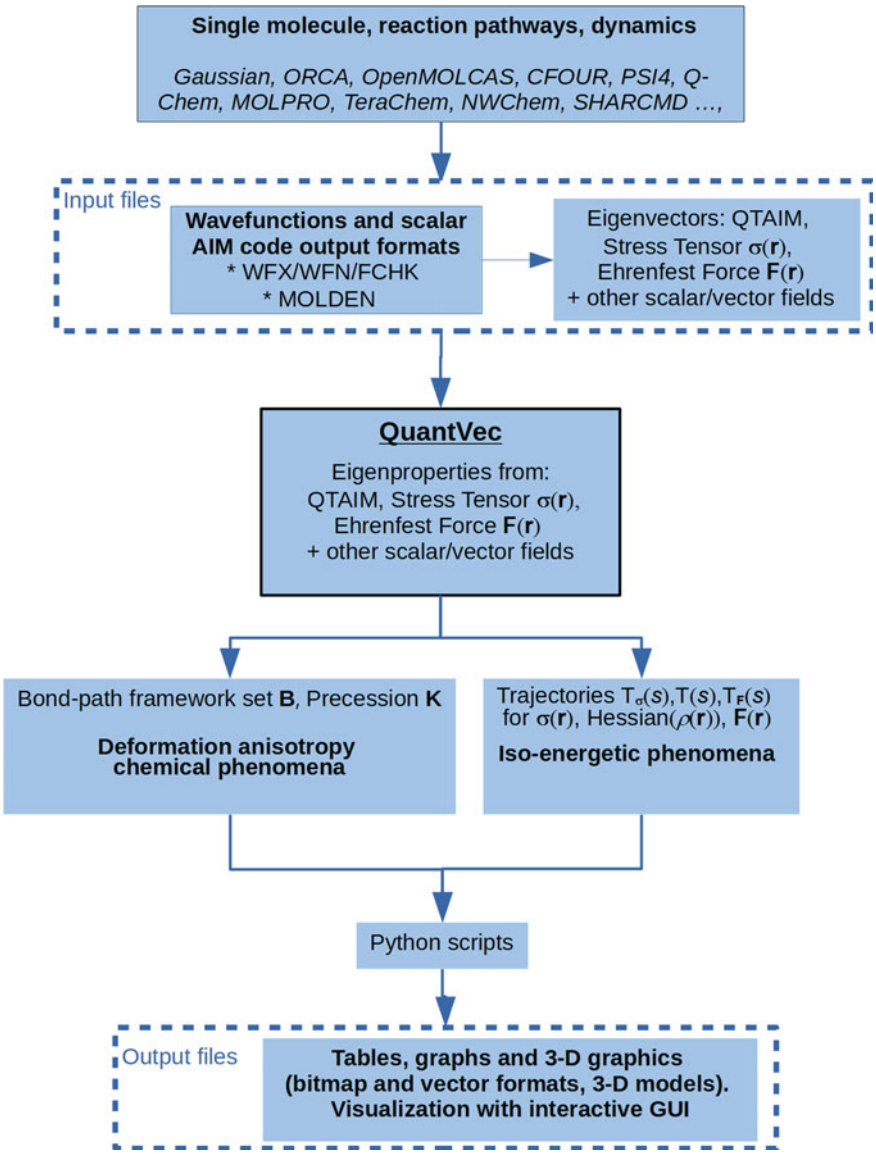
Single molecule, reaction pathways, dynamics
Gaussian, ORCA, OpenMOLCAS, CFOUR, PSI4, Q-Chem, MOLPRO, TeraChem, NWChem, SHARCMD …,
Input files
Wavefunctions and scalar AIM code output formats
* WFX/WFN/FCHK
* MOLDEN
Eigenvectors: QTAIM, Stress Tensor σ(r), Ehrenfest Force F(r) + other scalar/vector fields
QuantVec
Eigenproperties from: QTAIM, Stress Tensor σ(r), Ehrenfest Force F(r) + other scalar/vector fields
Bond-path framework set B, Precession K
Deformation anisotropy chemical phenomena
Trajectories Tσ(s),T(s),TF(s) for σ(r), Hessian(ρ(r)), F(r)
Iso-energetic phenomena
Python scripts
Output files
Tables, graphs and 3-D graphics (bitmap and vector formats, 3-D models). Visualization with interactive GUI

**Fig. 6.2** Note that the computational details are covered in Chap. 1, basic scalar QTAIM in Chap. 2. The theoretical background of the bond-path framework set B and corresponding precessions K are presented in Chap. 4

## 6.3 Applications of the Eigenvector-Space Trajectories $\mathbf{T}_i(s)$; $i = \{\rho\}$: the Hessian of $\rho(\mathbf{r})$ Trajectory $\mathbf{T}(s)$

*In this section we will provide in this section an overview of the applications of the trajectory $T_{\rho}(s)$.*

### *6.3.1 Normal Modes of Vibration: Isotope Effects and Bond Coupling*

In the 90 years since the discovery of deuterium (D), an isotope of hydrogen (H), has been used in an ever-increasing number of chemical and biochemical applications.

The chemical properties of deuterium and hydrogen are considered identical because of the identical structure of the valence shell of the atom. The physical properties of deuterium and hydrogen are sometimes different referred to as the isotope effect and is the largest for all elements and originates largely from the nuclear motions that are observed by spectroscopic measurements. Clear differences in the spectral signature, as in the case of O-H/O-D normal modes of free molecules, may not be available when other elements are present because the isotopic shift is much smaller, either when the relative mass difference is small or because clear spectral lines are not available, as is often the case in solids. A consequence of the isotope effect is that different isotopes can result in different properties of isotopomer molecules beyond the differences in molecular mass. Using the Born-Oppenheimer (B.O.) approximation, relevant for most applications, the electronic spectra of isotopomers are identical because the electronic Hamiltonian $\widehat{H}_e$ in the BO approximation is not explicitly dependent on nuclear masses; however, their nuclei dynamics are different. A consequence of this is different (ro-)vibrational spectra [29, 30], which allows isotopomer -selective excitation and ionization with infrared lasers. Advantages over electronic excitation include larger relative differences in spectral lines and therefore lower requirements on the degree of coherence as well as ready availability of powerful IR lasers.

The differences in the nuclei dynamics of isotopomers go beyond differences in (ro-) vibrational spectra. Differences in nuclei wavefunctions $\psi_n(\boldsymbol{R})$ and in classical turning points exist where wavefunctions of lighter isotopomers span wider regions of configuration space $\boldsymbol{R}$. The vibrational spectrum, that is differences between vibrational levels, $E_n = \langle \psi_n(\boldsymbol{R}) | \widehat{H}_n | \psi_n(\boldsymbol{R}) \rangle$, where $\widehat{H}_n$ is the nuclear Hamiltonian, is a composite, derivative quantity reflecting these differences. While nuclei wavefunctions of isotopomers are determined by the same, isotopomer-independent, potential energy surfaces (PES), as the nuclei they are distributed differently in $\boldsymbol{R}$, as generally they sample different regions of the PES, under nuclei dynamics the electronic structure of different isotopomers will not be the same *even in the B.O. approximation*, see Fig. 6.3.

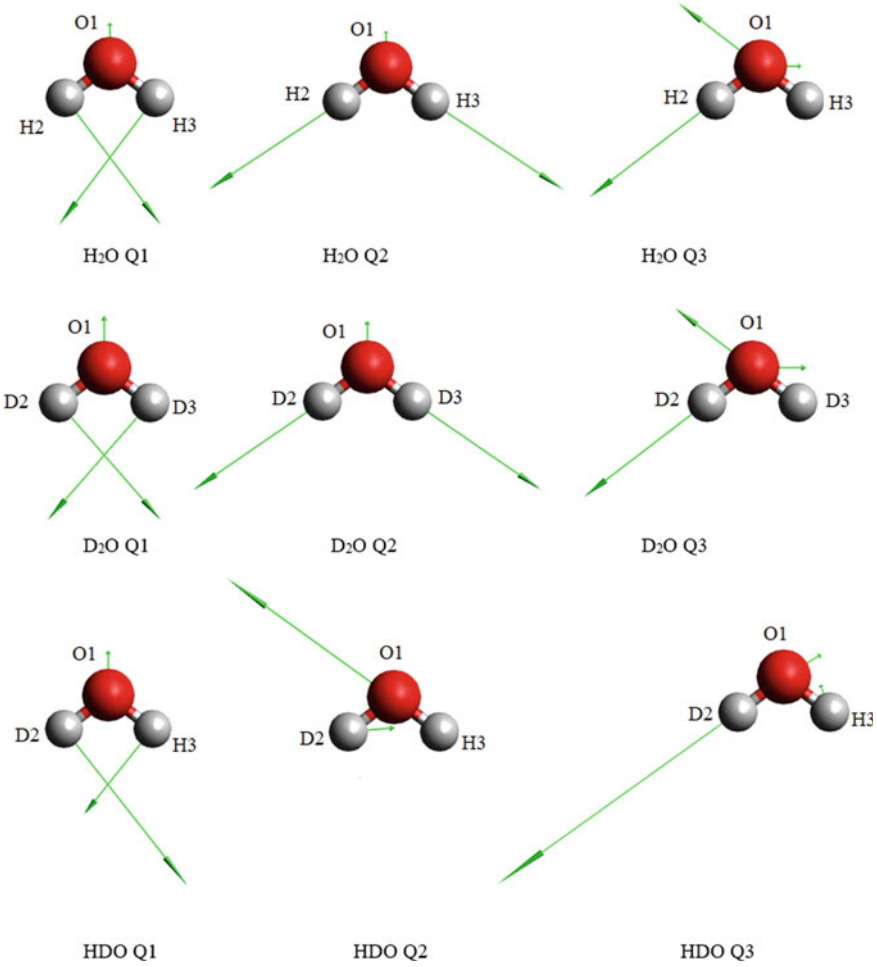


**Fig. 6.3** The normal mode vectors (green arrows) for intramolecular vibrational normal modes corresponding to the bond-bending (Q1), symmetric-stretch (Q2) and anti-symmetric-stretch (Q3) of water isotopomers

NG-QTAIM enables the quantification of bond-flexing, bond-twist and bond-axiality of the $H_2O/D_2O/HDO$ isotopomers of water during the bending (Q1), symmetric-stretch (Q2) and anti-symmetric-stretch (Q3) normal modes of vibration [31]. The Hessian of $\rho(\mathbf{r})$ trajectories $\mathsf{T}(s)$ quantify the coupling of the intramolecular bending and symmetric-stretch normal modes as well as distinguishing all three isotopomers within the harmonic approximation. The coupling of the bending and symmetric-stretch normal modes are hypothesized to be facilitated by the absence of bond-twist that would disrupt the coupling between sigma O-H bonds and hydrogen-bonding. Furthermore, partial coupling was detected for the mixed isotopomer HDO for the N

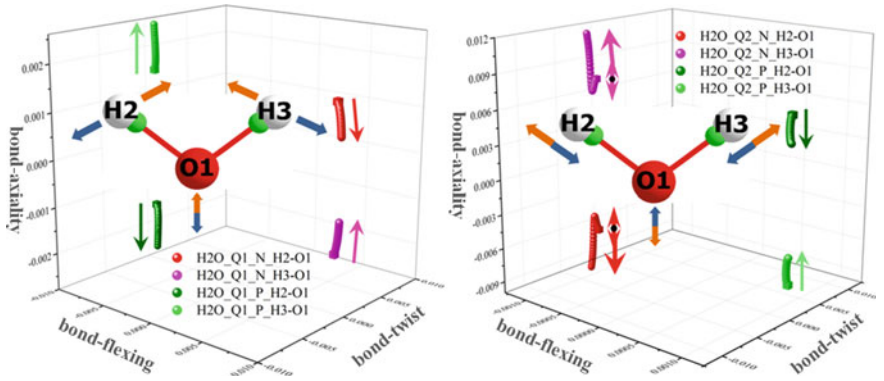


**Fig. 6.4** The Hessian of $\rho(\mathbf{r})$ trajectories $\mathsf{T}(s)$ for $H_2O$ for the bending (Q1) mode (left-panel), the axes labels of the trajectory $\mathsf{T}(s)$, the corresponding $\mathsf{T}(s)$ for $H_2O$ for the symmetric-stretch (Q2) mode (right-panel). The green spheres correspond to the bond critical point (*BCP*s)

branch of bending mode and the P branch of the symmetric-stretch with the bending and symmetric-stretch modes of the $H_2O$ and $D_2O$ isotopomers.

Comparison of the $\mathsf{T}(s)$ for the $H_2O$ and $D_2O$ for the symmetric and anti-symmetric-stretching modes with broadband 2-D infrared spectroscopy experiment [32] demonstrated the potential for this approach to be used in future for other hydrogen bonded systems.

A 'bouncing' of the $\mathsf{T}(s)$ for the compressive (N) branch symmetric-stretch normal mode was detected and proposed to be due to repulsion is caused by the sufficiently close approach of the H/D *NCP*s and O1 *NCP*, see Fig. 6.4. This finding can be explained by the significantly larger bond-flexing component for the N branch than that observed for the corresponding stretching (P) branch, see Table 6.1.

The bending mode possesses a much greater magnitude of bond-flexing (associated with the $(\underline{\mathbf{e}}_1)$ preferred direction) for the P branch of the Q1 normal mode of the $D_2O$ isotopomer compared with the P branch of the $H_2O$ isotopomer. This effect can be explained by the greater mass of the D compared with H, resulting in the larger displacement of $O_1$ for the $D_2O$ compared with the $H_2O$, with the consequence that the bond-path deviates, i.e. bond-flexing, correspondingly more for the former from a straight line during the vibration.

## 6.4 Applications of the Eigenvector-Space Trajectories $\mathsf{T}_i(s)$; $i = \{\sigma\}$: the Stress Tensor Trajectory $\mathsf{T}_\sigma(s)$

*In this section we will provide in this section an overview of the applications of the stress tensor trajectory $T(s)$.*

**Table 6.1** The ranges of values of the components of $\mathsf{T}(s)$ are denoted by $\mathsf{T}(s)_{\max} = \{(\underline{\mathbf{e}}_1\mathbf{.dr})_{\mathbf{max}} \rightarrow$ bond-flexing, $(\underline{\mathbf{e}}_2\mathbf{.dr})_{\mathbf{max}} \rightarrow$ bond-twist, $(\underline{\mathbf{e}}_3\mathbf{.dr}_{\mathbf{max}}) \rightarrow$ bond-axiality$\}$ for (N,P) negative *BCP* and positive *BCP* displacements of the Q1, Q2 and Q3 normal modes. Note that table entries indicated as 0.000 are effectively 0 to machine precision and all values have been multiplied by a factor of $10^2$

| {bond-flexing, bond-twist, bond-axiality} | | | | |
|---|---|---|---|---|
| *BCP* | N $H_2O$ | P | N $D_2O$ | P |
| | | Q1 | | |
| O1-H2/O1-D2 | {0.039, 0.000, 0.069} | {0.015, 0.000, 0.100} | {0.037, 0.000, 0.080} | {0.119, 0.000, 0.050} |
| O1-H3/O1-D3 | {0.039, 0.000, 0.069} | {0.015, 0.000, 0.100} | {0.037, 0.000, 0.080} | {0.119, 0.000, 0.050} |
| | | Q2 | | |
| O1-H2/O1-D2 | {0.013, 0.000, 0.509} | {0.002, 0.000, 0.232} | {0.525, 0.000, 0.158} | {0.233, 0.000, 0.050} |
| O1-H3/O1-D3 | {0.013, 0.000, 0.509} | {0.002, 0.000, 0.232} | {0.525, 0.000, 0.158} | {0.233, 0.000, 0.050} |
| | | Q3 | | |
| O1-H2/O1-D2 | {0.141, 0.000, 0.857} | {0.243, 1.187, 0.321} | {0.343, 0.798, 0.453} | {0.335, 1.339, 0.443} |
| O1-H3/O1-D3 | {1.012, 0.000, 0.700} | {0.289, 0.738, 0.382} | {0.335, 1.339, 0.443} | {0.343, 0.798, 0.453} |

| | **N** HDO **P** |
|---|---|
| | Q1 |
| O1-D2 | {0.608, 0.000, 0.486} {0.116, 0.031, 0.153} |
| O1-H3 | {0.631, 0.000, 0.300} {0.048, 0.091, 0.063} |
| | Q2 |
| O1-D2 | {0.165, 1.497, 0.218} {0.071, 0.000, 0.487} |
| O1-H3 | {0.050, 0.635, 0.066} {0.339, 0.000, 0.137} |
| | Q3 |
| O1-D2 | {0.073, 0.591, 0.096} {0.125, 0.372, 0.165} |
| O1-H3 | {0.141, 1.379, 0.186} {0.203, 0.403, 0.268} |

### *6.4.1 Normal Modes of Vibration and Dynamic Coupling*

A stress tensor eigenvector projection $\mathsf{U}_\sigma$-space formalism provided a detailed description of the participation of each of the bonds of the four infrared active benzene normal modes: mode 5, mode 14, mode 21 and mode 28 [33]. A mixture of C-C and C-H bonding characteristics was subsequently revealed, the four infrared active $\mathsf{U}_\sigma$-space trajectories were found to be unique. The normal mode with the highest infrared intensity (mode 5) was also the only mode with non-zero maximum

$\mathsf{U}_\sigma$ space trajectory projections in $\underline{\mathbf{e}}_{1\sigma}$ and $\underline{\mathbf{e}}_{2\sigma}$ directions for the C-C and C-H bond critical points respectively.

The maximum distortion of the bond-paths occurring during the normal was quantified by the excess bond-path length (BPL) distortions relative to equilibrium benzene structure. Secondly and more advanced, we were able to quantify each of the four IR active normal modes as the movement of the *BCP*s of each of the bond-paths of the stress tensor trajectories $\mathsf{T}_\sigma(s)$. The extent of the $\mathsf{T}_\sigma(s)$ along the most/least preferred directions and bond-path stretch/compression directions, using the associated maximum projections $\{(\underline{\mathbf{e}}_{2\sigma}.\mathbf{dr})_{\max}, (\underline{\mathbf{e}}_{2\sigma}.\mathbf{dr})_{\max}, (\underline{\mathbf{e}}_{3\sigma}.\mathbf{dr})_{\max}\}$ respectively, enabled this quantification, see Table 6.2. Values of $(\underline{\mathbf{e}}_{2\sigma}.\mathbf{dr})_{\max} = 0.0000$ that occur for the C-H *BCP*s mode 14, mode 21 and mode 28 with less intense IR activity, indicated that the C-H *BCP* motion comprised only $\underline{\mathbf{e}}_{1\sigma}$ and the bond-path stretching direction $\underline{\mathbf{e}}_{3\sigma}$. The converse situation was found for the C-C *BCP*s in that the less IR active modes had values of $(\underline{\mathbf{e}}_{1\sigma}.\mathbf{dr})_{\max} = 0.000$ indicating the lower participation of the C-C *BCP* motion. The most IR active mode benzene (mode 5) was dominated by C-C *BCP* motion in the $\underline{\mathbf{e}}_{1\sigma}$ with a negligible contribution from the C-C *BCP* bond-path stretch. It was noted that the presence of the non-nuclear attractors (*NNA*s) disrupted the normal modes of vibration for mode 21. We explained the relative differences in the intensities of the IR active modes associated with changes in the dipole moment [3–5, 11, 12] where larger changes in the dipole moments led to greater intensities of the normal mode of vibrations.

### 6.4.2 *Covalent (Sigma) OH and Hydrogen-Bond Coupling on the $(H_2O)_5$ MP2 Potential Energy Surface*

Another example covalent (sigma) OH and hydrogen-bond coupling that we investigated with NG-QTAIM quantified the reaction pathways on the $(H_2O)_5$ MP2 potential energy surface, see Fig. 6.5 [34].

Use of the $\mathsf{T}_\sigma(s)$ provided evidence for the stabilizing role of the O---O bonding interactions from comparison the length of the $\mathsf{T}_\sigma(s)$, longer $\mathsf{T}_\sigma(s)$ being associated with greater topological stability. The $\mathsf{T}_\sigma(s)$ demonstrated strong chemical coupling of the adjacent covalent (sigma) O-H and hydrogen-bonds because of the donation of covalent character from the covalent (sigma) O-H and hydrogen-bonds. The $\mathsf{T}_\sigma(s)$ additionally, demonstrated dynamic coupling effects of pairs of covalent (sigma) bonds and of pairs of hydrogen bonds caused by the stretching motion of the central $H_3$-$O_1$-$H_2$ centrally located water molecule, see Fig. 6.6.

**Table 6.2** The maximum projections $\{(\underline{\mathbf{e}}_{1\sigma}.\mathbf{dr})_{\max}, (\underline{\mathbf{e}}_{2\sigma}.\mathbf{dr})_{\max}, (\underline{\mathbf{e}}_{3\sigma}.\mathbf{dr})_{\max}\}$ for the four selected normal modes are calculated using the benzene equilibrium state eigenvectors. The presence of non-nuclear attractors (*NNA*s) for benzene mode 21 is indicated by the "---"

| | *Benzene mode 5* | *Benzene mode 14* | *Benzene mode 21* | *Benzene mode 28* |
|---|---|---|---|---|
| | | *BCP* | | |
| C1-C2 | {0.0034, 0.0003, 0.0000} | {0.0000, 0.0079, 0.0000} | {---} | {0.0000, 0.0039, 0.0000} |
| C2-C3 | {0.0034, 0.0003, 0.0000} | {0.0000, 0.0037, 0.0038} | {0.0000, 0.0053, 0.0121} | {0.0000, 0.0015, 0.0036} |
| C3-C4 | {0.0034, 0.0003, 0.0000} | {0.0000, 0.0037, 0.0038} | {0.0000, 0.0053, 0.0121} | {0.0000, 0.0015, 0.0036} |
| C4-C5 | {0.0034, 0.0003, 0.0000} | {0.0000, 0.0079, 0.0000} | {---} | {0.0000, 0.0039, 0.0000} |
| C5-C6 | {0.0034, 0.0003, 0.0000} | {0.0000, 0.0037, 0.0038} | {0.0000, 0.0053, 0.0121} | {0.0000, 0.0015, 0.0036} |
| C1-C6 | {0.0034, 0.0003, 0.0000} | {0.0000, 0.0037, 0.0038} | {0.0000, 0.0053, 0.0121} | {0.0000, 0.0015, 0.0036} |
| C1-H7 | {0.0000, 0.0229, 0.0014} | {0.0168, 0.0000, 0.0120} | {0.0122, 0.0000, 0.0113} | {0.0004, 0.0000, 0.0942} |
| C2-H8 | {0.0000, 0.0229, 0.0014} | {0.0168, 0.0000, 0.0120} | {0.0122, 0.0000, 0.0113} | {0.0004, 0.0000, 0.0942} |
| C3-H9 | {0.0000, 0.0229, 0.0014} | {0.0344, 0.0000, 0.0024} | {0.0268, 0.0000, 0.0055} | {0.0000, 0.0000, 0.0008} |
| C4-H10 | {0.0000, 0.0229, 0.0014} | {0.0168, 0.0000, 0.0120} | {0.0122, 0.0000, 0.0113} | {0.0004, 0.0000, 0.0942} |
| C5-H11 | {0.0000, 0.0229, 0.0014} | {0.0168, 0.0000, 0.0120} | {0.0122, 0.0000, 0.0113} | {0.0004, 0.0000, 0.0942} |
| C6-H12 | {0.0000, 0.0229, 0.0014} | {0.0344, 0.0000, 0.0024} | {0.0268, 0.0000, 0.0055} | {0.0000, 0.0000, 0.0008} |

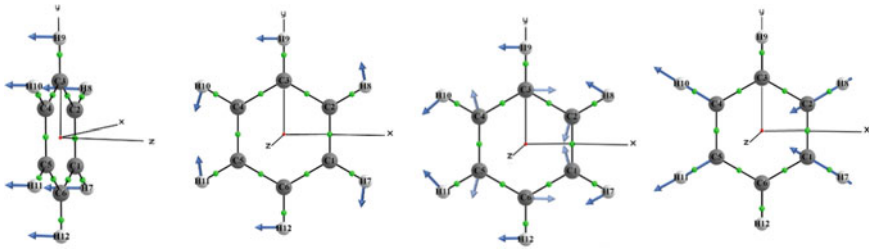

benzene mode 5 benzene mode 14 benzene mode 21 benzene mode 28

**Fig. 6.5** Conventional rendering of four normal modes of benzene superimposed onto the molecular graphs of the relaxed structure of benzene. The four infrared (IR) active normal modes of benzene are ordered according to their increasing frequency, corresponding to 721.568 $cm^{-1}$ (mode 5), 1097.691 $cm^{-1}$ (mode 14), 1573.927 $cm^{-1}$ (mode 21) and 3298.320 $cm^{-1}$ (mode 28) respectively, arrows are not drawn to scale. The corresponding intensities ($10^{-7}$ $cm^2$ $mol.^{-1}$ $s^{-1}$ ln) are 136.47, 5.78, 10.92 and 24.86 respectively

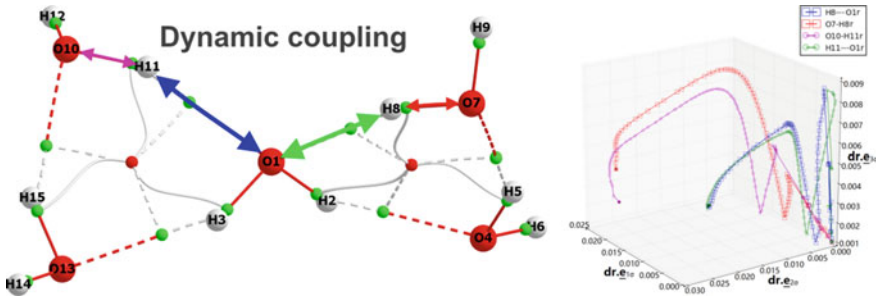


**Fig. 6.6** Values of the total local energy density $H(\mathbf{r_b}) < 0$ and $H(\mathbf{r_b}) > 0$ for a given hydrogen-bond H--O *BCP* are indicated by "--" and "---" respectively. The 'dynamic coupling' for the $\mathsf{T}_\sigma(s)$ of the sigma bonds; O7-H8 *BCP* and O10-H11 *BCP* is evident as well as for the $\mathsf{T}_\sigma(s)$ of the H8---O1 *BCP* and the H11---O1 *BCP* the $\mathsf{T}_\sigma(s)$ of the 04_0028 $(H_2O)_5$

### 6.4.3 *Iso-Energetic Phenomena I: Prediction of the Flip Rearrangement in the Water Pentamer*

NG-QTAIM was used to investigate the response of all five water molecules to the flip of molecule $H_6$-$O_4$-$H_5$ of the flip rearrangement of $(H_2O)_5$ [18]. The use of the 3-D trajectories $\mathsf{T}(s)$ expressed in terms of bond-flexing, bond-twist and bond-axiality provided a means to quantify the response of the electronic charge density $\rho(\mathbf{r_b})$ to the flip rearrangement between permutation-inversion isomers. Scalar measures were unable to distinguish the two sides: reverse ($r$) and forward ($f$) of the asymmetric energy profile path, see Fig. 6.7.

NG-QTAIM enables provided additional sources of symmetry breaking by the construction of the $\mathsf{T}_\sigma(s)$ since the construction of the $\mathsf{T}_\sigma(s)$ involved the mapping of the *BCP* shifts $\pm\underline{\mathbf{dr}}$ step in Cartesian space to a point in $\mathsf{U}_\sigma$-space. The $\mathsf{T}_\sigma(s)$ that that are unique and non-overlapping for $r$ and $f$ for all points in the IRC including the transition state.

We quantified the response of the external torsion of the $H_6$-$O_4$-$H_5$ water molecule on all of the bonding in terms of the lengths of the $\mathsf{T}_\sigma(s)$ in $\mathsf{U}_\sigma$-space ($\mathsf{L}_\sigma$) and real space ($l$) as well as the separation ($\mathsf{D}_\mathsf{T}$) of the start and end of the $\mathsf{T}_\sigma(s)$, see Tables 6.3 and 6.4. The separation of the $r$ and $f$ permutation isomers in $\mathsf{U}_\sigma$-space at the transition state was quantified by $\mathsf{D}_{\mathrm{TS}\sigma}$ was largest for the $\mathsf{T}_\sigma(s)$, corresponding to the externally rotated $H_6$-$O_4$ *BCP* bond-path.

The circular character of the trajectory $\mathsf{T}_\sigma(s)$ was more evident in the $(H_2O)_5$ ring shared-shell O-H *BCP*s for the $f$ compared with the $r$ permutation isomer, see Fig. 6.7.

The corresponding $\mathsf{L}_\sigma$ and $l$ were longer for the $f$ compared with the $r$ permutations isomers for all *BCP*s. The $(\underline{\mathbf{e}}_{\mathbf{1}\sigma}.\mathbf{dr})_{\max}$ are larger for the $f$ isomer for both the O4-H5 *BCP* and $O_4$-$H_6$ *BCP*, that constitute the externally rotated molecule, than for the $r$ isomer. Conversely, $(\underline{\mathbf{e}}_{\mathbf{2}\sigma}.\mathbf{dr})_{\max}$, the largest directional component in $\mathsf{U}_\sigma$-space, is

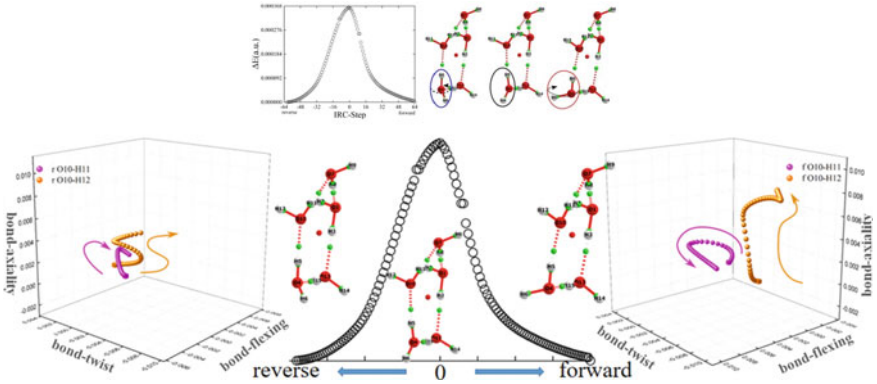


**Fig. 6.7** The variation of the relative energy ΔE (top left-panel) with the IRC-Step coordinate for the $(H_2O)_5$ permutation isomerization reaction pathway. The corresponding molecular graphs highlighting the H12-O10-H11 molecule (top-right panel) of the counter clockwise (CCW) reverse ($r$) energy minimum (left), transition state (middle) and the clockwise (CW) forward ($f$) energy minimum (right). The $\mathsf{T}_\sigma(s)$ of the H12-O10-H11 molecule for the clockwise direction of the $(H_2O)_5$ flip rearrangement (lower left-panel). Schematic of the ΔE for the $(H_2O)_5$ flip rearrangement reaction pathway (lower middle-panel). The corresponding $\mathsf{T}_\sigma(s)$ of the counter-clockwise direction (lower right-panel)

**Table 6.3** The maximum projections $\mathsf{T}_\sigma(s)_{\max} = \{(\underline{\mathbf{e}}_{1\sigma}.\mathbf{dr})_{\max} \rightarrow$ bond-twist, $(\underline{\mathbf{e}}_{2\sigma}.\mathbf{dr})_{\max} \rightarrow$ bond-flexing $(\underline{\mathbf{e}}_{3\sigma}.\mathbf{dr}_{\max}) \rightarrow$ bond-axiality$\}$ for the O-H bonding in reverse ($r$) and forward ($f$) directions. The length $\mathsf{D}_\mathsf{T}$ is the separation distance of end point to start point of the $\mathsf{T}_\sigma(s)$

| ***BCP*** | $r$ | $\mathsf{D}_\mathsf{T}$ | | $f$ | $\mathsf{D}_\mathsf{T}$ |
|---|---|---|---|---|---|
| $H_5$--$O_{10}$ | {2.794, 1.148, 2.822} | 2.423 | $H_5$--$O_{10}$ | {2.720, 1.605, 3.570} | 2.329 |
| $H_{11}$--$O_7$ | {0.955, 1.304, 1.859} | 1.879 | $H_{11}$--$O_7$ | {1.970, 2.606, 2.223} | 1.181 |
| $H_8$--$O_1$ | {1.293, 1.952, 0.363} | 2.064 | $H_8$--$O_1$ | {3.640, 3.095, 0.547} | 2.205 |
| $H_3$--$O_{13}$ | {1.463, 1.607, 1.433} | 1.958 | $H_3$--$O_{13}$ | {3.264, 2.940, 3.172} | 3.439 |
| $H_{15}$--$O_4$ | {2.962, 1.980, 0.624} | 3.960 | $H_{15}$--$O_4$ | {2.760, 2.140, 0.555} | 1.765 |
| *BCP* $(H_2O)_5$ ring | | | | | |
| **$O_4$-$H_5$** | **{3.003, 3.840, 2.657}** | **3.407** | **$O_4$-$H_5$** | **{5.750, 3.560, 3.988}** | **2.921** |
| $O_{10}$-$H_{11}$ | {2.465, 2.492, 1.675} | 3.032 | $O_{10}$-$H_{11}$ | {4.860, 5.100, 1.981} | 4.576 |
| **$O_7$-$H_8$** | {2.690, 1.153, 0.345} | 2.718 | $O_7$-$H_8$ | {3.988, 3.527, 0.849} | 3.537 |
| $O_1$-$H_3$ | {0.913, 1.237, 1.511} | 1.793 | $O_1$-$H_3$ | {0.711, 2.131, 3.160} | 1.975 |
| $O_{13}$-$H_{15}$ | {1.698, 3.213, 2.615} | 4.007 | $O_{13}$-$H_{15}$ | {5.639, 5.650, 3.872} | 5.805 |
| *BCP* non-ring | | | | | |
| $O_4$-$H_6$ | **{28.02, 6.940, 15.66}** | **24.62** | **$O_4$-$H_6$** | **{29.87, 1.819, 11.97}** | **26.21** |
| $O_{10}$-$H_{12}$ | {7.270, 4.058, 9.800} | 4.695 | $O_{10}$-$H_{12}$ | {3.430, 1.155, 3.614} | 12.21 |
| $O_7$-$H_9$ | {8.360, 0.791, 3.552} | 3.927 | $O_7$-$H_9$ | {3.554, 0.768, 1.836} | 8.349 |
| $O_1$-$H_2$ | {3.059, 3.460, 0.816} | 3.882 | $O_1$-$H_2$ | {3.755, 1.237, 0.718} | 2.466 |
| $O_{13}$-$H_{14}$ | {8.000, 4.054, 7.060} | 4.228 | $O_{13}$-$H_{14}$ | {2.410, 3.590, 2.331} | 6.451 |

The bold entries correspond to the $H_5$-$O_4$-$H_6$ water molecule undergoing the flip rearrangement. All distances are stated in a.u. and have been multiplied by a factor of $10^3$

**Table 6.4** The stress tensor trajectory $\mathsf{T}_\sigma(s)$ lengths corresponding to the $\mathsf{U}_\sigma$-space lengths $\mathsf{L}_\sigma$ and real space lengths $l$ in au for the $(r, f)$ directions respectively

| *BCP* | $\mathsf{L}_\sigma$ | $D_{TS\sigma}$ | *BCP* | $l$ |
|---|---|---|---|---|
| $H_5$--$O_{10}$ | (0.007, 0.010) | 0.002 | $H_5$--$O_{10}$ | (0.120, 0.125) |
| $H_{11}$--$O_7$ | (0.003, 0.007) | 0.001 | $H_{11}$--$O_7$ | (0.074, 0.089) |
| $H_8$--$O_1$ | (0.003, 0.008) | 0.000 | $H_8$--$O_1$ | (0.066, 0.133) |
| $H_3$--$O_{13}$ | (0.004, 0.009) | 0.001 | $H_3$--$O_{13}$ | (0.089, 0.154) |
| $H_{15}$--$O_4$ | (0.007, 0.016) | 0.005 | $H_{15}$--$O_4$ | (0.124, 0.169) |
| *BCP* $(H_2O)_5$ ring | | | | |
| **$O_4$-$H_5$** | **(0.009, 0.015)** | **0.001** | **$O_4$-$H_5$** | **(0.151, 0.202)** |
| $O_{10}$-$H_{11}$ | (0.005, 0.012) | 0.002 | $O_{10}$-$H_{11}$ | (0.108, 0.198) |
| $O_7$-$H_8$ | (0.004, 0.008) | 0.000 | $O_7$-$H_8$ | (0.081, 0.186) |
| $O_1$-$H_3$ | (0.004, 0.007) | 0.001 | $O_1$-$H_3$ | (0.067, 0.114) |
| $O_{13}$-$H_{15}$ | (0.007, 0.017) | 0.007 | $O_{13}$-$H_{15}$ | (0.140, 0.199) |
| *BCP* non-ring | | | | |
| **$O_4$-$H_6$** | **(0.043, 0.051)** | **0.061** | **$O_4$-$H_6$** | **(0.806, 1.197)** |
| $O_{10}$-$H_{12}$ | (0.010, 0.017) | 0.005 | $O_{10}$-$H_{12}$ | (0.150, 0.584) |
| $O_7$-$H_9$ | (0.005, 0.011) | 0.002 | $O_7$-$H_9$ | (0.122, 0.300) |
| $O_1$-$H_2$ | (0.005, 0.008) | 0.002 | $O_1$-$H_2$ | (0.063, 0.157) |
| $O_{13}$-$H_{14}$ | (0.007, 0.020) | 0.005 | $O_{13}$-$H_{14}$ | (0.115, 0.296) |

The bold entries are vector-based quantities.. The length $D_{TS\sigma}$ is the separation in $U_\sigma$-space corresponding to the transition state (TS) of $\mathsf{T}_\sigma(s)$ of the $r$ and $f$ permutation isomers, see the caption of Table 6.3 for further details.

larger for the $r$ direction for both the O4-H5 *BCP* and $O_4$-$H_6$ *BCP*, than for the $f$ isomer.

On the basis of the $\mathsf{L}_\sigma$, $l$ lengths and the $(\underline{\mathbf{e}}_{\mathbf{1}\sigma}.\mathbf{dr})_{max}$ (bond-twist) and $(\underline{\mathbf{e}}_{\mathbf{2}\sigma}.\mathbf{dr})_{max}$ (bond-flexing) values and the increased preservation of the circular character of the $\mathsf{T}_\sigma(s)$ we therefore demonstrated that the CW and CCW directions of torsion of the flip rearrangement are the most and least facile respectively. The $\mathsf{T}_\sigma(s)$ can additionally quantify the asymmetry of the flip rearrangement pathway and therefore distinguish the $f$ and $r$ isomers at the transition state.

### *6.4.4 Iso-Energetic Phenomena II: Torquoselectivity in Competitive Ring-Opening Reactions*

Current theories to explain and predict the classification of the electronic reorganization due to the torquoselectivity of a ring-opening reaction cannot accommodate the directional character of the reaction pathway; the torquoselectivity is a type of stereoselectivity and therefore is dependent on the pathway.

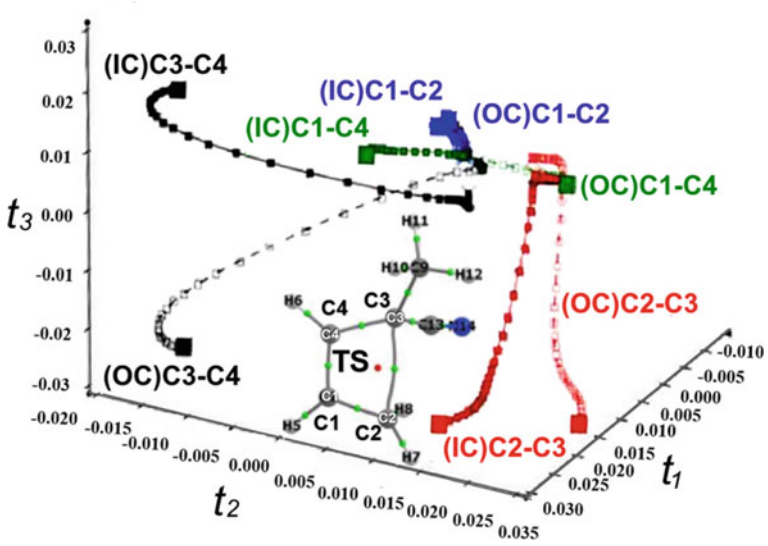


**Fig. 6.8** The $\mathsf{T}_\sigma(s)$ calculated using the transition state (TS) eigenvectors at each step of the IRC of 1-cyano-1-methylcyclobutene competitive ring-opening reaction for the (IC) inward conrotatory and (OI) outward conrotatory with inset molecular graph of the TS, adapted from Li et al. 14

NG-QTAIM was therefore used to distinguish and quantify the transition state inward conrotatory (TSIC) and transition state outward conrotatory (TSOC) paths of *competitive* ring-open reactions for 3-(trifluoromethyl)cyclobut-1-ene and 1-cyano-1-methylcyclobutene [16]. The competitive case being the most difficult test for any method to analyze torquoselectivity. The torquoselectivity is a type of stereoselectivity that benefits from the unique ability of NG-QTAIM to quantify the directional nature of the mechanisms of the TSIC and TSOC ring-opening reactions. We determined the directional properties of the ring-opening reactions by constructing a stress tensor $\mathsf{U}_\sigma$-space with trajectories $\mathsf{T}_\sigma(s)$, see Fig. 6.8. We noted that the real space lengths $l$ of the $\mathsf{T}_\sigma(s)$ correlated with the lowest total energy barrier and hence will be more thermodynamically favored. This was explained by the fact that a *BCP* corresponding to a longer $l$ travels further from the transition state to a given minimum than a *BCP* corresponding to a shorter $l$.

## 6.5 Applications of the Eigenvector-Space Trajectories $\mathsf{T}_i(s)$; $i = \{\mathrm{F}\}$: Ehrenfest Force F(r) $\mathsf{T}_\mathrm{F}(s)$

*In this section we will provide in this section an overview of an application of the Ehrenfest Force* $\boldsymbol{F(r)}$ *trajectory* $T_{\boldsymbol{F}}(s)$.

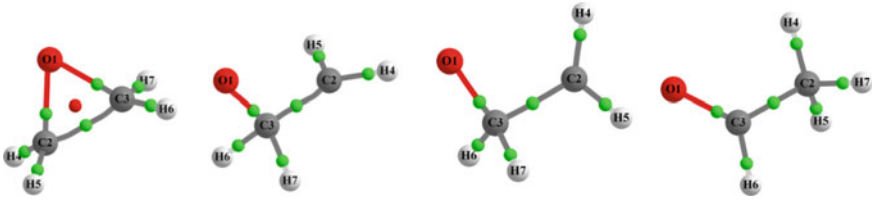


**Fig. 6.9** Molecular graphs and atomic numbering schemes of the oxirane ring-opening reaction along the minimum energy path (MEP) corresponding to FC → CI-asym → $CH_3CHO$ (reaction pathway **I**), FC → CI-asym-tw → $CH_3CHO$ (reaction pathway **II**)

### *6.5.1 Determining Photochemical Ring-Opening Reactions of Oxirane with the Ehrenfest Force F(r)*

We used the Ehrenfest Force $\mathbf{F}(\mathbf{r})$ trajectories $\mathsf{T}_{\mathbf{F}}(s)$ in $\mathsf{U}_{\mathbf{F}}$-space corresponding to the $S_0$ and $S_1$ states for the ring-opening reactions reaction pathway **I** {FC → CI-asym → $CH_3CHO$} and reaction pathway **II** {FC → CI-asym-tw → $CH_3CHO$}, see Fig. 6.9 [35].

Hybrid Ehrenfest Force $\mathbf{F}(\mathbf{r})$-stress tensor trajectories $\mathsf{T}_{\mathbf{F}\sigma}(s)$ were constructed also using the Ehrenfest Force $\mathbf{F}(\mathbf{r})$ *BCP*s with the stress tensor $\boldsymbol{\sigma}(\mathbf{r})$ eigenvectors, see Fig. 6.11. The ring-opening reaction commences with the rupturing of the C2-O1 *BCP* bond-path and occurs most easily for the $S_1$ state of reaction pathway **II** as demonstrated by the $(\underline{\mathbf{e}}_{\mathbf{2F}}.\mathbf{dr})_{max} > (\underline{\mathbf{e}}_{\mathbf{1F}}.\mathbf{dr})_{max}$ components of $\mathsf{T}_{\mathbf{F}}(\mathbf{s})_{max}$. Differences between the $S_0$ and $S_1$ electronic states for the reaction pathway **I** and reaction pathway **II** were a result of the torsion of the $C_2$-$H_4H_5$ group. Ehrenfest Force $\mathbf{F}(\mathbf{r})$ trajectories were constructed for the C-O ring-opening photo-reactions of oxirane, see Fig. 6.10.

The $C_2$-$H_4H_5$ torsion that was only on reaction pathway **II** had the effect of a lower degree of symmetry breaking in reaction pathway **II** compared with reaction pathway **I**. The evidence of the lower degree of symmetry breaking in reaction pathway **I** is provided by the visually similar duplicated/parallel morphologies of the $\mathsf{T}_{\mathbf{F}}(s)$ of the $S_0$ and $S_1$ states. The $\mathsf{T}_{\mathbf{F}}(s)$ for the $S_0$ and $S_1$ states however, possessed distinct morphologies that indicated significant symmetry breaking resulting from the torsion of the $C_2$-$H_4H_5$ group. This result of increased symmetry breaking for reaction pathway **II** also occurred for the hybrid $\mathsf{T}_{\mathbf{F}\sigma}(s)$. The increased symmetry breaking, had the additional consequence for reaction pathway **II** of generally larger $\mathsf{U}_{\mathbf{F}}$-space and $\mathsf{U}_{\sigma}$-space separations at the CI than is the case for reaction pathway **I**. Consistent with this finding was that the real space lengths $l$ to the CI were found to be much greater for reaction pathway **II** than for reaction pathway **I** in both the $\mathsf{U}_{\mathbf{F}}$-space and $\mathsf{U}_{\sigma}$-space representations, see Table 6.5. This indicated that greater symmetry breaking corresponds to the more preferred reaction pathway since greater real space

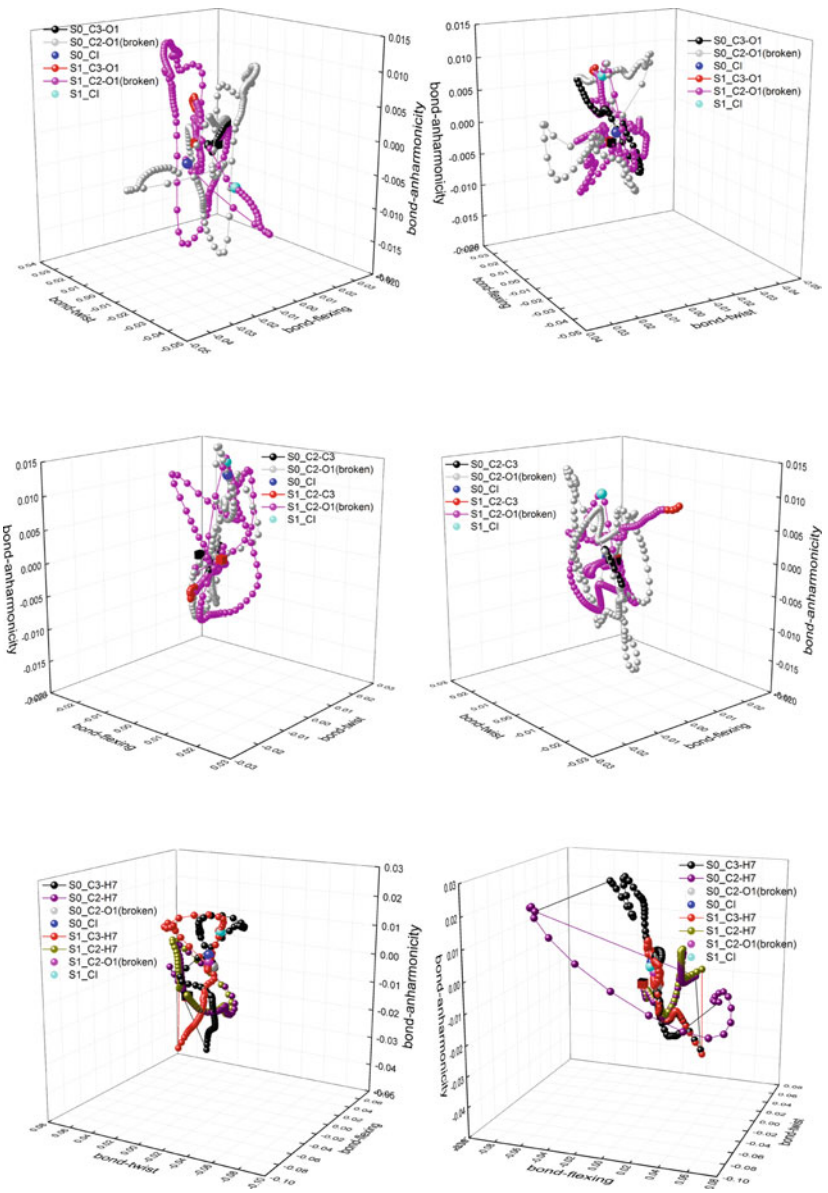


**Fig. 6.10** The Ehrenfest Force $\mathbf{F}(\mathbf{r})$ trajectories $\mathsf{T}_{\mathbf{F}}(s)$ (left pair of panels: reaction pathway **I**, reaction pathway **II**) for the $S_0$ and $S_1$ states and the corresponding results for the hybrid trajectories $\mathsf{T}_{\mathbf{F}\sigma}(s)$ are presented in the right pair of panels. The grey and magenta markers indicate for the $S_0$ and $S_1$ states respectively where the ring-opening C2-O1 *BCP* bond-path is broken. The CI points of the $S_0$ and $S_1$ are denoted by mid-blue and cyan markers respectively. The end points of the $\mathsf{T}_{\mathbf{F}}(s)$ are indicated by cube markers. Note, for clarity we have shortened the reaction path names FC(Franck-Condon point) → CI-asym → $CH_3CHO$ and FC → CI-asym-tw → $CH_3CHO$ to reaction pathway **I** and reaction pathway **II** respectively. See Fig. 6.9 for details of the atomic numbering scheme. Atomic units are used for the axes

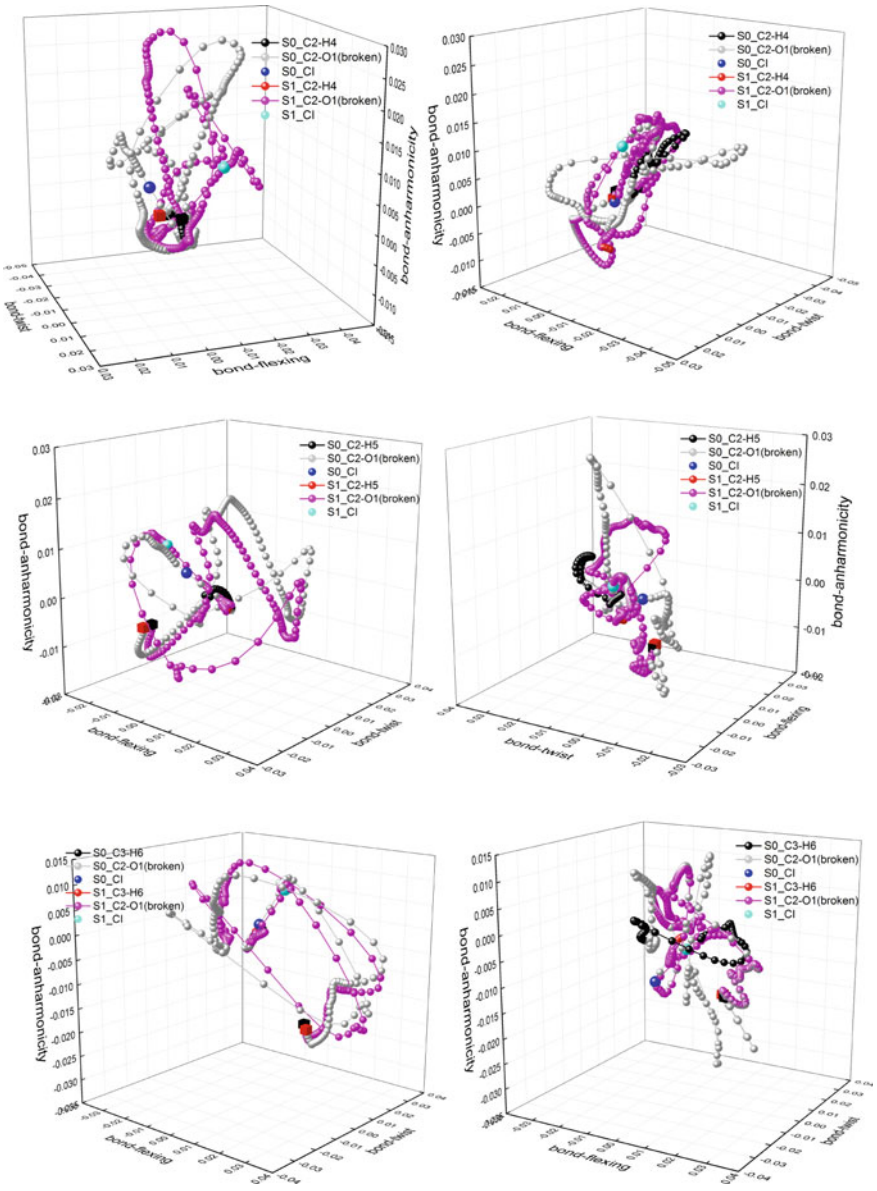


**Fig. 6.10** (continued)

lengths $l$ are known to correspond to more preferred reaction pathways [16]. Hence, reaction pathway **II** precedes more readily to the CI than reaction pathway **I**.

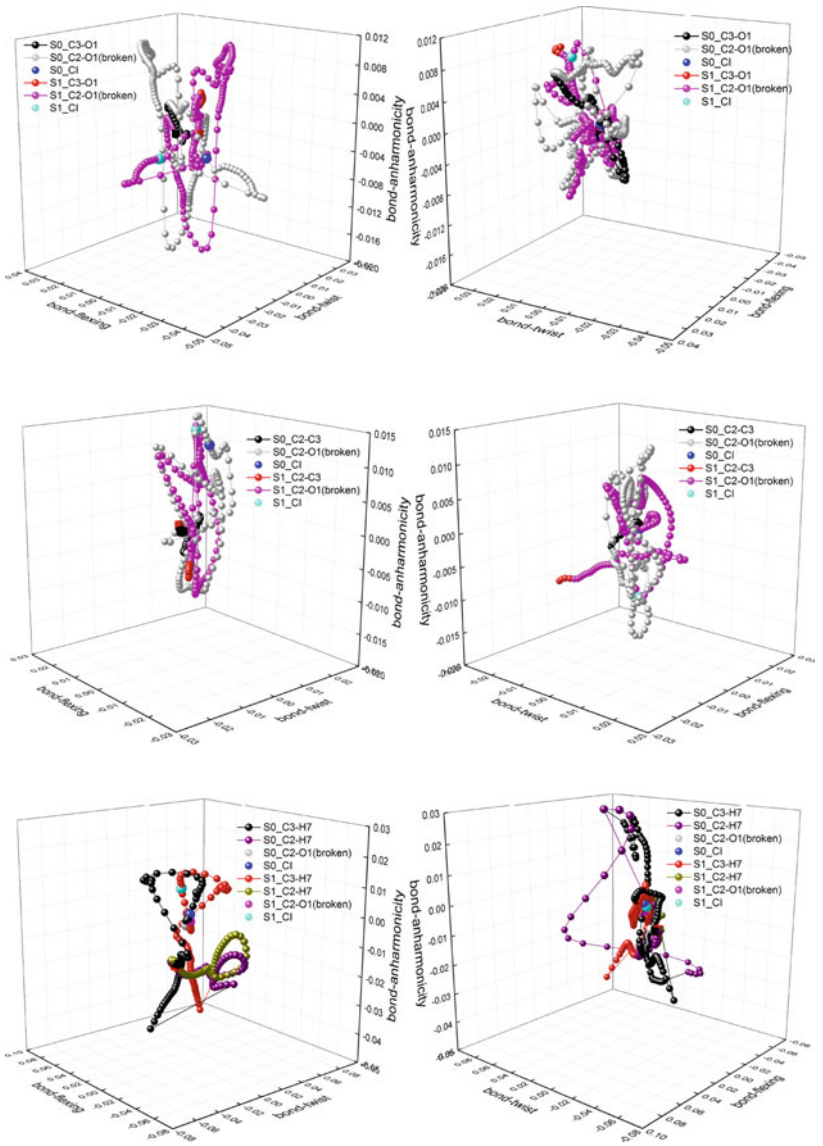


**Fig. 6.11** The corresponding results to Fig. 6.10 for the hybrid trajectories $\mathsf{T}_{\mathbf{F}\sigma}(s)$ are presented in the right pair of panels

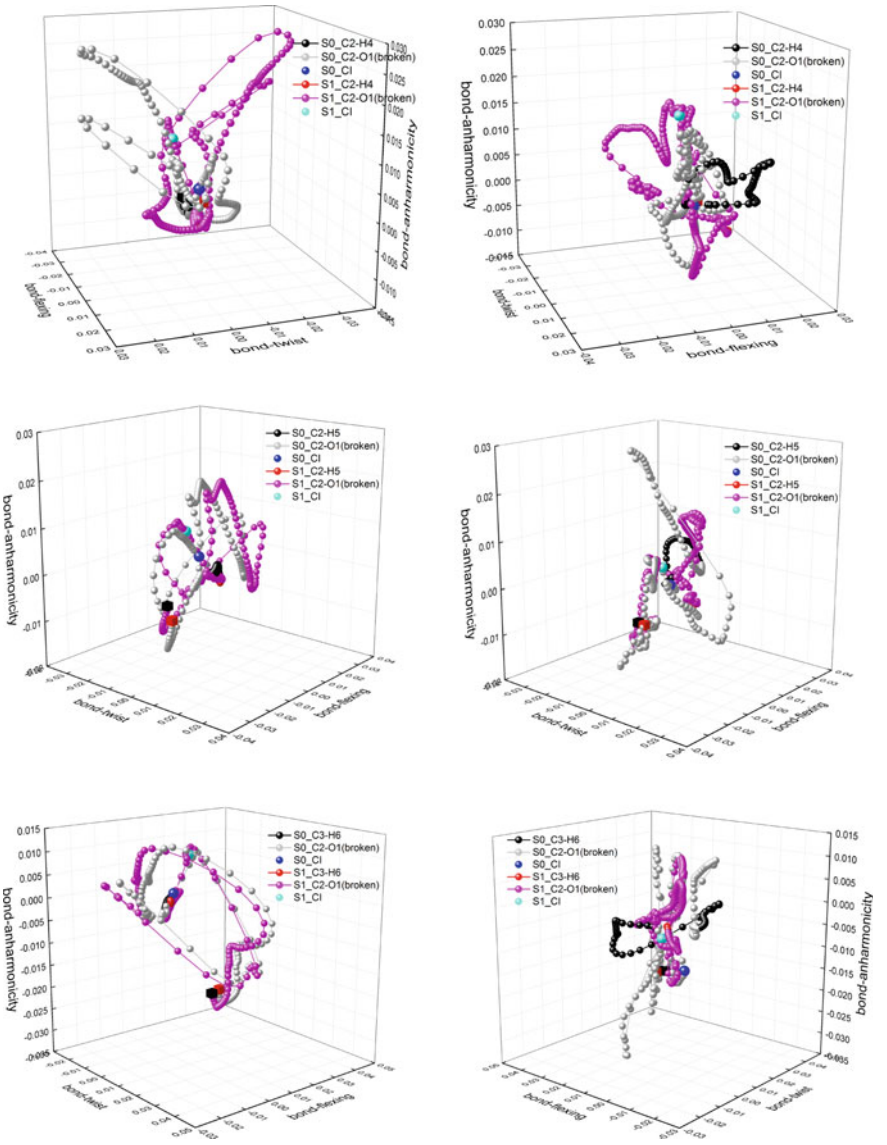


**Fig. 6.11** (continued)

## 6.6 Summary

Next Generation Quantum Theory of Atoms in Molecules (NG-QTAIM) is currently the only vector-based quantum chemical theory since all other quantum chemical theories are scalar-based and NG-QTAIM can therefore investigate phenomena that

**Table 6.5** The real space lengths $l$ of the $S_0$ and $S_1$ for the oxirane ring-opening reactions along with the corresponding values to the CI in brackets. Atomic units (a.u.) are used throughout

| | $l$ | | |
|---|---|---|---|
| *BCP* | $S_0$ | $S_1$ | $\mathsf{U}_{\mathbf{F}}$-space separation at C.I. |
| | *Reaction pathway* ***I*** | | |
| $C_2$-$O_1$ | 0.3066(---) | 0.2138(---) | --- |
| $C_3$-$O_1$ | 3.4365(0.7871) | 3.4707(0.7802) | 0.0040 |
| $C_3$-$H_7$ | 2.2060(0.4542) | 2.1273(0.3890) | 0.0071 |
| $C_2$-$H_7$ | 2.1420(---) | 1.9735(---) | --- |
| $C_2$-$H_4$ | 2.9774(0.5871) | 2.9612(0.5455) | 0.0061 |
| $C_2$-$H_5$ | 3.6232(0.5871) | 3.5640(0.5456) | 0.0008 |
| $C_3$-$H_6$ | 3.7061(0.4542) | 3.6198(0.3890) | 0.0012 |
| $C_2$-$C_3$ | 1.6008(0.3750) | 1.9570(0.6017) | 0.0065 |
| | *Reaction pathway* ***II*** | | |
| $C_2$-$O_1$ | 0.6214(---) | 0.2203(---) | --- |
| $C_3$-$O_1$ | 3.9926(2.3788) | 2.9688(1.3314) | 0.0084 |
| $C_3$-$H_7$ | 2.7445(2.0608) | 2.0009(1.1214) | 0.0032 |
| $C_2$-$H_7$ | 3.7110(---) | 2.1364(---) | --- |
| $C_2$-$H_4$ | 3.9034(2.2203) | 3.9193(2.2366) | 0.0180 |
| $C_2$-$H_5$ | 3.9671(2.3238) | 3.6276(2.0604) | 0.0167 |
| $C_3$-$H_6$ | 4.4853(2.4384) | 3.3423(1.0809) | 0.0063 |
| $C_2$-$C_3$ | 1.8963(1.1528) | 1.6112(0.8508) | 0.0095 |
| | $l$ | | |
| *BCP* | S | $S_1$ | $\mathsf{U}_{\mathbf{F}}$-space separation at C.I. |
| | *Reaction pathway* ***I*** | | |
| $C_2$-$O_1$ | 0.3066(---) | 0.2138(---) | --- |
| $C_3$-$O_1$ | 3.4365(0.7871) | 3.4707(0.7802) | 0.0041 |
| $C_3$-$H_7$ | 2.2060(0.4542) | 2.1273(0.3890) | 0.0050 |
| $C_2$-$H_7$ | 2.1420(---) | 1.9735(---) | --- |
| $C_2$-$H_4$ | 2.9774(0.5871) | 2.9612(0.5455) | 0.0035 |
| $C_2$-$H_5$ | 3.6232(0.5871) | 3.5640(0.5456) | 0.0045 |
| $C_3$-$H_6$ | 3.7061(0.4542) | 3.6198(0.3890) | 0.0045 |
| $C_2$-$C_3$ | 1.6008(0.3750) | 1.9570(0.6017) | 0.0097 |
| | *Reaction pathway* ***II*** | | |
| $C_2$-$O_1$ | 0.6214(---) | 0.2203(---) | --- |
| $C_3$-$O_1$ | 3.9926(2.3788) | 2.9688(1.3314) | 0.0133 |
| $C_3$-$H_7$ | 2.7445(2.0608) | 2.0506(1.1214) | 0.0118 |
| $C_2$-$H_7$ | 3.7110(---) | 2.1364(---) | --- |
| $C_2$-$H_4$ | 3.9034(2.2203) | 3.9193(2.2366) | 0.0215 |

(continued)

**Table 6.5** (continued)

| | | $l$ | |
|---|---|---|---|
| *BCP* | $S_0$ | $S_1$ | $U_F$-space separation at C.I. |
| $C_2$-$H_5$ | 3.9671(2.3238) | 3.6276(2.0604) | 0.0163 |
| $C_3$-$H_6$ | 4.4853(2.4384) | 3.3423(1.0809) | 0.0057 |
| $C_2$-$C_3$ | 1.8963(1.1528) | 1.6112(0.8508) | 0.0066 |

**Table 6.6** The main QTAIM $\rho(\mathbf{r})$, stress tensor $\boldsymbol{\sigma}(\mathbf{r})$ and Ehrenfest Force $\mathbf{F}(\mathbf{r})$ vector-based concepts, not including the scalar distance measures that we have also developed, with the relevant references listed

| Vector-based | Definition | Reference |
|---|---|---|
| Hessian of $\rho(\mathbf{r})$ trajectory in U-space | $\mathsf{T}(s) = \{\mathbf{dr}(s).\underline{\mathbf{e}}_1, \mathbf{dr}(s).\underline{\mathbf{e}}_2, \mathbf{dr}(s).\underline{\mathbf{e}}_3\}$ | [31] |
| Stress tensor $\boldsymbol{\sigma}(\mathbf{r})$ trajectory in $U_\sigma$-space | $\mathsf{T}_\sigma(s) = \{\mathbf{dr}(s).\underline{\mathbf{e}}_{1\sigma}, \mathbf{dr}(s).\underline{\mathbf{e}}_{2\sigma}, \mathbf{dr}(s).\underline{\mathbf{e}}_{3\sigma}\}$ | [14, 16, 18, 33–35] |
| Stress tensor trajectory length in $U_\sigma$-space | $\mathsf{L}_\sigma = \sum_{s=0} \lvert\mathbf{dr}'(s+1) - \mathbf{dr}'(s)\rvert$ | [18] |
| Ehrenfest Force $\mathbf{F}(\mathbf{r})$ in $U_F$-space | $\mathsf{T}_F(s) = \{\mathbf{dr}(s).\underline{\mathbf{e}}_{1F}, \mathbf{dr}(s).\underline{\mathbf{e}}_{2F}, \mathbf{dr}(s).\underline{\mathbf{e}}_{3F}\}$ | [16, 35] |
| Hybrid $\boldsymbol{\sigma}(\mathbf{r})$:$\mathbf{F}(\mathbf{r})$ trajectory in $\mathsf{T}_{F\sigma}(s)$ | $\mathsf{T}_{F\sigma}(s) = \{\mathbf{dr}(s).\underline{\mathbf{e}}_{1\sigma}, \mathbf{dr}(s).\underline{\mathbf{e}}_{2\sigma}, \mathbf{dr}(s).\underline{\mathbf{e}}_{3\sigma}\}$ | [16, 35] |

The bold entries are vector-based quantities.

no other method is capable of such as directional or iso-energetic phenomena (Table 6.6).

In this chapter we explain how NG-QTAIM is used to construct the eigenvector-space trajectory $\mathsf{T}(s)$**;** $i = \{\boldsymbol{\sigma}, \rho, \mathbf{F}\}$ using the eigenvectors of the stress tensor $\sigma(\mathbf{r})$, Hessian of $\rho(\mathbf{r})$ and Ehrenfest Force $\mathbf{F}(\mathbf{r})$ respectively. In future NG-QTAIM analysis on normal modes could be performed on any type of molecule and for any vibrational mode regardless of experiment activity.

We have considered isotopomers undergoing normal modes of vibration, predict ring-opening reaction products, ground and excited states at a conical intersection and predict reaction pathways of permutation-inversion isomers. As a consequence, NG-QTAIM can uniquely be used to investigate iso-energetic phenomena where the reliance on differences in geometric measures is removed. The isoenergetic phenomena we have considered include predicted the preferred reverse ($r$) or forward ($f$) reaction pathways in response to the of all five water molecules of the water pentamer to the flip rearrangement of a single water molecule. Another iso-energetic process is the successful prediction of the transition state inward conrotatory (TSIC) and transition state outward conrotatory (TSOC) paths of *competitive* ring-open reactions for 3-(trifluoromethyl)cyclobut-1-ene and 1-cyano-1-methylcyclobutene torquoselectivity in competitive ring-opening reactions.

On the basis of the directional character of NG-QTAIM, new information and insight is also provided for non-iso-energetic phenomena including the nature of the coupling between the covalent (sigma-bonds) and hydrogen-bonds of the water molecules and differences due to presence of deuterium in place of hydrogen atoms. Considerations of bond-twist that would disrupt the coupling between sigma O-H bonds and hydrogen-bonding were included. The normal modes of benzene were revisited with subtle details provided by the use of NG-QTAIM not apparent in the traditional treatments of normal modes and without the need to calculate expensive integrated atomic charges. The coupling between covalent(sigma-bonds) and hydrogen-bonding was visualized in an investigation of the pentamer MP2 potential energy surface. The photochemical ring opening reaction (oxirane) we used the Ehrenfest Force $\mathbf{F}(\mathbf{r})$ trajectories $\mathsf{T}_{\mathbf{F}}(\boldsymbol{s})$ for the ring-opening reactions FC $\rightarrow$ CI-asym $\rightarrow$ $CH_3CHO$ and FC $\rightarrow$ CI-asym-tw $\rightarrow$ $CH_3CHO$. This indicated greater symmetry breaking corresponded to the reaction pathway **II** that preceded more readily to the conical intersection (CI) than reaction pathway **I**.

The QuantVec software was introduced, that coordinates external programs and efficiently computes the NG-QTAIM analyses using the wavefunctions from a wide range of ground and excited states computed with DFT, coupled-cluster, complete active space SCF, configuration interaction or quantum dynamics methods.

Future work could therefore include investigations on the IR-*inactive* modes using NG-QTAIM that does not require the nuclei to move then comparisons could be made with the experimentally observed vibrational corrections [24]. We think is possible since NG-QTAIM needs the electronic charge density distribution $\rho(\mathbf{r})$ to change.

In Chap. 7 we will see how NG-QTAIM can be used for stereochemistry including being used to distinguish enantiomers as well as identify chiral and mixed chiral character in formally achiral and chirality respectively.

**Target learning outcomes:**:

- Understand the basic construction of the eigenvector-space trajectories $\mathsf{T}_i(\boldsymbol{s})$ using the Hessian of $\rho(\mathbf{r})$ trajectory $\mathsf{T}(\boldsymbol{s})$, stress tensor trajectory $\mathsf{T}_{\boldsymbol{\sigma}}(\boldsymbol{s})$ and the Ehrenfest Force $\mathbf{F}(\mathbf{r})$ (Sect. 6.1).
- Understand how to use the eigenvector-space trajectories $\mathsf{T}_i(\boldsymbol{s})$ for a variety of directional applications (Sects. 6.3, 6.4 and 6.5).
- Understand why the directional (vector-based) approach of NG-QTAIM is required for iso-energetic phenomena (Sects. 6.3, 6.4 and 6.5).
- Understand the directional characteristic torquoselectivity and ring-opening reactions cannot be fully considered with any scalar measures (Sect. 6.4).

## 6.7 Further Reading

Further reading materials include the use of isotope effects of H and D in biomolecular chemistry, mass spectrometry, nuclear magnetic resonance (NMR) spectroscopy, astrochemistry and deuterium labeling for reaction analysis [21–27]. In addition, the H/D ratio in the star-planet formation region is quite different from that of the earth and so contributes significantly to the formation of heavier molecules [28].

Earlier extensive studies of the vibrational modes of benzene that used both semi-empirical and ab initio methods [13–15] and theoretical treatments on the normal coordinate treatment of benzene [2, 16, 17].

## References

1. Yang W, Zurbenko I (2010) Kolmogorov-Zurbenko filters. WIREs Comp Stat 2:340–351
2. Zou W (2021) Molden2AIM
3. Xing H, Yang Y, Nie X, Xu T, Kirk SR, Jenkins S (2021) Understanding chemical coupling in cyclic versus compact water clusters with the Ehrenfest Force. Chem Phys Lett 781:138983
4. Tian T, Xu T, Kirk SR, Filatov M, Jenkins S (2019) Next-generation quantum theory of atoms in molecules for the ground and excited state of the ring-opening of cyclohexadiene (CHD). Int J Quant Chem 119:e25862
5. Xu T, Momen R, Azizi A, van Mourik T, Früchtl H, Kirk SR, Jenkins S (2019) The destabilization of hydrogen bonds in an external E-field for improved switch performance. J Comput Chem 40:1881–1891
6. Xu T, Wang L, Ping Y, van Mourik T, Früchtl H, Kirk SR, Jenkins S (2018) Quinone-based switches for candidate building blocks of molecular junctions with QTAIM and the stress tensor. Int J Quantum Chem 118:e25676
7. Yang P, Xu T, Momen R, Azizi A, Kirk SR, Jenkins S (2018) Fatigue and photochromism S1 excited state reactivity of diarylethenes from QTAIM and the stress tensor. Int J Quantum Chem 118:e25565
8. Nie X, Yang Y, Xu T, Kirk SR, Jenkins S (2021) Fatigue and fatigue resistance in S1 excited state diarylethenes in electric fields. Int J Quantum Chem 121:e26527
9. Azizi A, Momen R, Früchtl H, van Mourik T, Kirk SR, Jenkins S (2020) Next-generation QTAIM for scoring molecular wires in E-fields for molecular electronic devices. J Comput Chem 41:913–921
10. Bin X, Xu T, Kirk SR. Jenkins S (2019) The directional bonding of [1.1.1]propellane with next generation QTAIM. Chem Phys Lett 730:506–512
11. Azizi A, Momen R, Kirk SR, Jenkins S (2019) 3-D bond-paths of QTAIM and the stress tensor in neutral lithium clusters, Lim (m = 2–5), presented on the Ehrenfest force molecular graph. Phys Chem Chem Phys 22:864–877
12. Xu T, Li JH, Momen R, Huang WJ, Kirk SR, Shigeta Y, Jenkins S (2019) Chirality-helicity equivalence in the S and R stereoisomers: a theoretical insight. J Am Chem Soc 141:5497–5503
13. Xu T, Nie X, Li S, Yang Y, Früchtl H, Mourik T, Kirk SR, Paterson MJ, Shigeta Y, Jenkins S (2021) Chirality without stereoisomers: insight from the helical response of bond electrons. ChemPhysChem 22:1989–1995
14. Li Z, Nie X, Xu T, Li S, Yang Y, Früchtl H, van Mourik T, Kirk SR, Paterson MJ, Shigeta Y, Jenkins S (2021) Control of chirality, bond flexing and anharmonicity in an electric field. Int J Quantum Chem 121:e26793

15. Azizi A, Momen R, Morales-Bayuelo A, Xu T, Kirk SR, Jenkins S (2018) A vector-based representation of the chemical bond for predicting competitive and noncompetitive torquoselectivity of thermal ring-opening reactions. Int J Quantum Chem 118:e25707
16. Guo H, Morales-Bayuelo A, Xu T, Momen R, Wang L, Yang P, Kirk SR, Jenkins S (2016) Distinguishing and quantifying the torquoselectivity in competitive ring-opening reactions using the stress tensor and QTAIM. J Comput Chem 37:2722–2733
17. Wang L, Azizi A, Momen R, Xu T, Kirk SR, Filatov M, Jenkins S (2020) Next-generation quantum theory of atoms in molecules for the S1/S0 conical intersections in dynamics trajectories of a light-driven rotary molecular motor. Int J Quant Chem 120:e26062
18. Xu T, Bin X, Kirk SR, Wales DJ, Jenkins S (2020) Flip rearrangement in the water pentamer: analysis of electronic structure. Int J Quantum Chem 120:e26124
19. Bin X, Azizi A, Xu T, Kirk SR, Filatov M, Jenkins S (2019) Next-generation quantum theory of atoms in molecules for the photochemical ring-opening reactions of oxirane. Int J Quantum Chem 119:e25957
20. Wang L, Azizi A, Xu T, Filatov M, Kirk SR, Paterson MJ, Jenkins S (2020) The role of the natural transition orbital density in the S0 → S1 and S0 → S2 transitions of fulvene with next generation QTAIM. Chem Phys Lett 751:137556
21. Kaltashov I, Eyles S (2012) Mass spectrometry based approaches to study biomolecular higher order structure. pp 89–126. https://doi.org/10.1002/9781118232125.CH4
22. Ma L, Fitzgerald CM (2004) A new H/D exchange- and mass spectrometry-based method for thermodynamic analysis of protein-DNA interactions. Chem Biol 10:1205–1213
23. Balasubramaniam D, Komives EA (2013) Hydrogen-exchange mass spectrometry for the study of intrinsic disorder in proteins. Biochim Biophys Acta (BBA) Proteins Proteomics 1834:1202–1209
24. Rand KD, Zehl M, Jørgensen TJ (2014) Measuring the hydrogen/deuterium exchange of proteins at high spatial resolution by mass spectrometry: overcoming gas-phase hydrogen/deuterium scrambling. Acc Chem Res 47:3018–3027
25. Sattler M, Fesik SW (1996) Use of deuterium labeling in NMR: overcoming a sizeable problem. Structure 4:1245–1249
26. Marion D (2013) An introduction to biological NMR spectroscopy. Mol Cell Proteomics 12:3006–3025
27. Sawama Y, Yabe Y, Iwata H, Fujiwara Y, Monguchi Y, Sajiki H (2012) Stereo- and regioselective direct multi-deuterium-labeling methods for sugars. Chemistry 18:16436–16442
28. Aikawa Y, Furuya K, Hincelin U, Herbst E (2018) Multiple paths of deuterium fractionation in protoplanetary disks. Astrophys J 855
29. Lin ST, Lee SM, Ronn AM (1978) Laser isotope separation in SF6. Chem Phys Lett 53:260–265
30. Manzhos S, Carrington T, Laverdure L, Mosey N (2015) Computing the anharmonic vibrational spectrum of $UF_6$ in 15 dimensions with an optimized basis set and rectangular collocation. J Phys Chem A 119:9557–9567
31. Tian T, Xu T, Kirk SR, Rongde IT, Tan YB, Manzhos S, Shigeta Y, Jenkins S (2020) Intramolecular mode coupling of the isotopomers of water: a non-scalar charge density-derived perspective. Phys Chem Chem Phys 22:2509–2520
32. De Marco L, Carpenter W, Liu H, Biswas R, Bowman JM, Tokmakoff A (2016) Differences in the vibrational dynamics of $H_2O$ and $D_2O$: observation of symmetric and antisymmetric stretching vibrations in heavy water. J Phys Chem Lett 7:1769–1774
33. Hu MX, Xu T, Momen R, Azizi A, Kirk SR, Jenkins S (2017) The normal modes of vibration of benzene from the trajectories of stress tensor eigenvector projection space. Chem Phys Lett 677:156–161
34. Xu T, Farrell J, Momen R, Azizi A, Kirk SR, Jenkins S, Wales DJ (2017) A stress tensor eigenvector projection space for the $(H_2O)_5$ potential energy surface. Chem Phys Lett 667:25–31
35. Nie X, Filatov M, Kirk SR, Jenkins S (2021) Photochemical ring-opening reactions of oxirane with the ehrenfest force topology. Chem Phys Lett 769:138432

# Chapter 7
# Stereochemistry Beyond Chiral Discrimination

*To the Looking-Glass world it was Alice that said 'I've a scepter in hand, I've a crown on my head. Let the Looking-Glass creatures, whatever they be, come and dine with the Red Queen, the White Queen and me.*
*Lewis Carroll*

In this chapter we build on the work of Chap. 6 that introduced the eigenvector-Space Trajectories $\mathsf{T}_i(\boldsymbol{s})$; $i = \{\sigma, \rho, \mathbf{F}\}$ including chiral discrimination and apply to stereochemistry with the stress tensor trajectory $\mathsf{T}_\sigma(\boldsymbol{s})$ and the Hessian of $\rho(\mathbf{r})$ trajectories $\mathsf{T}(\boldsymbol{s})$. We open the chapter in Sect. 7.1 by explaining the insufficiency of scalar chemical measures for use with chiral discrimination. The long known existence of unknown helical characteristics of stereoisomers as the origin of chirality is discussed in Sect. 7.1.1. The requirement for symmetry breaking to reveal helical character is explained in Sect. 7.1.2. In Sect. 7.2 the construction of the first generation stress tensor trajectories is explained and provides the NG-QTAIM interpretation of chirality $\mathsf{C}_\sigma$. The differences between the Hessian of $\rho(\mathbf{r})$ trajectory $\mathsf{T}(\boldsymbol{s})$ and the stress tensor trajectory $\mathsf{T}_\sigma(\boldsymbol{s})$ for chiral discrimination are provided in Sect. 7.2.1. Application of first generation $\mathsf{T}_\sigma(\boldsymbol{s})$ is provided by determining the dependence of the chirality $\mathsf{C}_\sigma$ on an **E**-field in Sect. 7.3. In Sect. 7.3 refinements of the first generation $\mathsf{T}_\sigma(\boldsymbol{s})$ are provided. The chirality of isotopomers of glycine is compared in Sect. 7.3.1. The chirality-helicity function $\mathsf{C}_{helicity}$ is defined in Sect. 7.3.2. Examples of the use of the $\mathsf{C}_{helicity}$ are provided in Sects. 7.3.3 and 7.3.4 in the form of $S_N2$ reactions and cumulenes respectively. In Sects. 7.4 and 7.4.1 second generation $\mathsf{T}_\sigma(\boldsymbol{s})$ are explained and illustrated with ethane respectively.

The chapter concludes in Sect. 7.5 by summarizing, outlining benefits of the ideas introduced for stereochemistry.

**Scientific goals to be addressed**:

- Explain why scalar measures are always insufficient for chiral discrimination.
- Locate the unknown helical character that underpins the concept of chirality.
- Reveal the helical character of a chiral molecule with sufficient symmetry breaking.

© The Author(s), under exclusive license to Springer Nature Singapore Pte Ltd. 2023

S. Jenkins and S. R. Kirk, *Next Generation Quantum Theory of Atoms in Molecules*, Lecture Notes in Chemistry 110, https://doi.org/10.1007/978-981-99-0329-0_7

- Explain why the stress tensor trajectory $\mathsf{T}_{\boldsymbol{\sigma}}(\boldsymbol{s})$ is better than the Hessian of $\rho(\mathbf{r})$ trajectory $\mathsf{T}_{\rho}(\boldsymbol{s})$ for chiral discrimination.
- Track the chirality for achiral species in $\mathsf{U}_{\boldsymbol{\sigma}}$-space where the CIP rules are not applicable.
- Construct second generation stress tensor trajectories $\mathsf{T}_{\boldsymbol{\sigma}}(\boldsymbol{s})$.
- Explain why ethane is overall achiral and locate a unique achiral isomer classification.
- Relate the chiral and steric effects in ethane.
- Determine the presence of mixed (S and R) chiral character in chiral molecules.
- Explain why the cis-rule is the exception rather than the rule.

## 7.1 Insufficiency of Scalar Measures for Chiral Discrimination

*In this section we demonstrate that scalar measures are insufficient for chiral discrimination and how locating the chirality-helicity equivalence overcomes this shortfall.*

Chirality is widely observed in nature and is defined as the geometric property of a molecule whereby its mirror image is non-superposable. Enantiomers are a pair of stereoisomers related to each other by a reflection in terms of being mirror images of each other that possess identical chemical properties when using scalar chemical measures and demonstrate strong enantiomeric preference during chemical reactions. Chiral molecules usually have at least one chiral center and the relative configuration (R/S) of the chiral molecule is determined by the Cahn–Ingold–Prelog (CIP) priority rules without any calculation [1, 2]. Optical isomers of coordination compounds used as stereoselectivity catalysts however, cannot be assigned from CIP rules, therefore, a quantitative method to distinguish stereoisomers is significant.

Examination of the variation with $\theta$ of the scalar measures by QTAIM: relative energy, $\Delta E$, bond-path length (BPL), local total energy density $H(\mathbf{r_b})$, stiffness $\mathsf{S}$, stress tensor stiffness $\mathsf{S}_{\boldsymbol{\sigma}}$, and the ellipticity [3] $\varepsilon$ indicates that only the ellipticity $\varepsilon$ reveals *partial* symmetry breaking but doesn't distinguish the S and R stereoisomers for *all* values of $\theta$ including $\theta = 0.0°$, see Fig. 7.1.

This is explained by the fact that the scalar measures that depend on the bond-path ($\Delta E$ and $H(\mathbf{r_b})$) or depend on the $\lambda_3$ eigenvalue ($\mathsf{S}$ and $\mathsf{S}_{\boldsymbol{\sigma}}$) cannot be used to distinguish either the stereoisomers or rotational isomers of the S and R stereoisomers as demonstrated by the results for lactic acid. Consequently, the ellipticity $\varepsilon$ can therefore, distinguish the rotational isomers of the S and R stereoisomers because it does not contain a dependency on the $\lambda_3$ eigenvalue. The ellipticity $\varepsilon$, fails to distinguish the S and R stereoisomers, i.e., at $\theta$ values of $\theta = 0.0°$ or the rotational isomers corresponding to the extrema in the relative energy $\Delta E$ values for $\theta = \pm 60.0°, \pm 120.0°$ and $\pm 180.0°$.

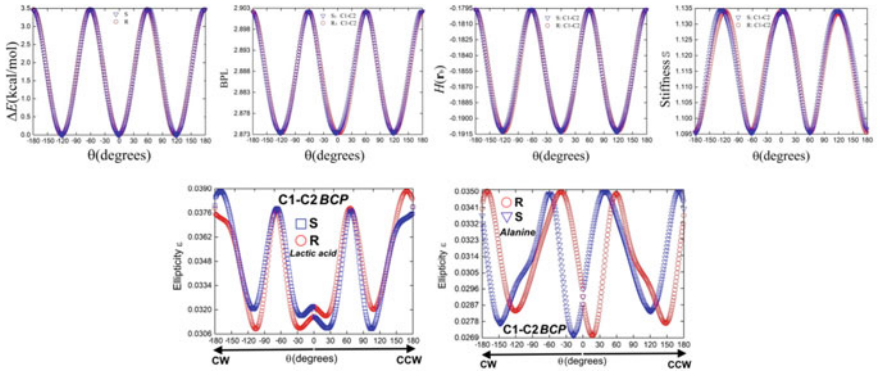


**Fig. 7.1** **Top**: Variation of the relative energy $\Delta E$, the bond-path lengths (BPL), local total energy density $H(\mathbf{r_b})$, stiffness S, stress tensor of the C1-C2 *BCP* with torsion θ of the rotational isomers and S and R stereoisomers of lactic acid with the CW ($-180.0° \leq \theta \leq 0.0°$) and CCW ($0.0° \leq \theta \leq 180.0°$). **Bottom**: The corresponding variation of the ellipticity ε with θ for the S and R stereoisomers and rotational isomers of lactic acid and alanine

### *7.1.1 Location of the Unknown Helical Character Associated with Chirality*

As early as 1821 Fresnel [4] hypnotized the existence of unknown helical characteristics of stereoisomers as the origin of chirality. The evidence for this hypothesis originates from optical experiments that reveal different refractive indices for right (R) and left (S) circularly polarized light, that exhibits circular dichroism, a form of optical activity [5]. This optical activity is in agreement with optical activity theories that correlate the inherent helical identities with direction of rotation of the circularly polarized light [6–8].

Wang proposed a 'helix theory for molecular chirality and chiral interaction' realized that the evidence for helix character from an examination of molecular geometries had proved elusive [9]. In his investigation, Wang suggested that in future the unknown chirality-helicity equivalence would be discovered by examination of the molecular electronic properties and not be solely attributed to steric hindrance.

Recent experiments by Beaulieu, Comby et al. [10] revealing the helical motion of bound electrons provide further evidence that the total electronic charge density distribution is be useful in the search for the chiral-helicity equivalence. Inspired by Wang's suggestion we located this helical character by undertaking in first instance, an in-depth investigation of the molecular properties of the commonly occurring S and R stereoisomers of lactic acid [11]. We therefore need a measure that can capture the asymmetry of the chiral center C1.

### 7.1.2 *Inducing the Required Symmetry-Breaking to Reveal Helical Character*

The asymmetry in the distribution of $\rho(\boldsymbol{r})$ is already well known in the form of the scalar ellipticity ε and can be used to quantify the asymmetry that arises as a consequence of the chiral center C1. The ellipticity ε may not however be used to locate the chirality-helicity equivalence due it lack directional information.

The reason for symmetry [12] breaking is to induce the helical character: this is undertaken by constructing a series of rotational isomers for the S and R stereoisomers on the molecular electronic properties in the form of the total electronic charge density distribution $\rho(\boldsymbol{r})$. The symmetry breaking was created by the construction of the stress tensor trajectories $\mathsf{T}_{\boldsymbol{\sigma}}(\boldsymbol{s})$ that enabled the chirality-helicity equivalence to be located. The $\mathsf{T}_{\boldsymbol{\sigma}}(\boldsymbol{s})$ were created from a series of rotational isomers for the S and R stereoisomers by the use of an applied Cartesian torsion θ, $-180.0°(\text{CW}) \leq \theta \leq +180.0°(\text{CCW})$.

We note that the observe that the scalar measures associated with the stress tensor trajectory $\mathsf{T}_{\boldsymbol{\sigma}}(\boldsymbol{s})$: the $\mathsf{T}_{\boldsymbol{\sigma}}(\boldsymbol{s})_{\text{max}}$, the lengths $\mathsf{L}_{\boldsymbol{\sigma}}$ and the real space lengths $l$ were able to distinguish the rotational isomers of S and R everywhere except for $\theta = 0.0°$, $\pm 60.0°$, $\pm 120.0°$ and $\pm 180.0$ as is found for the ellipticity ε. We were able to obtain the correct assignment of S and R stereoisomers using the $\mathsf{T}_{\boldsymbol{\sigma}}(\boldsymbol{s})$ in agreement with optical experiment i.e. S ($\text{CCW}_{\text{H}}$, left-handed) and R ($\text{CW}_{\text{H}}$, right-handed). Verification was then provided by the same analysis performed on the stereoisomers and rotational isomers S and R of the amino acid Alanine.

Evidence for the symmetry breaking properties of the $\mathsf{T}_{\boldsymbol{\sigma}}(\boldsymbol{s})$ is found by examining the gap at $\theta = 0.0°$ between the $\mathsf{T}_{\boldsymbol{\sigma}}(\boldsymbol{s})$ the CCW (S stereoisomer) and CW (R stereoisomer) torsions. This gap is explained by the corresponding *BCP* shift vectors **dr** being oppositely directed ($\pm\mathbf{dr}$), see Fig. 7.2. As an example, for a CCW torsion starting at $\theta = 0.0°$ with a finite *BCP* shift $\mathbf{dr} = \{\mathbf{+0.0001}, 0.000, 0.000\}$, the corresponding CW finite *BCP* shift $\mathbf{dr} \approx \{\mathbf{-0.0001}, 0.000, 0.000\}$, giving a $\mathsf{U}_{\boldsymbol{\sigma}}$-space separation **2dr**.

We quantified the directional behavior of all three of the associated $\underline{\mathbf{e}}_{\mathbf{1}\boldsymbol{\sigma}}$, $\underline{\mathbf{e}}_{\mathbf{2}\boldsymbol{\sigma}}$ and $\underline{\mathbf{e}}_{\mathbf{3}\boldsymbol{\sigma}}$ eigenvectors in the form of the $\mathsf{T}_{\boldsymbol{\sigma}}(\boldsymbol{s})$ as the source of the unknown chirality-helicity equivalence and as a consequence were able to determine the chirality quantitatively, see Table 7.1.

## 7.2 First Generation Stress Tensor Trajectories $\mathsf{T}_{\boldsymbol{\sigma}}(\boldsymbol{s})$

*This section defines and explains first generation* $\mathsf{T}_{\boldsymbol{\sigma}}(\boldsymbol{s})$ *that are sufficient for the understanding of chiral discrimination.*

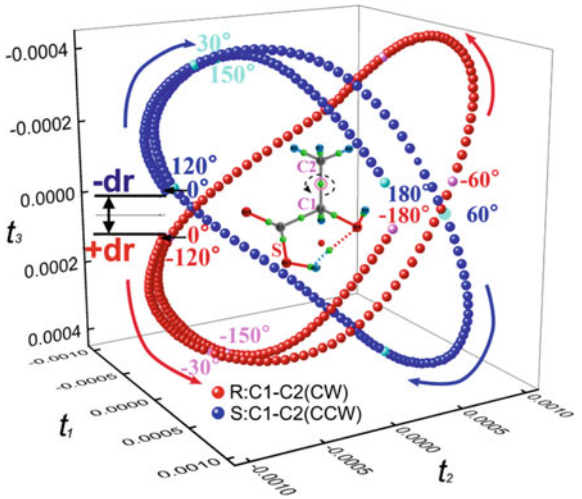


**Fig. 7.2** The stress tensor trajectories $\mathsf{T}_\sigma(s)$ of the S (blue) and R (red) stereoisomers ($\theta = 0.0°$) and rotational isomers of lactic acid for the torsional C1-C2 bond critical point (*BCP*) for the counterclockwise (CCW) and clockwise (CW) torsions, showing the symmetry-breaking shift (2**dr**), with molecular graph of the S stereoisomer inset with the torsional C1-C2 *BCP* and ring critical point (*RCP*) indicated by the undecorated green and red spheres respectively. The axes labels $t_1$, $t_2$ and $t_3$ correspond to the most preferred, least preferred directions and the motion along the bond-path of the *BCP* respectively, reprinted (adapted) with permission from reference [11]. Copyright 2019 American Chemical Society

**Table 7.1** The maximum stress tensor projections $\{t_{1\max}, t_{2\max}, t_{3\max}\}$ for the S and R stereoisomers for the torsional C1-C2 *BCP* corresponding are shown highlighted in a bold font. The molecular graph of the S stereoisomer is presented as the inset of Fig. 7.2

| | $\{t_{1\max}, t_{2\max}, t_{3\max}\}$ | | | |
|---|---|---|---|---|
| | $S_a$ | | $R_a$ | |
| | **CW** | **CCW** | **CW** | **CCW** |
| *BCP* **C1-C2** | {1.900, 0.971, 0.880} | {1.978, 1.077, 0.883} | {1.976, 1.066, 0.884} | {1.899, 0.967, 0.881} |

The first generation stress tensor trajectories $\mathsf{T}_\sigma(s)$ are used to define the chirality $\mathsf{C}_\sigma$ and are constructed using a single dihedral angle defined by four atoms involving a torsion bond associated with a chiral carbon atom. The stress tensor trajectory $\mathsf{T}_\sigma(s)$ is constructed from a sequence of points generated by performing a constrained bond-torsion $0.0° \leq \theta \leq 180.0°$(CCW) or $-180.0° \leq \theta \leq 0°$(CW) and tracking the *BCP*. The stress tensor trajectory $\mathsf{T}_\sigma(s)$ used to determine the NG-QTAIM stereoisomer $\mathsf{S}_\sigma$ or R classifications independent of the CIP rules is created from a pair of (CCW and CW) torsional distortions, this creates a symmetry breaking perturbation; note the subscript "$_\sigma$" that denotes use of the $\mathsf{T}_\sigma(s)$. The CCW and CW directions of torsion indicate left-handed and right-handed directions of bond torsion respectively

consistent with optical experiments that exhibit a form of optical activity (circular dichroism). These experiments reveal different refractive indices for left-handed (S) and right-handed (R) circularly polarized light. This is demonstrated for lactic acid; where $\theta = 0.0^{o}$ corresponds to the *minimum energy* geometry, see Fig. 7.2 (Top-right).

The maximum stress tensor projections $\mathsf{T}_{\sigma}(s)_{\mathbf{max}} = \{t_{1\mathbf{max}}, t_{2\mathbf{max}}, t_{3\mathbf{max}}\}$ define the dimensions of a 'bounding box' around each $\mathsf{T}_{\sigma}(s)$, the subscript "$_{\mathbf{max}}$" corresponds to the difference between the minimum and maximum value of the projection of the *BCP* shift $\mathbf{dr}$ onto $\underline{\mathbf{e}}_{\mathbf{1}\sigma}$, $\underline{\mathbf{e}}_{\mathbf{2}\sigma}$ or $\underline{\mathbf{e}}_{\mathbf{3}\sigma}$ along the entire $\mathsf{T}_{\sigma}(s)$. The $\mathbf{e}_{\mathbf{1}\sigma}$ corresponds to the direction in which the electrons at the *BCP* are subject to the most compressive forces [13], consequently, $\mathbf{e}_{\mathbf{1}\sigma}$ is the most *facile direction* for displacement of the *BCP* electrons when the *BCP* is torsioned. The $\mathbf{e}_{\mathbf{2}\sigma}$ and $\mathbf{e}_{\mathbf{3}\sigma}$ are the directions associated with the least compressive and the tensile forces on the *BCP* electrons respectively.

We located the unknown chirality-helicity equivalence in molecules with a chiral center and as a consequence the degeneracy of the S and R stereoisomers of lactic acid and alanine was lifted.

Earlier, we located the unknown chirality-helicity equivalence present in chiral molecules required to explain the *chemical* origins of differences in behaviors of the S and R stereoisomers that was implemented for lactic acid and alanine [11]. Agreement was found with the prediction made by Wang [9] that the molecular electronic properties and not solely steric hindrance would be the source of the unknown chirality-helicity equivalence. This finding was consistent with recent experimental work that uses the helical motion of bound electrons instead of the traditional magnetic field effects [10].

For first generation $\mathsf{T}_{\sigma}(\mathbf{s})$ for stereochemistry chirality $\mathsf{C}_{\sigma}$ is determined from the component $t_1 = \underline{\mathbf{e}}_{\mathbf{1}\sigma} \cdot \mathbf{dr}$ (bond-twist) *BCP* shift in the plane perpendicular to $\underline{\mathbf{e}}_{\mathbf{3}\sigma}$ (the bond-path) and is defined by the difference in the maximum $\mathsf{T}_{\sigma}(s)$ projections (the dot product of the stress tensor $\underline{\mathbf{e}}_{\mathbf{1}\sigma}$ eigenvector and the *BCP* shift $\mathbf{dr}$) of the $\mathsf{T}_{\sigma}(s)$ values between the CCW and CW torsions:

$$\mathsf{C}_{\sigma} = \left[\left(\underline{\mathbf{e}}_{\mathbf{1}\sigma} \cdot \mathbf{dr}\right)_{\mathbf{max}}\right]_{\mathbf{CCW}} - \left[\left(\underline{\mathbf{e}}_{\mathbf{1}\sigma} \cdot \mathbf{dr}\right)_{\mathbf{max}}\right]_{\mathbf{CW}} \tag{7.1}$$

The (+) or (−) sign of each of the chirality $\mathsf{C}_{\sigma}$ from Eq. (7.1) determines the presence of $\boldsymbol{S}_{\sigma}$ character for $\mathsf{C}_{\sigma} > 0$ and $\boldsymbol{R}_{\sigma}$ character for $\mathsf{C}_{\sigma} < 0$; note the use of the subscript "$_{\sigma}$" indicates that $\boldsymbol{S}_{\sigma}$ and $\boldsymbol{R}_{\sigma}$ are calculated using the stress tensor $\mathsf{T}_{\sigma}(s)$.

### 7.2.1 *The Choice of the Stress Tensor Trajectory $\mathsf{T}_{\sigma}(s)$ for Chiral Discrimination*

*We demonstrate the superior performance of the $\mathsf{T}_{\sigma}(s)$ over the hessian version $\mathsf{T}(s)$ and follow an $S_N2$ reaction.*

The Hessian of $\rho(\mathbf{r})$ trajectories $\mathsf{T}(\boldsymbol{s})$ were compared with the previously calculated stress tensor trajectories $\mathsf{T}_{\boldsymbol{\sigma}}(\boldsymbol{s})$ for the S and R stereoisomers of lactic acid and alanine and found broad agreement [3]. This finding demonstrated that the previously located chirality-helicity equivalence is a persistent feature regardless of using the $\mathsf{T}(\boldsymbol{s})$ or the $\mathsf{T}_{\boldsymbol{\sigma}}(\boldsymbol{s})$. Therefore the symmetry breaking that results from the use of the stress tensor $_{\boldsymbol{\sigma}}(\mathbf{r})$ within the QTAIM partitioning is not solely responsible for the formation of the helical characteristics known to be associated with chirality. For $\mathsf{T}_{\boldsymbol{\sigma}}(\boldsymbol{s})$ the most preferred ($t_{1\max}$) components for CCW > CW and CCW < CW corresponds to the left-handed ($S_a$) and right-handed ($R_a$) assignments respectively. This provided clear agreement with optical experiment, since see Table 7.2. The most preferred components ($t_{2\max}$) of the Hessian of $\rho(\boldsymbol{r})$ trajectories $\mathsf{T}(\boldsymbol{s})$ did not provide clear agreement with optical experiment but still displayed helical characteristics. The Hessian of $\rho(\boldsymbol{r})$ real space lengths $l$, however, did provide clear agreement with optical experiment with very similar results to the real space length $l$ of the $\mathsf{T}_{\boldsymbol{\sigma}}(\boldsymbol{s})$, see Table 7.3.

**Table 7.2** The maximum Hessian of $\rho(\boldsymbol{r})$ maximum trajectory projections $\mathsf{T}(\boldsymbol{s})_{\mathbf{max}} = \{t_{1\,\max}, t_{2\,\max}, t_{3\,\max}\}$ and corresponding stress tensor $_{\boldsymbol{\sigma}}(\boldsymbol{r})$ trajectory projections $\mathsf{T}_{\boldsymbol{\sigma}}(\boldsymbol{s})_{\mathbf{max}} = \{t_{1\,\max}, t_{2\,\max}, t_{3\,\max}\}$ for the $S_a$ and $R_a$ geometric stereoisomers of lactic acid for the torsional C1-C2 *BCP*, a multiplication factor of $10^2$ is used throughout

| $\mathsf{T}(\boldsymbol{s})_{\mathbf{max}} = \{t_{1\max}, t_{2\max}, t_{3\max}\} \times 10^2$ | | | |
|---|---|---|---|
| $S_a$ | | $R_a$ | |
| **CW** | **CCW** | **CW** | **CCW** |
| {0.1365, 0.1629, 0.0881} | {0.1552, 0.1632, 0.0884} | {0.1545, 0.1625, 0.0885} | {0.1373, 0.1621, 0.0881} |
| $\mathsf{T}_{\boldsymbol{\sigma}}(\boldsymbol{s})_{\mathbf{max}} = \{t_{1\boldsymbol{\sigma}\max}, t_{2\boldsymbol{\sigma}\max}, t_{3\boldsymbol{\sigma}\max}\} \times 10^2$ | | | |
| {1.8998, 0.9708, 0.8803} | {1.9782, 1.0769, 0.8835} | {1.9763, 1.0657, 0.8843} | {1.8989, 0.9668, 0.8814} |

**Table 7.3** The real space $l$ lengths ($\mathsf{T}(\boldsymbol{s})_{\max}$) of the maximum Hessian of $\rho(\boldsymbol{r})$ maximum trajectory projections $\mathsf{T}(\boldsymbol{s})$ in atomic units (a.u.) of the $S_a$ and $R_a$ geometric stereoisomers of lactic acid along the clockwise (CW) and counter-clockwise (CCW) directions of torsion θ respectively

| $l$ of the $\mathsf{T}(\boldsymbol{s})_{\max}$ | | | |
|---|---|---|---|
| $S_a$ | | $R_a$ | |
| **CW** | **CCW** | **CW** | **CCW** |
| 0.1308 | 0.1413 | 0.1407 | 0.1308 |
| $l$ of the $\mathsf{T}_{\boldsymbol{\sigma}}(\boldsymbol{s})_{\max}$ | | | |
| $S_a$ | | $R_a$ | |
| 0.1308 | 0.1414 | 0.1407 | 0.1308 |

## 7.3 Refinements of the First Generation Stress Tensor Trajectories $\mathsf{T}_{\sigma}(s)$

The refinement of the first generation $\mathsf{T}_{\sigma}(\mathbf{s})$ for stereochemistry again use the stress tensor projections $\mathsf{T}_{\sigma}(s)_{\mathbf{max}}$ to calculate the chirality $\mathsf{C}_{\sigma}$ from $t_1 = \underline{\mathbf{e}}_{\mathbf{1}\sigma}\cdot\mathbf{dr}$ in Sect. 7.2.1, the bond-flexing $\mathsf{F}_{\sigma}$ and bond-axiality $\mathsf{B}_{\sigma}$ are now considered. The bond-flexing $\mathsf{F}_{\sigma}$ is formed from $t_2 = \underline{\mathbf{e}}_{\mathbf{2}\sigma}\cdot\mathbf{dr}$ where $\underline{\mathbf{e}}_{\mathbf{2}\sigma}$ corresponds to the least facile stress tensor $_{\sigma}(\boldsymbol{r})$ eigenvector and $\mathsf{F}_{\sigma}$ is useful for determining the effects of an applied electric field to glycine to induce stereoisomers [14]:

$$\mathsf{F}_{\sigma} = \left[\left(\underline{\mathbf{e}}_{\mathbf{2}\sigma}\cdot\mathbf{dr}\right)_{\mathbf{max}}\right]_{\mathbf{CCW}} - \left[\left(\underline{\mathbf{e}}_{\mathbf{2}\sigma}\cdot\mathbf{dr}\right)_{\mathbf{max}}\right]_{\mathbf{CW}} \tag{7.2}$$

The bond-axiality $\mathsf{B}_{\sigma}$ is formed from the axial *BCP* sliding $t_3 = \underline{\mathbf{e}}_{\mathbf{3}\sigma}\cdot\mathbf{dr}$ [15], where the *BCP* sliding is the shift of the *BCP* position along the containing bond-path:

$$\mathsf{B}_{\sigma} = \left[\left(\underline{\mathbf{e}}_{\mathbf{3}\sigma}\cdot\mathbf{dr}\right)_{\mathbf{max}}\right]_{\mathbf{CCW}} - \left[\left(\underline{\mathbf{e}}_{\mathbf{3}\sigma}\cdot\mathbf{dr}\right)_{\mathbf{max}}\right]_{\mathbf{CW}} \tag{7.3}$$

and quantifies the resultant extent of *axial* displacement of the *BCP* in response to the bond torsion (CCW vs. CW), corresponding to the sliding of the *BCP* along the bond-path [15].

The (+) or (−) sign of each of the assignments: chirality $\mathsf{C}_{\sigma}$, bond-flexing $\mathsf{F}_{\sigma}$ and bond-axiality $\mathsf{B}_{\sigma}$ from Eqs. (7.1)–(7.3) respectively determines the presence of $\boldsymbol{S}_{\sigma}$ character for $\mathsf{C}_{\sigma} > 0$, $\mathsf{F}_{\sigma} > 0$ or $\mathsf{B}_{\sigma} > 0$ and $\mathbf{R}_{\sigma}$ character for $\mathsf{C}_{\sigma} < 0$, $\mathsf{F}_{\sigma} < 0$ or $\mathsf{B}_{\sigma} < 0$; note the use of the subscript "$_{\sigma}$" indicates that $\mathbf{S}_{\sigma}$ and $\mathbf{R}_{\sigma}$ are calculated using the stress tensor $\mathsf{T}_{\sigma}(\boldsymbol{s})$.

The simple arithmetic product of the circular ($\mathsf{C}_{\sigma}$) and axial ($\mathsf{B}_{\sigma}$) displacement defines the chirality-helicity chin rality-helicity function $\mathsf{C}_{helicity}$ and quantifies the resultant displacement of the torsional *BCP*:

$$\mathsf{C}_{helicity} = (\text{chirality}\ \mathsf{C}_{\sigma}) \times (\text{bond} - \text{axiality}\ \mathsf{B}_{\sigma}) = \mathsf{C}_{\sigma}\mathsf{B}_{\sigma} \tag{7.4}$$

A chirality measure of the degree of the helical displacement of the torsional *BCP* is provided by the chirality-helicity function $\mathsf{C}_{helicity}$, from Eq. (7.4), consistent with photoexcitation circular dichroism experiments, for chiral discrimination, that utilize the helical motion of the bound electrons.

### 7.3.1 *Hydrogen and Deuterium Isotopomers of Glycine Compared*

Isotopic effects were accounted for by using the mass-dependent diagonal Born–Oppenheimer energy correction (DBOC) at the CCSD level of theory along with NG-QTAIM. This resulted in the ability to determine the effect of the presence of a deuterium (D) or tritium (T) isotope bonded to the alpha carbon of glycine without the need to apply external forces e.g. electric fields or using normal mode analysis. The S-character chirality was maintained after the substitution of the H on the alpha C1 carbon for a D isotope but transformed to R-character chirality after replacement with the T isotope, see Table 7.4. The reversal of the chirality was dependent on the presence of a single D or T isotope bound to the alpha carbon and added to the debate on the nature of the extraterrestrial origins of chirality in simple amino acids.

We discovered $\mathbf{S}_\sigma$ character chirality $\mathsf{C}_\sigma$ components for the dominant torsional C1-N7 *BCP* in HH (ordinary) i.e. formally achiral glycine, the associated bond-flexing $\mathsf{F}_\sigma$ and bond-axiality $\mathsf{A}_\sigma$ possessed $\boldsymbol{R}_\sigma$ and $\boldsymbol{S}_\sigma$ character respectively [16]. The $\boldsymbol{R}_\sigma$ and $\boldsymbol{S}_\sigma$ character torsional C1-N7 *BCP* of the bond-flexing $\mathsf{F}_\sigma$ and bond-axiality $\mathsf{A}_\sigma$ was reversed by the introduction of the D and T isotopes. Reversal of the chirality $\mathsf{C}_\sigma$ when a D or T isotope on the alpha carbon is switched contributes to the debate as to the nature of the extraterrestrial origins of chirality in simple amino acids. In hostile extraterrestrial environments either D or T isotopes of hydrogen may be present, albeit at rather low concentrations e.g. in glycine that is present in meteoritic organic compounds, therefore isotopic chirality could have some influence over homochirality [17, 18].

This theoretical analysis presents a new challenge for the eventual observation of glycine chiral properties such as future experiments [10] to detect coherent helical motion of bound electrons of formally achiral glycine. Our analysis can in future be

**Table 7.4** The values of the chirality $\mathsf{C}_\sigma = [(\mathbf{e}_{1\sigma}\cdot\mathbf{dr})_{max}]\text{CCW} - [(\mathbf{e}_{1\sigma}\cdot\mathbf{dr})_{max}]\text{CW}$, bond-flexing $\mathsf{F}_\sigma = [(\mathbf{e}_{2\sigma}\cdot\mathbf{dr})_{max}]\text{CCW} - [(\mathbf{e}_{2\sigma}\cdot\mathbf{dr})_{max}]\text{CW}$ and bond-axiality $\mathsf{A}_\sigma = [(\mathbf{e}_{3\sigma}\cdot\mathbf{dr})_{max}]\text{CCW} - [(\mathbf{e}_{3\sigma}\cdot\mathbf{dr})_{max}]\text{CW}$ of the torsional C1-N7 *BCP* for the isotopomers of glycine are presented, all entries are multiplied by $10^3$. The stereoisomeric excess $\mathsf{X}_\sigma$ is defined as the ratio of the magnitude of the $\mathsf{C}_\sigma$ values of the $S_a$ and $R_a$ stereoisomers of the torsional C1-N7 *BCP*

| $\{\mathsf{C}_\sigma, \mathsf{F}_\sigma\ \mathsf{A}_\sigma\}$ | | | |
|---|---|---|---|
| *Isotopomer* | $S_a$ | $R_a$ | $\mathsf{X}_\sigma$ |
| *HD* | $\{0.20806[\mathbf{S}_\sigma], 0.45640[\mathbf{S}_\sigma], -0.18720[\mathbf{R}_\sigma]\}$ | $\{0.20819[\mathbf{S}_\sigma], 0.45631[\mathbf{S}_\sigma], -0.18918[\mathbf{R}_\sigma]\}$ | 0.99938 |
| *HT* | $\{-0.02734[\mathbf{R}_\sigma], 0.59509[\mathbf{S}_\sigma], -0.23374[\mathbf{R}_\sigma]\}$ | $\{-0.12153[\mathbf{R}_\sigma], 0.68896[\mathbf{S}_\sigma], -0.04297[\mathbf{R}_\sigma]\}$ | 0.22497 |
| $\{\mathsf{C}_\sigma, \mathsf{F}_\sigma\ \mathsf{A}_\sigma\}$ | | | |
| *HH* | $\{0.18963[\mathbf{S}_\sigma], -0.33054[\mathbf{R}_\sigma], 0.17961[\mathbf{S}_\sigma]\}$ | | |

used for the interpretation of infrared (IR) spectra to provide explanations of classical mass-dependent isotopic shifts as well as in mode coupling and intensity changes.

The feasibility such experiments is currently very limited due to the expected very weak chiroptical signals, and the need to create alpha carbon monosubstitued D/T glycine in suitable amounts. This analysis demonstrated the possibility of directly relating the $\boldsymbol{R_\sigma}/\boldsymbol{S_\sigma}$ chirality to the specific D/T isotopic substitution for a molecule in natural conditions without the introduction of e.g. external electric fields or perform challenging and difficult to interpret spectroscopic experiments.

### *7.3.2 Subjecting Glycine to an Electric (E)-Field*

Despite the lack of a chiral centre for glycine, clear CW versus CCW torsion preferences were demonstrated on the basis of larger $t_{2\max}$ component the Hessian of $\rho(\boldsymbol{r})$ trajectory $\mathsf{T}(\boldsymbol{s})_{\max}$ that is associated with the most preferred direction and larger real space lengths $l^3$, see Table 7.5. This led to the work subjecting achiral glycine to an **E**-field oriented along one the C–H bonds to render the two hydrogen atoms non-equivalent and therefore induce chirality [14], as previously undertaken by Wolk and Hoz [19], see Fig. 7.3. We sought to locate the presence of chiral character and manipulate the induced chirality in glycine by varying the direction and magnitude of an applied electric (**E**)-field to create **S and R stereoisomers**.

**E**-fields are known to be able to alter a PES in general [20–26]. In extraterrestrial regions molecular and ionic species in excited states generated by a strong **E**-field can polarize chirality, have been observed [27]. Recently, we demonstrated atomic polarization of the shifted C-C and C-H bond critical points (*BCPs*) [28] by the application of a directional (±)**E**-field on the ethene molecule. The recent Perspective by Shaik et al. considers the prospects of oriented external-electric-fields (OEEF) as 'smart reagents', for the control of reactivity and structure for chemical catalysis [29].

The creation of enantiomers using formally achiral glycine enables the use of lower **E**-fields that would result in less structural distortion of a molecule, to manipulate the S and R chirality than would be the case with chiral compounds. We used a wide range of **E**-fields from $\pm 20 \times 10^{-4}$ a.u. to $\pm 200 \times 10^{-4}$ a.u., $\approx \pm 1.1 \times 10^9$ $\mathrm{Vm}^{-1}$ to $11 \times 10^9$ $\mathrm{Vm}^{-1}$, that included **E**-fields that are easily accessible experimentally, for example within a Scanning Tunneling Microscope (STM).

Formally achiral glycine were demonstrated to be made chiral by the application of an electric (**E**)-field that induces the formation of $S_a$ and $R_a$ stereoisomers. The chirality $\mathsf{C}_\sigma$ was demonstrated to be controlled. This study established and quantified the robustness of the **E**-field-induced chirality $\mathsf{C}_\sigma$ of stereoisomers of glycine ($S_a$ or $R_{a)}$ and demonstrated that chirality increased with increase in the **E**-field. This result was indicated by the increase in the **E**-field amplification $\mathsf{EA}_\sigma$ with the application of a non-structurally distorting **E**-field. The bond-axiality $\mathsf{A}_\sigma$ was rather invariant

**Table 7.5** The chirality $C_\sigma$, bond-flexing $F_\sigma$ and bond-axiality $A_\sigma$ and the **E**-field amplification $EA_\sigma$ of the dominant torsional C1-N7 *BCP* for the electric field induced $S_a$ and $R_a$ stereoisomers of glycine. The **E**-field amplification $EA_\sigma$, is defined for each $S_a$ and $R_a$ stereoisomer as the ratio $EA_\sigma = C_\sigma/C_\sigma|_{\mathbf{E}=0}$. For **E**-field = 0, $\{C_\sigma = 0.18963[\mathbf{S}_\sigma], F_\sigma = -0.33054[\mathbf{R}_\sigma], A_\sigma = 0.17961[\mathbf{S}_\sigma]\}$

| | $S_a$ | | $R_a$ | | |
|---|---|---|---|---|---|
| *Molecule* (±) electric-field $\times 10^{-4}$ a.u. | $\{C_\sigma, F_\sigma, A_\sigma\}$ | $EA_\sigma$ | $\{C_\sigma, F_\sigma, A_\sigma\}$ | $EA_\sigma$ | $X_\sigma$ |
| **−20** | $\{0.296[\mathbf{S}_\sigma], -0.313[\mathbf{R}_\sigma], 0.207[\mathbf{S}_\sigma]\}$ | 1.558 | $\{-0.161[\mathbf{R}_\sigma], 0.341[\mathbf{S}_\sigma], -0.226[\mathbf{R}_\sigma]\}$ | −0.847 | 1.839 |
| **−100** | $\{0.404[\mathbf{S}_\sigma], 1.037[\mathbf{S}_\sigma], 0.169[\mathbf{S}_\sigma]\}$ | 2.126 | $\{-0.381[\mathbf{R}_\sigma], -1.037[\mathbf{R}_\sigma], -0.174[\mathbf{R}_\sigma]\}$ | −2.005 | 1.060 |
| **−200** | $\{0.751[\mathbf{S}_\sigma], 0.573[\mathbf{S}_\sigma], 0.168[\mathbf{S}_\sigma]\}$ | 3.953 | $\{-0.667[\mathbf{R}_\sigma], -0.867[\mathbf{R}_\sigma], -0.235[\mathbf{R}_\sigma]\}$ | −3.512 | 1.126 |
| **+20** | $\{-0.142[\mathbf{R}_\sigma], 0.352[\mathbf{S}_\sigma], -0.225[\mathbf{R}_\sigma]\}$ | −0.747 | $\{0.283[\mathbf{S}_\sigma], -0.317[\mathbf{R}_\sigma], 0.183[\mathbf{S}_\sigma]\}$ | 1.489 | 0.502 |
| **+100** | $\{-0.478[\mathbf{R}_\sigma], 0.093[\mathbf{S}_\sigma], -0.194[\mathbf{R}_\sigma]\}$ | 2.516 | $\{0.681[\mathbf{S}_\sigma], -0.075[\mathbf{R}_\sigma], 0.161[\mathbf{S}_\sigma]\}$ | 3.584 | 0.702 |
| **+200** | $\{0.302[\mathbf{S}_\sigma], -0.332[\mathbf{R}_\sigma], 0.181[\mathbf{S}_\sigma]\}$ | 1.589 | $\{0.361[\mathbf{R}_\sigma], 0.303[\mathbf{S}_\sigma], -1.189[\mathbf{R}_\sigma]\}$ | 1.900 | 0.837 |

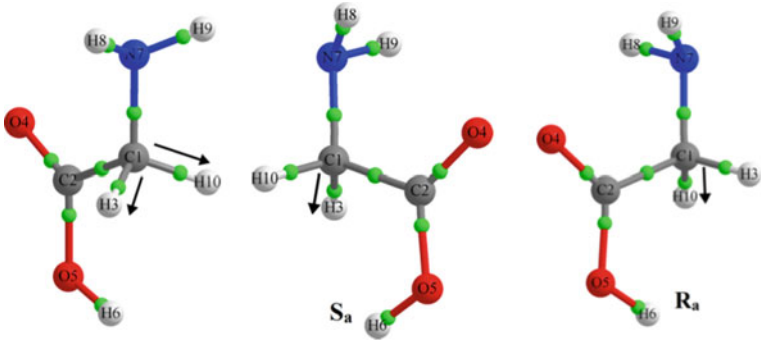


**Fig. 7.3** The molecular graphs of glycine (left panel) with arrows indicating the directions of the positive electric (+)**E**-field of the C1-H3 *BCP* bond-path and C1-H10 *BCP* bond-path. The unlabeled green spheres indicate the bond critical points (*BCP*s). The $S_a$ and $R_a$ stereoisomers (right panel) are defined for alignment of the (+)**E**-field along each of the C1-H3 *BCP* bond-path and C1-H10 *BCP* bond-path respectively

to the magnitude of the applied **E**-field, as was the stereoisomeric excess $\mathsf{X}_\sigma$. The magnitude of the bond-flexing $\mathsf{F}_\sigma$, however, displayed significant variations, both larger and smaller than in the absence of an applied **E**-field, with noticeable increases and decreases for $\mathbf{E} = -100 \times 10^{-4}$ a.u. and $\mathbf{E} = +100 \times 10^{-4}$ a.u., respectively. This finding indicated the importance of the role of monitoring the **E**-field direction to minimize the bond-strain as indicated by the magnitude of the bond-flexing $\mathsf{F}_\sigma$, to achieve less destructive manipulation of the chirality $\mathsf{C}_\sigma$.

The proportional response of the chirality $\mathsf{C}_\sigma$, **E**-field amplification $\mathsf{EA}_\sigma$ and the stereoisomeric excess, $\mathsf{X}_\sigma$ for modest **E**-field demonstrated the potential use of such NG-QTAIM measures as molecular similarity measures.

### 7.3.3 *The Chirality-Helicity Function* $\mathsf{C}_{\mathbf{helicity}}$ *for Cumulenes*

We investigated the presence of helical character and chirality using NG-QTAIM instead of energetic or structural measures [30]. The use of NG-QTAIM discovers the presence of induced symmetry-breaking for $\alpha,\omega$-disubstituted [4]cumulenes as the end groups are torsioned, see Fig. 7.4. The S-1,5-dimethyl-[4]cumulene was found to contain a very low degree of chiral character but significant bond-axiality(helicity) that resulted in a weakly helical morphology of the corresponding $\mathsf{T}_\sigma(\boldsymbol{s})$, see Fig. 7.5. The (−)S(−), (+)S(−) and (+)S(+) conformations of S-1,5-diamino-[4]cumulene contain very significant degrees of chirality and helical character and consequently the helical morphology of the corresponding $\mathsf{T}_\sigma(\boldsymbol{s})$, see Fig. 7.6. Very large values of the chirality-helicity function $\mathsf{C}_{helicity}$ are evident from the helix form of the $\mathsf{T}_\sigma(\boldsymbol{s})$, see Eq. 7.4.

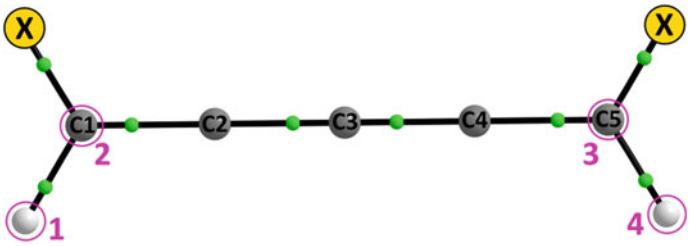


**Fig. 7.4** The molecular graph of [4]cumulene, S-1,5-dimethyl-[4]cumulene and the (−)S(−), (+)S(−) and (+)S(+) conformations of S-1,5-diamino-[4]cumulene, where X = [H, $CH_3$, (−)S(−)$NH_2$, (+)S(−)$NH_2$, (+)S(+)$NH_2$]. The magenta circled atoms define the geometric dihedral angle $\phi$ specified in the order listed. The undecorated green spheres indicate the locations of the bond critical points (*BCP*s)

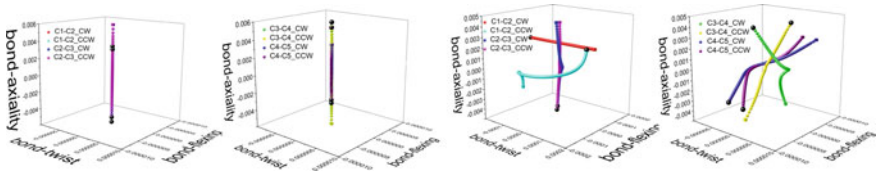


**Fig. 7.5** The stress tensor trajectories $\mathsf{T}_\sigma(s)$ of the C1-C2 *BCP*, C2-C3 *BCP*, C3-C4 *BCP* and C4-C5 *BCP* [4]cumulene and S-1,5-dimethyl-[4]cumulene. The end of each $\mathsf{T}_\sigma(s)$ is denoted by a cube marker

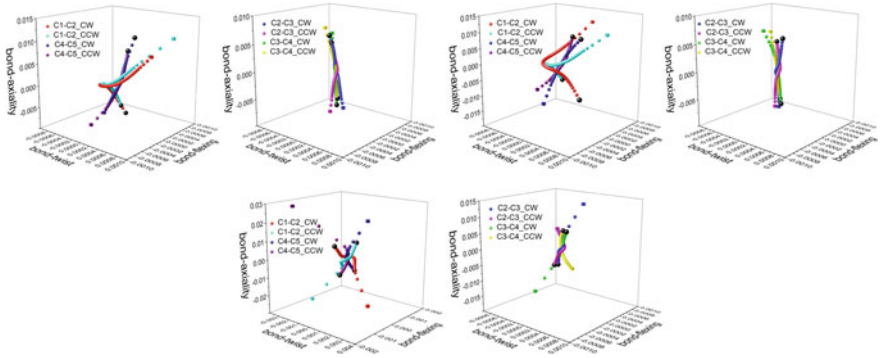


**Fig. 7.6** The stress tensor trajectories $\mathsf{T}_\sigma(s)$ of the C1-C2 *BCP*, C4-C5 *BCP* (left panel) and C2-C3 *BCP*, C3-C4 *BCP* (right panel) of the (−)S(−), (+)S(−) and (+)S(+) conformations of S-1,5-diamino-[4]cumulene. The end of each $\mathsf{T}_\sigma(s)$ is denoted by a cube marker

The chirality-helicity function $\mathsf{C}_{helicity}$ of S-1,5-dimethyl-[4]cumulene comprises a mix of $\boldsymbol{S}_\sigma$ chirality and $\boldsymbol{R}_\sigma$ bond-axiality and the low values of bond-twist $\mathsf{T}_\sigma$ but significant bond-axiality $\mathsf{A}_\sigma$ results in the weakly helical morphology of the $\mathsf{T}_\sigma(s)$.

[4]Cumulene is the first molecular graph, analyzed with NG-QTAIM, that we have discovered possesses an absence of bond-twist $T_\sigma$ *and* a very large value of the bond-axiality $A_\sigma$ and consequently a negligible value of the chirality-helicity function $C_{helicity}$. We do not therefore expect the presence of chiral and helical properties in cumulene[4] to be discoverable by experiments [10] due to the insignificant degree of the chirality-helicity function $C_{helicity}$. Conversely, on the basis of the very large values of the $C_{helicity}$, that the chiral and helical properties of the (−)S(−), (+)S(−) and (+)S(+) conformations of S-1,5-diamino-[4]cumulene could be discoverable by optical experiments.

We do not use the term "chirality $C_\sigma$" which is reserved for use for a single chiral atom in a molecule which is not the case for the cumulenes where we are investigating the C1-C2-C3-C4-C5 chain of *BCP*s, however the method of calculation for the bond-twist $T_\sigma$ is the same, see Table 7.6. We demonstrated that the presence of chirality-helicity by the helical shaped stress tensor trajectories $T_\sigma(s)$ for the S-1,5-dimethyl-[4]cumulene, (−)S(−), (+)S(−) and (+)S(+) conformations of S-1,5-diamino-[4]cumulene. We used $T_\sigma(s)$ to determine the bond-twist $T_\sigma$, the bond-axiality $A_\sigma$ and the chirality-helicity function $C_{helicity}$. Very large values of the $C_{helicity}$ are evident from the helix form of the stress tensor trajectories $T_\sigma(s)$, consistent with the helical orbitals found in earlier investigations into lactic acid and alanine [11].

### *7.3.4 The Chirality with Stereoisomers for $S_N2$ Reactions*

$S_N2$ reactions are one of the basic building blocks for understanding more complex asymmetric reactions. The chirality-helicity measure consistent with photoexcitation circular dichroism experiments is used to determine the association between molecular chirality and helical characteristics The calculation of the chirality-helicity function $C_{helicity}$ enabled the classification of the stereochemistry of chiral and achiral $S_N2$ reactions as undergoing front-side nucleophilic attacks [31]. A formally achiral $S_N2$ reaction and a chiral $S_N2$ reaction are used to demonstrate this chirality-helicity measure that we refer to as the chirality-helicity function $C_{helicity}$. The achiral and chiral $S_N2$ reactions both display a Walden inversion, i.e. an inversion of the chirality between the reactant and product. Therefore, the concept of Walden inversion can be extended to achiral $S_N2$ reactions.

The chirality-helicity $C_{helicity}$ along the reaction path are used to discover the presence of chirality at the transition state and two intermediate structures for both $S_N2$ reactions where the Cahn–Ingold–Prelog (CIP) rules cannot be used due to the five-fold coordination of the chiral carbon atom.

We detected and quantified, for the first time, the 'chirality-helicity equivalence', postulated by Wang to be the origin of chirality [9], as the chirality-helicity measure $C_{helicity}$, for the formally achiral and chiral $S_N2$ reactions of the nucleophilic attack of $Br^-$ on chloroethane and (R)-1-chloro-1-phenylethane, see Fig. 7.7 and Table

**Table 7.6** The values of the bond-twist $T_\sigma$, bond-flexing $F_\sigma$ and the bond-axiality $A_{\sigma s}$ and of the chirality-helicity function $C_{helicity}$ = (bond-twist $T_\sigma$)(axiality $A_\sigma$) for the C-C *BCPs* of the unsubstituted and substituted cumulenes

| | $\{T_\sigma, F_\sigma, A_\sigma\}$ | $C_{helicity}$ | $[T_\sigma, A_\sigma]$ |
|---|---|---|---|
| *[4]cumulene* | | | |
| C1-C2 *BCP* | {0.00000**[S$_\sigma$]**, 0.00001**[S$_\sigma$]**, 0.36621**[S$_\sigma$]**} | 0.00000 | **[S$_\sigma$,S$_\sigma$]** |
| C2-C3 *BCP* | {0.00001**[S$_\sigma$]**, −0.00002**[R$_\sigma$]**, 0.58335**[S$_\sigma$]**} | 0.00001 | **[S$_\sigma$,S$_\sigma$]** |
| C3-C4 *BCP* | {−0.00002**[R$_\sigma$]**, 0.00001**[S$_\sigma$]**, 0.58336**[S$_\sigma$]**} | −0.00001 | **[R$_\sigma$,S$_\sigma$]** |
| C4-C5 *BCP* | {−0.00006**[R$_\sigma$]**, 0.00000**[S$_\sigma$]**, 0.36633**[S$_\sigma$]**} | −0.00002 | **[R$_\sigma$,S$_\sigma$]** |
| *S-1,5-dimethyl-[4]cumulene* | | | |
| C1-C2 *BCP* | {−0.02677**[R$_\sigma$]**, −0.04781**[R$_\sigma$]**, 0.18036**[S$_\sigma$]**} | −0.00483 | **[R$_\sigma$,S$_\sigma$]** |
| C2-C3 *BCP* | {−0.00858**[R$_\sigma$]**, −0.01873**[R$_\sigma$]**, 0.33567**[S$_\sigma$]**} | −0.00288 | **[R$_\sigma$,S$_\sigma$]** |
| C3-C4 *BCP* | {0.00052**[S$_\sigma$]**, −0.00093**[R$_\sigma$]**, 0.34030**[S$_\sigma$]**} | 0.00018 | **[S$_\sigma$,S$_\sigma$]** |
| C4-C5 *BCP* | {−0.00282**[R$_\sigma$]**, 0.00050**[S$_\sigma$]**, 0.17749**[S$_\sigma$]**} | −0.00050 | **[R$_\sigma$,S$_\sigma$]** |
| *(−)S(−) S-1,5-diamino-[4]cumulene* | | | |
| C1-C2 *BCP* | {0.24690**[S$_\sigma$]**, −0.21197**[R$_\sigma$]**, 1.28073**[S$_\sigma$]**} | 0.31621 | **[S$_\sigma$,S$_\sigma$]** |
| C2-C3 *BCP* | {−0.14710**[R$_\sigma$]**, 0.04266**[S$_\sigma$]**, −0.45718**[R$_\sigma$]**} | 0.06725 | **[R$_\sigma$,R$_\sigma$]** |
| C3-C4 *BCP* | {0.14262**[S$_\sigma$]**, −0.04699**[R$_\sigma$]**, −0.45292**[R$_\sigma$]**} | −0.06460 | **[S$_\sigma$,R$_\sigma$]** |
| C4-C5 *BCP* | {0.31485**[S$_\sigma$]**, −0.19825**[R$_\sigma$]**, 1.25469**[S$_\sigma$]**} | 0.39561 | **[S$_\sigma$,S$_\sigma$]** |
| *(+)S(−) S-1,5-diamino-[4]cumulene* | | | |
| C1-C2 *BCP* | {0.17738**[S$_\sigma$]**, −0.66454**[R$_\sigma$]**, −1.80066**[R$_\sigma$]**} | −0.31940 | **[S$_\sigma$,R$_\sigma$]** |
| C2-C3 *BCP* | {−0.01920**[R$_\sigma$]**, −0.02399**[R$_\sigma$]**, −1.03702**[R$_\sigma$]**} | 0.01991 | **[R$_\sigma$,R$_\sigma$]** |
| C3-C4 *BCP* | {−0.08852**[R$_\sigma$]**, −0.068 36**[R$_\sigma$]**, −1.01975**[R$_\sigma$]**} | 0.09027 | **[R$_\sigma$,R$_\sigma$]** |
| C4-C5 *BCP* | {0.08485**[S$_\sigma$]**, −0.17413**[R$_\sigma$]**, −1.86474**[R$_\sigma$]**} | −0.15822 | **[S$_\sigma$,R$_\sigma$]** |
| *(+)S(+) S-1,5-diamino-[4]cumulene* | | | |
| C1-C2 *BCP* | {0.86363**[S$_\sigma$]**, −0.21694**[R$_\sigma$]**, 6.74465**[S$_\sigma$]**} | 5.82488 | **[S$_\sigma$,S$_\sigma$]** |
| C2-C3 *BCP* | {−0.16848**[R$_\sigma$]**, −0.23924 **[R$_\sigma$]**, −7.77013**[R$_\sigma$]**} | 1.30911 | **[R$_\sigma$,R$_\sigma$]** |
| C3-C4 *BCP* | {−0.18147**[R$_\sigma$]**, −0.34965**[R$_\sigma$]**, −7.77102**[R$_\sigma$]** | −1.41021 | **[R$_\sigma$,R$_\sigma$]** |
| C4-C5 *BCP* | {0.98399**[S$_\sigma$]**, 0.98398**[S$_\sigma$]**, 6.70333**[S$_\sigma$]**} | 6.59601 | **[S$_\sigma$,S$_\sigma$]** |

7.7b. The $C_{helicity}$ provides a global chirality measure of the degree of the helical displacement of the torsional *BCP*. This finding is consistent with photoexcitation circular dichroism experiments on neutral molecules that utilize the helical motion of the bound electrons [10, 32].

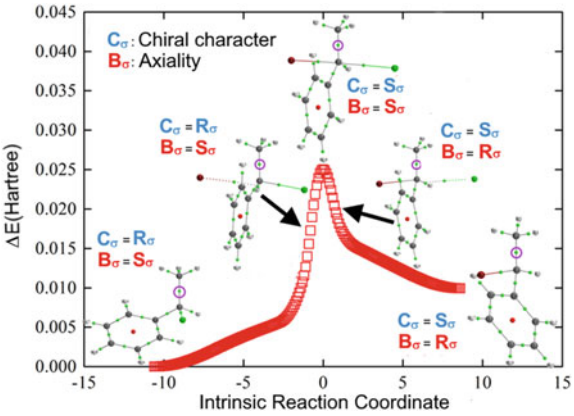


**Fig. 7.7** The chirality $C_\sigma$ and bond-axiality $B_\sigma$ assignments, see Eq. (7.4) respectively, corresponding to the relative energy $\Delta E$ profile of the $S_N2$ reaction of the attack of $Br^-$ on (R)-1-chloro-1-phenylethane (reactant) resulting in (S)-1-bromo-1-phenylethane (product), with the transition state

**Table 7.7** **a** The chirality $C_\sigma$, helicity $B_\sigma$ and the chirality-helicity measure $C_{helicity}$ for the torsional C1-C2 *BCP* of the achiral $S_N2$ reaction of monochloroethane with Br. Values of the magnitude of $C_\sigma$ or $B_\sigma$ less than $10^{-5}$ indicate insignificant $C_{helicity}$. **b** The chirality $C_\sigma$, helicity $B_\sigma$ and the chirality-helicity measure $C_{helicity}$ for the torsional C1-C2 *BCP* of the chiral $S_N2$ reaction

| **$S_N2$ reaction species** | $\{C_\sigma, B_\sigma\}$ | $C_{helicity}$ | $[C_\sigma, B_\sigma]$ |
|---|---|---|---|
| | (a) | | |
| *Monochloroethane* | $\{0.5709[\mathbf{S}_\sigma], -0.0166[\mathbf{R}_\sigma]\}$ | −0.0095 | $[\mathbf{S}_\sigma,\mathbf{R}_\sigma]$ |
| *INTS1* | $\{-0.2401[\mathbf{R}_\sigma], -0.0487[\mathbf{R}_\sigma]\}$ | 0.0117 | $[\mathbf{R}_\sigma,\mathbf{R}_\sigma]$ |
| *Transition state* | $\{-0.0201[\mathbf{R}_\sigma], 0.0068[\mathbf{S}_\sigma]\}$ | −0.0001 | $[\mathbf{R}_\sigma,\mathbf{S}_\sigma]$ |
| *INTS2* | $\{0.2030[\mathbf{S}_\sigma], 0.0539[\mathbf{S}_\sigma]\}$ | 0.0109 | $[\mathbf{S}_\sigma,\mathbf{S}_\sigma]$ |
| *Monobromoethane* | $\{-0.5349[\mathbf{R}_\sigma], 0.0205[\mathbf{S}_\sigma]\}$ | −0.0109 | $[\mathbf{R}_\sigma,\mathbf{S}_\sigma]$ |
| | (b) | | |
| *(R)-1-chloro-1-phenylethane* | $\{-0.9859[\mathbf{R}_\sigma], -0.0110[\mathbf{R}_\sigma]\}$ | 0.0108 | $[\mathbf{R}_\sigma,\mathbf{R}_\sigma]$ |
| *INTS1* | $\{-0.3005[\mathbf{R}_\sigma], 0.0597[\mathbf{S}_\sigma]\}$ | −0.0179 | $\mathbf{R}_\sigma,\mathbf{S}_\sigma]$ |
| *Transition state* | $\{0.0318[\mathbf{S}_\sigma], 0.1898[\mathbf{S}_\sigma]\}$ | 0.0060 | $[\mathbf{S}_\sigma,\mathbf{S}_\sigma]$ |
| *INTS2* | $\{0.1959[\mathbf{S}_\sigma], -0.0216[\mathbf{R}_\sigma]\}$ | −0.0042 | $[\mathbf{S}_\sigma,\mathbf{R}_\sigma]$ |
| *(S)-1-bromo-1-phenylethane* | $\{0.7285[\mathbf{S}_\sigma], -0.0142[\mathbf{R}_\sigma]\}$ | −0.0103 | $[\mathbf{S}_\sigma,\mathbf{R}_\sigma]$ |
| **Stereoisomers** | | | |
| *(S)-1-chloro-1-phenylethane* | $\{0.9859[\mathbf{S}_\sigma], 0.0111[\mathbf{S}_\sigma]\}$ | 0.0110 | $[\mathbf{S}_\sigma,\mathbf{S}_\sigma]$ |
| *(R)-1-bromo-1-phenylethane* | $\{-0.7285[\mathbf{R}_\sigma], 0.0141[\mathbf{S}_\sigma]\}$ | −0.0103 | $[\mathbf{R}_\sigma,\mathbf{S}_\sigma]$ |

**Table 7.8** The torsion C1-C2 *BCP* $\mathsf{U}_\sigma$-space distortion sets $\{\mathsf{C}_\sigma, \mathsf{F}_\sigma, \mathsf{A}_\sigma\}$, the sum $\sum\{\mathsf{C}_\sigma, \mathsf{F}_\sigma, \mathsf{A}_\sigma\}$ and the chirality-helicity function $\mathsf{C}_{helicity}$ with the total chirality $\mathsf{C}_{\sigma T}$ and $\mathsf{A}_\sigma$ chirality assignments denoted by $[\mathsf{C}_\sigma,\mathsf{A}_\sigma]$ in the absence and presence of an applied $-100 \times 10^{-4}$ a.u. **E**-field. The four-digit sequence in the left column refers to the atom numbering used in the dihedral angles (H3-C1-C2-H6, H4-C1-C2-H8, H5-C1-C2-H7) used to construct the stress tensor trajectories $\mathsf{T}_\sigma(s)$, which also correspond to the $D_{3126}$, $D_{4128}$, $D_{5127}$ isomer names respectively, see Fig. 7.9. The $-100 \times 10^{-4}$ a.u. **E**-field is directed along the C1-H3 *BCP* bond-path to create the $A_{3\mathbf{E}\sigma}$ isomers. The corresponding $\pm\mathbf{E}$-field results for $\pm 50 \times 10^{-4}$ a.u. and $+100 \times 10^{-4}$ a.u. for the C1-H4 *BCP* ($A_{5\mathbf{E}\sigma}$ isomers) and C1-H5 *BCP* ($A_{5\mathbf{E}\sigma}$ isomers) are equivalent

| *Isomer* | $\{\mathsf{C}_\sigma, \mathsf{F}_\sigma, \mathsf{A}_\sigma\}$ | $\mathsf{C}_{helicity}$ | $[\mathsf{C}_{\sigma T},\mathsf{A}_\sigma]$ |
|---|---|---|---|
| **E-field = 0** | | | |
| $D_{3126}$ | $\{-0.00010[\mathbf{R}_\sigma], 0.00003[\mathbf{S}_\sigma], -0.000003[\mathbf{R}_\sigma]\}$ | $\approx 0\ (2.47 \times 10^{-10})$ | $[\mathbf{Q}_\sigma]$ |
| $]D_{4128}$ | $\{-0.29110[\mathbf{R}_\sigma], -0.12644[\mathbf{R}_\sigma], -0.00094[\mathbf{R}_\sigma]\}$ | $-0.0003$ | $[\mathbf{R}_\sigma,\mathbf{R}_\sigma]$ |
| $D_{5127}$ | $\{0.29096[\mathbf{S}_\sigma], 0.12635[\mathbf{S}_\sigma], 0.00099[\mathbf{S}_\sigma]\}$ | 0.0003 | $[\mathbf{S}_\sigma,\mathbf{S}_\sigma]$ |
| $\sum\{\mathsf{C}_\sigma, \mathsf{F}_\sigma, \mathsf{A}_\sigma\}$ | $\{-0.00024[\mathbf{R}_\sigma], -0.00006[\mathbf{R}_\sigma],0.000047[\mathbf{S}_\sigma]\}$ | $\approx 0\ (-1.13 \times 10^{-8})$ | $[\mathbf{Q}_\sigma]$ |
| **E-field = $-100 \times 10^{-4}$ a.u** | | | |
| $D_{3126}$ | $\{-0.00020\ [\mathbf{R}_\sigma], -0.00011[\mathbf{R}_\sigma], -0.00004[\mathbf{R}_\sigma]\}$ | $\approx 0\ (7.06 \times 10^{-9})$ | $[\mathbf{Q}_\sigma]$ |
| $D_{4128}$ | $\{-0.14638[\mathbf{R}_\sigma], -0.28745[\mathbf{R}_\sigma], -0.00124[\mathbf{R}_\sigma]\}$ | $-0.0002$ | $[\mathbf{R}_\sigma,\mathbf{R}_\sigma]$ |
| $D_{5127}$ | $\{0.14677[\mathbf{S}_\sigma],0.28763[\mathbf{S}_\sigma],0.00112[\mathbf{S}_\sigma]\}$ | 0.0002 | $[\mathbf{S}_\sigma,\mathbf{S}_\sigma]$ |
| $\sum\{\mathsf{C}_\sigma, \mathsf{F}_\sigma, \mathsf{A}_\sigma\}$ | $\{0.000191[\mathbf{S}_\sigma],0.000073[\mathbf{S}_\sigma], -0.000158[\mathbf{R}_\sigma]\}$ | $\approx 0\ (-3.02 \times 10^{-8})$ | $[\mathbf{Q}_\sigma]$ |

## 7.4 Second Generation Stress Tensor Trajectories $\mathsf{T}_\sigma(s)$

*We explain the spanning dihedral construction for the* $\mathsf{T}_\sigma(s)$.

For second generation $\mathsf{T}_\sigma(\mathbf{s})$ for stereochemical applications we follow a similar scheme in that we subject the interrogated bond to a pair of torsions: CCW ($0.0° \leq \theta \leq +180.0°$) or CW ($-180.0° \leq \theta \leq 0.0°$).

The $\mathsf{T}_\sigma(s)$ for all nine possible ordered sets of four atoms that define the dihedral angle {(H3-C1-C2-H6, H3-C1-C2-H7, H3-C1-C2-H8), (H4-C1-C2-H6, H4-C1-C2-H7, H4-C1-C2-H8), (H5-C1-C2-H6, H5-C1-C2-H7, H5-C1-C2-H8)}, see Fig. 7.8.

### *7.4.1 Chiral and Steric Effects in Ethane*

We investigated of the chirality of ethane [34] with second generation $\mathsf{T}_\sigma(s)$ that searched all nine possible torsion C1-C2 *BCP* $\mathsf{T}_\sigma(s)$ to determine the three symmetry

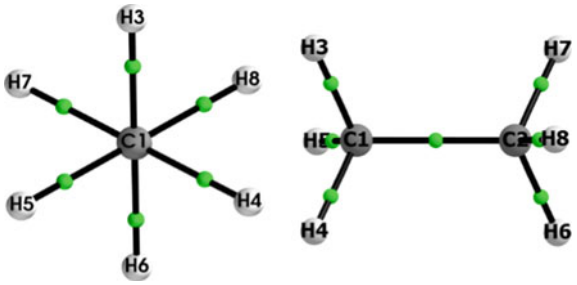


**Fig. 7.8** An axial view down the torsion C1-C2 *BCP* bond-path (left-panel) of the molecular graph of ethane with the atomic numbering scheme used for the dihedral angles in the construction of the torsion C1-C2 *BCP* stress tensor trajectories $\mathsf{T}_\sigma(s)$. The H3, H4 and H5 atoms are bonded to the C1 atom and the H6, H7 and H8 atoms are bonded to the C2 atom. The corresponding side view of the molecular graph is presented (right-panel)

inequivalent $\mathsf{T}_\sigma(s)$. We included all contributions to the $\mathsf{U}_\sigma$-space chirality by considering the entire bonding environment of the 'chiral' carbon atom (C1) by constructing all nine torsion C1-C2 *BCP* $\mathsf{T}_\sigma(s)$ using dihedral angles that include the C1 atom, see Fig. 7.3. The linear sum of each components of the symmetry inequivalent $\mathsf{U}_\sigma$-space distortion sets $\sum\{\mathsf{C}_\sigma, \mathsf{F}_\sigma, \mathsf{A}_\sigma\}$ was calculated to provide the resultant chiral character for the ethane molecular graph. The $\mathsf{C}_{helicity}(=\mathsf{C}_\sigma|\mathsf{A}_\sigma|)$ of the resultant was calculated as the linear sum $\sum\{\mathsf{C}_\sigma, \mathsf{F}_\sigma, \mathsf{A}_\sigma\}$ as well as the sum of the individual $\mathsf{C}_{helicity}$; values of $\mathsf{C}_{helicity} \approx 0$ correspond to the null-chirality assignment $\boldsymbol{Q}_\sigma$, see Table 7.8.

The resultant chiral nature of the ethane molecule was determined to be achiral in $\mathsf{U}_\sigma$-space. As a consequence of the vector-based nature of $\mathsf{U}_\sigma$-space it was possible to obtain this resultant achiral character from additive contributions to $\mathsf{C}_{helicity}$ ($\approx$ 0) of the symmetry inequivalent $D_{3126,}$ $D_{4128}$ and $D_{5127}$ isomers. A new isomer type $\boldsymbol{Q}_\sigma$ is discovered in addition to $\boldsymbol{S}_\sigma$ and $\boldsymbol{R}_\sigma$ stereoisomers in the stress tensor trajectory $\mathsf{U}_\sigma$-space. This new $\boldsymbol{Q}_\sigma$ isomer is defined to be a 'null-isomer' since the value of the chirality-helicity function $\approx 0$. The strong presence of the chiral contributions suggests that steric effects, rather than hyper-conjugation, explain the staggered geometry of ethane.

A null-chirality assignment $\boldsymbol{Q}_\sigma$ is present where a plot of ellipticity $\varepsilon$ versus torsion $\theta$ displays CCW and CW portions that are symmetrical about torsion $\theta = 0.0°$, see Fig. 7.9 (left-panel). The choice of $\pm$ sign is not used with the chirality assignment $\boldsymbol{Q}_\sigma$ as it is for the $\boldsymbol{S}_\sigma$ and $\boldsymbol{R}_\sigma$ assignments, since for the latter mirror symmetry is only present for the $\mathbf{S}_\sigma$ CCW versus $\boldsymbol{R}_\sigma$ CW and $\boldsymbol{S}_\sigma$ CW versus $\boldsymbol{R}_\sigma$ CCW plots of ellipticity $\varepsilon$ versus torsion $\theta$, see Fig. 7.9 (right-panel).

The resultant $\boldsymbol{Q}_\sigma$ assignment of ethane was determined by summing the nine individual $\mathsf{C}_\sigma$, $\mathsf{F}_\sigma$ and $\mathsf{A}_\sigma$ components of the $\mathsf{U}_\sigma$-space distortion sets $\{\mathsf{C}_\sigma,\mathsf{F}_\sigma,\mathsf{A}_\sigma\}$ of the torsion C1-C2 *BCP*, see Fig. 7.10. The $D_{4128}$ and $D_{5127}$ isomers were determined to be stereoisomers in $\mathsf{U}_\sigma$-space both in the absence and presence of an applied **E**-field.

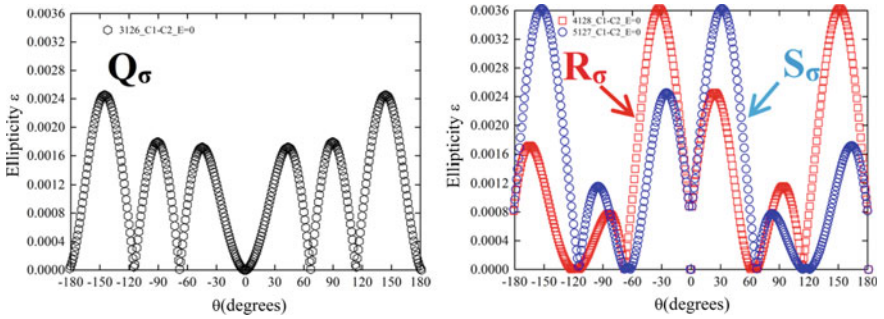


**Fig. 7.9** The variation of the ellipticity ε for the clockwise (CW) ($-180.0^o \leq \theta \leq 0.0^o$) and counter-clockwise (CCW) ($0.0^o \leq \theta \leq +180.0^o$) torsion θ isomers of the ethane C1-C2 *BCP* in the absence of an **E**-field. For the $\boldsymbol{Q_\sigma}$ isomer (black, left-panel) the CCW and CW portions are symmetrical about torsion $\theta = 0.0^o$. The corresponding $\boldsymbol{R_\sigma}$ (red) and $\boldsymbol{S_\sigma}$ (blue) isomers are presented in the right-panel. Note, the ellipticity ε at the torsion C1-C2 *BCP* = 0 (left and right panels)

The presence of large chirality $C_\sigma$ values for the $D_{4128}$ and $D_{5127}$ isomers of ethane demonstrates relevance for understanding why steric effects are a significant factor in explaining the staggered geometry of ethane. Large values of the chirality $C_\sigma$ indicate an asymmetry in the CCW versus CW torsion for the C1-C2 *BCP*, i.e. relating to steric effects in $U_\sigma$-space. These large (±) chirality $C_\sigma$ values for the $D_{4128}$ and $D_{5127}$ isomers are also consistent with the equal and opposite torsions of the $CH_3$ groups that are located in a staggered configuration either side of the torsional C1-C2 *BCP* bond-path of the relaxed structure of ethane. The chirality $C_\sigma$ values of the $D_{4128}$ and $D_{5127}$ isomers, which are two orders of magnitude greater than the corresponding values of the C1-C2 *BCP* bond-axiality $A_\sigma$, also indicate the dominance of steric effects over hyper-conjugation within the NG-QTAIM interpretation.

The application of the **E**-field reduced the steric effects by a factor of two, although no measurable changes in the ethane molecular geometry were observed since the steric effects are determined in $U_\sigma$-space.

### *7.4.2 Mixed Chiral and Achiral Character in Substituted Ethane*

We investigated singly and doubly substituted ethane using use all nine possible $U_\sigma$-space distortion sets [33] $\{C_\sigma, F_\sigma, A_\sigma\}$, see Figs. 7.11 and 7.12, Tables 7.9 and 7.10.

The NG-QTAIM interpretation of the chirality of the singly substituted (F or Cl or Br) ethane is that ethane is an achiral molecule with constituent chirality assignments $\boldsymbol{Q_\sigma}, \mathbf{S_\sigma}$ or $\boldsymbol{R_\sigma}$, see Table 7.9. In comparison the pure ethane molecule possesses values

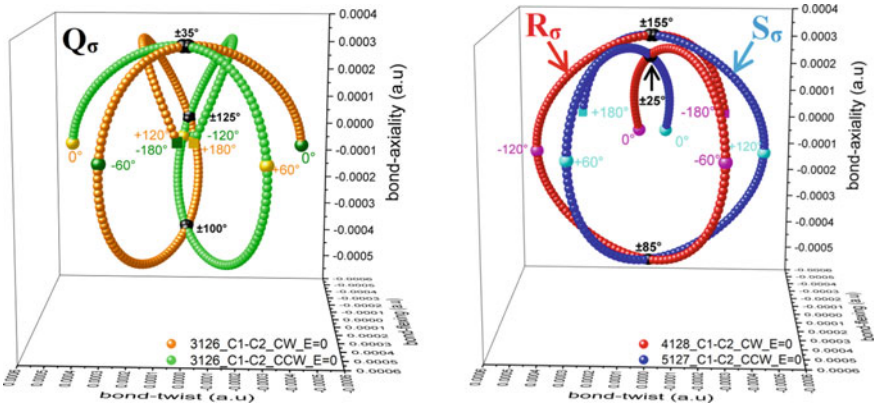


**Fig. 7.10** The ethane C1-C2 *BCP* stress tensor trajectories $\mathsf{T}_{\sigma}(s)$ in the absence of an **E**-field for the Cartesian CW and CCW torsions for the $\boldsymbol{Q}_{\sigma}$ (top-left) and $\boldsymbol{S}_{\sigma}$ (top-right, blue) and $\mathbf{R}_{\sigma}$ (top-right, red) $\mathsf{U}_{\sigma}$-space isomers

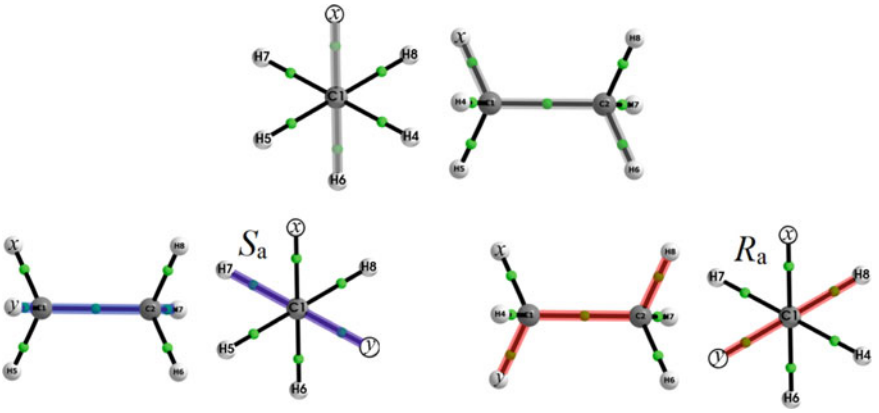


**Fig. 7.11** Axial and in-plane views down/along the torsion C1-C2 *BCP* bond-path of the molecular graph of singly substituted ethane (top) with $x$ = F, Cl, Br, where $x$ is bonded to the C1 atom. For the doubly substituted ethane the $S_a$-stereoisomer (bottom-left) and $R_a$-stereoisomer (bottom-right), the heaviest halogen atom is located at $x$ and the lighter one at $y$; therefore the three pairs of $S_a$-stereoisomer and $R_a$-stereoisomer correspond to $\{x = \text{Cl}, y = \text{F}\}$, $\{x = \text{Br}, y = \text{Cl}\}$, $\{x = \text{Br}, y = \text{F}\}$. Note that $y$ is replacing the H4 and H5 atom for the $S_a$-stereoisomer and $R_a$-stereoisomer, respectively, see Tables 7.9 and 7.10. The grey, blue and red shading indicate the dihedral angles used to construct the symmetrically inequivalent $D_{3127}$, $D_{4127}$ and $D_{5128}$ isomers respectively, see Fig. 7.12

of the chirality helicity function $\mathsf{C}_{helicity} = 0, +0.0003$ and $-0.0003$ for the $\boldsymbol{Q}_{\sigma}$, $\mathbf{S}_{\sigma}$ and $\boldsymbol{R}_{\sigma}$ stereoisomers in $\mathsf{U}_{\sigma}$-space, respectively [34].

The ($D_{3127}$ and $D_{3128}$), ($D_{4128}$ and $D_{5127}$) and ($D_{4127}$ and $D_{5128}$) isomers are regarded as stereoisomers in $\mathsf{U}_{\sigma}$-space. The singly substituted ethane the $D_{3126}$, $D_{4126}$ and

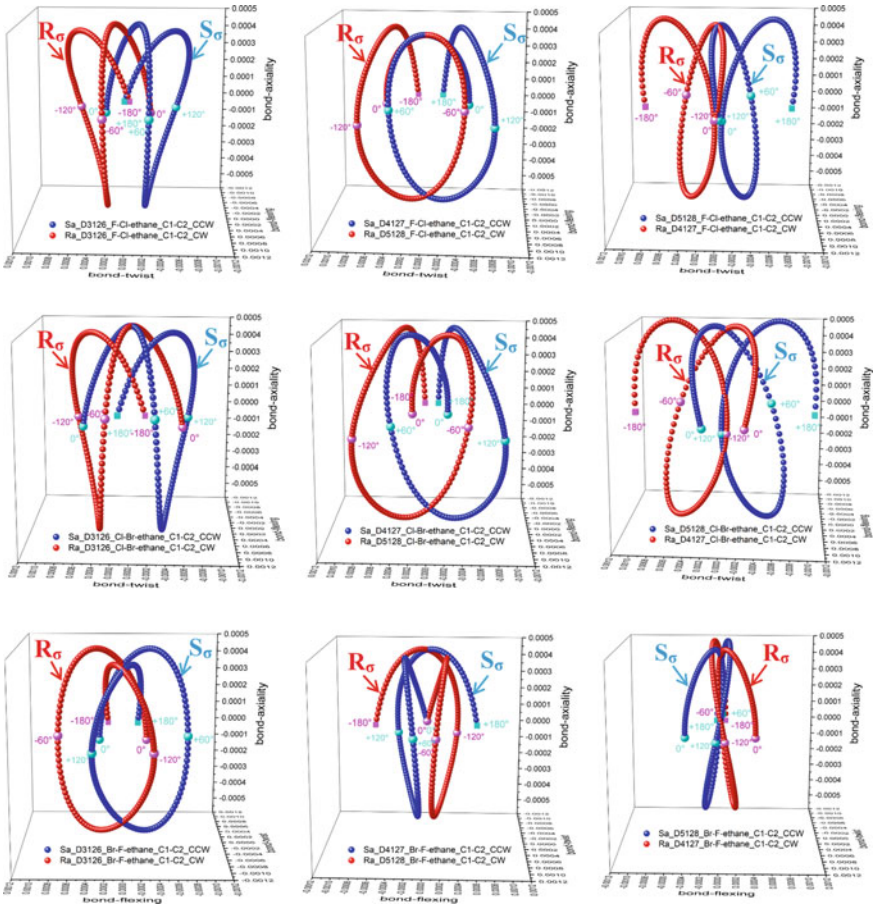


**Fig. 7.12** The doubly F-Cl (top-panel), Cl-Br (middle-panel) and Br-F (lower-panel) substituted ethane C1-C2 *BCP* stress tensor trajectories $\mathsf{T}_\sigma(s)$ for the Cartesian CW and CCW torsions for $S_a$ and $R_a$ geometric stereoisomers of the $\mathbf{S}_\sigma$ (blue) and $\mathbf{R}_\sigma$ (red) $\mathsf{U}_\sigma$-space stereoisomers, see Table 7.10

$D_{5126}$ isomers are possess chirality assignment $\mathbf{Q}_\sigma$ corresponding to null-chirality. This is determined on the basis of the very low values of the chirality $\mathsf{C}_\sigma$ and bond-axiality $\mathsf{B}_\sigma$, i.e. an order of magnitude lower than for the $\mathbf{S}_\sigma$ or $\mathbf{R}_\sigma$. The linear sum of the distortion sets $\sum\{\mathsf{C}_\sigma, \mathsf{F}_\sigma, \mathsf{A}_\sigma\} = 0$ for the complete set of nine isomers of the singly substituted ethane corresponds to a chirality assignment $\boldsymbol{Q}_\sigma$, consistent with the singly substituted ethane being formally achiral. This is consistent with the values of $\sum \mathsf{C}_{helicity} = 0$ for the complete set of nine distortion sets $\{\mathsf{C}_\sigma, \mathsf{F}_\sigma, \mathsf{A}_\sigma\}$ also corresponding to a chirality assignment $\boldsymbol{Q}_\sigma$. The stereoisomer character of the singly substituted ethane in $\mathsf{U}_\sigma$-space is demonstrated by the presence of the $\mathbf{S}_\sigma$ components $\sum_{\mathbf{S}\sigma}\{\mathsf{C}_\sigma, \mathsf{A}_\sigma\}$ and $\mathbf{R}_\sigma$ components $\sum_{\mathbf{R}\sigma}\{\mathsf{C}_\sigma,\mathsf{A}_\sigma\}$ being approximately

**Table 7.9** The singly substituted ethane torsion C1-C2 *BCP* $U_\sigma$-space distortion sets {chirality $C_\sigma$, bond-flexing $F_\sigma$, bond-axiality $A_\sigma$}, sum of the nine isomers: $\sum_{S\sigma,R\sigma}\{C_\sigma,F_\sigma,A_\sigma\}$, sum of the $\mathbf{S}_\sigma$ components $\sum_{S\sigma}\{C_\sigma,A_\sigma\}$and $\mathbf{R}_\sigma$ components $\sum_{R\sigma}\{C_\sigma,A_\sigma\}$, chirality-helicity function $C_{helicity} = (C_\sigma)(|A_\sigma|)$ and the sum of $C_{helicity}$ over the nine isomers $\sum C_{helicity}$. The four-digit sequence (left column) refers to the atom numbering sequence for the dihedral angles used to construct the $T_\sigma(s)$. The displayed entries correspond to the symmetry inequivalent $D_{3126}$, $D_{4127}$ and $D_{5128}$ isomers, see Fig. 7.11. The values of the total sums in the table correspond to all nine isomers. Values of the $C_{helicity}$ with a magnitude of less than $10^{-5}$ are considered insignificant

*F-ethane*

| *Isomer* | $\{C_\sigma, F_\sigma, A_\sigma\}$ | $C_{helicity}[C_\sigma,A_\sigma]$ |
|---|---|---|
| $D_{3126}$ | $\{-0.000014[\mathbf{R}_\sigma], -0.000002[\mathbf{R}_\sigma], -0.000022[\mathbf{R}_\sigma]\}$ | 0 $[\mathbf{Q}_\sigma]$ |
| $D_{4127}$ | $\{0.235443[\mathbf{S}_\sigma], -0.291961[\mathbf{R}_\sigma], -0.001050[\mathbf{R}_\sigma]\}$ | 0.0002 $[\mathbf{S}_\sigma,\mathbf{R}_\sigma]$ |
| $D_{5128}$ | $\{-0.235470[\mathbf{R}_\sigma], 0.291163[\mathbf{S}_\sigma], 0.001052[\mathbf{S}_\sigma]\}$ | $-0.0002$ $[\mathbf{R}_\sigma,\mathbf{S}_\sigma]$ |

| *Sum of the $\boldsymbol{S}_\sigma$ subset from all nine isomers* | *Sum of the $\boldsymbol{R}_\sigma$ subset from all nine isomers* |
|---|---|
| $\sum_{S\sigma}\{C_\sigma,A_\sigma\}$ $\{0.6141[\mathbf{S}_\sigma], 0.0192[\mathbf{S}_\sigma]\}$ | $\sum_{R\sigma}\{C_\sigma,A_\sigma\}$ $\{-0.6141[\mathbf{R}_\sigma], -0.0193[\mathbf{R}_\sigma]\}$ |

*Total sum of all nine isomers*

| $\sum_{S\sigma,R\sigma}\{C_\sigma, F_\sigma, A_\sigma\}$ | $\sum C_{helicity}$ |
|---|---|
| $\{-0.00001[\mathbf{R}_\sigma], -0.0029[\mathbf{R}_\sigma], -0.00003[\mathbf{R}_\sigma]\}$ | 0 $[\mathbf{Q}_\sigma]$ |

*Cl-ethane*

| *Isomer* | $\{C_\sigma, F_\sigma, A_\sigma\}$ | $C_{helicity}$ $[C_\sigma,A_\sigma]$ |
|---|---|---|
| $D_{3126}$ | $\{-0.000001[\mathbf{R}_\sigma], -0.000009[\mathbf{R}_\sigma], 0.000006[\mathbf{S}_\sigma]\}$ | 0 $[\mathbf{Q}_\sigma]$ |
| $D_{4127}$ | $\{0.525440[\mathbf{S}_\sigma], -0.156354[\mathbf{R}_\sigma], -0.019219[\mathbf{R}_\sigma]\}$ | 0.0101 $[\mathbf{S}_\sigma,\mathbf{R}_\sigma]$ |
| $D_{5128}$ | $\{-0.525488[\mathbf{R}_\sigma], 0.156356[\mathbf{S}_\sigma], 0.019231[\mathbf{S}_\sigma]\}$ | $-0.0101$ $[\mathbf{R}_\sigma,\mathbf{S}_\sigma]$ |

| *Sum of the $\boldsymbol{S}_\sigma$ subset from all nine isomers* | *Sum of the $\boldsymbol{R}_\sigma$ subset from all nine isomers* |
|---|---|
| $\sum_{S\sigma}\{C_\sigma,A_\sigma\}$ $\{1.5282[\mathbf{S}_\sigma], 0.0498[\mathbf{S}_\sigma]\}$ | $\sum_{R\sigma}\{C_\sigma,A_\sigma\}$ $\{-1.5272[\mathbf{R}_\sigma], -0.0498[\mathbf{R}_\sigma]\}$ |

*Total sum of all nine isomers*

| $\sum_{S\sigma,R\sigma}\{C_\sigma, F_\sigma, A_\sigma\}$ | $\sum C_{helicity}$ |
|---|---|
| $\{0.0010[\mathbf{S}_\sigma], 0.0012[\mathbf{S}_\sigma], 0.000006[\mathbf{S}_\sigma]\}$ | 0 $[\mathbf{Q}_\sigma]$ |

*Br-ethane*

| *Isomer* | $\{C_\sigma, F_\sigma, A_\sigma\}$ | $C_{helicity}$ $[C_\sigma,A_\sigma]$ |
|---|---|---|
| $D_{3126}$ | $\{-0.000049[\mathbf{R}_\sigma], 0.000013[\mathbf{S}_\sigma], -0.000012[\mathbf{R}_\sigma]\}$ | 0 $[\mathbf{Q}_\sigma]$ |
| $D_{4127}$ | $\{0.540902[\mathbf{S}_\sigma], -0.166512[\mathbf{R}_\sigma], -0.028603[\mathbf{R}_\sigma]\}$ | 0.0155 $[\mathbf{S}_\sigma,\mathbf{R}_\sigma]$ |
| $D_{5128}$ | $\{-0.540781[\mathbf{R}_\sigma], 0.166429[\mathbf{S}_\sigma], 0.028581[\mathbf{S}_\sigma]\}$ | $-0.0155[\mathbf{R}_\sigma,\mathbf{S}_\sigma]$ |

| *Sum of the $\boldsymbol{S}_\sigma$ subset from all nine isomers* | *Sum of the $\boldsymbol{R}_\sigma$ subset from all nine isomers* |
|---|---|

(continued)

**Table 7.9** (continued)

| *F-ethane* | |
|---|---|
| $\sum_{\mathbf{S}\sigma}\{\mathsf{C}_\sigma,\mathsf{A}_\sigma\}$<br>$\{1.5918[\mathbf{S}_\sigma], 0.0820[\mathbf{S}_\sigma]\}$ | $\sum_{\mathbf{R}\sigma}\{\mathsf{C}_\sigma,\mathsf{A}_\sigma\}$<br>$\{-1.5917[\mathbf{R}_\sigma], -0.0820[\mathbf{R}_\sigma]\}$ |
| *Total sum of all nine isomers* | |
| $\sum_{\mathbf{S}\sigma,\mathbf{R}\sigma}\{\mathsf{C}_\sigma, \mathsf{F}_\sigma, \mathsf{A}_\sigma\}$<br>$\{0.00005[\mathbf{S}_\sigma], -0.0009[\mathbf{R}_\sigma], 0.000006[\mathbf{S}_\sigma]\}$ | $\sum \mathsf{C}_{helicity}$<br>$0\ [\mathbf{Q}_\sigma]$ |

equal in magnitude with the $\sum_{\mathbf{S}\sigma}\{\mathsf{C}_\sigma,\mathsf{A}_\sigma\}$ increasing with atomic number (F, Cl, Br). The strongest correlation was discovered for $\mathsf{A}_\sigma$.

Agreement with the CIP rules for the largest value of $\sum_{\mathbf{S}\sigma}\{\mathsf{C}_\sigma\}$ or $\sum_{\mathbf{R}\sigma}\{\mathsf{C}_\sigma\}$ for the doubly substituted ethane for the $S_a$ and $R_a$ geometric stereoisomers of the $S_a$ and $R_a$ stereoisomers, see Table 7.9. The stereoisomer characteristics in $\mathsf{U}_\sigma$-space are demonstrated by the sum over all nine isomers $\sum_{\mathbf{S}\sigma,\mathbf{R}\sigma}\{\mathsf{C}_\sigma, \mathsf{F}_\sigma, \mathsf{A}_\sigma\}$. This results in equal magnitudes of each of the $\mathsf{C}_\sigma$, $\mathsf{F}_\sigma$ and $\mathsf{A}_\sigma$, e.g. for the F-Cl ethane: $\mathsf{C}_\sigma = 0.901\ [\mathbf{S}_\sigma]$ and $-0.901[\mathbf{R}_\sigma]$ for the $S_a$ and $R_a$ geometric stereoisomers respectively. Therefore, the $S_a$ geometric stereoisomer is demonstrated to comprise a *mix* of chirality contributions, dominated by contributions from the $\mathbf{S}_\sigma$, with a sizable contribution with a $\mathbf{R}_\sigma$ chirality assignment, the converse being true for the $R_a$ geometric stereoisomer. This presence of a mix of $\mathbf{S}_\sigma$ and $\mathbf{R}_\sigma$ chirality for each of the $S_a$ and $R_a$ geometric stereoisomers is referred to as mixed chirality in $\mathsf{U}_\sigma$-space. The doubly substituted (chiral) ethane possessing the lowest mixed chirality in $\mathsf{U}_\sigma$-space is Cl-Br-ethane with $\sum_{\mathbf{S}\sigma}\{\mathsf{C}_\sigma\}/|\sum_{\mathbf{R}\sigma}\{\mathsf{C}_\sigma\}| \approx 12$, in contrast, both F-Br-ethane and Br-F-ethane possess $\sum_{\mathbf{S}\sigma}\{\mathsf{C}_\sigma\}/|\sum_{\mathbf{R}\sigma}\{\mathsf{C}_\sigma\}| \approx 2$.

The three singly substituted ethane molecular graphs comprised the $\mathbf{Q}_\sigma$ (the 'null' chirality assignment) along with $\mathbf{S}_\sigma$ and $\mathbf{R}_\sigma$ chirality $\mathsf{C}_\sigma$ assignments, but the total resultant contribution to $\sum \mathsf{C}_{helicity} = 0$ indicated an overall lack of chiral character in $\mathsf{U}_\sigma$-space. The bond-axiality $\mathsf{A}_\sigma$ was found to be much more responsive to the increase in atomic number of the singly substituted halogen than did the chirality $\mathsf{C}_\sigma$. The F atom substitution was found to significantly lower the chirality $\mathsf{C}_\sigma$ contributions compared with the Cl and Br that suggested that the presence of the very light F atom increased the achiral characteristics of doubly substituted ethane.

Examination of the doubly halogen (F, Cl and Br) substituted ethane demonstrates agreement with the CIP naming schemes for all the $S_a$ and $R_a$ geometric stereoisomers for the symmetry inequivalent $\mathsf{U}_\sigma$-space $\mathbf{S}_\sigma$ and $\mathbf{R}_\sigma$ chirality stereoisomers. An additional benefit provided by NG-QTAIM, compared with the CIP rules, is that we demonstrate there is a *mix* of $\mathbf{S}_\sigma$ and $\mathbf{R}_\sigma$ chirality for each of the $S_a$ and $R_a$ geometric stereoisomers.

On the basis of the lowest ratio for the $S_a$ geometric stereoisomer $\sum_{\mathbf{S}\sigma}\{\mathsf{C}_\sigma/|\sum_{\mathbf{R}\sigma}\{\mathsf{C}_\sigma\}|\}$, it was demonstrated that the F containing doubly halogen substituted stereoisomers in $\mathsf{U}_\sigma$-space are the most achiral. This is due to the very

**Table 7.10** The doubly substituted ethane torsion C1-C2 *BCP* $\mathsf{U}_\sigma$-space distortion sets $\{\mathsf{C}_\sigma, \mathsf{F}_\sigma, \mathsf{A}_\sigma\}$ and the $\mathsf{U}_\sigma$-space achirality ratio $\sum_{\mathbf{S}\sigma}\{\mathsf{C}_\sigma\}/|\sum_{\mathbf{R}\sigma}\{\mathsf{C}_\sigma\}|$. Refer to the caption of Table 7.9 for further details. Note that $S_a$ and $R_a$ correspond to the geometric stereoisomers, see Fig. 7.11. The values of the total sums in the table correspond to all nine isomers

| *F-Cl-ethane* | | | | |
|---|---|---|---|---|
| | $S_a$ | | $R_a$ | |
| *Isomer* | $\{\mathsf{C}_\sigma, \mathsf{F}_\sigma, \mathsf{A}_\sigma\}$ | $\mathsf{C}_{helicity}$ $[\mathsf{C}_\sigma,\mathsf{A}_\sigma]$ | $\{\mathsf{C}_\sigma, \mathsf{F}_\sigma, \mathsf{A}_\sigma\}$ | $\mathsf{C}_{helicity}$ $[\mathsf{C}_\sigma,\mathsf{A}_\sigma]$ |
| $D_{3126}$<br>$D_{4127}$<br>$D_{5128}$ | $\{0.142058[\mathbf{S}_\sigma], 0.098417[\mathbf{S}_\sigma], 0.023993[\mathbf{S}_\sigma]\}$<br>$\{0.532049[\mathbf{S}_\sigma], 0.095174[\mathbf{S}_\sigma], -0.032489[\mathbf{R}_\sigma]\}$<br>$0.362224[\mathbf{R}_\sigma], -0.574683[\mathbf{R}_\sigma], 0.02396[\mathbf{S}_\sigma]\}$ | $0.0034$ $[\mathbf{S}_\sigma,\mathbf{S}_\sigma]$<br>$0.0173$ $[\mathbf{S}_\sigma,\mathbf{R}_\sigma]$<br>$-0.0087[\mathbf{R}_\sigma,\mathbf{S}_\sigma]$ | $\{-0.142118[\mathbf{R}_\sigma], -0.099095[\mathbf{R}_\sigma], -0.023983[\mathbf{R}_\sigma]\}$<br>$\{0.362047[\mathbf{S}_\sigma], 0.574724[\mathbf{S}_\sigma], -0.023964[\mathbf{R}_\sigma]\}$<br>$\{-0.532089[\mathbf{R}_\sigma], -0.095057[\mathbf{R}_\sigma], 0.032494[\mathbf{S}_\sigma]\}$ | $-0.0034$ $[\mathbf{R}_\sigma,\mathbf{R}_\sigma]$<br>$0.0087$ $[\mathbf{S}_\sigma,\mathbf{R}_\sigma]$<br>$-0.0173$ $[\mathbf{R}_\sigma,\mathbf{S}_\sigma]$ |
| *Total sum of all nine isomers of* $S_a$ | | | *Total sum of all nine isomers of* $R_a$ | |
| $\sum_{\mathbf{S}\sigma,\mathbf{R}\sigma}\{\mathsf{C}_\sigma, \mathsf{F}_\sigma, \mathsf{A}_\sigma\}$<br>$\{0.9008$ $[\mathbf{S}_\sigma]$, $-1.1910$ $[\mathbf{R}_\sigma]$, $0.0585$ $[\mathbf{S}_\sigma]\}$ | | $\sum \mathsf{C}_{helicity}$<br>$0.0340$ $[\mathbf{S}_\sigma,\mathbf{S}_\sigma]$ | $\sum_{\mathbf{S}\sigma,\mathbf{R}\sigma}\{\mathsf{C}_\sigma, \mathsf{F}_\sigma, \mathsf{A}_\sigma\}$<br>$\{-0.9006$ $[\mathbf{R}_\sigma]$, $1.1898$ $[\mathbf{S}_\sigma]$, $-0.0589$ $[\mathbf{R}_\sigma]\}$ | $\sum \mathsf{C}_{helicity}$<br>$-0.0342$ $[\mathbf{R}_\sigma,\mathbf{R}_\sigma]$ |
| *Sum of the* $\boldsymbol{S}_\sigma$, $\boldsymbol{R}_\sigma$ *subsets from all nine* $S_a$ *isomers* | | | *Sum of the* $\boldsymbol{S}_\sigma$, $\boldsymbol{R}_\sigma$ *subsets from all nine* $R_a$ *isomers* | |
| $\sum_{\mathbf{S}\sigma}\{\mathsf{C}_\sigma,\mathsf{A}_\sigma\}$<br>$\{1.8984$ $[\mathbf{S}_\sigma]$, $0.1597$ $[\mathbf{S}_\sigma]\}$ | | $\sum_{\mathbf{R}\sigma}\{\mathsf{C}_\sigma,\mathsf{A}_\sigma\}$<br>$\{-0.9977$ $[\mathbf{R}_\sigma]$, $-0.1013$ $[\mathbf{R}_\sigma]\}$ | $\sum_{\mathbf{S}\sigma}\{\mathsf{C}_\sigma,\mathsf{A}_\sigma\}$<br>$\{0.9984$ $[\mathbf{S}_\sigma]$, $0.1013$ $[\mathbf{S}_\sigma]\}$ | $\sum_{\mathbf{R}\sigma}\{\mathsf{C}_\sigma,\mathsf{A}_\sigma\}$<br>$\{-1.8989$ $[\mathbf{R}_\sigma]$, $-0.1602$ $[\mathbf{R}_\sigma]\}$ |

(continued)

**Table 7.10** (continued)

| *Ratio of the $S_\sigma$ and $R_\sigma$ subsets from all nine $S_a$ isomers* | | | | |
|---|---|---|---|---|
| $\sum_{S\sigma}\{C_\sigma\}/\|\sum_{R\sigma}\{C_\sigma\}\|\}\|S_a = 1.9028$ | | | | |
| *Cl-Br-ethane* | | | | |
| *Isomer* | $\{C_\sigma, F_\sigma, A_\sigma\}$ | $C_{helicity}[C_\sigma,A_\sigma]$ | $\{C_\sigma, F_\sigma, A_\sigma\}\ C_{helicity}$ | $[C_\sigma,A_\sigma]$ |
| $D_{3126}$<br>$D_{4127}$<br>$D_{5128}$ | {0.142347**[$S_\sigma$]**, −0.126939**[$R_\sigma$]**, 0.030052**[$S_\sigma$]**}<br>{0.804689**[$S_\sigma$]**, 0.410931**[$S_\sigma$]**, −0.050652**[$R_\sigma$]**}<br>{−0.113693**[$R_\sigma$]**, −0.315810**[$R_\sigma$]**, 0.003891**[$S_\sigma$]**} | 0.0043**[$S_\sigma$,$S_\sigma$]**<br>0.0408**[$S_\sigma$,$R_\sigma$]**<br>−0.000**[$R_\sigma$,$S_\sigma$]** | {−0.142405**[$R_\sigma$]**, 0.125579**[$S_\sigma$]**, −0.030034**[$R_\sigma$]**}<br>{0.114210**[$S_\sigma$]**, 0.315839**[$S_\sigma$]**, −0.004005**[$R_\sigma$]**}<br>{−0.804516**[$R_\sigma$]**, −0.410188**[$R_\sigma$]**, 0.050681**[$S_\sigma$]**} | −0.0043 **[$R_\sigma$,$R_\sigma$]**<br>0.0005 **[$S_\sigma$,$R_\sigma$]**<br>−0.0408 **[$R_\sigma$,$S_\sigma$]** |
| *Total sum of all nine isomers of $S_a$* | | | *Total sum of all nine isomers of $R_a$* | |
| $\sum_{S\sigma,R\sigma}\{C_\sigma, F_\sigma, A_\sigma\}$<br>{2.2161 **[$S_\sigma$]**, −0.0656 **[$R_\sigma$]**, −0.0504 **[$R_\sigma$]**} | | $\sum C_{helicity}$<br>0.1239 **[$S_\sigma$,$R_\sigma$]** | $\sum_{S\sigma,R\sigma}\{C_\sigma, F_\sigma, A_\sigma\}$<br>{−2.2173 **[$R_\sigma$]**, 0.0646 **[$S_\sigma$]**, 0.0504 **[$S_\sigma$]**} | $\sum C_{helicity}$<br>−0.1239 **[$R_\sigma$,$S_\sigma$]** |
| *Sum of the $S_\sigma$, $R_\sigma$ subsets from all nine $S_a$ isomers* | | | *Sum of the $S_\sigma$, $R_\sigma$ subsets from all nine $R_a$ isomers* | |
| $\sum_{S\sigma}\{C_\sigma,A_\sigma\}$<br>{2.4135 **[$S_\sigma$]**, 0.1184 **[$S_\sigma$]**} | | $\sum_{R\sigma}\{C_\sigma,A_\sigma\}$<br>{−0.1973 **[$R_\sigma$]**, −0.1688 **[$R_\sigma$]**} | $\sum_{S\sigma}\{C_\sigma,A_\sigma\}$<br>{0.1973 **[$S_\sigma$]**, 0.1688 **[$S_\sigma$]**} | $\sum_{R\sigma}\{C_\sigma,A_\sigma\}$<br>{−2.4146 **[$R_\sigma$]**, −0.1185 **[$R_\sigma$]**} |

(continued)

**Table 7.10** (continued)

| *Ratio of the $\boldsymbol{S_\sigma}$ and $\boldsymbol{R_\sigma}$ subsets from all nine $S_a$ isomers* | | | | |
|---|---|---|---|---|
| $\sum_{S\sigma}\{C_\sigma\}/\|\sum_{R\sigma}\{C_\sigma\}\|\|S_a = 12.2326$ | | | | |
| *Br-F-ethane* | | | | |
| *Isomer* | $\{C_\sigma, F_\sigma, A_\sigma\}$ | $C_{helicity}$ $[C_\sigma,A_\sigma]$ | $\{C_\sigma, F_\sigma, A_\sigma\}$ | $C_{helicity}[C_\sigma,A_\sigma]$ |
| $D_{3126}$<br>$D_{4127}$<br>$D_{5128}$ | {0.186670**[$\mathbf{S_\sigma}$]**, 0.033778**[$\mathbf{S_\sigma}$]**, 0.024561**[$\mathbf{S_\sigma}$]**}<br>{0.445947**[$\mathbf{S_\sigma}$]**, 0.187811**[$\mathbf{S_\sigma}$]**, −0.042255**[$\mathbf{R_\sigma}$]**}<br>{−0.329263**[$\mathbf{R_\sigma}$]**, −0.653104**[$\mathbf{R_\sigma}$]**, 0.025360**[$\mathbf{S_\sigma}$]**} | 0.0046**[$\mathbf{S_\sigma}$,$\mathbf{S_\sigma}$]**<br>0.0188**[$\mathbf{S_\sigma}$,$\mathbf{R_\sigma}$]**<br>−0.008**[$\mathbf{R_\sigma}$,$\mathbf{S_\sigma}$]** | {−0.186563**[$\mathbf{R_\sigma}$]**, −0.033845**[$\mathbf{R_\sigma}$]**, −0.024561**[$\mathbf{R_\sigma}$]**}<br>{0.328508**[$\mathbf{S_\sigma}$]**, 0.653119**[$\mathbf{S_\sigma}$]**, −0.025453**[$\mathbf{R_\sigma}$]**}<br>{−0.445767**[$\mathbf{R_\sigma}$]**, −0.187671**[$\mathbf{R_\sigma}$]**, 0.042154**[$\mathbf{S_\sigma}$]**} | −0.0046**[$\mathbf{R_\sigma}$,$\mathbf{R_\sigma}$]**<br>0.0084**[$\mathbf{S_\sigma}$,$\mathbf{R_\sigma}$]**<br>−0.0188 **[$\mathbf{R_\sigma}$,$\mathbf{S_\sigma}$]** |
| *Total sum of all nine isomers of $S_a$* | | | *Total sum of all nine isomers of $R_a$* | |
| $\sum_{S\sigma,R\sigma}\{C_\sigma, F_\sigma, A_\sigma\}$<br>{0.8728 **[$\mathbf{S_\sigma}$]**, −1.4535 **[$\mathbf{R_\sigma}$]**, 0.0332 **[$\mathbf{S_\sigma}$]**} | | $\sum C_{helicity}$<br>0.0431 **[$\mathbf{S_\sigma}$,$\mathbf{S_\sigma}$]** | $\sum_{S\sigma,R\sigma}\{C_\sigma, F_\sigma, A_\sigma\}$<br>{−0.8729 **[$\mathbf{R_\sigma}$]**, 1.4542 **[$\mathbf{S_\sigma}$]**, −0.0334 **[$\mathbf{R_\sigma}$]**} | $\sum C_{helicity}$<br>−0.0430 **[$\mathbf{R_\sigma}$,$\mathbf{R_\sigma}$]** |
| *Sum of the $\boldsymbol{S_\sigma}$, $\boldsymbol{R_\sigma}$ subsets from all nine $S_a$ isomers* | | | *Sum of the $\boldsymbol{S_\sigma}$, $\boldsymbol{R_\sigma}$ subsets from all nine $R_a$ isomers* | |
| $\sum_{S\sigma}\{C_\sigma,A_\sigma\}$<br>{1.6984 **[$\mathbf{S_\sigma}$]**, 0.1672 **[$\mathbf{S_\sigma}$]**} | | $\sum_{R\sigma}\{C_\sigma,A_\sigma\}$<br>{−0.8256 **[$\mathbf{R_\sigma}$]**, −0.1340 **[$\mathbf{R_\sigma}$]**} | $\sum_{S\sigma}\{C_\sigma,A_\sigma\}$<br>{0.8255 **[$\mathbf{S_\sigma}$]**, 0.1339 **[$\mathbf{S_\sigma}$]**} | $\sum_{R\sigma}\{C_\sigma,A_\sigma\}$<br>{−1.6984 **[$\mathbf{R_\sigma}$]**, −0.1673 **[$\mathbf{R_\sigma}$]**} |
| *Ratio of the $\boldsymbol{S_\sigma}$ and $\boldsymbol{R_\sigma}$ subsets from all nine $S_a$ isomers* | | | | |
| $\sum_{S\sigma}\{C_\sigma\}/\|\sum_{R\sigma}\{C_\sigma\}\|\|S_a = 2.0572$ | | | | |

light F atom, which is much closer to the atomic weight of the hydrogen atom of the singly substituted ethane than Cl or Br, is responsible for the higher degree of achiral character present for the F-Cl-ethane and Br-F-ethane. This result is consistent with the results from the singly (F) substituted ethane.

Future work on the nature of chirality could be undertaken using $\mathsf{T}_\sigma(s)$ constructed from all possible torsion *BCP*s associated with any potential chiral center. Further exploration of the newly discovered mixed chirality of stereoisomers in $\mathsf{U}_\sigma$-space could be undertaken by manipulating the degree of chiral/achiral character in $\mathsf{U}_\sigma$-space with applied electric fields. For example, a chiral molecule could be subjected to an applied **E**-field to explore the extent to which achiral character can be increased.

### 7.4.3 *Controlling Achiral and Chiral Properties of Alanine with an Electric Field*

We undertook an NG-QTAIM investigation of the effect of an electric field on the $S_a$ and $R_a$ geometric stereoisomers of alanine [35], see Fig. 7.13.

We used the spanning stress tensor trajectories $\mathsf{T}_\sigma(s)$ to sample the relative ease of motion of the electronic charge density $\rho(\mathbf{r_b})$ using the least ($\mathbf{e_{2\sigma}}$) and most ($\mathbf{e_{1\sigma}}$) preferred stress tensor eigenvectors sampled by subjecting the bond critical point (*BCP*) of alanine's Cα-C(methyl) bond onto torsions around this bond, see Fig. 7.14.

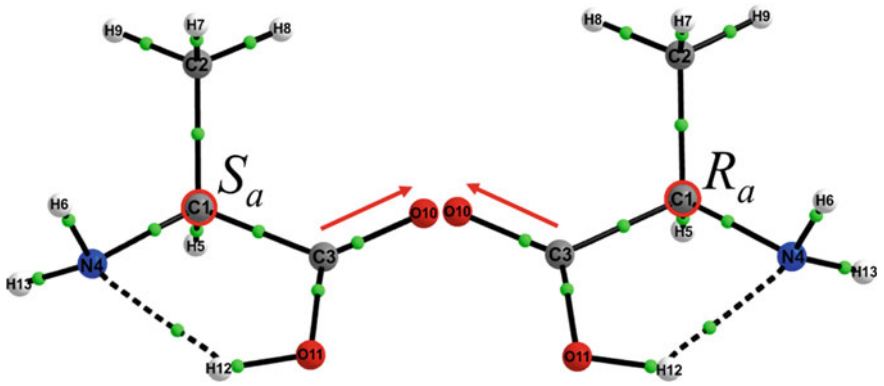


**Fig. 7.13** Molecular graphs of the $S_a$ stereoisomer (left panel) and $R_a$ stereoisomer (right panel) of alanine. The green spheres indicate the bond critical points (*BCP*s). The red arrows indicate directions of the positive (+**E**)-field along the C3 → O10 *BCP* bond-path and negative (−**E**)-field along the C3 ← O10 *BCP* bond-path. The C3, N4 and H5 atoms are bonded to the C1 atom and the H6, H7 and H8 atoms are bonded to the C2 atom. Numbered atoms in black define the dihedral angles {(3127, 3128, 3129), (4127, 4128, 4129), (5127, 5128, 5129)} used to construct the spanning stress tensor trajectory $\mathsf{T}_\sigma(s)$

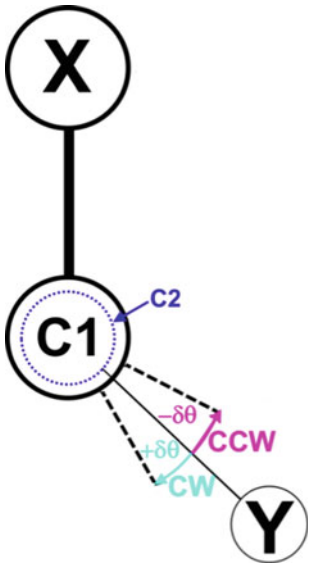


**Fig. 7.14** Definition of clockwise (CW) and counter-clockwise (CCW) directions of torsion using the conventional geometric dihedral angle θ defined by the sequence of atoms X sequentially further away from the viewing plane perpendicular to the C1-C2 direction, with atom X closest to the viewer and in the "12 o'clock" position. A negative step (−δθ) in the dihedral angle θ corresponds to C2---Y rotating in a CCW direction in the viewing plane; conversely a positive step (+δθ) in the dihedral angle θ corresponds to C2---Y rotating in a CW direction in the viewing plane

We found agreement with the CIP rules and consistency with earlier work that only used a single dihedral angle to construct the $\mathsf{T}_{\sigma}(s)$. The spanning $\mathsf{T}_{\sigma}(s)$ use all of the possible nine dihedral angles in its construction and as a result detected the presence of up to 7% mixing of the $\mathbf{S}_{\sigma}$ and $\mathbf{R}_{\sigma}$ chirality $\mathsf{C}_{\sigma}$ assignments in the electric field, which indicated the presence of up to 7% achiral character [36], see Table 7.11. In the absence of the electric field 2% achiral character was discovered. The electric field roughly doubled the magnitude of the chirality-helicity function $\mathsf{C}_{helicity}$, the NG-QTAIM interpretation of chirality, due to the very strong interaction of the electric field with the torsion *BCP*. In all cases the electric field reduced the bond-flexing $\mathsf{F}_{\sigma}$ associated with bond strain, which indicated a protective effect. See Fig. 7.15 and Table 7.12

Future investigations could be undertaken to manipulate chirality in $\mathsf{U}_{\sigma}$-space whilst monitoring the potentially damaging effect of bond-flexing $\mathsf{F}_{\sigma}$ with laser irradiation fast enough to avoid disrupting atomic positions.

**Table 7.11** The variation of the total $\mathsf{U}_{\sigma}$-space distortion sets $\sum\{\text{chirality } \mathsf{C}_{\sigma}, \text{bond-flexing } \mathsf{F}_{\sigma}, \text{bond-axiality } \mathsf{A}_{\sigma}\}$ with **E**-field of the $\mathbf{S}_{\sigma}$ and $\mathbf{R}_{\sigma}$ components for the $S_{\mathrm{a}}$ and $R_{\mathrm{a}}$ geometric stereoisomers, also see Fig. 7.13. The sums of the corresponding mixing ratios are defined as $\mathsf{C}_{\sigma mixing} = \sum_{\mathbf{S}\sigma}\{\mathsf{C}_{\sigma}\}/|\sum_{\mathbf{R}\sigma}\{\mathsf{C}_{\sigma}\}|$, $\mathsf{F}_{\sigma mixing} = \sum_{\mathbf{S}\sigma}\{\mathsf{F}_{\sigma}\}/|\sum_{\mathbf{R}\sigma}\{\mathsf{F}_{\sigma}\}|$ and $\mathsf{A}_{\sigma mixing} = \sum_{\mathbf{S}\sigma}\{\mathsf{A}_{\sigma}\}/|\sum_{\mathbf{R}\sigma}\{\mathsf{A}_{\sigma}\}|$

| | $S_{\mathrm{a}}$ | $R_{\mathrm{a}}$ | | | |
|---|---|---|---|---|---|
| **(±)E-field** $\times 10^{-4}$ au | $\sum\{\mathsf{C}_{\sigma}, \mathsf{F}_{\sigma}, \mathsf{A}_{\sigma}\}$ | $\sum\{\mathsf{C}_{\sigma}, \mathsf{F}_{\sigma}, \mathsf{A}_{\sigma}\}$ | $\mathsf{C}_{\sigma mixing}$ | $\mathsf{F}_{\sigma mixing}$ | $\mathsf{A}_{\sigma mixing}$ |
| **0** | $\{4.1229[\mathbf{S}_{\sigma}], -4.0252[\mathbf{R}_{\sigma}], -0.2815[\mathbf{R}_{\sigma}]\}$ | $\{-4.1230[\mathbf{R}_{\sigma}], 4.0254[\mathbf{S}_{\sigma}], 0.2792[\mathbf{S}_{\sigma}]\}$ | 0.0226 | 0.0000 | 0.0000 |
| **−25** | $\{2.9650[\mathbf{S}_{\sigma}], -2.6204[\mathbf{R}_{\sigma}], -0.4810[\mathbf{R}_{\sigma}]\}$ | $\{-2.9635[\mathbf{R}_{\sigma}], 2.6176[\mathbf{S}_{\sigma}], 0.4815[\mathbf{S}_{\sigma}]\}$ | 0.0000 | 0.0507 | 0.0000 |
| **−50** | $\{3.2299[\mathbf{S}_{\sigma}], -0.9131[\mathbf{R}_{\sigma}], -0.4853[\mathbf{R}_{\sigma}]\}$ | $\{-3.2299[\mathbf{R}_{\sigma}], 0.9131[\mathbf{S}_{\sigma}], 0.4855[\mathbf{S}_{\sigma}]\}$ | 0.0671 | 0.2927 | 0.0000 |
| **−100** | $\{3.0467[\mathbf{S}_{\sigma}], -1.2629[\mathbf{R}_{\sigma}], -0.4664[\mathbf{R}_{\sigma}]\}$ | $\{-3.0464[\mathbf{R}_{\sigma}], 1.2629[\mathbf{S}_{\sigma}], 0.4660[\mathbf{S}_{\sigma}]\}$ | 0.0697 | 0.1654 | 0.0000 |
| **+25** | $\{3.3800[\mathbf{S}_{\sigma}], -2.5347[\mathbf{R}_{\sigma}], -0.4756[\mathbf{R}_{\sigma}]\}$ | $\{-3.3812[\mathbf{R}_{\sigma}], 2.5328[\mathbf{S}_{\sigma}], 0.4752[\mathbf{S}_{\sigma}]\}$ | 0.0000 | 0.0619 | 0.0000 |
| **+50** | $\{3.8112[\mathbf{S}_{\sigma}], -1.0034[\mathbf{R}_{\sigma}], -0.5104[\mathbf{R}_{\sigma}]\}$ | $\{-3.8113[\mathbf{R}_{\sigma}], 1.0036[\mathbf{S}_{\sigma}], 0.5108[\mathbf{S}_{\sigma}]\}$ | 0.0387 | 0.2947 | 0.0000 |
| **+100** | $\{4.3111[\mathbf{S}_{\sigma}], -0.9069[\mathbf{R}_{\sigma}], -0.5638[\mathbf{R}_{\sigma}]\}$ | $\{-4.3111[\mathbf{R}_{\sigma}], 0.9071[\mathbf{S}_{\sigma}], 0.5642[\mathbf{S}_{\sigma}]\}$ | 0.0202 | 0.3232 | 0.0000 |

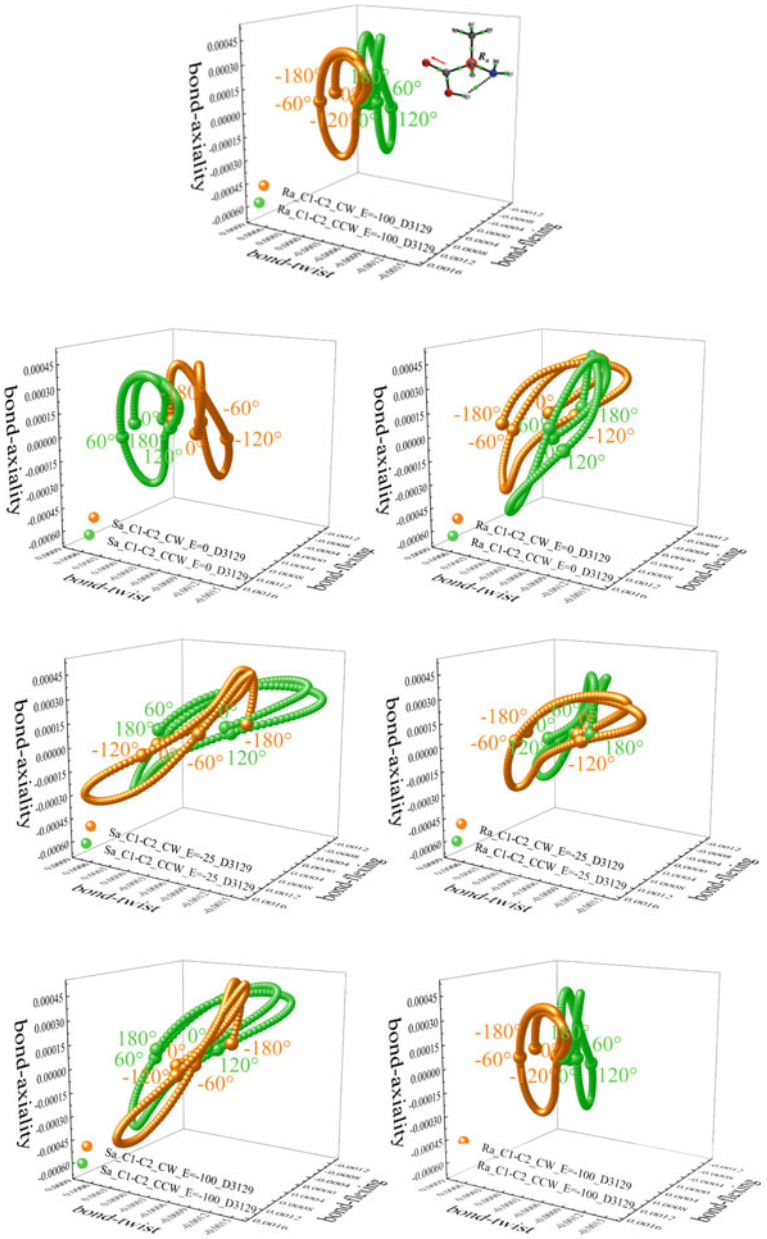


**Fig. 7.15** The stress tensor trajectory $\mathsf{T}_{\boldsymbol{\sigma}}(\boldsymbol{s})$ of the torsional C1-C2 *BCP* for the CW ($-90.0^{\circ} \leq \theta \leq 0.0^{\circ}$) and CCW ($0.0^{\circ} \leq \theta \leq +90.0^{\circ}$) directions for the electric (**E**)-field = 0 (top-panel). The $\mathsf{T}_{\boldsymbol{\sigma}}(\boldsymbol{s})$ of the $S_a$ and $R_a$ stereoisomers for an **E**-field $= -25.0 \times 10^{-4}$ au (middle-panel) and the corresponding $\mathsf{T}_{\boldsymbol{\sigma}}(\boldsymbol{s})$ for an **E**-field $= -100.0 \times 10^{-4}$ au (bottom-panel). The degree markers for the torsion θ are indicated at steps of 30.0°. All $\mathsf{T}_{\boldsymbol{\sigma}}(\boldsymbol{s})$ are shown for the C3-C1-C2-H9 dihedral angle, see Fig. 7.13

**Table 7.12** The variation of the chirality $C_\sigma$, bond-flexing $F_\sigma$ and bond-axiality $A_\sigma$ with ±**E**-field specified by the ratios $C_{\sigma E} = \sum C_\sigma / \sum C_\sigma|_{E=0}$, $F_{\sigma E} = \sum F_\sigma / \sum F_\sigma|_{E=0}$ and $A_{\sigma E} = \sum A_\sigma / \sum A_\sigma|_{E=0}$ of the $S_a$ and $R_a$ stereoisomers of alanine

| | $S_a$ | | | $R_a$ | | | $C_{helicityE}$ |
|---|---|---|---|---|---|---|---|
| **(±)E-field** $\times 10^{-4}$ au | $C_{\sigma E}$ | $F_{\sigma E}$ | $A_{\sigma E}$ | $C_{\sigma E}$ | $F_{\sigma E}$ | $A_{\sigma E}$ | |
| **−25** | 0.7192 | 0.6510 | 1.7087 | 0.7188 | 0.6503 | 1.7246 | 1.2291 |
| **−50** | 0.7834 | 0.2268 | 1.7240 | 0.7834 | 0.2268 | 1.7389 | 1.3509 |
| **−100** | 0.7390 | 0.3137 | 1.6568 | 0.7389 | 0.3137 | 1.6691 | 1.2245 |
| **+25** | 0.8198 | 0.6297 | 1.6895 | 0.8201 | 0.6292 | 1.7020 | 1.3852 |
| **+50** | 0.9244 | 0.2493 | 1.8131 | 0.9244 | 0.2493 | 1.8295 | 1.6764 |
| **+100** | 1.0456 | 0.2253 | 2.0028 | 1.0456 | 0.2253 | 2.0208 | 2.0947 |

The chirality-helicity function $\sum C_{helicity}$ is presented for the $S_a$ stereoisomer. The $C_{helicityE}$ is defined by the product $C_{\sigma E}|A_{\sigma E}|$ where the value of $\sum C_{helicityE=0} = 1.1604$, i.e. in the absence of an **E**-field

### 7.4.4 *Explanation of Why the* Cis*-Effect is the Exception and Not the Rule*

The molecules of this recent investigation were all formally achiral according to the Cahn–Ingold–Prelog (CIP) priority rules, but all comprised at some degree of chiral character in $U_\sigma$ space. This finding reflected the conventional understanding that steric effects are among the reasons for the differences between the relative energetic stabilities of *cis*- and *trans*-isomers, consistent with our previous association of chiral character in $U_\sigma$ space for the steric effects for ethane, see Sect. 7.4.2.

Here we explain the reasons for our earlier scalar QTAIM findings [37] that determined the *cis*-effect related to C1-C2 or N1-N2 bond-bending [38]. This was undertaken with doubly halogen substituted (F, Cl) ethene and diazene where unsubstituted ethene is included as a control and we found that $C_2X_2$ and $N_2X_2$ (X = F, Cl) displayed the *cis*-effect, see Figs. 7.16 and 7.17.

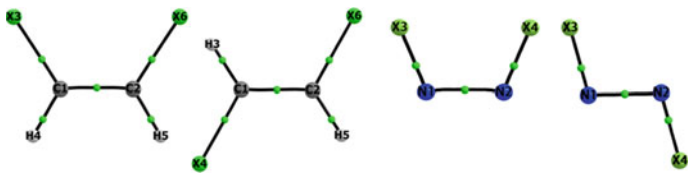


**Fig. 7.16** In-plane views of the *cis*- and *trans*-isomers for substitutions of the ethene (left panel) and diazene (right panel) molecular graphs, where X3 = X6 = H, F, Cl. The atomic numbering scheme of the four substituted ethene isomers for the *cis*- (X3-C1-C2-X6, X3-C1-C2-H5, H4-C1-C2-H5, H4-C1-C2-X6) and *trans*-isomers (X4-C1-C2-X6, X4-C1-C2-H5, H3-C1-C2-H5, H3-C1-C2-X6). The dihedral X3-N1-N2-X4 is used for the *cis*- and *trans*-isomers of the diazenes. The undecorated green spheres indicate the locations of the bond critical points (*BCP*s)

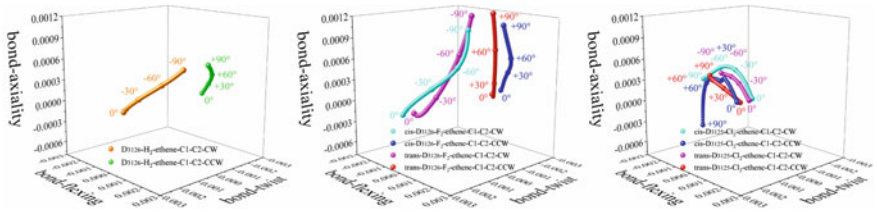


**Fig. 7.17** The torsion C1-C2 *BCP* stress tensor trajectories $\mathsf{T}_{\boldsymbol{\sigma}}(\boldsymbol{s})$ for the Cartesian clockwise (CW) and counter-clockwise (CCW) torsion directions for the geometric *cis*- and *trans*-isomers of $H_2$-ethene (left-panel), $F_2$-ethene (middle-panel) and $Cl_2$-ethene (right-panel) see Table 7.1. Notice the markers at 30° intervals

The *cis*-effect is determined on the basis of the much larger values of the bond-flexing $\mathsf{F}_{\boldsymbol{\sigma}}$ for the *cis*- compared with the *trans*-isomer. We found agreement with existing experimental data and predicted that $N_2X_2$ (X = Cl),

for which experimental data is absent displayed the *cis*-effect, see Table 7.14. The explanation on the basis of physical intuition as to why the *cis*-effect is the exception rather than the rule is because it is more difficult to bend ($\mathsf{F}_{\boldsymbol{\sigma}}$) than to twist ($\mathsf{T}_{\boldsymbol{\sigma}}$) the C1-C2 *BCP* bond-path and N1-N2 *BCP* bond-path, see Tables 7.13 and 7.14.

The difference the difficulty in deforming the *cis*- or *trans*-isomers is explained by the bond-bend ($\mathsf{F}_{\boldsymbol{\sigma}}$) and bond-twist ($\mathsf{T}_{\boldsymbol{\sigma}}$) construction that used the least preferred $\mathbf{e}_{2\boldsymbol{\sigma}}$ and most preferred $\mathbf{e}_{1\boldsymbol{\sigma}}$ eigenvectors, respectively.

## 7.5 Summary

To date all chemical explanations of chirality are incomplete and stated only in terms of steric effects such as the eclipsing effect, the reason for this failure, we suggest, is due to the sole use of scalar measures. There have been no theoretical considerations of helicity and the relationship with chirality that include specific examples, apart from the conjectures and predictions by D. Z. Wang. Previously this was not possible as no scalar measure can capture the directional character of chirality and therefore can never locate the unknown chirality-helicity equivalence, see Table 7.15.

First generation stress tensor trajectories $\mathsf{T}_{\boldsymbol{\sigma}}(\boldsymbol{s})$ are able to differentiate S and R stereoisomers due to the location of the presence of chirality-helicity in the form of helical shaped $\mathsf{T}_{\boldsymbol{\sigma}}(\boldsymbol{s})$ and chiral character in geometrically chiral molecules. First generation $\mathsf{T}_{\boldsymbol{\sigma}}(\boldsymbol{s})$ however, are unable to quantify the chirality-helicity.

The Hessian of $\rho(\mathbf{r})$ trajectories $\mathsf{T}(\boldsymbol{s})$ are useful in chemical situations where qualitative agreement is sufficient, the benefits being the simplicity of QTAIM and direct correspondence with well-known chemical measures such as the ellipticity ε. The

**Table 7.13** The $U_\sigma$-space bond cross-section sets {bond-twist $T_\sigma$, bond-flexing $F_\sigma$} of the torsion C1-C2 *BCP*, and the sum $\sum\{T_\sigma,F_\sigma\}$, of ethene and the *cis*- and *trans*-isomers of doubly substituted ethene

| $\{T_\sigma, F_\sigma\}$ | |
|---|---|
| $H_2$ | |
| $D_{3125}$ $\{-0.00096[R_\sigma], 0.00023[S_\sigma]\}$<br>$D_{3126}$ $\{0.00003[S_\sigma], 0.00006[S_\sigma]\}$<br>$D_{4125}$ $\{0.00560[S_\sigma], 0.00013[S_\sigma]\}$<br>$D_{4126}$ $\{0.00017[S_\sigma], -0.00012[R_\sigma]\}$ | |
| $\sum\{T_\sigma, F_\sigma\}$ | |
| $\{0.00483\mathbf{[S_\sigma]}, 0.00030\mathbf{[S_\sigma]}\}$ | |
| *Cis-ethene* | *Trans-ethene* |
| $\{T_\sigma, F_\sigma\}$ | $\{T_\sigma, F_\sigma\}$ |
| $F_2$ | |
| $D_{3125}$ $\{0.00056[S_\sigma], -0.00190[R_\sigma]\}$ | $\{0.01731[R_\sigma], 0.00000[Q_\sigma]\}$ |
| $D_{3126}$ $\{-0.01339[R_\sigma], 0.00004[S_\sigma]\}$ | $\{0.00111[S_\sigma], 0.00026[S_\sigma]\}$ |
| $D_{4125}$ $\{0.00002[S_\sigma], -0.00149[R_\sigma]\}$ | $\{-0.00030[R_\sigma], 0.00028[S_\sigma]\}$ |
| $D_{4126}$ $\{0.00143[S_\sigma], -0.00158[R_\sigma]\}$ | $\{-0.00060[R_\sigma], -0.00011[R_\sigma]\}$ |
| $\sum\{T_\sigma, F_\sigma\}$ | $\sum\{T_\sigma, F_\sigma\}$ |
| $\{-0.01138[R_\sigma], -0.00493[R_\sigma]\}$ | $\{-0.01710[R_\sigma], 0.00043[S_\sigma]\}$ |
| $Cl_2$ | |
| $D_{3125}$ $\{0.14080[S_\sigma], 0.95259[S_\sigma]\}$ | $\{0.00009[S_\sigma], 0.00022[S_\sigma]\}$ |
| $D_{3126}$ $\{-0.00093[R_\sigma], 0.00088[S_\sigma]\}$ | $\{-0.40475[R_\sigma], 0.19420[S_\sigma]\}$ |
| $D_{4125}$ $\{-0.00093[R_\sigma], -0.00001[R_\sigma]\}$ | $\{0.00017[S_\sigma], -0.00091[R_\sigma]\}$ |
| $D_{4126}$ $\{-0.38727[R_\sigma], 0.11232[S_\sigma]\}$ | $\{0.00033[S_\sigma], 0.00001[S_\sigma]\}$ |
| $\sum\{T_\sigma, F_\sigma\}$ | $\sum\{T_\sigma, F_\sigma\}$ |
| $\{-0.24833[R_\sigma], 1.06578[S_\sigma]\}$ | $\{-0.40417[R_\sigma], 0.19351[S_\sigma]\}$ |

The atom numbering sequence for the dihedral angles used to construct the $T_\sigma(s)$ is indicated by the four-digit sequence (left column); see Fig. 7.16

**Table 7.14** The $U_\sigma$-space bond cross-section sets $\{T_\sigma, F_\sigma\}$ of the C1-C2 *BCP* for the doubly substituted diazene torsion

| *Cis*-diazene | *Trans*-diazene |
|---|---|
| $\{T_\sigma, F_\sigma\}$ | $\{T_\sigma, F_\sigma\}$ |
| $H_2$ | |
| $\{0.00812[S_\sigma], 0.00016[S_\sigma]\}$ | $\{-0.00176[R_\sigma]\}, \{0.00070[S_\sigma]\}$ |
| $F_2$ | |
| $\{-0.01077[R_\sigma], -0.00886[R_\sigma]\}$ | $\{0.00023[S_\sigma]\}, \{0.00014[S_\sigma]\}$ |
| $Cl_2$ | |
| $\{0.00020[S_\sigma], 0.00672[S_\sigma]\}$ | $\{-0.00022[R_\sigma]\}, \{-0.00402[R_\sigma]\}$ |

stress tensor $\mathsf{T}_{\sigma}(\boldsymbol{s})$, although more complex and abstract is preferred in situations where quantitative agreement with experiment is required.

Future avenues of investigation for the application of **E**-fields to chiral or formally achiral molecules could also follow on from the recent work of Ayuso et al., generating synthetic controllable chiral light for ultrafast imaging of chiral dynamics in gases, liquids and solids [39]. This can also be used to imprint chirality on achiral matter efficiently [40] and to provide insights into laser-driven achiral–chiral phase transitions in matter [41]. Our approach could open up a wide scientific field for chiral solid state and molecular systems to track and quantify the chirality for the first time, e.g. in a wide range of molecular devices including substituted dithienylethene photochromic switches [42], azobenzene chiroptical switches [43] and the design of chiral-optical molecular rotary motors [44].

Refinements of the first generation $\mathsf{T}_{\sigma}(\boldsymbol{s})$ again use the stress tensor projections $\mathsf{T}_{\sigma}(\boldsymbol{s})_{\mathbf{max}}$ to calculate the chirality $\mathsf{C}_{\sigma}$ from $t_1 = \underline{\mathbf{e}}_{\mathbf{1\sigma}}\cdot\mathbf{dr}$ but also consider the $t_2 = \underline{\mathbf{e}}_{\mathbf{2\sigma}}\cdot\mathbf{dr}$ (bond-flexing $\mathsf{F}_{\sigma}$) and $t_3 = \underline{\mathbf{e}}_{\mathbf{3\sigma}}\cdot\mathbf{dr}$ (bond-axiality $\mathsf{B}_{\sigma}$). Consequently it is possible to quantify the chirality-helicity in the form of the chirality-helicity function $\mathsf{C}_{helicity}$ and so can consider both achiral and chiral molecules.

Future work using the $\mathsf{C}_{helicity}$ could include application to chiral selectivity during a chemical reaction, in particular for the design of reactions with post-transition state bifurcations (PTSB) where an asynchronous nitrene insertion into C–C sigma bonds can be used to modulate the product sensitivity [45]. Also the determination of the $\mathsf{C}_{helicity}$ for molecules with multiple chiral centers: each dominant torsional bond associated with a separate chiral center would be considered independently. The requirement to constrain corresponding torsional dihedral angle, renders the possibility of treating multiple chiral centers independently due to the remaining relaxation of the atoms and molecular electronic density distribution to an energetic minimum in response. In future we expect, on the basis of the $\mathsf{C}_{helicity}$ values, that photoexcitation circular dichroism experiments can be used to detect the effects of chirality for the species of the formally achiral $S_N2$ reaction. Future applications could include chiral catalysis and the prediction of asymmetric synthetic reactions of all intermediates. Therefore, enabling the prediction of asymmetric synthetic reactions, which is one of the most fundamental problems in industrial organic and catalytic chemistry [12, 46]. In particular, we can in future characterize the heterotopicity in the addition/substitution of a chemical group to a planar molecule quantitatively in relation to the energetically favorable reaction pathway. This extension can be used to explain the reactivity towards both prochiral planes and helps one to understand the origin of the (homo-) chirality in the enantio-selective synthesis using catalysis. This approach, therefore, removes the requirement for the trial and error screening methods currently used for such reactions.

Future cumulene design strategies to maximize the helical response of the $\mathsf{T}_{\sigma}(\boldsymbol{s})$ could be to select end group substituents using the QTAIM interpreted *para*- Hammett

substituent constants on the basis of electron donating or electron withdrawing behaviors that include $SiH_3$, ZnCl, $COOCH_3$, $SO_2NH_2$, $SO_2OH$, COCl, $CB_3$, where to the authors best knowledge, no Hammett substituent constants are available [47].

Second generation $\mathsf{T}_\sigma(s)$ are constructed with all possible dihedral angles passing through the torsion bond involving the chiral or suspected chiral centre. The second generation $\mathsf{T}_\sigma(s)$ enables the explanation of the well-known steric effects of ethene subjected to a torsion as due to the presence of chiral character. In other words any the presence of true chiral character in formally achiral molecules can be differentiated from steric effects.

For achiral and chiral reactions, using second generation $\mathsf{T}_\sigma(s)$, the symmetry inequivalent set of isomers with $\mathbf{Q}_\sigma$, $\mathbf{S}_\sigma$ or $\mathbf{R}_\sigma$ chirality assignments could be kept separate and tracked for the duration of the reaction. So far, i.e. with ethane [34] and halogen substituted ethane [33] with second generation $\mathsf{T}_\sigma(\mathbf{s})$ it is possible using the chirality-helicity function $\mathsf{C}_{helicity}$ to define a formally achiral as achiral in $\mathsf{U}_\sigma$-space for $\mathsf{C}_{helicity} = 0$. Another potential application of **E**-fields would be in heterogeneous enantioselective catalysis that is usually achieved through adsorbing chiral molecules on a surface. Using molecules that are only chiral in the presence of an **E**-field allows the use of a much wider range of molecules and allows changing the chirality of the product by changing the direction of the **E**-field. Apart from catalysis, **E**-field or laser-field induced chirality could be used to grow chiral MOFs (metal organic frameworks) or other self-assembled structures on a surface.

The ability to track and control chirality could be used in asymmetric autocatalysis [46] or contribute to the design of enantioselective catalytic processes [48].

In Chap. 8 we provide the developments of NG-QTAIM for molecular devices design

**Target learning outcomes**:

- Understand the necessity for vector-based measures for chiral discrimination (Sect. 7.1).
- Understand the unknown helical character associated with chirality (Sect. 7.1.1).
- Relate helical character to inducing the sufficient symmetry breaking (Sect. 7.1.2).

**Table 7.15** The scalar QTAIM and stress tensor concepts that we have developed with the relevant references listed

| Vector-based | Definition | References |
|---|---|---|
| $\{\mathsf{C}_\sigma, \mathsf{F}_\sigma, \mathsf{A}_\sigma\}$ | $\mathsf{U}_\sigma$-space distortion set | [3, 14, 28] |
| $\mathsf{C}_\sigma = [(\underline{\mathbf{e}}_{1\sigma}\cdot\mathbf{dr})_{\max}]_{CCW} - [(\underline{\mathbf{e}}_{1\sigma}\cdot\mathbf{dr})_{\max}]_{CW}$ | Chirality | [11, 16] |
| $\mathsf{T}_\sigma = [(\underline{\mathbf{e}}_{1\sigma}\cdot\mathbf{dr})_{\max}]_{CCW} - [(\underline{\mathbf{e}}_{1\sigma}\cdot\mathbf{dr})_{\max}]_{CW}$ | Bond-twist | [11, 3, 14, 15, 33] |
| $\mathsf{F}_\sigma = [(\underline{\mathbf{e}}_{2\sigma}\cdot\mathbf{dr})_{\max}]_{CCW} - [(\underline{\mathbf{e}}_{2\sigma}\cdot\mathbf{dr})_{\max}]_{CW}$ | Bond-flexing | [14, 16] |
| $\mathsf{B}_\sigma = [(\underline{\mathbf{e}}_{3\sigma}\cdot\mathbf{dr})_{\max}]_{CCW} - [(\underline{\mathbf{e}}_{3\sigma}\cdot\mathbf{dr})_{\max}]_{CW}$ | Bond-axiality | [15] |
| $\mathsf{C}_{helicity}$ | $\mathsf{C}_\sigma\mathsf{B}_\sigma$ | [11, 31, 30, 33, 44] |

- Why the stress tensor trajectory $\mathsf{T}_{\sigma}(s)$ better than the Hessian of $\rho(\mathbf{r})$ trajectory $\mathsf{T}_{\rho}(s)$ for chiral discrimination (Sect. 7.2.1).
- Understand how to use the chirality-helicity function $\mathsf{C}_{helicity}$ to include formally achiral molecules (Sect. 7.2).
- Understand how to follow the chirality of chiral and achiral species in $\mathsf{U}_{\sigma}$-space without the CIP rules (Sect. 7.3).
- Understand construction of second generation stress tensor trajectories $\mathsf{T}_{\sigma}(s)$ and how they differ from first and the first generation $\mathsf{T}_{\sigma}(s)$ (Sect. 7.3).
- Understand the chiral and steric effects in ethane (Sect. 7.4.1).
- Understand the factors determining the mixed chiral and achiral character (Sect. 7.4.2).
- Understand the effect of a homogenous electric field on a chiral molecule (Sect. 7.4.3).
- Explained why the *cis*-effect is the exception and not the rule (Sect. 7.4.4).

## 7.6 Further Reading

The original Cahn-Ingold-Prelog (CIP) rules are provided along with updates [1, 2]. The work of Wang that proposed a 'helix theory for molecular chirality and chiral interaction' inspired us to better understand why chiral molecules tend to produce helical shaped trajectories [9]. Shaik et al. provides an overview of the effects and application of oriented external electric fields create absolute enantioselectivity in Diels–Alder reactions [26].

## References

1. Cahn RS, Ingold C, Prelog V (1966) Specification of molecular chirality. Angew Chem Int Ed Engl 5:385–415
2. Prelog V, Helmchen G (1982) Basic principles of the CIP-system and proposals for a revision. Angew Chem Int Ed Engl 21:567–583
3. Xu T, Kirk SR, Jenkins S (2020) A comparison of QTAIM and the stress tensor for chirality-helicity equivalence in S and R stereoisomers. Chem Phys Lett 738:136907
4. Fresnel A (1821) Mémoire sur la double réfraction. Mémoires de l'Académie des Sciences de l'Institut de France 7:45–176
5. Brewster JH (1974) On the helicity of variously twisted chains of atoms. In: Stereochemistry I. Springer, Berlin, pp 29–71. https://doi.org/10.1007/3-540-06648-9_8.
6. Rosenfeld L (1929) Quantenmechanische theorie der natürlichen optischen Aktivität von Flüssigkeiten und Gasen. Z Physik 52:161–174
7. Caldwell DJ, Eyring H, Chang TY (1972) The theory of optical activity. Phys Today 25:53
8. Tinoco I, Woody RW (1964) Optical rotation of oriented helices. IV. A free electron on a helix. J Chem Phys 40:160–165
9. Zhigang Wang D (2004) A helix theory for molecular chirality and chiral interaction. Mendeleev Commun 14:244–247

10. Beaulieu S, Comby A, Descamps D, Fabre B, Garcia GA, Géneaux R, Harvey AG, Légaré F, Mašín Z, Nahon L, Ordonez AF, Petit S, Pons B, Mairesse Y, Smirnova O, Blanchet V (2018) Photoexcitation circular dichroism in chiral molecules. Nat Phys 14:484–489
11. Xu T, Li JH, Momen R, Huang WJ, Kirk SR, Shigeta Y, Jenkins S (2019) Chirality-helicity equivalence in the S and R stereoisomers: a theoretical insight. J Am Chem Soc 141:5497–5503
12. Kondepudi DK, Asakura K (2001) Chiral autocatalysis, spontaneous symmetry breaking, and stochastic behavior. Acc Chem Res 34:946–954
13. Szarek P, Sueda Y, Tachibana A (2008) Electronic stress tensor description of chemical bonds using nonclassical bond order concept. J Chem Phys 129:094102
14. Li Z, Nie X, Xu T, Li S, Yang Y, Früchtl H, van Mourik T, Kirk SR, Paterson MJ, Shigeta Y, Jenkins S (2021) Control of chirality, bond flexing and anharmonicity in an electric field. Int J Quantum Chem 121:e26793
15. Tian T, Xu T, Kirk SR, Rongde IT, Tan YB, Manzhos S, Shigeta Y, Jenkins S (2020) Intramolecular mode coupling of the isotopomers of water: a non-scalar charge density-derived perspective. Phys Chem Chem Phys 22:2509–2520
16. Nie X, Yang Y, Xu T, Biczysko M, Kirk SR, Jenkins S (2022) The chirality of isotopomers of glycine compared using next-generation QTAIM. Int J Quantum Chem 122:e26917
17. Kawasaki T, Matsumura Y, Tsutsumi T, Suzuki K, Ito M, Soai K (2009) Asymmetric autocatalysis triggered by carbon isotope (13C/12C) chirality. Science 324:492–495
18. Burton AS, Berger EL (2018) Insights into abiotically-generated amino acid enantiomeric excesses found in meteorites. Life 8:14
19. Wolk JL, Hoz S (2014) Inducing chirality ex nihilo by an electric field. Can J Chem 93:459–462
20. Saenz A (2000) Enhanced ionization of molecular hydrogen in very strong fields. Phys Rev A 61:051402
21. Saenz A (2002) Behavior of molecular hydrogen exposed to strong dc, ac, or low-frequency laser fields. I. Bond softening and enhanced ionization. Phys Rev A 66:063407
22. Medin Z, Lai D (2006) Density-functional-theory calculations of matter in strong magnetic fields. II. Infinite chains and condensed matter. Phys Rev A 74:062508
23. Petretti S, Vanne YV, Saenz A, Castro A, Decleva P (2010) Alignment-dependent ionization of $N_2$, $O_2$, and $CO_2$ in intense laser fields. Phys Rev Lett 104:223001
24. Shaik S, Mandal D, Ramanan R (2016) Oriented electric fields as future smart reagents in chemistry. Nat Chem 8:1091–1098
25. Shaik S, Ramanan R, Danovich D, Mandal D (2018) Structure and reactivity/selectivity control by oriented-external electric fields. Chem Soc Rev 47:5125–5145
26. Wang Z, Danovich D, Ramanan R, Shaik S (2018) Oriented-external electric fields create absolute enantioselectivity in diels-alder reactions: importance of the molecular dipole moment. J Am Chem Soc 140:13350–13359
27. Ayuso D, Ordonez A, Decleva P, Ivanov M, Smirnova O (2020) Polarization of chirality. arXiv: 2004.05191 [physics].
28. Azizi A, Momen R, Früchtl H, van Mourik T, Kirk SR, Jenkins S (2020) Next-generation QTAIM for scoring molecular wires in E-fields for molecular electronic devices. J Comput Chem 41:913–921
29. Shaik S, Danovich D, Joy J, Wang Z, Stuyver T (2020) Electric-field mediated chemistry: uncovering and exploiting the potential of (oriented) electric fields to exert chemical catalysis and reaction control. J Am Chem Soc 142:12551–12562
30. Xing H, Azizi A, Momen R, Xu T, Kirk SR, Jenkins S (2022) Chirality–helicity of cumulenes: a non-scalar charge density derived perspective. Int J Quantum Chem 122:e26884
31. Xu T, Nie X, Li S, Yang Y, Früchtl H, Mourik T, Kirk SR, Paterson MJ, Shigeta Y, Jenkins S (2021) Chirality without stereoisomers: insight from the helical response of bond electrons. ChemPhysChem 22:1989–1995
32. Banerjee-Ghosh K, Ben Dor O, Tassinari F, Capua E, Yochelis S, Capua A, Yang S-H, Parkin SSP, Sarkar S, Kronik L, Baczewski LT, Naaman R, Paltiel Y (2018) Separation of enantiomers by their enantiospecific interaction with achiral magnetic substrates. Science 360:1331–1334

33. Li Z, Xu T, Früchtl H, van Mourik T, Kirk SR, Jenkins S (2022) Mixed chiral and achiral character in substituted ethane: a next generation QTAIM perspective. Chem Phys Lett 803:139762
34. Li Z, Xu T, Früchtl H, van Mourik T, Kirk SR, Jenkins S (2022) Chiral and steric effects in ethane: a next generation QTAIM interpretation. Chem Phys Lett 800:139669
35. Yu W, Li Z, Peng Y, Feng X, Xu T, Früchtl H, van Mourik T, Kirk SR, Jenkins S (2022) Controlling achiral and chiral properties with an electric field: a next-generation QTAIM interpretation. Symmetry 14:2075
36. Yu W, Li Z, Peng Y, Feng X, Xu T, Früchtl H, van Mourik T, Kirk SR, Jenkins S (2022) Controlling achiral and chiral properties with an electric field: a next-generation QTAIM interpretation. Symmetry 14(10):2075
37. Jenkins S, Kirk SR, Rong C, Yin D (2012) The cis-effect using the topology of the electronic charge density. Mol Phys 111:1–13. https://doi.org/10.1080/00268976.2012.745631
38. Peng Y, Yu W, Feng X, Xu T, Früchtl H, van Mourik T, Kirk SR, Jenkins S (2022) The Cis-effect explained using next-generation QTAIM. Molecules 27(18):6099
39. Ayuso D, Neufeld O, Ordonez AF, Decleva P, Lerner G, Cohen O, Ivanov M, Smirnova O (2019) Synthetic chiral light for efficient control of chiral light–matter interaction. Nat Photonics 13:866–871
40. Ordonez AF, Smirnova O (2019) Propensity rules in photoelectron circular dichroism in chiral molecules. I. Chiral hydrogen. Phys Rev A 99:043416
41. Cireasa R, Boguslavskiy AE, Pons B, Wong MCH, Descamps D, Petit S, Ruf H, Thiré N, Ferré A, Suarez J, Higuet J, Schmidt BE, Alharbi AF, Légaré F, Blanchet V, Fabre B, Patchkovskii S, Smirnova O, Mairesse Y, Bhardwaj VR (2015) Probing molecular chirality on a sub-femtosecond timescale. Nat Phys 11:654–658
42. de Jong JJD, van Rijn P, Tiemersma-Wegeman TD, Lucas LN, Browne WR, Kellogg RM, Uchida K, van Esch JH, Feringa BL (2008) Dynamic chirality, chirality transfer and aggregation behaviour of dithienylethene switches. Tetrahedron 64:8324–8335
43. Weingart O, Lan Z, Koslowski A, Thiel W (2011) Chiral pathways and periodic decay in cis-azobenzene photodynamics. J Phys Chem Lett 2:1506–1509
44. Nikiforov A, Gamez JA, Thiel W, Filatov M (2016) Computational design of a family of light-driven rotary molecular motors with improved quantum efficiency. J Phys Chem Lett 7:105–110
45. Campos RB, Tantillo DJ (2019) Designing reactions with post-transition-state bifurcations: asynchronous nitrene insertions into C-$C_\sigma$ bonds. Chem 5:227–236
46. Matsumoto A, Ozaki H, Tsuchiya S, Asahi T, Lahav M, Kawasaki T, Soai K (2019) Achiral amino acid glycine acts as an origin of homochirality in asymmetric autocatalysis. Org Biomol Chem 17:4200–4203
47. Jiajun D, Maza JR, Xu Y, Xu T, Momen R, Kirk SR, Jenkins S (2016) A stress tensor and QTAIM perspective on the substituent effects of biphenyl subjected to torsion. J Comput Chem 37:2508–2517
48. Wilkins LC, Melen RL (2016) Enantioselective main group catalysis: modern catalysts for organic transformations. Coord Chem Rev 324:123–39

# Chapter 8
# The Design of Molecular Devices

*There's plenty of room at the bottom.*
*Richard Feynman*

In this chapter we use the work of Chaps. 4–6 that introduced the bond-path framework set B and stress tensor trajectory $T_\sigma(s)$. In Sect. 8.1 we introduce background to molecular devices and the role of NG-QTAIM. The molecular devices with the greatest degree of nuclear motion, the molecular rotary motors are presented in Sect. 8.2. The background to the 'ON' and 'OFF' mechanisms of functioning of a switch that is triggered by hydrogen transfer tautomerization in the absence and presence of an applied electric (**E**)-field are highlighted and explained in Sects. 8.3, 8.3.1 and 8.3.2 respectively. In Sect. 8.4 ring-opening reactions as switches are presented. The fatigue of switches is explained in the absence and presence of an applied **E**-field in Sect. 8.5.1. In Sects. 8.5 and 8.5.1 the assembly of electronic devices including the scoring of molecular wires is explained. In Sect. 8.6 the design of emitters exhibiting thermally-activated delayed fluorescence (TADF) is introduced. The impact of NG-QTAIM of the TADF emitters subject to a static **E**-field and laser pulse on the energy gap $\Delta E(S_1\text{-}T_1)$ are presented Sects. 8.6.1 and 8.6.2 respectively.

The chapter concludes in Sect. 8.7 by outlining the benefits for NG-QTAIM for the design of molecular devices.

**Scientific goals to be addressed**:

- Develop non-scalar measures for molecular devices design.
- Determine the mechanisms of switches 'ON'/'OFF' mechanisms: hydrogen transfer tautomerization and effect of **E**-Fields.
- Determine the directional mechanism of switch ring-opening (open/closed) reactions.
- Determine the effects of atom doping and **E**-Fields on the mechanism of fatigue of switches.

© The Author(s), under exclusive license to Springer Nature Singapore Pte Ltd. 2023

S. Jenkins and S. R. Kirk, *Next Generation Quantum Theory of Atoms in Molecules*,
Lecture Notes in Chemistry 110, https://doi.org/10.1007/978-981-99-0329-0_8

- Use laser pulses for the manipulation of the $\Delta E(S_1\text{-}T_1) < 0$ energy gap for TADF emitters.

## 8.1 Steering Molecular Devices: With Vector-Based Measures

*In this section we provide the background to molecular electronics and a brief discussion of the relevance of NG-QTAIM.*

The term *molecular electronics* was introduced by Ratner in 2002 [1] and launched a significant area of research has around molecule-sized switches. Molecular electronics is becoming increasingly realizable as silicon and semiconductor-based microelectronics are approaching the limits of miniaturisation resulting in switches, transistors or memory elements attaining the size of a single molecule. A review by Zhang et al. [2] is recommended for an overview of the breadth of the field. Molecular junctions are of particular interest for the purposes of electronic components and has been reviewed by Komoto et al. [3].

The ability to control a molecular device using light, a clean and efficient form of energy, will allow the synthesis of novel molecular devices and steering of new physical phenomena. The availability of tunable ultra-short laser pulses has therefore generated renewed interest in photochromic molecules [4]. One of the main challenges for materials science in actively controlling molecular devices using laser pulses is the ability to understand the time-scales and control the intramolecular energy and electron redistribution in molecules [5]. In contrast, kinetic and thermodynamic control are both types of *passive* control that are unable to access molecular device mechanisms on a bond-by-bond basis. There is therefore an increasing need to find mechanistic theoretical models to interpret and understand how a shaped laser pulse, down to the sub-femtosecond timescale, perturbs and induces phenomena in the molecular devices to implement coherent control strategies. The phenomena associated with switches and light-driven devices in response to external agents such as laser irradiation are inherently directional in nature. The associated phenomena relate to the redistribution of the total charge density $\rho(\mathbf{r})$ and are understood in terms of well-developed physics-based descriptions of potential energy surfaces (PES). Conventional computational treatments, however, reduce the response of a given molecule to external agents to a set of scalar-based measures either using conventional QTAIM, orbital or orbital-free electronic structure methods. Conventional QTAIM, using scalar measures, only acts as a magnifying lens on the $\rho(\mathbf{r})$-derived properties of separate electronic states, due to being constructed from multiple derivatives of $\rho(\mathbf{r})$.

NG-QTAIM provides the directional and 3-D perspective required to adapt to the needs of new molecular device environments. The Ehrenfest force $\mathbf{F}(\mathbf{r})$, the force on the electrons, provides the quantum analogue of pressure and is effectively a force

field for electrons which is directly related to the quantum stress tensor $\boldsymbol{\sigma}(\mathbf{r})$ [6, 7]. NG-QTAIM can include the analysis of the Ehrenfest force $\mathbf{F}(\mathbf{r})$ [8]. Examples of the redistribution of the total charge density $\rho(\mathbf{r})$ include changes to the three-stranded NG-QTAIM interpretation of the chemical bond, for multiple electronic states. The NG-QTAIM $\{\boldsymbol{q}, \boldsymbol{q}'\}$ and $\{\boldsymbol{p}, \boldsymbol{p}'\}$ path-packets are directional analogues of a bond and are constructed along the entire conventional QTAIM bond-path from the most preferred and least preferred directions of charge density accumulation $\rho(\mathbf{r})$ respectively. An example of the failure of scalar measures is the treatment of the S and R stereo-isomers of lactic acid, where although the bond critical point (*BCP*) ellipticity ε can partially separate out the rotational isomers [9], it fails to do so at the for the stereoisomers i.e. at the global energy minima, see ($\theta = 0.0°$) in the right panel, see Chap. 7.

The development of attosecond lasers will render electron control accessible [10] where NG-QTAIM is the ideal tool for analysis.

## 8.2 Controlling Molecular Rotary Motors

*In this section we demonstrate the relevance of NG-QTAIM to the functional of molecular rotatory motors.*

Feringa and coworkers presented a chiroptical molecular switch with perfect stereo-control based on a modified version of his light-driven unidirectional molecular rotor [11].

Using conventional QTAIM we earlier determined that torsional motion of the (F-NAIBP) molecular motor [12] blades was steered by strongly coupled "sticky" intramolecular bond critical points (*BCP*s) and bond-paths between the atoms of the rotor and stator blades [13]. The F-NAIBP motor was revisited using NG-QTAIM, where the stress tensor trajectories $\mathbf{T}_{\boldsymbol{\sigma}}(\boldsymbol{s})$ associated with the $S_0$ and $S_1$ electronic states were separate and distinct at the C.I. and provided a new measure to assess the degree of purity of the axial bond torsion for the F-NAIBP rotary motor [14]. Central to achieving highly efficient operational molecular rotary motors with directed functionality is the ability to control the excited-state properties, e.g. maintenance of full (360°) unidirectional, non-'jittery' torsional motion. More recently we examined the functioning of these rotary motors that follow non-adiabatic dynamics trajectories through a conical intersection (CI) [14], see Figs. 8.1 and 8.2.

We calculated the $\mathbf{T}_{\boldsymbol{\sigma}}(\boldsymbol{s})$ for selected fast **(F)** and slow **(S)** non-adiabatic molecular dynamics trajectories with the electron densities obtained using the ensemble density functional theory method. Scalar QTAIM was able to account for the differences in the fast **(F)** and slow **(S)** dynamics trajectories in terms of an unusually strong and "sticky" coupling connecting the atoms comprising the rotor and the stator blades that stalled the progression along the torsional path of the slow **(S)** dynamics trajectory

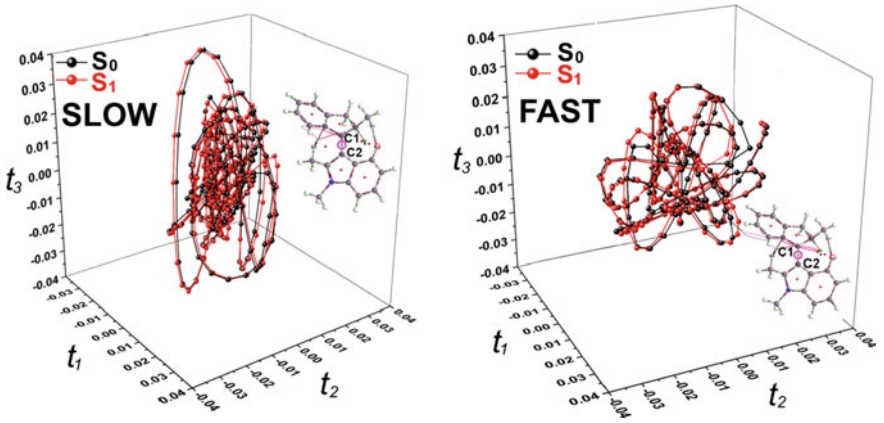


**Fig. 8.1** The $T_{\sigma}(s)$ for the slow and fast non-adiabatic dynamics trajectories for the C1-C2 *BCP* of the F-NAIBP molecular rotary motor before the conical intersection (CI) for the $S_0$ and $S_1$ states with inset molecular graphs

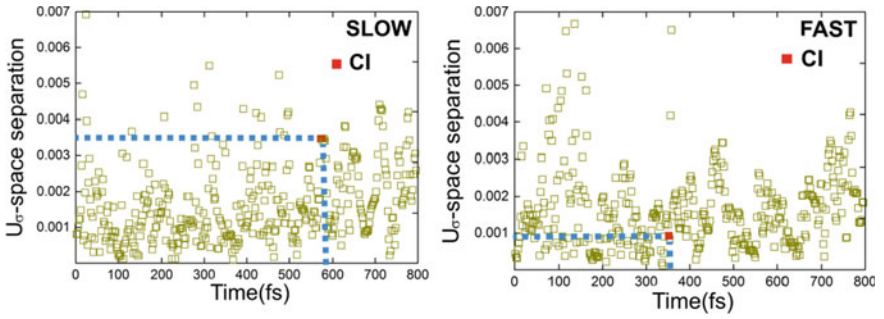


**Fig. 8.2** The $U_{\sigma}$-space separations of $S_0$ and $S_1$ for the slow and fast C1-C2 *BCP* dynamics trajectories respectively; the CI is indicated in red, adapted [15]

for an extended period of time. The NAMD simulations of the chemically modified molecular motors of the 3-[(2S)-2-fluoro-2-methyl-1-indanylidene]-1-methyl-2-methylindole (F-NAIBP) molecular rotary motor demonstrated the presence of fast (**F**) and slow **(S)** categories of dynamics trajectory [12]. The fast **(F)** and slow **(S)** non-adiabatic molecular dynamics trajectories reached the $S_1/S_0$ conical intersection in about 300 and 600 fs respectively. In other words, the $T_{\sigma}(s)$ were used to explain the different $S_1$ lifetimes of the slow **(S)** and fast (**F**) dynamics trajectories to the corresponding CIs.

2-D plots are not ideal for the analysis of the inherently 'noisy' dynamical trajectories due to the lack of any clear functional dependency of independent and dependent variables often present for minimum energy pathways (MEPs). The $T_{\sigma}(s)$ remove the requirement for functional relationships and dependencies present with 2-D plots,

**Table 8.1** A summary of the stress tensor trajectory $T_{\sigma}(s)$ for the reaction pathways ($S_1$) leading to the hop events at the conical intersections (CI) of the fast (**F**) and slow **(S)** dynamics trajectories for the F-NAIBP motor for the C1-C2-*BCP*. The duration (Time$^{CI}$ in fs) from the start of the (**F**) and **(S)** dynamics trajectories to the respective $T_{\sigma}(s)^{CI}$, corresponding real space length $l^{CI}{}_{S0}$, $l^{CI}{}_{S1}$ and stress tensor trajectory space length $L_{\sigma}{}^{CI}{}_{S0}$, $L_{\sigma}{}^{CI}{}_{S1}$, in a.u, and the locations in $U_{\sigma}$ space, $\{t_1, t_2, t_3\}^{CI}{}_{S0}$ and $\{t_1, t_2, t_3\}^{CI}{}_{S1}$ corresponding to the $S_1$ and $S_0$ states respectively

| $Time^{CI}$ | $l^{CI}{}_{S0}$ | $l^{CI}{}_{S1}$ | $L_{\sigma}{}^{CI}{}_{S0}$ | $L_{\sigma}{}^{CI}{}_{S1}$ | $\{t_1, t_2, t_3\}^{CI}{}_{S0}$ | $\{t_1, t_2, t_3\}^{CI}{}_{S1}$ |
|---|---|---|---|---|---|---|
| Fast (**F**) | | | | | | |
| 352 | 3.387 | 3.405 | 0.948 | 0.964 | {(−0.0042), (0.0184), (−0.0009)} | {(−0.0047), (0.0177), (−0.0006)} |
| Slow (**S**) | | | | | | |
| 574 | 5.341 | 5.342 | 1.626 | 1.642 | {(0.0198), (0.0033), (0.0138)} | {(0.0225), (0.0052), (0.0149)} |

therefore we used them to visualize the non-adiabatic molecular dynamical trajectories in $U_{\sigma}$-space to capture in 3-D differences between fast (**F**) and slow **(S)** trajectories with regards to most/least preferred directions of electron motion along the reaction pathway.

Different values for the $S_1$ and $S_0$ states of the real space length $l_{CI}$ and stress tensor trajectory space length $L_{\sigma CI}$, exist, see Table 8.1. The variation in these properties associated with the $S_1$ and $S_0$ states at the CI is due to the use of $U_{\sigma}$-space [9]. The presence of longer real space length $l_{CI}$ as well as the stress tensor trajectory space length $L_{\sigma CI}$ associated with the $S_1$ compared with the $S_0$ state indicates the greater ease of progression of the molecular rotary motor in the $S_1$ state.

The preference of the rotary molecular motor to proceed via the $S_1$ state, as opposed to the $S_0$ state and the $\{\boldsymbol{q}, \boldsymbol{q}'\}$ path-packets provided the was explanation and were used to quantify the covalent character of the bond-path associated with a closed-shell *BCP*.

The "sticky" F13--H36 *BCP* was found to be present only for the slow **(S)** dynamics trajectory. The explanation for the breaking/hindering effect of the "sticky" F13--H36 *BCP* on the desired torsioning of the motor was provided by new evidence in the form of the twisted $\{\boldsymbol{q}, \boldsymbol{q}', \boldsymbol{r}\}$ path-packet of the H23--H36 *BCP* and the large in-plane extent of the corresponding $\{\boldsymbol{p}, \boldsymbol{p}', \boldsymbol{r}\}$ path-packet indicating resistance to torsion.

The morphology of associated $T_{\sigma}(s)$ of the fast (**F**) dynamics trajectory was found to be rather isotropic possessing evenly spaced $T_{\sigma}(s)$ steps with a relatively small $t_{3,max} = (\underline{\mathbf{e}_3} \cdot \mathbf{dr})_{\mathbf{max}}$ component which corresponded to motion along the axial C1-C2 *BCP* bond-path. Conversely, the slow **(S)** dynamics trajectory consisted of initially closely spaced steps followed by a large stretching motion along the axial C1-C2 *BCP* bond-path immediately before the onset of the CI. The large $t_{3,max} = (\underline{\mathbf{e}_3} \cdot \mathbf{dr})_{\mathbf{max}}$ component accounted for the lower degree of pure axial rotation, why the slow **(S)** dynamics trajectory was less efficient at undergoing the light driven molecular rotatory motion

torsion than the fast (**F**) dynamics trajectory. Therefore, the large/small magnitude of the $t_{3,max}$ component due to the presence/absence of sticky ($H(\mathbf{r_b}) < 0$ for closed-shell *BCP*s) intramolecular bonding provided a measure of the low/high efficiency of a molecular rotary motor. This is because in the ideal limit of pure torsion a 100% efficient molecular rotary motor would not spend time undergoing oscillations along the extent of the axial C1-C2 *BCP* bond-path.

## 8.3 Switches: 'ON' and 'OFF' Mechanisms: Hydrogen Transfer Tautomerization

*In this section we provide a variety of switches to which NG-QTAIM is usefully applied.*

### *8.3.1 Deformation of a Nuclear Skeleton via Hydrogen Atom Sliding*

Azophenine, attached to a Cu(110) surface has been discovered to exist in two energetically identical states connected by hydrogen transfer from an amino to imino group and can be switched using the tip of a Scanning Tunnelling Microscope (STM) [1]. The energy difference of the most energetically stable "*meta*" state and the energetically metastable "*para*" structure has been calculated to be only 0.15 eV, with a conversion barrier of 0.42 eV. A family of molecular switches based was recently proposed [16] and initial calculations demonstrated that a single iron atom, coordinated to the central quinone ring, could significantly lower the energy difference and barrier height, similar to the effect of a metal surface, see Fig. 8.3. The Fe atom used for this so-called quinone switch would need to be confined. This would enable us to propose molecules with similar switching properties that might be more easily synthesised and networked than the model system proposed [16] since we could predict the effect of different side groups attached to the quinone core. This approach would include formalism not in conventional Cartesian space but constructed from a 'phase-space' of the stress tensor trajectories to capture the directional behaviour of switches.

We investigated a candidate building blocks based on molecular junctions from hydrogen transfer tautomerization in the benzoquinone-like core of an azophenine molecule NG-QTAIM [17]. We found that in particular the $T_{\sigma}(s)$ are well suited to describe the hydrogen transfer tautomerization mechanism of the switching process. In addition to the effects of an Fe-dopant atom coordinated to the quinone ring with F and Cl substitution. This was undertaken to determine the effectiveness of such molecules as molecular switches in nano-sized electronic circuits. The coordinated

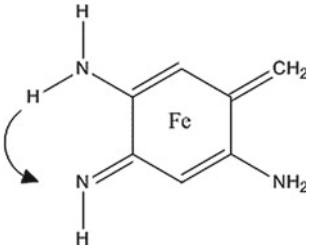


**Fig. 8.3** Quinone-based switch candidate building blocks of molecular junctions, the arrow indicates the hydrogen transfer involved in the switching process

Fe-dopant was found, from the $T_\sigma(s)$ analysis, to greatly improve the switching properties, both in terms of the tautomerisation barrier that has to be crossed in the switching process as well as the effects of hydrogen substitution. The $T_\sigma(s)$ highlighted the effect of the absence of the Fe-dopant atom in an impaired functioning of the switch 'OFF' mechanism. This impaired switch 'OFF' functioning mechanism was associated with the formation of closed-shell H---H bond critical points that indicated a strained and electron deficient environment, see Fig. 8.4.

The Hessian of $\rho(\mathbf{r})$ bond-path framework set B and the stress tensor $\boldsymbol{\sigma}(\mathbf{r})$ bond-path framework $B_\sigma$ visualized and uncovered the destabilizing effects on the hydrogen bond of the presence of an Fe atom [18]. The lengths of B and $B_\sigma$ quantified referred to as H and $H_\sigma$ this effect and the dependence on the position of a fluorine substituent, see Fig. 8.5.

The $\{\boldsymbol{q}, \boldsymbol{q}'\}$ and $\{\boldsymbol{q}_\sigma, \boldsymbol{q}'_\sigma\}$ path-packets for the Fe-doped switch displayed much larger extents in the vicinity of the N10--H13 *BCP* than for the undoped switch, this information was not extractable from scalar QTAIM or energy based analysis. The easier passage of the *BCP* and associated H *NCP* for the Fe-doped compared with the undoped switch was indicated by the larger extents of the $\{\boldsymbol{q}, \boldsymbol{q}'\}$ and $\{\boldsymbol{q}_\sigma, \boldsymbol{q}'_\sigma\}$ path-packets. The stress tensor $\{\boldsymbol{p}_\sigma, \boldsymbol{q}_\sigma\}$ and the original QTAIM $\{\boldsymbol{p}, \boldsymbol{q}\}$ path-packets both display significant sensitivity to the application of the applied **E**-field compared with the minimal definition of bonding $\boldsymbol{r}$.

### *8.3.2 E-Fields for Improved "ON" and "OFF" Switch Performance*

Recent work demonstrated the ability of the directionality of NG-QTAIM to differentiate between degenerate energy minima associated with a common energy maximum or transition state [9, 19]. This required the ability to differentiate between very similar or degenerate energy minima for the 'ON' and 'OFF' switch positions. In addition, insight gained about the 'ON' and 'OFF' switch functioning enabled

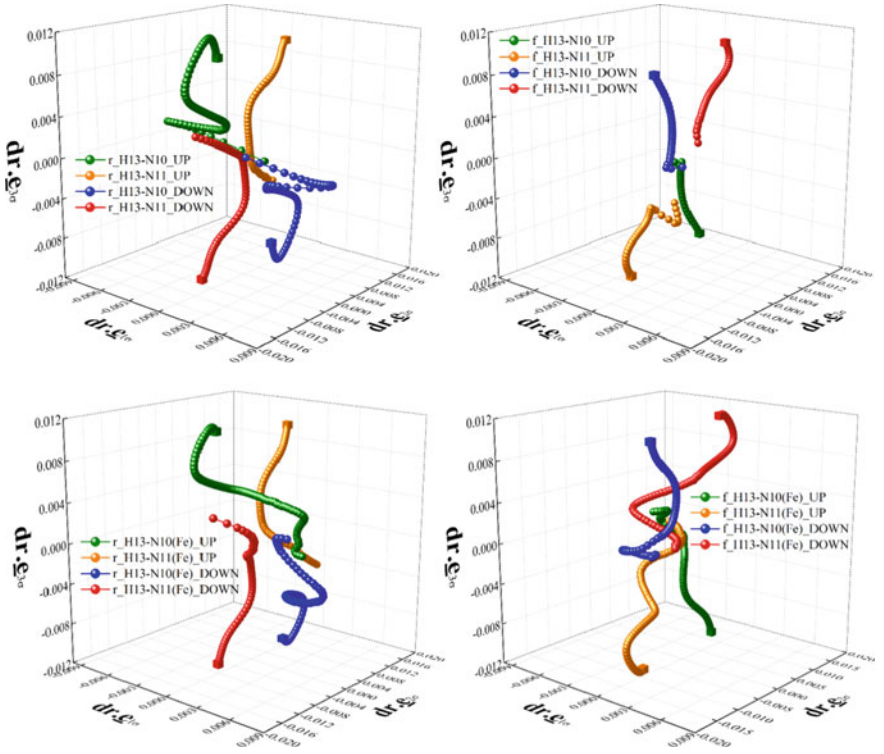


**Fig. 8.4** The trajectories $T_{\sigma}(s)$ in the eigenvector projection space $U_{\sigma}(s)$ for the N-H *BCP*s with no Fe (top-panel) and Fe (bottom-panel)

better feedback on how to trigger mechanisms that control the switching between the isomeric switch positions [20].

The switch functioned in terms destabilization of the H atom participating in the tautomerization process along the hydrogen bond that defines the switch. More specifically, the 'ON' functioning of the switch, from the position of the tautomerization barrier, is also improved by the reversal of the homogenous **E**-field: this result was previously inaccessible. The 'ON' and 'OFF' switch functioning was visualized in terms of the response of the response of the $T_{\sigma}(s)$ to the **E**-field, see Fig. 8.6.

The H14--N16 *BCP* weakened and was ruptured by an increase in the (+)**E**-field as was evidenced by the total local energy $H(\mathbf{r_b})$ and stress tenors eigenvalue $\lambda_{3\sigma}$ results. This resulted in the switch being easier to move from the energetic transition state to the 'OFF' position and ultimately increase a better performing switch. The converse is true for an increase in the (−)**E**-field, i.e. the H14--N16 *BCP* is less easily ruptured. The presence of a more easily ruptured H14--N13 *BCP* resulted in a switch with improved performance in the 'ON' position. This insight into the switch performance in the 'ON' position was not accessible from analysis of the relative energy

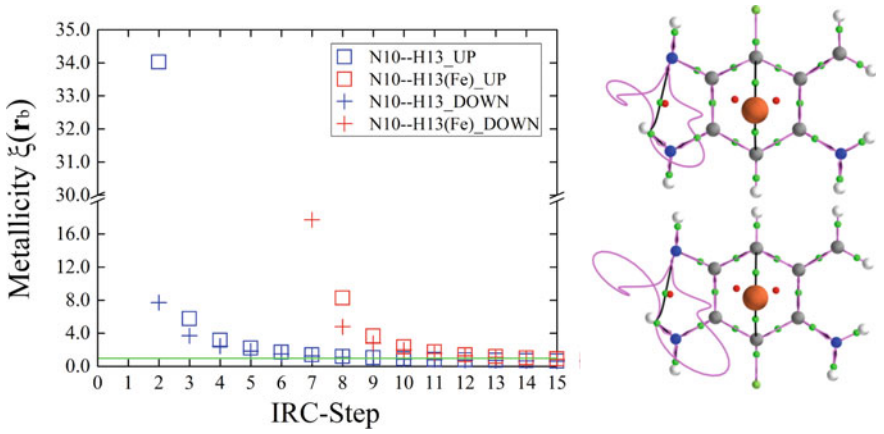


**Fig. 8.5** The variation of the metallicity $\xi(\mathbf{r}_b)$ with the IRC from the transition state at IRC-Step = 0 towards the forward minimum for N10--H13 *BCP* of the F-decorated quinone switch in the UP and DOWN positions for the undoped and Fe-doped molecular graph (left-panel). The horizontal green line indicates values of metallicity $\xi(\mathbf{r}_b) = 1.0$. Bond-path framework sets (magenta lines) for the most preferred directions of accumulation of the electronic charge density, corresponding to the N10--H13 bond for the F (UP) (upper-right) and F (DOWN) (lower-right)

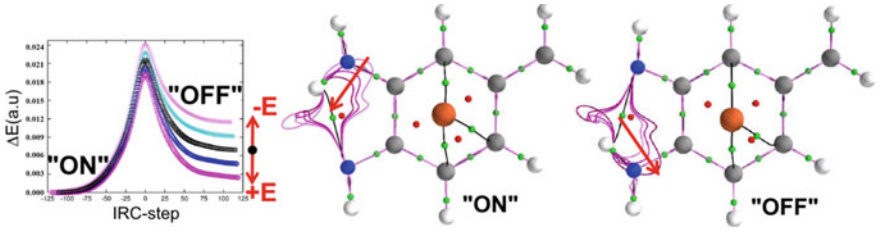


**Fig. 8.6** The variation of the relative energy ΔE along the IRC with values of the external electric field $\mathbf{E} = 0, \pm 20 \times 10^{-4}$ au and $\pm 40 \times 10^{-4}$ au (left panel) is presented for the 'ON' and 'OFF' switch positions. The $\{\boldsymbol{q}, \boldsymbol{q}'\}$ path-packets indicating the most preferred directions of electronic charge density motion for values of the external **(+)E**-field = 0 for the 'ON' (middle panel) and 'OFF'(right panel) (pale-magenta), $20 \times 10^{-4}$ au (mid-magenta) and $40 \times 10^{-4}$ au (dark-magenta)

ΔE plots because there is no variation with respect to the applied **E**-field, see Fig. 8.6. Therefore the relative energy ΔE plots could not provide insight into the *mechanism* of the switching process because of the lack of information on changes to the chemical behavior incurred during the H14 hydrogen atom participating tautomerization process.

Greater energetic stabilities, determined from the relative energy ΔE values correlated with a greater persistence of the metallic ($\xi(\mathbf{r}_b) > 1$, where $\xi(\mathbf{r}_b) = \rho(\mathbf{r}_b)/\nabla^2\rho(\mathbf{r}_b)$

$\geq 1$, i.e. for a closed shell *BCP*, see Chap. 2) H16--N14 *BCP* along the forward direction of the IRC. This provided an indication that the H14 atom transfer tautomerization is facilitated by the presence of a more metallic H16--N14 *BCP* where the metallicity $\xi(\mathbf{r}_b)$ was maximized in presence of larger (+)**E**-fields. Conversely, the presence of larger (−)**E**-fields hindered the H14 atom transfer tautomerization process. Therefore, the metallicity $\xi(\mathbf{r}_b)$ values explain the effect of the presence of larger (+)**E**-fields in facilitating the H14 atom transfer tautomerization process by inducing greater destabilization of the H16--N14 *BCP* bond-path. Consequently, the H14 *NCP* was able to more easily traverse the destabilized H16--N14 *BCP* bond-path. The variation of $\Delta$(*BCP-RCP*) with respect to the absence of the **E**-field also provided a method to determine the increase (positive values) or decrease (negative values) in the relative topological stability of *BCP*s when the $\pm$**E**-field is applied.

The $\{\boldsymbol{q}, \boldsymbol{q}'\}$ path-packets were shaped by the response of $\rho(\mathbf{r})$ to a change in direction of the applied **E**-field, this provided a novel method to visualize the effects of the applied **E**-field, see Fig. 8.6. The larger distortions induced for a given value of the external **E**-field for the BPL compared with the GBL demonstrated that the BPL provides a more sensitive response to the external **E**-field.

Improved 'OFF' switch function was provided by larger (+)**E**-field values that enable the H14 atom tautomerization process to occur more easily by destabilizing the closed-shell H14--N16 *BCP* bond-path that exists in the switching process from the transition state to the forward minimum ('OFF' position), relative to the absence of an **E**-field. The functioning of the switch to the 'OFF' position was worsened by the application of larger (−)**E**-fields that stabilized the H14--N16 *BCP* bond-path relative to the absence of an **E**-field. Improved 'ON' switch functioning was enabled by the application of the (−)**E**-field to the closed-shell H14--N13 *BCP* that exists for the transition state and the reverse minimum ('ON' position). The functioning of the switch towards the 'ON' position was worsened by the application of larger (+)**E**-fields that stabilize the H14--N13 *BCP* bond-path relative to the absence of an **E**-field.

## 8.4 Switches: Ring-Opening Reactions

If two conformers (switch positions) are connected by a photochemical pathway then the switch function may be initiated by a laser pulse that transfers the electronic wave-packet to an excited electronic state. Subsequently, an ultra-fast return to the ground state will ensure a rapid switching process, where the ultra-fast transfer can be mediated by C.I.s, for instance the ring-opening of photochromic (1,3-cyclohexadiene) CHD $\rightarrow$ HT (1,3,5-hexatriene) [21]. The factors underlying the experimentally observed branching ratio (70:30) of the (1,3-cyclohexadiene) CHD $\rightarrow$ HT (1,3,5-hexatriene) photochemical ring-opening reaction were investigated. The ring-opening reaction path was optimized by a high-level multi-reference DFT

method and the density along the path. For both the $S_1$ and $S_0$ electronic states a bonding interaction was found between the ends of the fissile sigma-bond of CHD that steered the ring-opening reaction predominantly in the direction of restoration of the ring. The orientation of the nuclear momentum vector to cause ring opening known to be relatively rare during the dynamics that explained the observed low quantum yield of the ring-opening reaction.

## 8.5 Fatigue of Photo-Switches

*In this section we consider the effects of atom doping and applied electric fields on the fatigue of switches. We are able to quantify the effects of fatigue with NG-QTAIM.*

Previously, we provided candidate sites for alteration by future experiment with a consistent theoretical justification to partner the successful substitution patterns obtained from experiments of the fatigue and photochromism in $S_1$ excited state reactivity of diarylethenes (DTE) [22]. In particular NG-QTAIM was used to characterize the photochromism reaction as reusable and the fatigue reaction as irreversible and find candidate sites for alteration by future experiment. The realization of technologically relevant functional systems from idealized photochromic compounds is elusive due to the double requirement that such switches must possess highly efficient photoisomerization reactivity and extremely low fatigue over a large number of switching cycles. We saw a preservation of the topological characteristics of the $\mathbf{T_\sigma(s)}$ between the reverse (ring-closed) and forward (ring-opened) portions the photochromism reaction showing the nature of the reusability of the DTE switch in keeping with the spirit of the Hammond's postulate. Conversely, for the fatigue reaction there is no preservation of the topological characteristics of the $\mathbf{T_\sigma(s)}$ between the reverse and forward portions of the functioning of the DTE switch. This demonstrated the irreversible character of the fatigue mechanism. On the basis of having the most equal lengths $L_\sigma$ of the $\mathbf{T_\sigma(s)}$ for the reverse and forward photochromism reactions we discovered that the sulphur decorated DTE possessed more favorable switching characteristics than the undecorated DTE.

We explained the difficulties experimentalists have in identifying useful sites for substitution on the DTEs to tune their chemical properties in terms of the lack of independence of the fatigue and photochromism reactions for some of the *BCP*s. The nature of the electronic reorganization explained the lack of independence for some of the *BCP*s in terms of the presence of high values of metallicity $\xi(\mathbf{r_b})$ i.e. $\xi(\mathbf{r_b}) > 1$, see Chap. 2.

### 8.5.1 *Photo-Switch Fatigue Response to External Fields Electric(E)-Fields*

We provided insight into the tendency of bonds towards fatigue and fatigue resistance in the absence and presence of a directional applied **E**-field $= \pm 0.02$ au, in undoped and sulphur doped DTE structures [23]. In particular, application of an **E**-field decreased the tendency towards bond-path rupture as determined by an increase in the $\{\boldsymbol{q}, \boldsymbol{q}'\}$ path-packet. Examples included the C7-C11 *BCP* bond-path subject to an $\mathbf{E}_{para}$-field $= +0.02$ au and the C6-C12 *BCP* with an $\mathbf{E}_{para}$-field $= -0.02$au for the undoped DTE. The converse effect of increasing the closed-shell *BCP* character i.e. increasing the tendency towards *BCP* bond-path rupture and fatigue, was undertaken for the C7-C11 *BCP* bond-path for an applied $\mathbf{E}_{para}$-field $= -0.02$ au, see Fig. 8.7.

A use of this analysis is to explain differences in the tendencies towards nonreversible fatigue bond behavior that we previously found characteristic of fatigue bonds in the undoped but not the sulphur doped DTE structures. Scalar QTAIM was able to

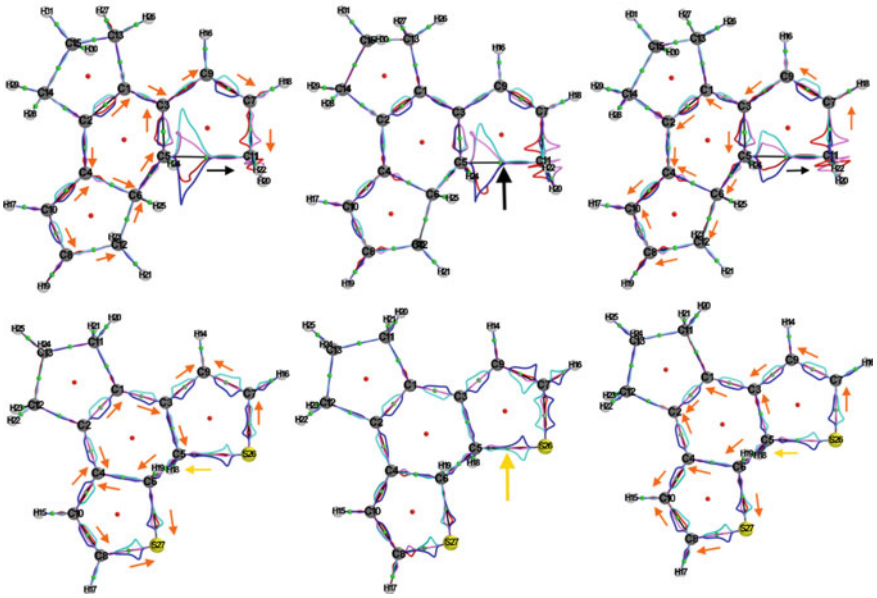

**Fig. 8.7** The relative movement (arrows not to scale) of the non-fatigue *BCP*s (orange arrows) $\{\boldsymbol{q}, \boldsymbol{q}'\}$ path-packets (magenta, red) and $\{\boldsymbol{p}, \boldsymbol{p}'\}$ path-packets (light-blue, dark-blue) of the undoped DTE (top-panel) fatigue C5-C11 *BCP* (black arrow) of the $\mathbf{E}_{para}$-field $= -0.02$ au (left panel), $\mathbf{E}_{para}$-field $= 0$ (middle panel) and $\mathbf{E}_{para}$-field $= +0.02$ au (right panel). The $\{\boldsymbol{q}, \boldsymbol{q}'\}$ and $\{\boldsymbol{p}, \boldsymbol{p}'\}$ path-packets correspond to the most preferred and least preferred directions of charge density accumulation $\rho(\mathbf{r})$ respectively. The corresponding results for the sulphur doped DTE fatigue (bottom-panel) C5-S26 *BCP* (yellow arrow) with $\mathbf{E}_{para}$-field $= -0.02$ au (left panel), $\mathbf{E}_{para}$-field $= 0$ (middle panel) and $\mathbf{E}_{para}$-field $= +0.02$ au (right panel)

demonstrate a response to the applied **E**-field in terms of the *BCP* motion along the bond-path and the variation of the ellipticity ε profiles along the bond-path. The limitations of scalar QTAIM were the inability to provide the directional information on the tendency for the *BCP* and the neighboring *RCP* to coalesce and annihilate the associated bond-path which is a nonreversible process. The BPL and the total local density $H(\mathbf{r_b})$ of scalar QTAIM were limited since they displayed only a very weak response to the applied **E**-field. Conversely, NG-QTAIM was able to track the effect of the applied **E**-field from variations of the ΔH (length of the $\boldsymbol{q}$-path) and $\Delta H^{*}$' (length of the $\boldsymbol{p'}$-path) correlated sensitively. The $\{\boldsymbol{p}, \boldsymbol{p'}\}$ and $\{\boldsymbol{q}, \boldsymbol{q'}\}$ path-packet precessions K and K′ also provided a 3-D measure of the closed-shell and shared-shell character respectively along bond-paths, rather than being limited to the *BCP* as is the case for scalar QTAIM, see Fig. 8.8.

NG-QTAIM provided an understanding of chemical bonding, into the tendency of bonds towards fatigue and fatigue resistance in the absence and presence of a directional applied **E**-field = ±0.02 au, in undoped and sulphur doped DTE structures. The bond-path fatigue K and bond-path fatigue resistance K′ tendency were determined by the alignment of the direction of *BCP* → *RCP* path with the $\underline{\mathbf{e}}_1$ or $\underline{\mathbf{e}}_2$ eigenvectors, the least facile and most facile directions respectively. NG-QTAIM determined the response of bonding to an applied **E**-field = ±0.02 au without distorting the molecular geometry or needing to perform a scan over a reaction coordinate. In particular, NG-QTAIM could determine how an applied **E**-field decreased the tendency towards bond-path rupture. This was undertaken by determining the bond-path fatigue resistance K′. i.e. shared-shell *BCP* character, as determined by an increase in the $\{\boldsymbol{q}, \boldsymbol{q'}\}$ path-packet precession K′ associated with the most preferred direction of $\rho(\mathbf{r})$. The converse effect of increasing the closed-shell *BCP* character that is an increased tendency towards *BCP* rupture. i.e. bond-path fatigue, was also demonstrated possible in the case of the C7-C11 *BCP* bond-path, if the $\mathbf{E}_{para}$-field = −0.02 au was applied, see Fig. 8.7.

## 8.6 Assembly of Electronic Devices Using Molecules

*In this section we provide the elementary details of device design and their response to applied electric fields in addition to unchirped and chirped laser pulses.*

The assembly of electronic devices using individual atoms and/or molecules is an outstanding goal of the ultimate goals in electronics [1]. As the increasing miniaturization of semiconductor devices as described by Moore's Law[24] is approaching the physical limits, therefore the single-molecule-junction research field is currently attracting increased interest [3]. The interaction of a molecule with an oriented **E**-fields fields can significantly alter the potential energy surfaces (PES) via breaking and making of chemical bonds that control chemical reactions [25–31]. Sowlati-Hashjin and Matta have investigated strong external homogenous **E**-fields ($\pm 10 \times 10^9$ $\mathrm{Vm}^{-1}$) and discovered that parallel **E**-fields increasingly stretch a bond with

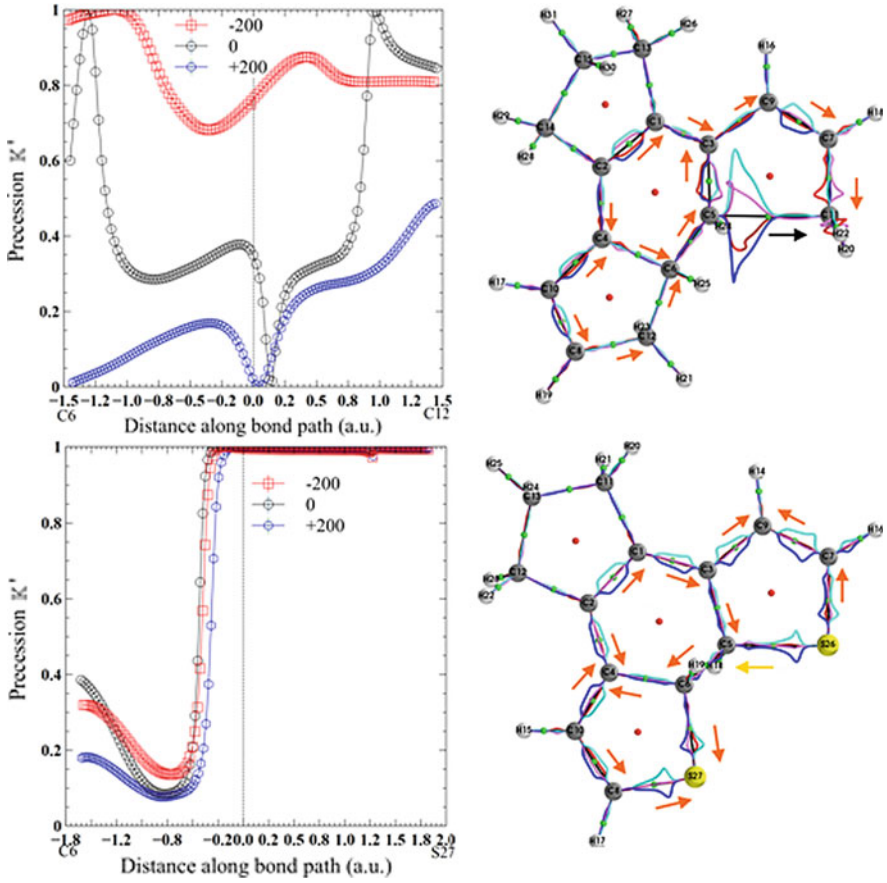


**Fig. 8.8** The C6-C12 *BCP* bond-path $\{q, q'\}$ path-packet precession K′ for the undoped DTE (top-left). Corresponding molecular graph with directions of bond critical point (*BCP*) shifts and $\{p, p'\}$ and $\{q, q'\}$ path-packets, the fatigue bond is indicated by the black arrow. The C6-S27 *BCP* bond-path $\{q, q'\}$ path-packet precession K′ for the sulphur doped DTE(bottom-left). Corresponding molecular graph with *BCP* shifts and $\{p, p'\}$ and $\{q, q'\}$ path-packets (bottom-right), the fatigue bond is indicated by the yellow arrow, see also Fig. 8.7.

increasing **E**-field strength; conversely antiparallel fields compress the bond although to a lesser extent [32].

### 8.6.1 *Scoring Molecular Wires in E-fields for Molecular Electronic Devices*

The sensitivity of NG-QTAIM to the application of an experimentally accessible **E**-field, to a molecular wire, was demonstrated [33], where there was no change in the nuclear coordinates, see Fig. 8.9. The B were used to quantify the effect of a varying and directional **E**-field on $\rho(\mathbf{r})$ of the ethene molecule that does not sigificantly alter the molecular geometry [33]. For the $\pm\mathbf{E}_x$-field, which coincides with the bond-path of the C1-C2 *BCP*, we found the associated $\{\boldsymbol{p}, \boldsymbol{p}'\}$ path-packet shifts along with the C1-C2 *BCP* parallel to the direction of the $\pm\mathbf{E}_x$-field due to the fact that there is insignificant spreading of the $\{\boldsymbol{p}, \boldsymbol{p}'\}$ path-packet. The $\{\boldsymbol{p}, \boldsymbol{p}'\}$ path-packet of the C1-C2 *BCP* subject to the $\pm\mathbf{E}_x$-field enclosed a constant area within the remains constant regardless of the magnitude of $\pm\mathbf{E}_x$, but the height increased with increase in the $\pm\mathbf{E}_x$-field, indicating a polarization effect that increased with applied $\pm\mathbf{E}_x$-field.

The C-H *BCP*s do not align parallel/anti-parallel to any of the $\mathbf{E}_x$, $\mathbf{E}_y$ and $\mathbf{E}_z$ orientations of the applied **E**-field the response of the $\{\boldsymbol{p}, \boldsymbol{p}'\}$ path-packets is asymmetrical, unlike the C1-C2 *BCP* which spread out by almost a factor of three for the $\pm\mathbf{E}_x$-field, see Fig. 8.10. The sensitivity of the $\{\boldsymbol{p}, \boldsymbol{p}'\}$ to the application of modest **E**-fields on $\rho(\mathbf{r})$ demonstrates the utility of considering more sublte details than molecular geometries that respond more slowly than applied **E**-fields can be varied. This is in contrast with QTAIM measures such as bond-path lengths were found invariant to the application of the **E**-field.

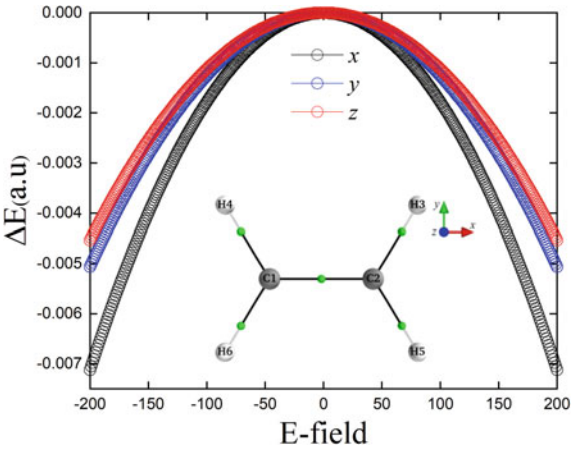


**Fig. 8.9** The variation of the relative energy ΔE for varying values of the **E**-field up to [200 × $10^{-5}$ a.u. (60.91 kJ/mol)] where $\mathbf{E}_x$, $\mathbf{E}_y$ and $\mathbf{E}_z$ correspond to the directions $x$, $y$, $z$ shown. Here a positive sign of $\mathbf{E}_x$ corresponds to the C1 → C2 direction and a negative sign to C1 ← C2. The numbering scheme used throughout for the molecular graph of the ethene molecule (insert)

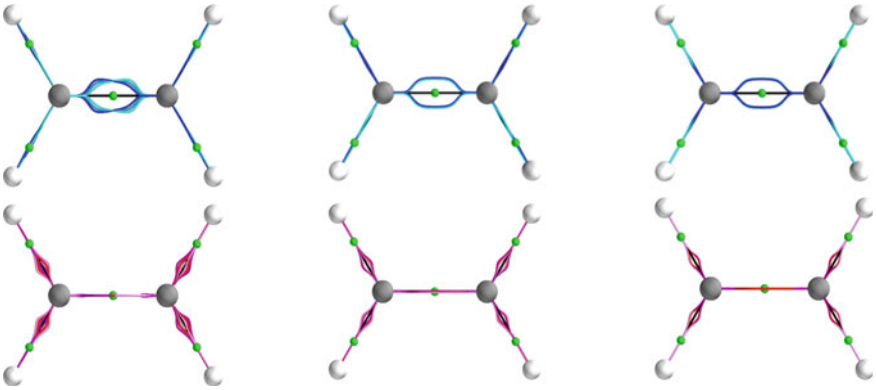

**Fig. 8.10** The response of the {$\boldsymbol{p}$(dark-blue), $\boldsymbol{p}'$(cyan)} and {$\boldsymbol{q}$(magenta), $\boldsymbol{q}'$(red)} path-packets on the bond-path ($\boldsymbol{r}$) with the applied **E**-field (in a.u.); $\mathbf{E}_x$, $\mathbf{E}_y$ and $\mathbf{E}_z$ are presented for the C1-C2 *BCP* of ethene

### *8.6.2 Design of Emitters Exhibiting Thermally-Activated Delayed Fluorescence (TADF)*

The optimization of the photo-physical properties of candidate organic emitter or absorber molecule for a given application requires the control of the low-lying excited states. Recent review articles highlight the computational and theoretical developments in the field [34–37]. Recently, an alternative pathway to the harvesting of triplet excitons has been proposed based on the phenomenon of thermally activated delayed fluorescence (TADF). This believed to be one of the most promising routes to increase the efficiency of organic light-emitting diode (OLED) devices [38]. A small gap, a between the lowest-lying singlet and triplet state $\Delta E(S_1\text{-}T_1)$ in the TADF process enables a thermal up-conversion from the triplet to the singlet manifold and as a consequence fluorescence from the not very bright $S_1$ state. The minimization of the singlet–triplet gap or even an inverted singlet–triplet gap $\Delta E(S_1\text{-}T_1)$, where $\Delta E(S_1\text{-}T_1) < 0$ [38] is a design principle for emitters exhibiting TADF. This would enable the fast reverse intersystem crossing (ISC). There is a growing interest in designing molecules where the up-conversion in TADF is replaced by the more efficient down-conversion [39–45] with an inverted singlet–triplet gap $\Delta E(S_1\text{-}T_1) < 0$. The $S_1$ state is not very bright for these molecules rendering the discovery of such molecules difficult making the systematic design of inverted singlet–triplet gap $\Delta E(S_1\text{-}T_1)$ emitters difficult. An example is cycl[3.3.3]azine violates Kasha's rule[46] and therefore displays a stronger emission from the $S_2$ than the $S_1$ state. Other mechanisms have been identified as feasible routes to overcome the exchange interactions and lead to negative singlet–triplet gaps. These include constrained density functional theory calculations undertaken by Difley et al., which indicate the possibility of inversion in exciplexes as was explained in terms of the kinetic exchange mechanism stabilizing singlet states [47]. A polarizable environment was found by Olivier et al. to also

lead to stabilization of singlets, which enables negative $\Delta E(S_1\text{-}T_1)$ [48]. A four-state model [49] proposed by de Silva et al. explained the possibility of efficient TADF as a consequence of mixing of diabatic charge-transfer (CT) and local excitation (LE) states, that resulted in mixed-chemical character adiabatic states that enabled simultaneously small $\Delta E(S_1\text{-}T_1)$ with relatively high spin–orbit coupling and oscillator strength. The work of Silivi et al. highlighted the need for better models to quantify the nature of the changing polarization environment that can be provided by NG-QTAIM.

### 8.6.3 *Effect of a Static E-field on the Energy Gap $\Delta E(S_1\text{-}T_1)$*

Insights into the response of the electronic structure in the form of fluctuations in the inverted singlet–triplet energy gap $\Delta E(S_1\text{-}T_1)$ due to the laser pulses were significant larger compared to those induced by the *static* **E**-field, were quantified by NG-QTAIM,. This was despite the magnitude of the **E**-field of the laser pulses being an order of magnitude lower than for the static **E**-field, the variation of the energy gap between the lowest lying singlet ($S_1$) and triplet ($T_1$) excited states was orders of magnitude greater for the laser pulse than for the static **E**-field. The response of the $S_1$ and $T_1$ excited states switched discontinuously between weak and strong chemical character for the static **E**-field, as determined by NG-QTAIM, was to induce a broad and continuous spectrum of chemical character, indicating the unique ability of the laser pulses to induce polarization effects in the form of 'mixed' bond types. More frequent instances of the desired outcome of an inverted singlet–triplet gap were induced by the chirped laser pulse than the unchirped pulse, indicating the laser as useful to design more efficient OLED devices. Therefore, NG-QTAIM was proven to be a useful tool for understanding the response to laser irradiation of the lowest-lying singlet $S_1$ and triplet $T_1$ excited states of emitters exhibiting thermally-activated delayed fluorescence (TADF). New insights into the behavior related to the electronic structure of a negative energy gap $\Delta E(S_1\text{-}T_1) < 0$ were provided by using precession K, particularly useful due to $S_1$ being a not very bright state and therefore difficult to detect. The application of a static **E**-field $= -0.20$ a.u. widened the negative energy gap $\Delta E(S_1\text{-}T_1) < 0$ by only 0.002 eV and reversing the **E**-field direction ($= 0.2$ a.u.) narrowed the negative energy gap by only 0.002 eV [50], see Fig. 8.11.

### 8.6.4 *Manipulation of the Energy Gap $\Delta E(S_1\text{-}T_1)$ with Laser Pulses*

The geometry optimized cycl[3.3.3]azine structures in the absence of applied laser were obtained at the CISD/cc-pVDZ theory level using the QChem code [51] along

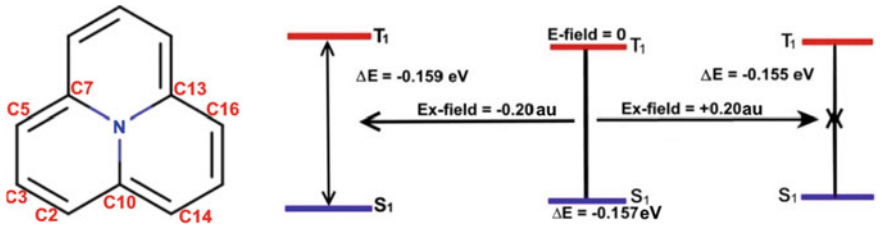


**Fig. 8.11** Schematic of the cycl[3.3.3]azine with numbering scheme (left-panel). The cycl[3.3.3]azine lowest-lying singlet ($S_1$) and triplet ($T_1$) states with the applied (+0.2/−0.2) **E**-field that is oriented parallel/anti-parallel to the C7-N *BCP* (right-panel)

with the corresponding singlet $S_0$, $S_1$ and triplet $T_1$ states. The static **E**-field results were calculated at the CASSCF (6,6)/cc-pVDZ theory level using the OpenMOLCAS code [52]. The laser pulse parameters used: phase = 0, **E**-field strength = 0.02 a.u. oriented parallel to the C7-N9 bond-path, laser central frequency matching energy = 0.35 eV, sinusoidal pulse shape 0.0–100.0 fs, with 1.0 fs rise and fall times, see Fig. 8.13. For the quadratic chirped pulse (inset figure of Fig. 8.13), the parameter in the frequency domain $b_2 = 1000\ fs^{-2}$ [53]. For the quantum mechanics: the ground-state structure was optimized using OpenMOLCAS at the CAS(RASSCF) (6,6)/6-31G* level state averaged over the three lowest CI roots, eploying spin–orbit coupling. For the dynamics, the same configuration was employed for the singlet $S_0$, $S_1$ and triplet $T_1$ states, more than ten instances of initial conditions were sampled from a Wigner distribution for each set of laser conditions and run as dynamics trajectories. Dynamics properties were sampled every 0.5 fs, with 25 intermediate dynamics steps, the SHARC hopping algorithm [53] was employed with spin–orbit coupling contributions included, states in diagonal representation, spin-corrected and fully adiabatic. An energy decoherence parameter of 0.1 a.u. was used [54], where frustrated hops not reflected and all electronic states active at selected points along the dynamics trajectories. The natural orbitals of the $S_1$ and $T_1$ electronic states were analyzed using the AIMALL software suite [55].

We found NG-QTAIM interpretation of the chemical bonding of the cycl[3.3.3]azine is that the directional characteristics of the bonding remains almost unchanged in response to the applied static electric-(**E**)-field, either taking values of K = 1.0 (weak, closed-shell *BCP* character) *or* K = 0.0 (strong, shared-shell *BCP* character). Furthermore, the use of unchirped and chirped laser pulses with an **E**-field with a magnitude of only 0.02 a.u. and 100 fs duration created regions of negative energy gaps $\Delta E(S_1\text{-}T_1) < 0$ and positive energy gaps $\Delta E(S_1\text{-}T_1) > 0$ that were orders of magnitude greater than was the case for the application of the static **E**-field, see Fig. 8.14. The response of the K to the laser pulses however, was very significant, since the effect in all cases was to remove the discontinuous transitions along the bond-paths between these two bonding character extremes. Therefore the unique ability of both chirped and unchirped laser pulses to induce polarization effects in the form of the smooth continuous twisting of the $\{\boldsymbol{p},\boldsymbol{p}'\}$ path-packet was indicated by

K possessing values *between* K = 1.0 and K = 0.0. Consequently, a broad spectrum of mixed bonding character types was induced, between the extremes of the rigid shared-shell character bonds, for K = 0.0 (strong, shared-shell *BCP* character) and the flexible closed-shell character bonds for K = 1.0 (weak, closed-shell *BCP* character). The continuous distribution of the precession K values indicated symmetry breaking effects for both the chirped and unchirped laser pulses, see Fig. 8.14.

The nuclear positions shift slightly as a consequence of the applied static **E**-field, but do not induce symmetry breaking effects in the form of continuous K values. This is because the electronic charge density distribution is allowed to relax to an energetic minimum, see Fig. 8.12. This symmetry breaking occurs, as a consequence of the application of the laser fields, because the nuclear positions shift slightly on much longer timescales than the response of the electronic charge density distribution. The response of the K to the laser pulses in all cases was to remove the discontinuous step-like transitions along the bond-paths between these two bonding character extremes. This indicates the unique ability of the laser pulses to induce polarization effects as determined by K possessing values *between* K = 1.0 and K = 0.0. Consequently, mixed bonding character types are induced, between the extremes of the rigid shared-shell character bonds, for K = 0.0 and the flexible closed-shell character bonds for K = 1.0. Therefore, the directional interpretation, the chemical bonding acquires a *range* of values between K = 1.0 (weak, closed-shell *BCP* character) and K = 0.0 (strong, shared-shell *BCP* character).

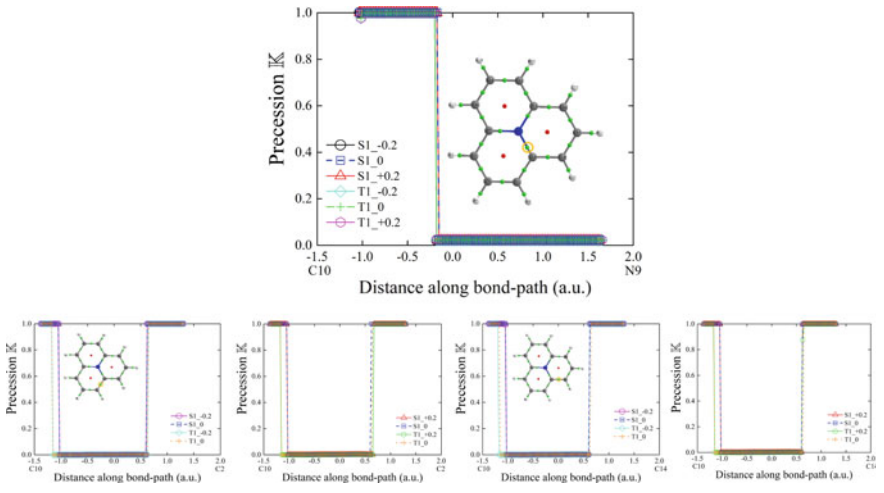


**Fig. 8.12** The values of the precessions K along the C10-N9 *BCP*, C10-C2 *BCP* and C10-C14 *BCP* bond-paths corresponding to the $S_1$ and $T_1$ excited states for an applied electric(**E**)-field = ±0.2 a.u are presented along with the corresponding precessions K for an **E**-field = 0, see Fig. 8.11 and the accompanying caption also

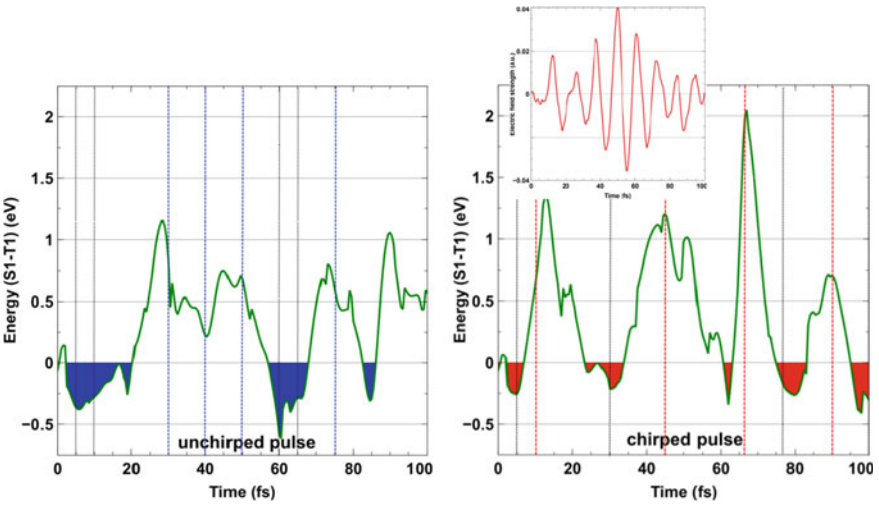


**Fig. 8.13** The cycl[3.3.3]azine lowest-lying singlet ($S_1$) and triplet ($T_1$) where the (±)**E**-field orientation is parallel/anti-parallel to the C7-N9 *BCP* bond-path. The $\Delta E(S_1\text{-}T_1)$ values of cycl[3.3.3]azine subject to unchirped laser pulses (left-panel) and chirped laser pulses (right-panel). The **E**-field was aligned parallel to the C7-N9 bond-path. Note, values of $\Delta E(S_1\text{-}T_1) < 0$ are contained within the blue shaded region and red shaded region. Black dotted lines indicate for the chirped pulse 10 fs, 45 fs, 67 fs, 90 fs ($\Delta E(S_1\text{-}T_1) > 0$) and red dashed lines for the chirped pulse 5 fs, 30 fs, 78 fs, 100 fs ($\Delta E(S_1\text{-}T_1) < 0$) in the left-panel. For the unchirped pulse (right-panel) the blue dashed lines indicate 30 fs, 40 fs, 50 fs, 75 fs ($\Delta E(S_1\text{-}T_1) > 0$) and black dotted lines indicate 5 fs, 10 fs, 60 fs, 65 fs ($\Delta E(S_1\text{-}T_1) < 0$)

## 8.7 Summary

Major breakthroughs have recently been reported [56–59] in the area of molecular electronics, but a workable strategy remains elusive. Therefore, to address this shortfall we used NG-QTAIM to provided new guiding principles to analyze a range of molecular devices with associated phenomena including molecular rotatory motors, switches, wires, emitters exhibiting thermally-activated delayed fluorescence (TADF), see Table 8.2. Conventionally, improvements of the switching properties, for instance of, complex diarylethene structures are generally attained using "trial and error" through chemical substitutions aimed at tuning the chemical properties of the core of the diarylethene. This provides consistent theoretical justification to partner the symmetric substitution patterns obtained from experiments and indicates more complex asymmetric patterns should be included for the systematic design of new technologically relevant functional compounds.

Our analysis of Fe-doped quinone-based switches as candidate building blocks of molecular junctions demonstrates promise for future use in design of molecular electronic devices. The ultimate aim of such research is to design a molecular electronic circuit, which would consist of assemblies of connected molecular switches. This will

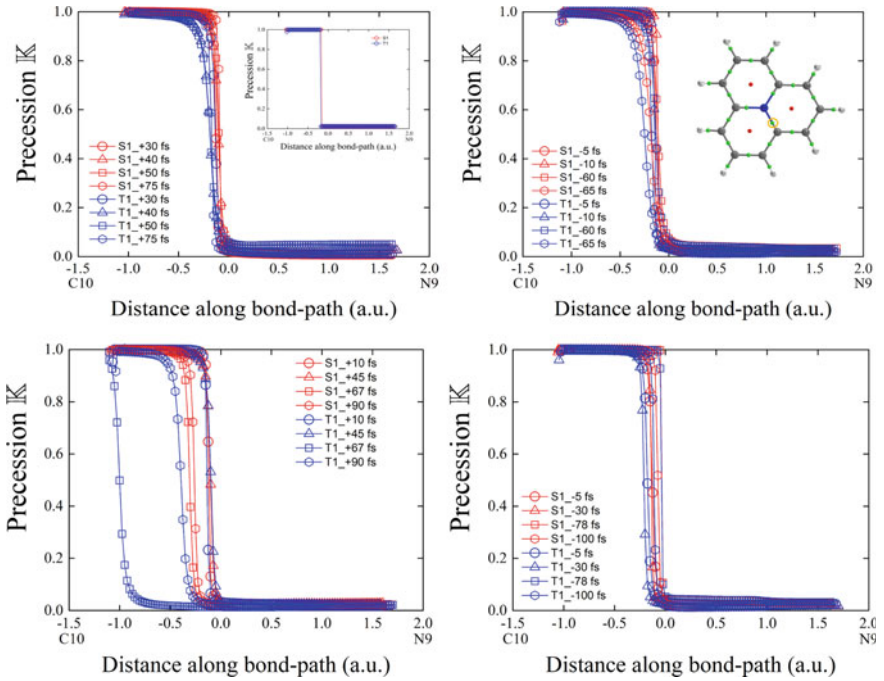


**Fig. 8.14** The values of the precession K along the C10-N9 *BCP* bond-paths for the $S_1$ and $T_1$ states. The unchirped pulses with a positive energy gap $\Delta E(S_1\text{-}T_1) > 0$ at 30 fs, 40 fs, 50 fs and 75 fs (top-left panel) with a negative energy gap $\Delta E(S_1\text{-}T_1) < 0$ at 5 fs, 10 fs, 60 fs and 65 fs (top-right panel). The chirped pulses with $\Delta E(S_1\text{-}T_1) > 0$ (bottom-left panel) at 10 fs, 45 fs, 67 fs and 90 fs and with $\Delta E(S_1\text{-}T_1) < 0$ (bottom-right) at 5 fs, 30 fs, 78 fs and 100 fs. The inset (top-left panel) displays the corresponding $S_1$ and $T_1$ states without the laser present. The highlighted C10-N9 *BCP* on the molecular graph is indicated by the orange circle on the (top-right panel)

require investigating the changes in switch behavior if multiple molecular switches are connected by molecular wires. As demonstrated NG-QTAIM has the ability to provide insights into switch performance such as 'ON' and 'OFF' functionality currently not attainable by other theoretical approaches. This will guide experimental investigations into building molecular electronic circuits. The determination of the directional effects e.g. of the precession K and K′, of an applied **E**-field on a given candidate switch molecule, for instance, can in future enable faster screening of candidate switch molecules to determine bond-path fatigue and bond-path fatigue resistance.

Future investigations of the F-NAIBP motor that was known to possess very 'jittery' $T_\sigma(s)$ associated with the axle bond for all the dynamics trajectories, could use laser irradiation to improve the F-NAIBP motor functioning. For instance, determining the dependency of the phase of a laser on gaining improvements in the quality of the unidirectional motion in terms of the smoothness and direction of the $T_\sigma(s)$ associated with the axle bond.

**Table 8.2** Summary of the mechanisms, dominant nuclear versus electronic motion. The degree of nuclear motion decreases for entries down the table. B denoted the bond-path framework set B. The energy gap of the cycl[3.3.3]azine lowest-lying singlet ($S_1$) and triplet ($T_1$) states is denoted by $\Delta E(S_1\text{-}T_1)$

| Molecular device | Mechanism | Nuclear versus electronic motion | Trigger | Sections |
|---|---|---|---|---|
| Molecular rotatory motor | Stereo-control | Nuclear skeleton torsion | Photoexcitation | 8.2 |
| Switch | 'ON'/'OFF' function | H-atom transfer tautomerization | Fe-doping | 8.3.1 |
| Switch | 'ON'/'OFF' function | H-atom transfer tautomerization | Fe-doping and **E**-field | 8.3.2 |
| Switch | Ring restoration | Ring 'open/closed' position | Photoexcitation | 8.4 |
| Switch | Fatigue | Anisotropic redistribution of $\rho(\mathbf{r})$ | Photoexcitation | 8.5.1 |
| Switch | Fatigue | Anisotropic redistribution of $\rho(\mathbf{r})$ | S-doping and **E**-field | 8.5.1 |
| Molecular wire | B polarization | Anisotropic redistribution of $\rho(\mathbf{r})$ | **E**-field | 8.6.1 |
| TADF emitter | B polarization | Anisotropic redistribution of $\rho(\mathbf{r})$ | **E**-field | 8.6.3 |
| TADF emitter | B polarization | Anisotropic redistribution of $\rho(\mathbf{r})$ | Chirped/unchirped laser | 8.6.4 |

The determination of the response of the lowest-lying singlet ($S_1$) and triplet ($T_1$) states of cycl[3.3.3]azine to a static electric-(**E**)-field and unchirped and chirped laser pulses with NG-QTAIM uncovered new insights. The time scale of the laser pulse is faster compared to that $T_1 \rightarrow S_1$ or $S_1 \rightarrow T_1$ state transitions because the latter is thermally activated, therefore the ability to account for the response of electrons is highly relevant.

In particular we found, in all cases, a greater response of the precessions K to the unchirped and chirped laser irradiation than to the static **E**-field, despite the magnitude of the **E**-field being an order of magnitude greater than that of the laser. The symmetry breaking effect of both the chirped and unchirped laser pulses occurs because the nuclear positions shift slightly as a consequence of the application of the laser fields, but on much longer timescales than the response of the electronic charge density distribution. The nuclear positions also shift slightly as a consequence of the applied static **E**-field, but no symmetry breaking effects, in the form of continuous K

values, are apparent because the corresponding electronic charge density distribution is allowed to relax to an energetic minimum. The dependency of the laser induced effects explains the success of NG-QTAIM due to the ability to remove the reliance on the very slow changing nuclear positions and instead consider the must faster changing electronic charge density distribution. Future investigations into the design of negative energy gap OLEDs could focus on engineering the shape of the chirped laser pulse to produce a higher rate of induced negative singlet–triplet gaps.

The results of this chapter demonstrate that NG-QTAIM has provided a useful tool for the future design of molecular electronic devices.

Electron dynamics and non-adiabatic molecular dynamics simulations of the effects of the non-ionizing ultra-fast laser irradiation on the electronic and nuclear coordinates down to the sub-femtosecond or lower (attosecond) timescales are in the process of being undertaken. Codes will be chosen that allow the propagation of electron dynamics due to multiple non-ionizing ultra-fast laser pulses with controlled duration, shape, polarization and frequency content, enabling control of molecular devices using laser-induced mixtures of states. The desired behavior of molecular devices will be obtained using a non-ionizing ultra-fast laser and NG-QTAIM feedback process which we refer to as third generation eigenvector-space directed trajectory $T_i(\boldsymbol{s})$:

I. NG-QTAIM properties of the molecular device will be determined by using a low intensity non-ionizing ultra-fast (sub-femtosecond) laser pulse to minimally perturb the total electronic charge density distribution whilst avoiding any perturbation of the nuclear coordinates.
II. A higher intensity non-ionizing ultra-fast laser pulse will perturb the total electronic charge density distribution without disturbing the nuclear coordinates.
III. Nuclear coordinates respond to the non-ionizing ultra-fast laser pulse on a much longer timescale. Finally the effects of the subsequent laser-induced nuclear rearrangements on the total electronic charge density distribution are then probed with a final non-ionizing ultra-fast low intensity laser pulse.
IV. Adapt the non-ionizing ultra-fast laser pulse parameters using NG-QTAIM to provide continuous feedback from steps (**II** and **III**) until optimal switch and molecular motor behaviors are obtained.

**Target learning outcomes**:

- The importance of using non-scalar measures for molecular devices design (Sects. 8.1–8.6.4).
- Understand the functioning of switches 'ON'/'OFF' mechanisms: hydrogen transfer tautomerization and effect of **E**-Fields (Sect. 8.3).
- Understand the directional effects of switch ring-opening (open/closed) reactions (Sect. 8.4).
- Understand the effects of atom doping and **E**-Fields on the mechanism of fatigue of switches (Sect. 8.5.1).
- Understand why laser pulses are much more effective than static **E**-fields for the manipulation of the $\Delta E(S_1\text{-}T_1)$ energy gap with (Sects. 8.6.3 and 8.6.4).

## 8.8 Further Reading

For an introduction to molecular electronics see Ratner [1]. The review by Zhang highlights recent advances in molecular switches triggered by various external stimuli [2]. The review of Komoto et al. presents a select of current methods used to address the electronic and structural details of a single-molecule junction [3].

## References

1. Ratner MA (2002) Introducing molecular electronics. Mater Today 5:20–27
2. Zhang JL, Zhong JQ, Lin JD, Hu WP, Wu K, Xu GQ, Wee ATS, Chen W (2015) Towards single molecule switches. Chem Soc Rev 44:2998–3022
3. Komoto Y, Fujii S, Iwane M, Kiguchi M (2016) Single-molecule junctions for molecular electronics. J Mater Chem C 4:8842–8858
4. Baum P, Lochbrunner S, Riedle E (2004) Tunable sub-10-fs ultraviolet pulses generated by achromatic frequency doubling. Ol/29/14/ol Pdf 29:1686
5. Zewail AH (2001) Femtochemistry: atomic-scale dynamics of the chemical bond using ultrafast lasers (nobel lecture). In: Femtochemistry. Wiley, 2001, pp 1–85
6. Maza JR, Jenkins S, Kirk SR, Anderson JSM, Ayers PW (2013) The Ehrenfest force topology: a physically intuitive approach for analyzing chemical interactions. Phys Chem Chem Phys 15:17823–17836
7. Azizi A, Momen R, Xu T, Kirk SR, Jenkins S (2018) Non-nuclear attractors in small charged lithium clusters, Limq ($m = 2–5$, $q = \pm 1$), with QTAIM and the Ehrenfest force partitioning. Phys Chem Chem Phys 20:24695–24707
8. Azizi A, Momen R, Kirk SR, Jenkins S (2019) 3-D bond-paths of QTAIM and the stress tensor in neutral lithium clusters, Lim ($m = 2–5$), presented on the ehrenfest force molecular graph. Phys Chem Chem Phys 22:864–877
9. Xu T, Li JH, Momen R, Huang WJ, Kirk SR, Shigeta Y, Jenkins S (2019) Chirality-helicity equivalence in the S and R stereoisomers: a theoretical insight. J Am Chem Soc 141:5497–5503
10. Kling MF, Vrakking MJJ (2008) Attosecond electron dynamics. Annu Rev Phys Chem 59:463–492
11. van Delden RA, ter Wiel MKJ, Feringa BL (2004) A chiroptical molecular switch with perfect stereocontrol. Chem Commun 200–201 (2004). https://doi.org/10.1039/B312170D
12. Nikiforov A, Gamez JA, Thiel W, Filatov M (2016) Computational design of a family of light-driven rotary molecular motors with improved quantum efficiency. J Phys Chem Lett 7:105–110
13. Wang L, Huan G, Momen R, Azizi A, Xu T, Kirk SR, Filatov M, Jenkins S (2017) QTAIM and stress tensor characterization of intramolecular interactions along dynamics trajectories of a light-driven rotary molecular motor. J Phys Chem A 121:4778–4792
14. Wang L, Azizi A, Momen R, Xu T, Kirk SR, Filatov M, Jenkins S (2020) Next-generation quantum theory of atoms in molecules for the S1/S0 conical intersections in dynamics trajectories of a light-driven rotary molecular motor. Int J Quantum Chem 120:e26062
15. Li Z, Nie X, Xu T, Li S, Yang Y, Früchtl H, van Mourik T, Kirk SR, Paterson MJ, Shigeta Y, Jenkins S (2021) Control of chirality, bond flexing and anharmonicity in an electric field. Int J Quantum Chem 121:e26793
16. Fruchtl H, van Mourik T (2018) A quinone based single-molecule switch as building block for molecular electronics. arXiv:1801.01001 [physics]
17. Xu T, Wang L, Ping Y, van Mourik T, Früchtl H, Kirk SR, Jenkins S (2018) Quinone-based switches for candidate building blocks of molecular junctions with QTAIM and the stress tensor. Int J Quantum Chem 118:e25676

18. Tian T, Xu T, van Mourik T, Früchtl H, Kirk SR, Jenkins S (2019) Next generation QTAIM for the design of quinone-based switches. Chem Phys Lett 722:110–118
19. Xu T, Bin X, Kirk SR, Wales DJ, Jenkins S (2020) Flip rearrangement in the water pentamer: analysis of electronic structure. Int J Quantum Chem 120:e26124
20. Xu T, Momen R, Azizi A, van Mourik T, Früchtl H, Kirk SR, Jenkins S (2019) The destabilization of hydrogen bonds in an external E-field for improved switch performance. J Comput Chem 40:1881–1891
21. Tian T, Xu T, Kirk SR, Filatov M, Jenkins S (2019) Next-generation quantum theory of atoms in molecules for the ground and excited state of the ring-opening of cyclohexadiene (CHD). Int J Quantum Chem 119:e25862
22. Yang P, Xu T, Momen R, Azizi A, Kirk SR, Jenkins S (2018) Fatigue and photochromism S1 excited state reactivity of diarylethenes from QTAIM and the stress tensor. Int J Quantum Chem 118:e25565
23. Nie X, Yang Y, Xu T, Kirk SR, Jenkins S (2021) Fatigue and fatigue resistance in S1 excited state diarylethenes in electric fields. Int J Quantum Chem 121:e26527
24. Moore GE (1998) Cramming more components onto integrated circuits. Proc IEEE 86:82–85
25. Saenz A (2000) Enhanced ionization of molecular hydrogen in very strong fields. Phys Rev A 61:051402
26. Saenz A (2002) Behavior of molecular hydrogen exposed to strong dc, ac, or low-frequency laser fields. I. Bond softening and enhanced ionization. Phys Rev A 66:063407
27. Medin Z, Lai D (2006) Density-functional-theory calculations of matter in strong magnetic fields. II. Infinite chains and condensed matter. Phys Rev A 74:062508
28. Petretti S, Vanne YV, Saenz A, Castro A, Decleva P (2010) Alignment-dependent Ionization of N2, O2, and CO2 in intense laser fields. Phys Rev Lett 104:223001
29. Shaik S, Mandal D, Ramanan R (2016) Oriented electric fields as future smart reagents in chemistry. Nat Chem 8:1091–1098
30. Shaik S, Ramanan R, Danovich D, Mandal D (2018) Structure and reactivity/selectivity control by oriented-external electric fields. Chem Soc Rev 47:5125–5145
31. Wang Z, Danovich D, Ramanan R, Shaik S (2018) Oriented-external electric fields create absolute enantioselectivity in Diels-Alder reactions: importance of the molecular dipole moment. J Am Chem Soc 140:13350–13359
32. Sowlati-Hashjin S, Matta CF (2013) The chemical bond in external electric fields: energies, geometries, and vibrational Stark shifts of diatomic molecules. J Chem Phys 139:144101
33. Azizi A, Momen R, Früchtl H, van Mourik T, Kirk SR, Jenkins S (2020) Next-generation QTAIM for scoring molecular wires in E-fields for molecular electronic devices. J Comput Chem 41:913–921
34. Olivier Y, Sancho-Garcia J-C, Muccioli L, D'Avino G, Beljonne D (2018) Computational design of thermally activated delayed fluorescence materials: the challenges ahead. J Phys Chem Lett 9:6149–6163
35. Chen X-K, Kim D, Brédas J-L (2018) Thermally activated delayed fluorescence (TADF) path toward efficient electroluminescence in purely organic materials: molecular level insight. Acc Chem Res 51:2215–2224
36. Penfold TJ, Dias FB, Monkman AP (2018) The theory of thermally activated delayed fluorescence for organic light emitting diodes. Chem Commun 54:3926–3935
37. Dias FB, Penfold TJ, Monkman AP (2017) Photophysics of thermally activated delayed fluorescence molecules. Methods Appl Fluoresc 5:012001
38. Uoyama H, Goushi K, Shizu K, Nomura H, Adachi C (2012) Highly efficient organic light-emitting diodes from delayed fluorescence. Nature 492:234–238
39. Huang S, Zhang Q, Shiota Y, Nakagawa T, Kuwabara K, Yoshizawa K, Adachi C (2013) Computational prediction for singlet- and triplet-transition energies of charge-transfer compounds. J Chem Theory Comput 9:3872–3877
40. Penfold TJ (2015) On predicting the excited-state properties of thermally activated delayed fluorescence emitters. J Phys Chem C 119:13535–13544

41. Sun H, Zhong C, Brédas J-L (2015) Reliable prediction with tuned range-separated functionals of the singlet-triplet gap in organic emitters for thermally activated delayed fluorescence. J Chem Theory Comput 11:3851–3858
42. Hait D, Zhu T, McMahon DP, Van Voorhis T (2016) Prediction of excited-state energies and singlet-triplet gaps of charge-transfer states using a restricted open-shell Kohn-Sham approach. J Chem Theory Comput 12:3353–3359
43. Valchanov G, Ivanova A, Tadjer A, Chercka D, Baumgarten M (2016) Understanding the fluorescence of TADF light-emitting dyes. J Phys Chem A 120:6944–6955
44. Moral M, Muccioli L, Son W-J, Olivier Y, Sancho-García JC (2015) Theoretical rationalization of the singlet-triplet gap in OLEDs materials: impact of charge-transfer character. J Chem Theory Comput 11:168–177
45. Chen T, Zheng L, Yuan J, An Z, Chen R, Tao Y, Li H, Xie X, Huang W (2015) Understanding the control of singlet-triplet splitting for organic exciton manipulating: a combined theoretical and experimental approach. Sci Rep 5:10923
46. Kasha M (1950) Characterization of electronic transitions in complex molecules. Discuss Faraday Soc 9:14–19
47. Difley S, Beljonne D, Van Voorhis T (2008) On the singlet−triplet splitting of geminate electron−hole pairs in organic semiconductors. J Am Chem Soc 130:3420–3427
48. Olivier Y, Yurash B, Muccioli L, D'Avino G, Mikhnenko O, Sancho-García JC, Adachi C, Nguyen T-Q, Beljonne D (2017) Nature of the singlet and triplet excitations mediating thermally activated delayed fluorescence. Phys Rev Mater 1:075602
49. de Silva P, Kim CA, Zhu T, Van Voorhis T (2019) Extracting design principles for efficient thermally activated delayed fluorescence (TADF) from a simple four-state model. Chem Mater 31:6995–7006
50. Li Z, Yang Y, Xu T, Früchtl H, van Mourik T, Paterson MJ, Shigeta Y, Kirk SR, Jenkins S (2022) Next generation QTAIM for the design of emitters exhibiting thermally-activated delayed fluorescence (TADF) with laser irradiation. J Comput Chem 43:206–214
51. Shao Y, Gan Z, Epifanovsky E, Gilbert ATB, Wormit M, Kussmann J, Lange AW, Behn A, Deng J, Feng X, Ghosh D, Goldey M, Horn PR, Jacobson LD, Kaliman I, Khaliullin RZ, Kuś T, Landau A, Liu J, Proynov EI, Rhee YM, Richard RM, Rohrdanz MA, Steele RP, Sundstrom EJ, III, HLW, Zimmerman PM, Zuev D, Albrecht B, Alguire E, Austin B, Beran GJO, Bernard YA, Berquist E, Brandhorst K, Bravaya KB, Brown ST, Casanova D, Chang C-M, Chen Y, Chien SH, Closser KD, Crittenden DL, Diedenhofen M, Jr RAD, Do H, Dutoi AD, Edgar RG, Fatehi S, Fusti-Molnar L, Ghysels A, Golubeva-Zadorozhnaya A, Gomes J, Hanson-Heine MWD, Harbach PHP, Hauser AW, Hohenstein EG, Holden ZC, Jagau T-C, Ji H, Kaduk,B, Khistyaev K, Kim J, Kim J, King RA, Klunzinger P, Kosenkov D, Kowalczyk T, Krauter CM, Lao KU, Laurent AD, Lawler KV, Levchenko SV, Lin CY, Liu F, Livshits E, Lochan RC, Luenser A, Manohar P, Manzer SF, Mao S-P, Mardirossian N, Marenich AV, Maurer SA, Mayhall NJ, Neuscamman E, Oana CM, Olivares-Amaya R, O'Neill DP, Parkhill JA, Perrine TM, Peverati R, Prociuk A, Rehn DR, Rosta E, Russ NJ, Sharada SM, Sharma S, Small DW, Sodt A, Stein T, Stück D, Su Y-C, Thom AJW, Tsuchimochi T, Vanovschi V, Vogt L, Vydrov O, Wang T, Watson MA, Wenzel J, White A, Williams CF, Yang J, Yeganeh S, Yost SR, You Z-Q, Zhang IY, Zhang X, Zhao Y, Brooks BR, Chan GKL, Chipman DM, Cramer CJ, III WAG, Gordon MS, Hehre WJ, Klamt A, III HFS, Schmidt MW, Sherrill CD, Truhlar DG, Warshel A, Xu X, Aspuru-Guzik A, Baer R, Bell AT, Besley NA, Chai J-D, Dreuw A, Dunietz BD, Furlani TR, Gwaltney SR, Hsu C-P, Jung Y, Kong J, Lambrecht DS, Liang W, Ochsenfeld C, Rassolov VA, Slipchenko LV, Subotnik JE, Voorhis TV, Herbert JM, Krylov AI, Gill PMW, Head-Gordon M (2015) Advances in molecular quantum chemistry contained in the Q-Chem 4 program package. Mol Phys 113:184–215
52. Fdez Galván I, Vacher M, Alavi A, Angeli C, Aquilante F, Autschbach J, Bao JJ, Bokarev SI, Bogdanov NA, Carlson RK, Chibotaru LF, Creutzberg J, Dattani N, Delcey MG, Dong SS, Dreuw A, Freitag L, Frutos LM, Gagliardi L, Gendron F, Giussani A, González L, Grell G, Guo M, Hoyer CE, Johansson M, Keller S, Knecht S, Kovačević G, Källman E, Li Manni G, Lundberg M, Ma Y, Mai S, Malhado JP, Malmqvist PÅ, Marquetand P, Mewes SA, Norell

J, Olivucci M, Oppel M, Phung QM, Pierloot K, Plasser F, Reiher M, Sand AM, Schapiro I, Sharma P, Stein CJ, Sørensen LK, Truhlar DG, Ugandi M, Ungur L, Valentini A, Vancoillie S, Veryazov V, Weser O, Wesołowski TA, Widmark P-O, Wouters S, Zech A, Zobel JP, Lindh R (2019) OpenMolcas: from source code to insight. J Chem Theory Comput 15:5925–5964
53. Mai S, Marquetand P, González L (2018) Nonadiabatic dynamics: the SHARC approach. WIREs Comput Mol Sci 8:e1370
54. Granucci G, Persico M, Zoccante A (2010) Including quantum decoherence in surface hopping. J Chem Phys 133:134111
55. Keith TA (2017) AIMAll, Revision 17.01.25. TK Gristmill Software
56. Ayers PW, Jenkins S (2015) Bond metallicity measures. Comput Theor Chem 1053:112–122
57. Jenkins S, Maza JR, Xu T, Jiajun D, Kirk SR (2015) Biphenyl: a stress tensor and vector-based perspective explored within the quantum theory of atoms in molecules. Int J Quantum Chem 115:1678–1690
58. Jiajun D, Maza JR, Xu Y, Xu T, Momen R, Kirk SR, Jenkins S (2016) A stress tensor and QTAIM perspective on the substituent effects of biphenyl subjected to torsion. J Comput Chem 37:2508–2517
59. Guo H, Morales-Bayuelo A, Xu T, Momen R, Wang L, Yang P, Kirk SR, Jenkins S (2016) Distinguishing and quantifying the torquoselectivity in competitive ring-opening reactions using the stress tensor and QTAIM. J Comput Chem 37:2722–2733

# Appendix A

See Tables A1 and A2.

**Table A1** Units of measurement

| | |
|---|---|
| 4.184 J (J) | 1 thermochemical calorie (cal) |
| 1 thermochemical calorie (cal) | $4.184 \times 10^{7}$ erg |
| Erg | $10^{-7}$ J (exact, definition) |
| Electron-volt (eV) | $1.60218 \times 10^{-19}$ J = 23.061 kcal $mol^{-1}$ |
| Nutritional calorie (Cal) | 1000 cal (exact, definition) = 4184 J |
| British thermal unit (BTU) | 1054.804 J |
| 1 Hartree (Eh) | 27.2113834 electron-volts (eV) |
| 1 $cm^{-1}$ | 29,979.2458 MHz |
| 1 $a_0$ | 0.5291772083 Å |

**Table A2** International system of units (SI) prefixes

| Symbol | Prefix | Multiplication factor |
|---|---|---|
| T | Tera | $10^{12}$ |
| G | Giga | $10^{9}$ |
| M | Mega | $10^{6}$ |
| k | Kilo | $10^{3}$ |
| h | Hecto | $10^{2}$ |
| da | Deka | $10^{1}$ |
| d | Deci | $10^{-1}$ |
| c | Centi | $10^{-2}$ |

(continued)

© The Editor(s) (if applicable) and The Author(s), under exclusive license to Springer Nature Singapore Pte Ltd. 2023

S. Jenkins and S. R. Kirk, *Next Generation Quantum Theory of Atoms in Molecules*, Lecture Notes in Chemistry 110, https://doi.org/10.1007/978-981-99-0329-0

**Table A2** (continued)

| Symbol | Prefix | Multiplication factor |
|---|---|---|
| m | Milli | $10^{-3}$ |
| μ | Micro | $10^{-6}$ |
| n | Nano | $10^{-9}$ |
| p | Pico | $10^{-12}$ |
| f | Femto | $10^{-15}$ |
| a | Atto | $10^{-18}$ |
| z | Zepto | $10^{-21}$ |
| y | Yocto | $10^{-24}$ |

# Appendix B

## Mathematical Derivations

Diagonalization of the 3 × 3 Hessian matrix $\boldsymbol{A}(\boldsymbol{r_c})$, see Eq. (B.1), at a critical point $\boldsymbol{r_c}$ critical points of $\nabla\rho(\boldsymbol{r})$ where $\nabla\rho(\boldsymbol{r}) = 0$ results in the eigenvectors ($\underline{\mathbf{e}}_1$, $\underline{\mathbf{e}}_2$, $\underline{\mathbf{e}}_3$) and eigenvalues $|\lambda_1| < |\lambda_2| < |\lambda_3|$. The sum of the eigenvalues corresponds to the Laplacian $\nabla^2\rho(\boldsymbol{r}_b) = \lambda_1 + \lambda_2 + \lambda_3$, see Eq. (2).

$$A(\boldsymbol{r_c}) = \begin{pmatrix} \frac{\partial^2\rho(\boldsymbol{r})}{\partial x^2} & \frac{\partial^2\rho(\boldsymbol{r})}{\partial x\partial y} & \frac{\partial^2\rho(\boldsymbol{r})}{\partial x\partial z} \\ \frac{\partial^2\rho(\boldsymbol{r})}{\partial y\partial x} & \frac{\partial^2\rho(\boldsymbol{r})}{\partial y^2} & \frac{\partial^2\rho(\boldsymbol{r})}{\partial y\partial z} \\ \frac{\partial^2\rho(\boldsymbol{r})}{\partial z\partial x} & \frac{\partial^2\rho(\boldsymbol{r})}{\partial z\partial y} & \frac{\partial^2\rho(\boldsymbol{r})}{\partial z^2} \end{pmatrix}_{\boldsymbol{r}=\boldsymbol{r_c}} \rightarrow \begin{pmatrix} \frac{\partial^2\rho(\boldsymbol{r})}{\partial x'^2} & 0 & 0 \\ 0 & \frac{\partial^2\rho(\boldsymbol{r})}{\partial y'^2} & 0 \\ 0 & 0 & \frac{\partial^2\rho(\boldsymbol{r})}{\partial z'^2} \end{pmatrix}_{\boldsymbol{r}'=\boldsymbol{r_c}} = \begin{pmatrix} \lambda_1 & 0 & 0 \\ 0 & \lambda_2 & 0 \\ 0 & 0 & \lambda_3 \end{pmatrix} \tag{B.1}$$

$$\nabla^2\rho(\boldsymbol{r}) = \nabla\cdot\nabla\,\rho(\boldsymbol{r}) = \underbrace{\frac{\partial^2\rho(\boldsymbol{r})}{\partial x'^2}}_{\lambda_1} + \underbrace{\frac{\partial^2\rho(\boldsymbol{r})}{\partial y'^2}}_{\lambda_2} + \underbrace{\frac{\partial^2\rho(\boldsymbol{r})}{\partial z'^2}}_{\lambda_3} \tag{B. 2}$$

### Recommended Reading


1. Steiner E (2008) The chemistry maths book, 2nd edn. Oxford University Press, Oxford
2. Pence TJ, Wichman IS (2020) Essential mathematics for engineers and scientists, 1st edn. Cambridge University Press, Cambridge
3. Doggett G, Cockett M (2012) Maths for chemists: RSC, Second edition, New edition. Royal Society of Chemistry, Cambridge


© The Editor(s) (if applicable) and The Author(s), under exclusive license to Springer Nature Singapore Pte Ltd. 2023

S. Jenkins and S. R. Kirk, *Next Generation Quantum Theory of Atoms in Molecules*, Lecture Notes in Chemistry 110, https://doi.org/10.1007/978-981-99-0329-0

# Index


**0-9**
[1,1,1]propellene, 22
[1.1.1]propellane molecule, 77, 80, 89
1,2-dichlorocyclobutane, 22
1,2-dichloroethane, 22
1,3,5-hexatriene (HT), 80, 81
1,3-cyclohexadiene (CHD), 80, 81, 89
1,4-dichlorobutane, 22
1-cyano-1-methylcyclobutene, 141, 148
1H NMR spectroscopy, 17
3-D, 15, 16, 20, 21, 24, 25, 29, 36
3-[(2S)-2-fluoro-2-methyl-1-indanylidene]-1-methyl-2-methylindole (F-NAIBP) molecular rotary motor, 194
3-(trifluoromethyl)cyclobut-1-ene, 141, 148
[4]cumulene, 22

**A**
*Ab-initio*, 1
Achiral, 130, 149
AIMALL software suite, 208
Alanine, 155, 156, 158, 159, 166, 179, 183
Allotrope, 24
Amino acid, 56–58, 61–63
Anharmonic, 73
Anions, 4, 6
Anti-symmetric stretch vibrational mode, 48, 50
Aromatic hydrocarbon, 18
Astrochemistry, 150
Asymmetric synthetic reaction, 186
Asymmetry, 55, 60, 62
Atomic coordination number, 16, 42
Atomic Interaction Line (AIL), 17
Atomic Natural Orbital (ANO-RCC) GTO basis set, 107
Atomic surface, 104
Attosecond laser, 193
Aug-cc-pV5Z basis set, 107
Azophenine, 196

**B**
B3LYP-D3(BJ), 7
Basin-Path set Area (BPA), 37, 38
Basis function, 2, 4, 5
Basis set, 2–6, 8, 10
Bending vibrational mode, 48–50
Benzene, 11, 22, 34
Benzoquinone, 38
Benzvalene, 11
Biomolecular chemistry, 150
Biphenyl, 33, 34, 36, 37
Bond, 16, 17, 23, 26, 33, 36–38, 40, 42
Bond-axiality, 133, 135, 138, 139
Bond-compression, 70
Bond Critical Point (*BCP*), 17–21, 25, 27, 28, 31–42
Bond-curving, 70, 72, 73
Bond distances, 1
Bonding interaction, 81
Bond metallicity, 15
Bond-path, 11, 17, 18, 20, 31, 36–40, 47, 48, 50–54, 57, 60, 62, 63, 65–78, 80–89, 93, 95–99, 101, 104, 105, 108, 112, 114, 115, 118–121, 123, 129, 131, 134, 136, 138, 142, 143, 154, 155, 158, 160, 164, 169–172, 179, 184, 191, 193, 195–197, 199, 200, 202–206, 208–212
Bond-path curvature, 68, 70–72


© The Editor(s) (if applicable) and The Author(s), under exclusive license to Springer Nature Singapore Pte Ltd. 2023

S. Jenkins and S. R. Kirk, *Next Generation Quantum Theory of Atoms in Molecules*, Lecture Notes in Chemistry 110, https://doi.org/10.1007/978-981-99-0329-0

Bond-path-flexibility, 69, 84, 86
Bond-path flexing, 73
Bond-path framework set, 11
Bond-Path Length (BPL), 18, 37
Bond-path twisting, 72
Bond-polarizability, 16
Bond stiffness, 16
Bond-stretching, 70
Bond torsion, 47, 48, 52, 63
Born-Oppenheimer (B.O.) approximation, 132
Bound state, 17
Branching ratio, 81

**C**
Cage Critical Point (*CCP*), 18–21, 23, 25
Cahn-Ingold-Prelog (CIP) rules, 154, 157, 175, 180, 188
Calculated spectra, 72
Candidate site, 201
Cartesian coordinate, 9
Catalytic chemistry, 186
Cc-pV5Z basis set, 107
Cc-pV6Z basis set, 107
Charge shift ratio, 40
Chemical bond, 11
Chemical coupling, 119, 122
Chemical half-life, 101
Chemical reactivity, 16
Chemical structure, 16
Chiral, 130, 149
Chiral center, 154–156, 158, 179, 186
Chiral discrimination, 12, 153, 154, 156, 158, 160, 187, 188
Chiral dynamics, 186
Chirality, 12
Chirality-helicity equivalence, 154–156, 158, 159, 166, 184
Chirality-helicity function, 12, 153, 160, 164–167, 169, 170, 174, 180, 183, 186–188
Chiral mixing, 12
Chiral-optical molecular rotary motor, 186
Chiral selectivity, 186
Chirped laser pulse, 203, 207–210, 212, 213
Chloroethane, 166
*Cis*-effect, 183, 184, 188
*Cis*-isomer, 23
Closed-shell bond, 16, 32, 36
Closed-shell bonding, 32, 36
Closed-shell system, 7
Cluster, 15, 16, 18–20, 24–26, 28, 31, 32, 36, 40, 42, 43
Competitive ring-opening reaction, 127, 130, 140, 141, 148
Complete Basis Set (CBS) limit, 6
Compressive eigenvector, 94, 95
Configuration interaction (HF/CIS, CASSCF and MRCI), 17
Conical intersection, 36
Conical Intersection (CI) seam, 55, 56, 62, 63
Conjugate gradient, 9
Coordinate frame, 128
Coordination compound, 154
Coordination number, 15, 16, 32, 42
Core electrons, 5, 6
Covalent character, 16, 18, 32, 33, 36, 42
Covalent electronic configuration, 87
CRITIC2, 17
Critical point, 15–21, 23, 24, 26, 31, 42, 43
Cubic Ice (ice Ic), 11, 24, 26, 33
Cycl[3.3.3]azine, 206–208, 210, 212
Cyclic contryphan-Sm peptide, 23

**D**
Delocalization, 38
Density Functional Theory (DFT), 6, 7, 10, 17
Deuterium, 11
Deuterium labeling, 150
Diagonal Born-Oppenheimer Energy Correction (DBOC), 161
Diels–Alder reaction, 188
Diffuse basis functions, 8
Dihedral, 1
Dihydrocostunolide (DHCL), 33
Dihydrogen bonding, 18
Diradical electronic configuration, 87
Dunning's correlation-consistent basis set, 5
Dynamic correlation, 87
Dynamic coupling, 127, 135, 136, 138

**E**
Eclipsing effect, 184
Effective Core Potentials (ECPs), 2, 5, 8
Ehrenfest Force, 11, 12
Ehrenfest Force partitioning, 40
Ehrenfest Force trajectory, 127–129, 141–143, 149
Ehrenfest potential, 105
Eigenfunction, 1
Eigenvalue, 1, 10, 17, 18, 36–38, 40
Eigenvector-following path, 67, 68, 70, 71

Eigenvector following path length, 98, 99, 105
Eigenvectors, 17, 18, 38
Eigenvector-space trajectories, 11
Electric (E)-field, 12
Electric field, 160–163, 179, 180, 188
Electron dynamics, 213
Electron following, 47
Electronic charge density, 1, 11
Electronic degrees of freedom, 1
Electronic structure, 87, 89
Electronic wave-packet, 80
Electron momentum transfer, 112, 115, 122
Electron-preceding, 53
Electrons, 3–8
Electrostatic potential, 16, 25, 43
Ellipticity, 18
Empirical dispersion correction, 7
Enantiomer, 149
Enantioselectivity, 188
Energetic stability, 87
Energy, 2, 3, 5–7, 9, 12
Ensemble density functional theory, 193
Ethane, 22, 153, 154, 169–176, 179, 183, 187, 188
Ethene, 93, 96, 97, 123
Ethylene oxide, 22
Ethyne, 22
Euclidian geometry, 15, 16, 43
Euler characteristic, 25–27, 40
Euler–Poincaré relation, 20
Excited state, 80, 82, 87–89
Excited state deactivation reaction, 82, 84
Expansion coefficient, 2
Experimental data, 16

**F**
Facile character, 58, 69, 86
Fatigue, 123
Fatigue bond, 202, 204
Fatigue mechanism, 201
Fatigue reaction, 201
Fatigue resistance, 202, 203, 211
Fe-doped quinone-based switch, 210
Femtosecond timescale, 192
First generation stress tensor trajectories, 153, 157, 160, 184
First-order density matrix, 38
Fissile σ-bond, 81
Flip rearrangement, 12
Fluorine, 197
*f* orbitals, 5
Fractional eigenvector-following path length, 71
Fulvene, 22

**G**
Gaussian function, 4, 6
Gaussian Type Orbital (GTOs), 3–5, 8
Gauss's theorem, 104
Geometric Bond Length (GBL), 18, 19
Geometry optimization, 2, 5, 6, 9
Global minimum structure, 9
Glycine, 12, 22
Gold sandwich complex $[Sb_3Au_3Sb_3]^{3-}$, 22
Gradient vector field, 17
Gridded densities, 17
Ground state, 66, 68, 69, 80, 82, 88

**H**
$H_2O$, 99, 100, 114–116, 119
$(H_2O)_2$, 114–116
$(H_2O)_4$, 22, 24, 29, 36
$(H_2O)_5$, 24, 27, 28, 33, 36, 42
$(H_2O)_6$, 15, 23, 24, 36
Halogenabenzene, 11
Halogen-bonding, 11
Hammett parameter, 16, 33, 40
Heavy atom, 4–6
Helical, 12
Helix theory, 155, 188
Hessian matrix, 10, 17
Heterotopicity, 186
H---H *BCP*, 18, 37, 38
Hybrid molecular graph, 67
Hybrid QTAIM-Ramachandran plot, 58
Hydrocarbon, 12
Hydrogen atom, 19, 42
Hydrogen bonding, 11, 16, 36
Hydrogen-bond network, 50
Hydrogen transfer tautomerization, 38
Hyper-conjugation, 170, 171

**I**
Ice phase, 47, 49
Ice XI, 24, 26
Iconicity, 87
Incommensurate phase transition, 37
Infrared, 11
Infrared active mode, 11
Intersystem Crossing (ISC), 206
Intramolecular bending, 133
Intra-molecular proton transfer, 33, 38

Inverted singlet-triplet gap, 206, 207
Ionic electronic configuration, 87
Ionization energy, 106
Ionization potential, 106
IR-inactive mode, 149
IR-responsivity, 74, 76, 77
Iso-energetic phenomena, 11, 12
Isomer, 15, 16, 20, 23, 25, 26, 30, 31, 40, 42
Isotope effect, 11

**K**
Kasha's rule, 206

**L**
Lactic acid, 22, 154, 155, 157–159, 166
Laplacian, 19, 36, 38
Laser pulse, 12, 80
Lewis structure, 82, 83
$Li_6Si_6$, 22
$Li_m$ ($m$= 2 − 5), 107–109
Light-driven device, 192
Linear Combination of Atomic Orbitals (LCAO) approximation, 2
Lithium, 93, 107, 109, 124
Localized electron pair, 16
Local kinetic energy density, 33
Local maximum, 17
Local minimum, 18
Local minimum structure, 9
Local potential energy density, 33
Lone pairs of electrons, 4
Low-lying excited state, 206
Lycosin peptide, 61, 62

**M**
Magainin-2 peptide, 56–62
Mass spectrometry, 150
Maximum degree of facile character, 86
Metallic, 15, 16, 37, 38, 42, 43
Metallic bond character, 16
Metallicity, 16, 31, 36, 38–40
Metal Organic Frameworks (MOFs), 187
*Meta*- substituent, 35
Minimum degree of facile character, 86
Mixed chirality, 175, 179
Mixed hybrid QTAIM-Ramachandran plot, 58
Molden2aim, 8
Molden wave function format, 8
Molecular boundary, 106
Molecular Coulomb potential integral, 104
Molecular device, 12
Molecular electronics, 192, 205, 210, 211, 213, 214
Molecular geometry, 16, 72
Molecular graph, 18–21, 23, 26–31, 33, 34, 36–41
Molecular rotary motor, 12, 191, 193–196
Molecular switch function, 130
Molecular wires, 12, 130
Molecule, 15–20, 23, 25, 31–33, 36, 40, 43
Monobromoethane, 22
Monochloroethene, 22
Monochloroethyne, 22
Moore's Law, 203
Morse relation, 20
MP2 potential energy surface, 11
Multi-electronic state, 11, 65, 80
Multi-reference DFT, 33

**N**
Natural Transition Orbital (NTO), 82, 84, 88, 89
Nearest Neighbor Ring Critical Points (*NNRCP*), 15, 31, 32, 42
Nearsightedness, 38
Newton-Raphson, 9
Next Generation QTAIM (NG-QTAIM), 47, 48, 62
NG-QTAIM, 11, 12
NG-QTAIM interpretation of the chemical bond, 88
Non-adiabatic dynamics, 193, 194
Non-Euclidian geometry, 15, 16, 19
Non-ionizing ultra-fast laser pulse, 213
Non-Nuclear Attractor (*NNA*), 17, 24, 29, 43
Non-reacting uniform electron gas, 6
Normal modes of vibration, 10, 11
Nuclear coordinate, 1
Nuclear Critical Point (*NCP*), 16–18, 20, 27, 31, 39, 43
Nuclear Hamiltonian, 132
Nuclear Magnetic Resonance (NMR) spectroscopy, 150
Nuclear motion, 12
Nuclei, 15, 17, 18, 31, 34, 42
Nucleophilic attack, 166
Nucleus, 17, 31, 42
Null-chirality, 170, 173

**O**
OpenMOLCAS code, 208

Open-shell system, 7
Optical activity, 155, 158
Optical isomer, 154
Organic emitter, 206
*Ortho-* substituent, 33, 35
Outer valence orbital, 5
Oxirane, 127, 142, 147, 149

**P**
*Para*-substituent, 33, 35–37
Partial symmetry breaking, 154
Path-packet, 66–70, 76, 84, 86–88
Penta-2,4-dieniminium cation (PSB3), 87, 89
Permutation-inversion isomer, 130, 138, 148
*p* function, 4
Phase transition, 24, 26, 37, 41
Phenanthrene, 18, 19
Photochemical, 11, 12
Photochemical ring-opening reaction, 33
Photochemistry, 65, 68, 89
Photochromic, 80
Photoexcitation circular dichroism experiment, 160, 166, 167, 186
Photo-isomerization, 47, 48, 54, 63
Photoreaction, 36
Poincaré-Hopf relation, 15, 19, 20, 23, 25, 28, 29, 40
Polarization basis functions, 4, 8
Polarization effect, 205, 207–209
Pople's Basis Set, 5
Post-Transition State Bifurcations (PTSB), 186
Potential Energy Surface (PES), 9, 11, 16, 24, 25, 27, 28, 33, 42, 43
Precession, 11
Projected Density of States (PDOS), 48–51, 62, 63
PV6Z basis set, 107
Pyridine, 22
Python, 130

**Q**
QChem code, 207
QTAIM interpreted Ramachandran plot, 48, 55, 58–60, 62, 63
Quantum geometry, 15
Quantum mechanics, 16
Quantum stress tensor, 94, 104
Quantum Theory of Atoms in Molecules (QTAIM), 1, 10, 11
Quantum Topology Phase Diagram (QTPD), 15, 21, 23–31, 36, 40–43
Quantum yield, 201
Quantvec NG-QTAIM software, 10

**R**
(R)-1-chloro-1-phenylethane, 166, 168
Ramachandran plot, 11
Reaction coordinate, 54, 55
Refractive indices, 155, 158
Relative energy, 154, 155, 168
Relativistic effects, 6, 11
Response, 49, 51, 53–58, 61
Retinal chromophore, 47, 48, 54, 63
Ring Critical Point (*RCP*), 21, 23
Ring-opened product, 81
Ring-opening reaction, 12
Ring restoring reactions, 88
Rotational band, 50
Rotational isomer, 154–157
Rotational vibrational mode, 48–50

**S**
S-1,5-diamino-[4]cumulene, 164–166
S-1,5-dimethyl-[4]cumulene, 164–166
Saddle point, 9, 10, 17, 18
Scalar measure, 138, 149
Scalar QTAIM, 10, 11, 15, 40, 41
Scanning Tunneling Microscope (STM), 162
Schrodinger equation, 1
Second generation stress tensor trajectories, 154, 169, 188
Self-consistent field calculation, 2
Semi-empirical calculations, 4
Sequence parameter, 128
*s* function, 4
Shared-shell bonding, 36
Shift vector, 128, 129
Single bond character, 80
Singlet-triplet gap, 206, 213
$(SiO_2)_6$, 23
Slater Type Orbitals (STOs), 4
Small water cluster, 15, 33, 42
$S_N2$ reaction, 153, 158, 166, 168, 186
Solid, 15–17, 20, 24–26, 28, 33, 36, 40, 41, 43
Spanning QTPD, 21, 23, 26, 29, 40
Spindle structure, 95
Spin restricted, 7, 8
Spin unrestricted, 7, 8
Split valence basis sets, 4

SR-ZORA Hamilton, 88
Stable minima, 21
Static E-field, 12
Steepest Descent, 9
Stereochemistry, 127, 130, 149
Stereo-control, 193, 212
Stereoisomer, 12
Stereoselectivity catalyst, 154
Steric hindrance, 61, 62, 155, 158
Stress tensor, 11, 12, 16, 17, 31, 33, 36–38, 40, 41
Stress tensor polarizability, 33, 35, 36, 40
Stress tensor response, 51
Stress tensor stiffness, 40
Stress tensor trajectory, 128–130, 134, 136, 140, 142, 148, 149
Stretching band, 50
Sulphur decorated DTE switch, 201
Surface integral, 104
Switch, 38, 39
Switch performance, 197, 198, 211
Switch position, 197–200
Symmetric stretch vibrational mode, 49, 50
Symmetrization, 84
Symmetry breaking, 11, 12, 138, 142, 149

**T**
Tautomerization, 12
Tensile eigenvector, 94, 95
Tetrahedran, 18, 19
Tetrasulfur tetranitride, 22, 24, 26, 29, 31, 40
Thermally-Activated Delayed Fluorescence (TADF), 12
Third generation eigenvector-space directed trajectory, 213
Thomas-Fermi-Dirac Mode, 6
Time Dependent (TD-DFT), 17
Topological catastrophe, 95
Topological complexity, 20, 40
Topological isomer, 16
Topologically stable, 17, 21, 25, 30
Topology, 16, 19–21, 23, 28, 30, 40
Torquoselectivity, 12
Torsion coordinate, 84
Total electronic charge density distribution, 16, 17
Total local energy density, 15, 18, 33
*Trans*-isomer, 23
Transition metal, 6
Transition metal atom, 6
Transition state, 4, 6, 7, 9, 10, 21, 39
Transition State Inward Conrotatory (TSIC), 141, 148
Transition State Outward Conrotatory (TSOC), 141, 148
Translational vibrational mode, 48, 50
Trigger mechanism, 198
Tritium, 11

**V**
Vector-based quantum chemical theory, 146
Vector-based representation of the chemical bond, 66, 72
Vertical excitation, 101
Vibrational frequency, 10

**W**
Walden inversion, 166
Water, 11
Water pentamer, 127, 138, 148
Wave-function, 1, 10, 17

**X**
X-ray Diffraction (XRD), 17, 114

**Z**
Zero-flux condition, 106